VISUALIZATION AND ANALYSIS OF MULTISPECTRAL IMAGE DATA

VISUALISIERUNG UND ANALYSE MULTISPEKTRALER BILDDATEN

DISSERTATION

zur Erlangung des Grades eines
Doktors der Ingenieurwissenschaften (Dr.-Ing.)

von
Dipl.-Inform. Björn Labitzke

eingereicht bei der Naturwissenschaftlich-Technischen Fakultät
der Universität Siegen
Siegen 2013

1. Gutachter:	Prof. Dr. Andreas Kolb
2. Gutachter:	Prof. Dr. Volker Blanz
Vorsitzender:	Prof. Dr. Roman Obermaisser

Tag der mündlichen Prüfung: 28. Oktober 2013

Printed on non-aging wood- and acid-free paper.
Gedruckt auf alterungsbeständigem holz- und säurefreiem Papier.

Zusammenfassung

Die multispektrale Bildgebung wird im Rahmen verschiedenster Anwendungsgebiete eingesetzt. Die neuesten technologischen Fortschritte, wie die Entwicklung von kostengünstigen und kompakten Multispektralkameras, zeigen die anhaltende Popularität dieses bildgebenden Verfahrens. Impliziert durch diese Popularität besteht ein großer Bedarf an generischen Lösungen mit denen Nutzer für eine Vielzahl von Anwendungsbereichen einen Zugang zu den relevanten Informationen eines Datensatzes erhalten können, z.B. zu den konstituierenden Spektren. Doch aufgrund der typischerweise hohen spektralen Informationsdichte ist die Interpretation der Daten zum einen komplex für den Nutzer und zum anderen zeitaufwendig für den Computer. Dementsprechend werden für die anspruchsvolle Interpretation der Daten effiziente Algorithmen und intuitive Visualisierungsmethoden zur Unterstützung benötigt, um das Verständnis für die Daten zu verbessern und letztlich einen Nutzen aus ihnen ziehen zu können.

Diese Arbeit befasst sich mit den genannten Herausforderungen vor allem durch die Präsentation von effizienten, intuitiven und generischen visuellen Analysemethoden zum einen zur multispektralen Bildsegmentierung und zum anderen zur spektralen Mischungsanalyse. Die Schlüsselfunktion dieser Ansätze ist jeweils die Einbindung des Nutzers durch visuelles Feedback, was eine zielführende Exploration erlaubt. Basierend auf dieser visuellen Unterstützung, wird es dem Nutzer ermöglicht Ergebnisse von automatischen Analysemethoden zu explorieren, zu beurteilen und diese, falls erforderlich, auch zu modifizieren.

Mit dem Ziel ein tiefergehendes Verständnis für die Verarbeitung von multispektralen Bilddaten zu schaffen, werden neben den visuellen Analysemethoden außerdem eher grundlegende Herausforderungen und Konzepte der Verarbeitung diskutiert.

Abstract

Multispectral imaging is applied in the context of various applications. Recent technological advances, like the development of low-cost and compact multispectral imaging cameras, show the ongoing popularity of this imaging technique. Because of this popularity, there is a high demand for generic solutions to enable a user to get access to relevant information, e.g. constituent spectra, for a large variety of application domains. But, due to the typically high-density of spectral information, usually the interpretation, on the one hand, is complex for humans and on the other hand, is time-consuming for computers. Thus, the challenging task of interpretation consequently requires efficient data analysis algorithms and intuitive visualization methods to support the understanding of the data and to finally make use out of them.

This thesis addresses the identified challenges mainly by the presentation of efficient, intuitive and generic visual analysis methods for both, multispectral image segmentation and linear spectral unmixing. The key function of these methods is the involvement of a user by visual feedback to enhance the guidance in the exploration. Based on the visual support, the user is enabled to explore and assess results of automatic analysis algorithms and to optimize them, if necessary.

In addition to the visual analysis methods and with the aim to provide a further understanding of the processing of multispectral image data, also more fundamental challenges and concepts of the processing are discussed.

Contents

Introduction

In the last years, multispectral sensors have been applied in a growing number of application areas, like remote sensing, astronomy, physics, cultural heritage, cosmetics, medicine, biometrics, safety, high-accuracy color printing and computer graphics, because of their strong potential [HSB02]. Recent technological advances in spectral imaging, like the development of low-cost and compact multispectral imaging cameras [HKW12] or 3D scanning systems that incorporate hyperspectral imaging [KHK*12], further show the popularity of this imaging technique.

In general, multispectral imaging yields an image series of a specific range of frequencies across the electromagnetic spectrum. Commonly, these data are referred to as multispectral image cubes that have three dimensions, two spatial dimensions representing the surface position and one spectral dimension that represents the spectral distribution, allowing for a very deep investigation of scene characteristics. Thus, each pixel in the multispectral image does not provide only grayscale or color information but in fact has associated a spectrum, i.e. n-dimensional vector of values with each value being the measurement of the reflectance for a specific spectral band. Based on this, one can differentiate materials not only on color but also on spectral properties beyond the visible range. But, due to the typically high-density of spectral information in multispectral image cubes, the interpretation, on the one hand, is complex for humans and on the other hand, is time-consuming for computers. Thus, the challenging task of interpretation consequently requires efficient data analysis algorithms and visualization methods to improve the understanding of the data and to finally make use out of them. Here, common analysis and visualization techniques typically provide domain-specific solutions. While these solutions are able to achieve good results for the addressed domain, these methods most often are failing when they are applied away from their original field of application. But, because of the increasing popularity of this imaging technique, there is a high demand for generic solutions to enable a user to get access to the relevant information, e.g. constituent spectra, i.e. materials, for a large variety of application domains.

Problem Statement

Visual analysis [KAF*08], combining automated analysis techniques with interactive visualizations allows users to explore data in an efficient and intuitive way for an effective understanding, reasoning and decision making on the basis of very large and complex datasets. Keim et al. [KAF*08] states that the aim of visual analysis includes the creation of tools and

techniques to enable users mainly to detect the expected and discover the unexpected. Here, regarding the authors, it is also vital to synthesize information and derive insight from massive, dynamic, ambiguous, and often conflicting data. In the context of multispectral imaging such an interactive exploration approach poses, beside intuitive interaction methodologies, the main objectives in three areas:

1. **High-Dimensional Data Analysis:** The data analysis of multispectral data, e.g. to determine a complete set of constituent spectra, is not a straight forward issue and has to deal with challenges like imperfections in the data or low signal-to-noise-ratio (SNR). Moreover, the similarity measures for vectors in high-dimensional space are challenging too. For instance because of the high-information loss due to mapping down to single scalar values or due to the fact that the choice of similarity measure strongly depends on the analysis task itself.

2. **Scientific Visualization:** The visualization must provide specialized methods to synthesize the analysis results and spectral information. Here, a general visualization problem is the high dimensionality of spectral information at each pixel, which makes it difficult, right up to impossible, to visualize all aspects in one single image [PvdH01].

3. **Processing Speed:** The usual complexity of multispectral image cubes needs efficient processing methods to provide the user in a timely manner with visual feedback during the interactive exploration.

In this dissertation, techniques and methods, which address the three challenging areas, are presented mainly with the focus to achieve descriptions of efficient, intuitive and generic visual analysis methods in order to facilitate the interpretation of the data and to enhance the knowledge. Thus, mainly is aiming to involve the user in the multispectral analysis process in order to achieve opportunities to explore, assess and to optimize results.

In addition to the visual analysis methods and with the aim to provide a further understanding of the processing of multispectral image data in general, also more fundamental challenges and concepts of the processing are discussed.

Contributions

As presented before, the aim of this dissertation poses the significant challenges in three areas. Correspondingly, the specific contributions are divided with respect to these areas:

1. **High-Dimensional Data Analysis**

   - A semi-automatic endmember extraction method for unsupervised generic constituent determination in multispectral data. Here, the robustness of automatic endmember extraction algorithms is improved by an interactive preprocessing step for outlier masking [LBK12]

- A general method for the assessment of vector attribute variability by measuring the minimum efforts that are needed to transform a variable vector into a representation of maximum similarity with a target vector [SLKV11, SLB11].
- Compensation of geometric and chromatic aberration in the acquisition of RGB-images, also with application to multispectral imaging, by high-quality estimation of point spread functions (PSF) and a cross-channel prior that enforces gradient consistency [HRH*13].

2. **Scientific Visualization**

   - A juxtaposed complementary view for the evaluation of the completeness of endmember sets, also including several exploration means [LBK12].
   - Expressive spectral error visualization which purposefully provides user guidance in a visual analysis approach in order to finally enhance the results of spectral mixture analysis [LUK13].
   - A Radviz-based visual analysis tool for the semi-automatic segmentation of multispectral images. This approach also includes a novel cluster evaluation view which subdivides cluster that consist of different constituents in order to improve the segmentation, if necessary [LPK13].

3. **Processing Speed**

   - The computation of non-negative coefficients for spectral mixture analysis with respect to a modified endmember set is accelerated by utilizing the information of a previous unmixing in order to predict the coefficients of the modified set. Moreover, a progressive unmixing scheme is included that allows user interaction during time-consuming calculations [LBK12].
   - An approach that directly estimates non-negative coefficients on the basis of residual errors that are generated by successive orthogonal subspace projections of alternating endmembers [LK13]. The major benefit of this approach, compared to [LBK12], is that no results of a prior unmixing run are required.

Outline

The structure of this dissertation consists of the following six chapters:

Chapter 1 provides the underlying terminology of this thesis and the necessary fundamentals about multispectral image processing.

Chapter 2 shows some exemplary application scenarios of multispectral imaging to provide some general impressions of application tasks. But, the focus of this chapter is the discussion of requirements and challenges of multispectral image processing in order to conclude in final

design goals for the proposed visual analysis methods.

Chapter 3 discusses reasons for blur in multispectral imaging and qualitatively evaluates the consequences for the data analysis. Moreover, a conceptional proposal of a deblurring approach is proposed for multispectral imaging, which uses means of computational photography. The chapter ends with a summary of the observations.

Chapter 4 focuses on distinct aspects of multispectral data analysis. Starting with the, more fundamental, discussion of similarity measures in high-dimensional data spaces, the chapter continues with an unsupervised approach for the generic determination of constituent spectra for spectral mixture analysis. Before the general speedup of inverse operations in spectral mixture analysis is discussed, the improvement of automatic analysis algorithms by interactive preprocessing is shown. The chapter concludes with a summary.

Chapter 5 introduces visualization method for purposeful user-interaction. First, it explains a complementary visualization method, including exploration means, for the evaluation of spectral mixture analysis results. Subsequently, methods for expressive spectral error visualizations in the context of spectral mixture analysis are presented. Before the chapter finally summarizes the achievements, a semi-automatic and Radviz-based segmentation approach for multispectral data is presented.

Chapter 6 shows an application example to demonstrate the usage of the proposed visual analysis methods.

Finally, the dissertations ends with a summary and conclusions, which also discusses some aspects of future work.

Chapter 1

Fundamentals

This chapter mainly gives a general overview of multispectral image processing. The explanation is oriented on an abstract processing pipeline to group the various techniques. Before the overview of the pipeline is presented, the underlying terminology and notation of this thesis is defined in the first section.

1.1 Terminology and Notation

In general, multi- and hyperspectral imaging devices acquire high dimensional datasets with high-density spectral information. Commonly, these datasets have three dimensions, two spatial dimensions and one spectral dimension, and are often denoted as multi- or hyperspectral image cubes (see. Fig. 1.1). Here, each pixel (x,y) in fact has associated a spectrum $\vec{s}(x,y)$, which is usually regarded as n-dimensional vector, where n is the number of spectral bands (wavelength λ). Consequently, each scalar value $\vec{s}(x,y,\lambda)$ in such a cube is the measured reflectance (or absorbance) value of a specific spectral band at (x,y).

Considering common literature related to multi- and hyperspectral imaging [Cha03, GGB07], the distinction of both imaging techniques is not well-defined. However, the con-

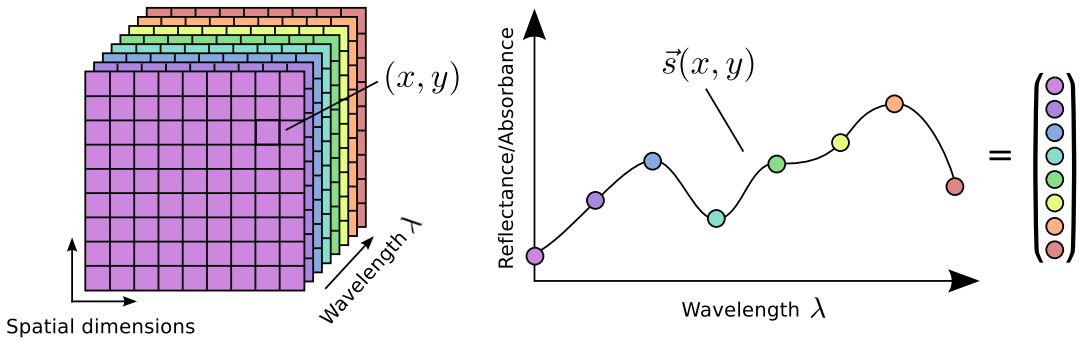

Figure 1.1: Multispectral image cube illustration (left) and a spectrum of an image location (right). A spectrum with n spectral bands is usually considered as n-dimensional vector.

Chapter 1

Fundamentals

This chapter mainly gives a general overview of multispectral image processing. The explanation is oriented on an abstract processing pipeline to group the various techniques. Before the overview of the pipeline is presented, the underlying terminology and notation of this thesis is defined in the first section.

1.1 Terminology and Notation

In general, multi- and hyperspectral imaging devices acquire high dimensional datasets with high-density spectral information. Commonly, these datasets have three dimensions, two spatial dimensions and one spectral dimension, and are often denoted as multi- or hyperspectral image cubes (see. Fig. 1.1). Here, each pixel (x,y) in fact has associated a spectrum $\vec{s}(x,y)$, which is usually regarded as n-dimensional vector, where n is the number of spectral bands (wavelength λ). Consequently, each scalar value $\vec{s}(x,y,\lambda)$ in such a cube is the measured reflectance (or absorbance) value of a specific spectral band at (x,y).

Considering common literature related to multi- and hyperspectral imaging [Cha03, GGB07], the distinction of both imaging techniques is not well-defined. However, the con-

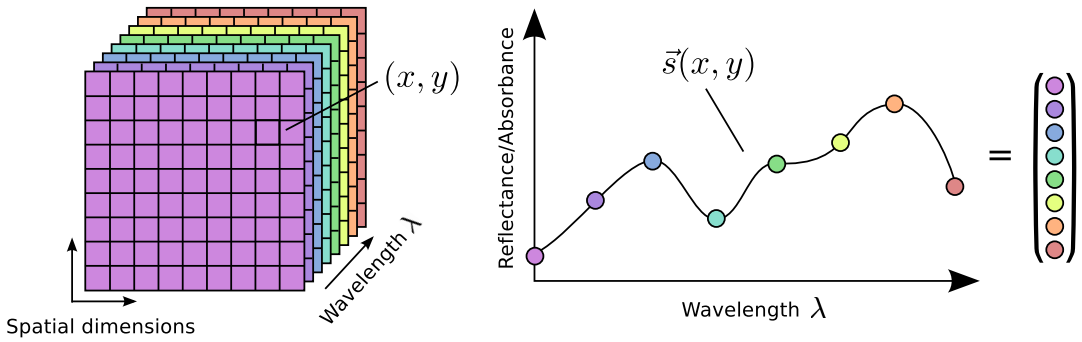

Figure 1.1: Multispectral image cube illustration (left) and a spectrum of an image location (right). A spectrum with n spectral bands is usually considered as n-dimensional vector.

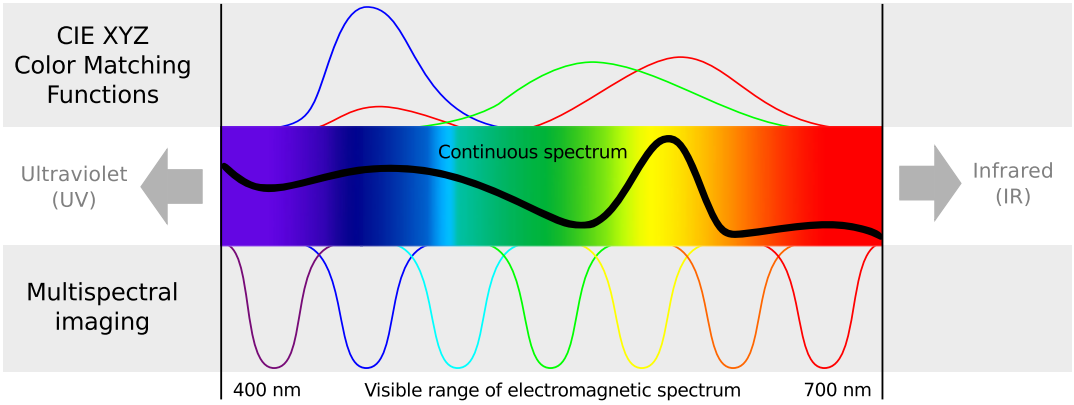

Figure 1.2: Illustrative comparison of RGB camera and multispectral imaging, where the common tristimulus CIE XYZ color matching functions, confer Appendix B.3, are used to visualize the concept of RGB cameras. As can be seen, multispectral imaging achieves a more accurate representation of the continuous spectrum. Thus, allows to for instance distinguish a mixed and a pure yellow tone.

sensus of the literature poses that, the distinction mainly is related to the number of spectral bands and the spectral density:

- Hyperspectral imaging usually consists of hundreds of narrow bands that typically cover a large range of the electromagnetic spectrum.
- Multispectral imaging usually consists of a smaller number of bands, typically lower than 100, and the spectral density is broader and covers a smaller range of the electromagnetic spectrum, e.g. 400 - 1000 nm.

Since there is no strict definition of the term hyperspectral and for the sake of simplicity, both techniques multi- and hyperspectral imaging and the corresponding data are collectively referred to as multispectral imaging and multispectral data in this thesis.

1.2 Multispectral Image Processing – A General Overview

Multispectral imaging is the process of acquiring images series of a specific range of frequencies across the electromagnetic spectrum. As seen in the previous section, this image series also can be considered as an multispectral image cube, where each pixel in fact has associated a discrete spectrum, which approximates the continuous electromagnetic spectrum. Compared to traditional RGB cameras, where the continuum of an electromagnetic spectrum is converted into three discrete values, the denser sampling and more narrow filters used in multispectral imaging lead to a more accurate, but still discrete representation of the continuum of a spectrum, see Fig. 1.2. Based on the more detailed representation of a continuous spectrum, one can more precisely differentiate materials, not only according to color but also according to spectral properties beyond the visible range. However, due to the associated complexity of the

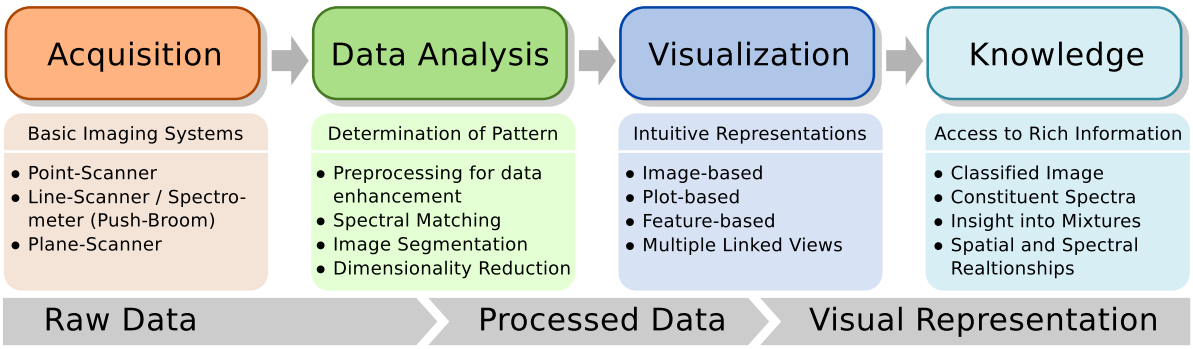

Figure 1.3: Conceptional overview of a multispectral image processing pipeline.

multispectral data, the creation of a visual representation to get access to the rich information is not a straightforward issue and usually needs sophisticated analysis or human interaction.

Common principles and methods of multispectral image processing are discussed in the following. Here, a general and conceptional multispectral image processing pipeline is introduced to achieve a more structured introductory discussion. The processing pipeline is illustrated in Fig. 1.3. Starting with the **acquisition** of the multispectral raw data, the next step usually corresponds to the **data analysis**, which determines pattern in the multispectral data, e.g. to extract spectral characteristics. After the analysis typically a **visualization** step follows to create intuitive visual representations of the processed data or achieved analysis results. Finally, based on the intuitive visual representations a human can gain **knowledge** of the high-dimensional data and gets access to the rich information. Here, rich information may include:

- a segmented or classified multispectral image,
- the constituents of the data to get insights to spectral mixtures,
- insights to the spectral distribution to identify spectral ranges of convergence or divergence,
- contextual relationships between spectral and non spectral features, e.g. relation of absorbance values and the water content of plants,

just to name a few. Thus, the basic goal of multispectral image analysis is mainly the classification or discrimination of objects [BG04]. Next, the essentials of the mentioned stages of the pipeline are discussed.

1.2.1 Acquisition

Multispectral imaging has a long history and originates from the field of remote sensing. Here, the high spectral density was used to facilitate the identification of materials [VG88]. In general, a multispectral imaging system mainly is composed of three elements:

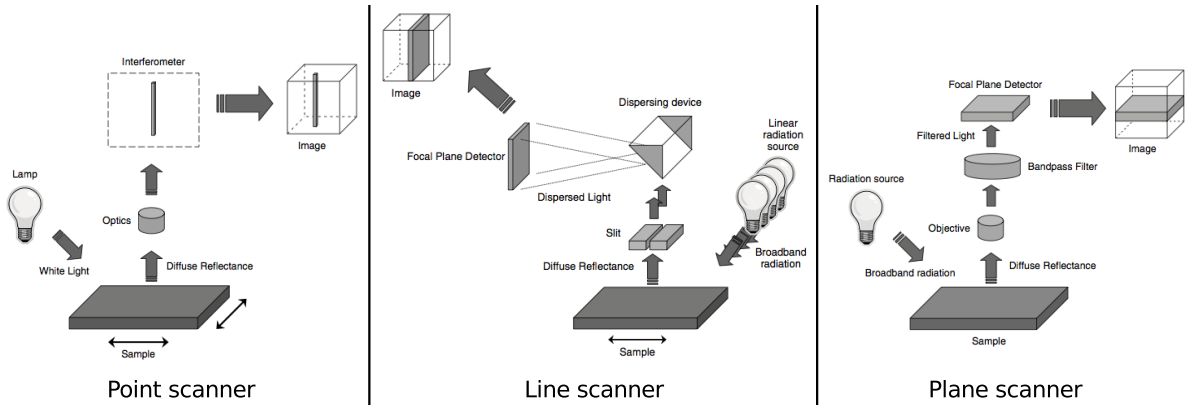

Figure 1.4: Overview of the three basic multispectral imaging setups: point scanner, line scanner and plane scanner. The images are taken from [GGB07].

1. a light source (covering the electromagnetic range of interest),
2. a filtering device to disperse the light into distinct spectral bands and
3. a sensor to detect and store the spectral contributions of a sample [GGB07].

Accordingly to Geladi et al. [GGB07], typically, the utilized filtering device defines the camera configuration, which basically can distinguished by the type of acquired spatial information: point scan, line scan, or plane scan (cf. Fig. 1.4). These three basic camera configurations are briefly described in the following paragraphs according to Geladi et al.

Point Scanner In this camera setup a spectrum is measured at a time for a single position on a sample. In order to measure a whole multispectral image of the sample, the sample has to be moved systematically in the two spatial dimensions, such that the whole surface is covered. Due to the continuous repositioning of the sample, the acquisition of a complete dataset can be very time consuming. But, on the other hand, these kind of setups are able to acquire very stable and high resolution spectra. Common devices that are based on this basic principle are interferometer or confocal Raman microscopy (CRM).

Line Scanner (Spectrometer) The line scanning devices acquire all spectra at a time of a spatial line by using a dispersing element, e.g. prism, that disperses the incident light into the wavelengths. Thus, these devices make use of the physical principle that the refraction index of a material typically is wavelength dependent. When acquiring a complete two-dimensional multispectral dataset the sample or the device has to be moved in one spatial dimension. Because of this successive line by line measuring, these scanning devices are also called push broom scanner. The movement of a sample most often is done by using assembly lines, e.g. for food quality inspections. When the device has to be moved there are mainly two common

ways, first by mounting the devices on e.g. airplanes or satellites, or second by using a rotating mirror to sweep across the sample. Since a whole spectral scan-line can be measured at a time, without changing the filter elements, these setups need less time to acquire a complete dataset than the point based scanners. The acquisition time is mainly limited by the read out time of the camera sensors. These scanning principle has a long history in the field of remote sensing, e.g. Airborne Visible/Infrared Imaging Spectrometer (AVIRIS) [VGC*93] or Hyperspectral Digital Imagery Collection Experiment (HYDICE) [BCA95].

Plane Scanner The plane scanning devices use bandpass filter in the optical path between the optical lens and the camera sensor. These filter-based scanners acquire a two-dimensional image of a selected wavelength. By successive adjusting the bandpass filter and capturing, a complete multispectral dataset is acquired. Here, the simplest example of a device is the utilization of a computer-controlled filter wheel that holds filters of different wavelengths, e.g. as described in [BSA10]. These setups usually are quite affordable. However, as they operate in a mechanical manner, they are quite slow and have a very limited number of bands, e.g. ten. The utilization of electronically tunable filter, like liquid crystal tunable filter (LCTF) [HSB02] or acousto-optic tunable filter (AOTF) [SOKH08], is very common for this scanning principle. These filter usually are quite costly, partially due to a small number of manufacturers. Beside the high costs, the major drawbacks are, that about the half of the transmittance is lost by the utilization of a LCTF and that an AOTF requires collimated light. However, compared to mechanical devices the acquisition is faster and the spectral resolution is much higher, e.g. by considering a full width at half maximum (FWHM) of 10 nm the number of spectral bands is 31 for the visible wavelength range. While all before mentioned methods are using a bandpass filter in the optical path of the multispectral imaging device to separate the wavelength ranges, it is also possible to achieve such a separation by narrow-band illumination, e.g. by using light emitting diodes. The main advantage of such methods, besides lower costs, is that there is not such a high loss of transmittance as for instance when using a LCTF. But those illumination approaches have a high demand on their lighting environment since they can easily be affected by extraneous light.

In summary, the common multispectral imaging systems remain complex, expensive and due to the huge amount of data they pose significant challenges in data management in terms of storage and processing [HSB02]. Moreover, typically no scanning device is able to acquire high-resolution spectra of moving samples, especially not for point scanners. Thus, unexpected movements of samples usually would cause image registration problems for filter-based scanners or uncontinuous spatial measures for spectrometers. In other words, moving objects of interest lead to spectral errors in filter-based measurements or to spatial errors for spectrometers. Comparing both, a filter-based system has the advantage, that the band selection is much more flexible and therefore the acquisition process can be accelerated by e.g. capturing only spectral bands that are of interest for a specific analysis task.

1.2.2 Data Analysis

Mutlispectral image data contain rich information, but the processing of the data poses several challenges, like computational requirements, information redundancy, the identification of relevant information, and the modeling accuracy [BG04]. The part of data analysis can be divided into two parts. On the one hand there is the **preprocessing** of the data to enhance the image quality, e.g. reducing the noise, and on the other hand, there is the general multispectral **data analysis** e.g. revealing spectral characteristics. Analysis tasks of the general data analysis stage commonly are

- similarity measures, so-called **spectral matching**,
- **segmentation**, or
- **redundancy reduction**.

Necessary details of all analysis tasks and methods for this thesis are presented within the upcoming sections.

Preprocessing of Multispectral Image Data

Preprocessing of multispectral image data can be expedient in order to improve the results of the subsequent data analysis. For instance, when considering the popular filed of remote sensing, Bioucas-Dias and Plaza [BDP10] stated that the atmosphere attenuates and scatters light, so that its presence affects the radiance at the sensor. Therefore, these effects of the atmosphere typically are removed by an **atmospheric correction** step, which arguably is the most important part of the preprocessing of remotely sensed data [HPA*10]. This is especially true, when it is the aim to compare and analyze several different images. According to Bioucas-Dias and Plaza [BDP10], the atmospheric effects usually can be compensated by converting the acquired radiance into reflectance (cf. Appendix B.4), which is an intrinsic property of the materials.

For an application independent view, a more important preprocessing task is the image enhancement by **noise reduction**. Based on the main idea that each channel is smoothed independently, the main challenge is to estimate how much each channel has to be smoothed. Many methods have been proposed in the literature for the noise reduction of multispectral data. One of the first attempts for noise reduction for multispectral data and some of the standard solutions in remote sensing are the maximum noise fraction (MNF) [GBSC88] and the noise adjusted principal components (NAPC) [LWB90], where NAPC mathematically is equivalent to MNF [BDP10]. Both methods order the channels in terms of image quality, i.e. they maximize the SNR. Here, noise reduction is achieved by smoothing or removing the noisiest channels. Moreover, also wavelet-based methods have been proposed, like in [Sch04] where a multiband thresholding method for multivalued images is presented. The rationale of this approach is that signals and noise can be separated in the wavelet-domain, since typically existing redundancies between multivalued bands are highly correlated while the sensor noise between these bands is decorrelated [Sch04]. All these methods individually

Distance measure	Formula
Spectral Angle Distance	$\mathrm{SAD}(\vec{x},\vec{y}) = \arccos\left(\frac{\langle\vec{x},\vec{y}\rangle}{\|\vec{x}\|_2\|\vec{y}\|_2}\right)$
Spectral Correlation Angle	$\mathrm{SCA}(\vec{x},\vec{y}) = \arccos\left(\frac{\mathrm{SC}(\vec{x},\vec{y})+1}{2}\right)$ with $\mathrm{SC}(\vec{x},\vec{y}) = \frac{\langle\vec{x}-\mu\vec{x},\vec{y}-\mu\vec{y}\rangle}{\|\vec{x}-\mu\vec{x}\|_2\|\vec{y}-\mu\vec{y}\|_2}$
Spectral Information Divergence	$\mathrm{SID}(\vec{x},\vec{y}) = \left\langle \frac{\vec{x}}{\mu\vec{x}} - \frac{\vec{y}}{\mu\vec{y}}, \log\left(\frac{\vec{x}}{\mu\vec{x}}\right) - \log\left(\frac{\vec{y}}{\mu\vec{y}}\right)\right\rangle$
Spectral Gradient Angle	$\mathrm{SGA}(\vec{x},\vec{y}) = \mathrm{SAD}\left(\mathrm{SG_x},\mathrm{SG_y}\right)$ with $\mathrm{SG_x} = (x_2-x_1, x_3-x_2, \ldots, x_n-x_{n-1})$, $\mathrm{SG_y}$ analog
Normalized Euclidean Distance	$\mathrm{NED}(\vec{x},\vec{y}) = \left\|\frac{\vec{x}}{\|\vec{x}\|_2} - \frac{\vec{y}}{\|\vec{y}\|_2}\right\|_2$

Table 1.1: Common similarity measures in multispectral data analysis.

smooth the different channels by applying a constant smoothing level to each image. Acton and Landis [AL97] presented the first approach to apply anisotropic diffusion to multispectral images. The main idea was to use the local gradient magnitude to influence the level of smoothing, e.g. inhibit smoothing at edges. Based on Acton and Landis, an approach that combines MNF with anisotropic diffusion was presented in [LMHM02]. One challenging task of anisotropic diffusion is the identification of edges in multispectral images, since not all materials are visible throughout all bands, because of the wavelength dependent index of refraction. Here, a very recent method have shown a very promising demonstration of the edge identification by computing the distances of materials in the space of a self organizing map [JA11]. Beside the challenge of edge detection in the context of anisotropic diffusion in general, all methods, as mentioned above, require a robust parameter estimation in order to enhance the data without destroying spectral characteristics.

Spectral Matching

Spectral matching is an important task in multispectral data analysis, e.g. for the classification of found spectra by matching them against a spectral library [VG08] or for the target detection [RG05]. The basic principle of the matching is, that the degree of similarity or dissimilarity between spectra typically is quantified by the outcome of distance measures. Here, the most important aspects are the choice of distance measure and the threshold used for differentiation between similarity and dissimilarity [RG05]. The mostly used distance measures are shown in Table 1.1. Beside these metrics, also the euclidean distance often is applied, whose deviate is the NED, which provides a range of resulting values. Such an interval of the resulting values is very important for unsupervised analysis methods to apply appropriate thresholds. In multispectral data analysis the most frequently used distance measure is the SAD, mainly since its measuring angle is invariant to the scaling of spectra [Kes03]. Robila and Gersham [RG05] have tested most of these matching functions and have discovered in their experiment that NED and SID had outperformed SAD, SCA and SGA. While SAD and SCA perform comparably, the SGA performs worst in the experiment. Recently, Jordan and Angelopoulou

[JA12] also have tested the influence of different metrics with respect to multispectral image segmentation results. The authors figured out, that SAD and NED perform comparable and most successful, but are prone to noise in dark image regions. Moreover, they included SID in their test, which often achieves results comparable to the other two, but is not as reliable due to a high standard deviation. Considering both, [RG05] and [JA12] already demonstrates that the choice of measure depends on the application and on the data itself, e.g. noise level. Finally, there is no general recommendation of a single metric that performs best with all conditions. Thus, a multispectral analysis approach usually should consider the usage of different metrics to achieve the best possible result. But at the same time, a vast collection of different measures can easily confuse a user by the choice of an appropriate measure which is suitable for his current problem.

Multispectral Image Segmentation

Unsupervised classification is a very common approach when no previous knowledge about the data, e.g. unlabeled data, is available. Typically clustering algorithms perform an unsupervised analysis to group unlabeled pattern into meaningful clusters that are obtained solely from the data [JMF99]. In the majority of cases, multispectral image data are unlabeled and therefore need unsupervised data analysis approaches, like clustering methods to achieve a segmented multispectral image. One of the most used and simplest algorithm is the *k*-means [Mac67]. Starting with randomly or user-based selected initial clusters, *k*-means keeps reassigning the pixels to clusters based on similarity measures between cluster means and pixels until convergence is reached [Mac67]. However, the simplicity of this famous algorithm introduces mainly two limitations:

1. The number of initial clusters has to be specified by the user. Since *k*-means does not automatically change the number of clusters, e.g. by splitting or merging, the initial number of clusters immediately is the final number of clusters.

2. The final clustering result heavily depends on the initial cluster selection.

Thus, a sophisticated results needs previous knowledge about the data in terms of both, expected number of clusters and good seeding points. According to [Mac67], these limitations have led to adaptive variants of *k*-means, e.g. ISODATA [BH65]. ISODATA allows to find optimal clusters for arbitrary initial cluster selections by splitting and merging of clusters with high variance or high similarity, respectively. In addition, the nonparametric Mean Shift [CM02] algorithm can be applied, which recursively estimates the nearest and densest region for each pixel. The densest region of each pixel is computed by defining a local search window for each pixel, whose center is shifted to the position of its mean value, until convergence.

Automatic segmentation methods often ignore the spatial topology. In order to exploit the spatial topology, often graph cut [BJ01] methods are applied to achieve a user-guided image segmentation. Here, a user mostly seeds source and sink pixels, which then are separated by considering the segmentation task as graph cut problem. Recently, Couprie et al. [CGNT09] introduced a mathematical framework, so-called power watersheds, that extends common

seeded segmentation methods, like graph cuts, to optimize more general models. Based on power watersheds, Jordan and Angelopoulou [JA12] have presented a supervised multispectral image segmentation approach. But, as mentioned before, the authors determined that the segmentation result heavily depends on the chosen similarity measure.

Redundancy Reduction of Multispectral Image Cubes

As seen before, one of the basic goals in multispectral data analysis is to classify or discriminate objects. Bajcsy and Groves [BG04] state that a higher dimensionality does not go along with better classification or discrimination accuracy, due to spectral redundancies in the data which can cause convergence instabilities of algorithms. Moreover the authors mention, that noise can lead to variations in redundant data which can be propagated in data analysis models. Thus, before the actual data analysis, often a dimensionality/redundancy reduction approach is applied. Beside the reason of redundancy, also the computational requirements for processing large multispectral datasets often is a reason for applying redundancy reduction methods. Approaches for redundancy reduction typically split into two categories:

- **Dimensionality Reduction** uses all spectral bands of the data and typically achieves less information loss.
- **Band Selection** uses only a subset of spectral bands of the data and can lead to information loss.

In the following, for both categories, common exemplary methods are briefly presented.

Dimensionality Reduction Many unsupervised methods can be applied to achieve a dimensionality reduction for multispectral data. Very common non-linear methods are for instance multidimensional scaling (MDS) [Kru64], locally linear embedding (LLE) [RS00], or Isomap [TDSL00]. The goal of MDS is to arrange data elements in a space in such a way that the pairwise element distances represent the measured similarities respectively dissimilarities of these elements. Different from MDS, both, LLE and Isomap try to preserve the intrinsic non-linear geometry of the data by the assumption that the pair-wise distances between elements are only known for neighboring elements. In particular, Isomap computes the geodesic distances between all pairs of elements and then uses MDS to rearrange the elements corresponding to the computed distances in a lower-dimensional space. The principle of LLE is the same as for Isomap, but instead of computing the geodesic distances, LLE first searches for the weights to describe an element by a linear combination of its adjacent neighbors. Then, a lower-dimensional embedding of elements is searched by optimization in such a way, that the before determined linear combinations of the original elements remain the same also in the lower-dimensional space.

Beside these unsupervised non-linear methods, principal component analsysis (PCA) [Jol02] is one of the most popular linear multivariate statistical method to perform a dimensionality reduction. PCA is an unsupervised method, which finds patterns, i.e. principal components, in high dimensional data which are uncorrelated and represent

orthogonal data space directions along a descending sequence of variance. Dimensionality reduction is achieved by choosing only a small number of principal components with higher variance. Since multispectral data have spatial as well as a large spectral dimension, PCA is well-suited to be applied on these data to discover high-dimensional patterns [KBF*07].

Results of dimensionality reduction methods typically lead to distinguishable clusters for distinct materials. But, since these methods do not focus on the spectral nature of the data, the resulting embeddings, e.g. principal components, only have little resemblance to the original wavelengths.

Band Selection Different from the above-mentioned approaches, the band selecting methods focus on the nature of the multispectral image data and have the goal to remove redundant bands. Thus, to reveal the significant information which still resemble the spectral characteristics of the original wavelengths. In order to find the most significant bands a variety of criteria based on, e.g. PCA [MKL90], indipendent component analysis [DQW*03], entropy [BG04], mutual information [SPK04], have been used to rank the influence of each band. Since worse ranked bands are removed from the data, these methods can lead to a high information lost when unsupervised methods are not able to properly estimate the influence of the bands, e.g. because of low SNR.

Dimensional Reduction: Spectral Mixture Analysis

So far, the aspect that spectra can be composed of a mixture of several distinct materials, i.e. constituent materials, was neglected. In such cases of mixed spectra, it is the aim to identify the constituents, i.e. pure materials, that are present in the mixture and their proportion [Kes03]. The notion pure material, on the one hand can be subjectively driven by the special interest of an expert and on the other hand can be problem dependent, i.e. the requirement to measure specific materials, thus the definition of the constituent spectra, so-called endmembers, typically depend upon the application [BDPD*12]. The procedure which decomposes mixed spectra into a set of endmembers and the corresponding coefficients that indicate the proportion of each endmember in each pixel is called spectral mixture analysis (SMA), also often referred to as spectral unmixing. Alternatively, SMA can be seen as compressing the spectral data [VP06], with minimal loss of application specific information, thus also achieves a dimensional reduction. Spectral unmixing has been an alluring exploitation goal from the earliest days of multispectral imaging to nowadays [PMP*10]. One reason for the large interest in SMA is that it provides capabilities to explore subpixel details [Kes03]. Thus, this approach allows a holistic exploration of the multispectral data to get a very deep understanding. Before the details of the mixing models are discussed, first the reasons for mixed spectra are introduced. Keshava [Kes03] states that mixed spectra arise for one of two reasons:

- The **spatial resolution** is too low, so that adjacent endmembers can jointly occupy a single sensor pixel. Thus, will composite a mixed spectra. This kind of mixture often is called macroscopic mixture and for instance occurs often in applications of remote sensing.

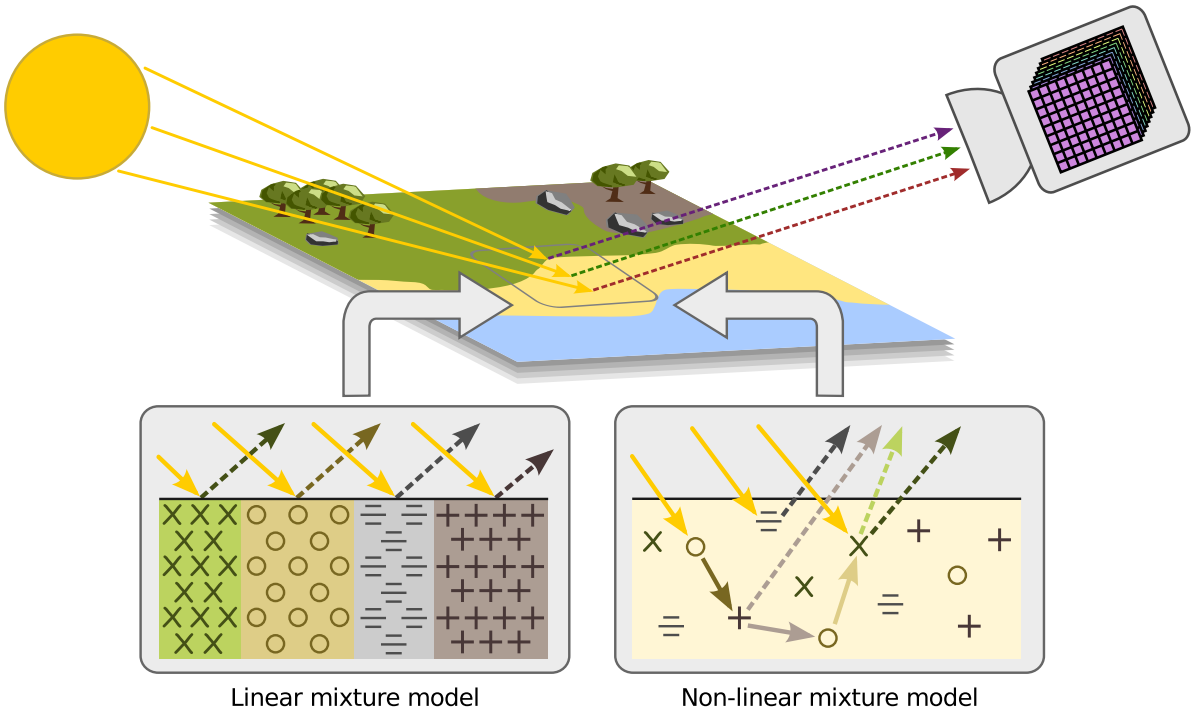

Figure 1.5: Illustration of linear and non-linear mixture models. While the linear mixture model assumes regular ordered materials like in a checkerboard, the non-linear mixture model allows that incident light multiple can scatter with different materials.

- Regardless of the imaging system, mixed spectra can also occur when distinct materials are combined to **homogeneous mixtures** (e.g. soil and grass or the overlay of semi-transparent materials). This kind of mixtures are also referred to as intimate mixtures.

The unmixing requires a model how constituent spectra in a pixel are combined to yield a mixed spectrum. The literature distinguishes two, linear and non-linear, models that represent the underlying physics that are the foundation for the inverse unmixing task [Kes03]. Both mixing models are conceptionally illustrated in Fig. 1.5. As can be seen, the non-linear mixing model describes the more realistic, but also more complicated, scenario. Compared to the linear model, the materials are not regularly ordered and incident radiation can scatter several times with different materials. Thus, resulting mixed spectra may not uphold linear proportions of the constituent spectra, as in the simpler linear model [Kes03]. Although many research on the non-linear model is already in progress, the current research level is immature compared to the linear mixing, which has been paid a tremendous research attention in the past decade, as stated by Bioucas-Dias et al. [BDPD*12]. The authors further mentioned, that the general requirement of a priori knowledge about the endmember in the data is one of the major limitations of the non-linear-based unmixing. A more detailed discussion of the non-linear mixture model would be beyond the scope of this thesis. Therefore readers that

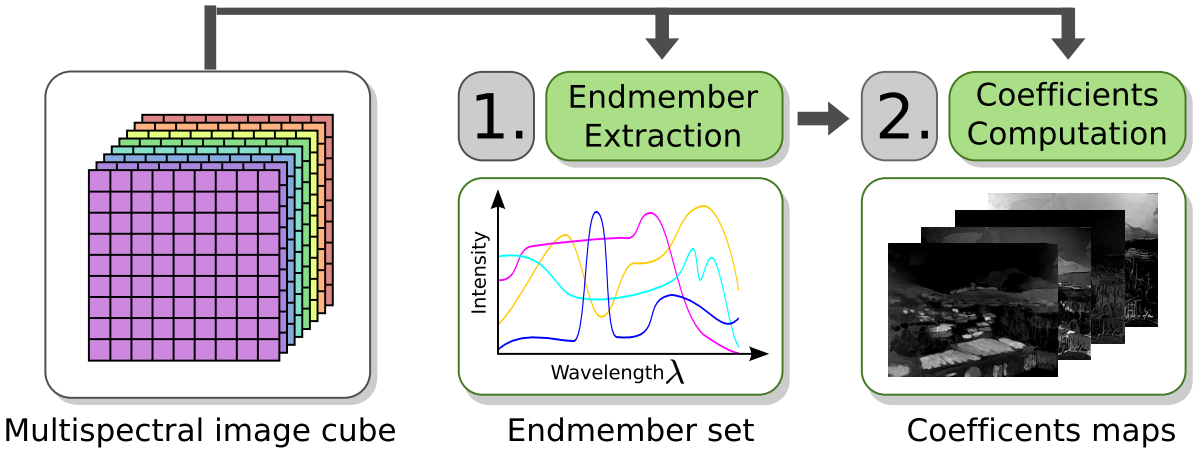

Figure 1.6: The process of linear spectral unmixing: In the first step the endmembers are selected, e.g. by automatic algorithms and then the corresponding coefficients are computed by inverse operations. Based on both, the endmember set and the coefficients maps, the original cube can be reconstructed and mixtures can be explored.

are interested in more details about this topic are referred to the common literature, where [Kes03, BDPD*12] are good starting points.

Although the linear mixture model assumes minimal secondary reflections and/or multiple scattering effects in the data collection procedure [PMP*10], the spectral unmixing based on the linear mixing model, also called linear spectral unmixing (LSU), has become a standard method that is applied in various applications, e.g. remote sensing [PMP*10] or confocal Raman microscopy [DHT10], and the number of applications is still increasing [QFMSP12]. Figure 1.6 illustrates the process of LSU, which usually consists of two steps [Kes03], an initial **endmember extraction** step and a consequential step for the **computation of the corresponding coefficients**. The details of both steps are discussed in the following paragraphs.

Endmember Extraction: This step identifies the set $V = \{\vec{v}_1, \ldots, \vec{v}_q\}$ of constituent spectra (endmembers), where q is the number of endmembers $\vec{v}_j$. According to Keshava [Kes03], there are two viewpoints for the identifications of endmembers:

- Mathematical: The search for V is comparable to the estimation of a non-orthogonal subset of basis vectors.
- Physical: Non-negativity of the spectra is required to be physically realizable. Moreover, the physical characteristics of the constituent substances should be retained by the endmembers.

The autonomous determination of endmembers with the constrained to satisfy both viewpoints is a challenging task and is the hardest part of the unmixing problem [Kes03]. At once,

for a high unmixing quality a proper determination of endmembers is most crucial. Beside manual and reference database based selection of endmembers, this task is mostly done by endmember extraction algorithms. These algorithms usually search for the extreme spectra in a dataset. This process can also be seen as identifying spectra which generate the convex hull of all spectra in the whole dataset (cf. Fig. 1.7). However, because of reasons, e.g. available sensor spatial resolution, the dataset yields no pure pixels and consequently the algorithm expresses mixed pixels by a mixture of other mixed pixels [PMPP04]. Supplementary to this fundamental introduction, more details of common endmember extraction methods are discussed after the next section.

Computation of Coefficients: As illustrated in Fig. 1.7, each spectrum $\vec{s}(x,y)$ of the dataset is expressed as a linear combination with respect to V, assuming a linear superposition of the endmembers in each pixel, i.e.

$$\vec{s}(x,y) = \sum_{j=1}^{q} \alpha_j(x,y) \cdot \vec{v}_j + \vec{n}(x,y) \text{ with } \sum_{j=1}^{q} \alpha_j(x,y) = 1,\ 0 \leq \alpha_j(x,y) \leq 1, \tag{1.1}$$

where $\vec{n}(x,y)$ is a noise vector of the current pixel (x,y). The coefficients $\alpha_j(x,y)$ of the linear combination are also called fractional coverages, or abundances. In this model usually two constraints are imposed, abundance non-negativity constraint (ANC) and abundance sum-to-one constraint (ASC), to ensure physical plausibility. Typically both, ANC and ASC, are enforced so that Eq. (1.1) is a convex combination and in this case LSU is called fully constraint LSU (FCLSU). LSU is referred to as non-negative constraint LSU (NCLSU) when only ANC is imposed and consequently called unconstrained LSU (UCLSU) when no constraint is enforced. Based on Eq. (1.1), inverse operations, e.g. Image Space Reconstruction Algorithm (ISRA) [DWM86] Eq. (B.13), are applied to compute the coefficients. Due to the constraints of the convex combination, it is obvious that the quality of the unmixed result strictly depends on the quality of the set of endmembers.

Endmember Extraction Methods

The overall LSU quality, in terms of reconstruction quality based on the constrained formulation in Eq. (1.1), relies on on a well-determined set of endmembers V [PMP*10], also see Fig. 1.7. Therefore, this part of the unmixing chain is most crucial for good results. According to Plaza et al. [PMPP04], common methods for the determination of V can be grouped into two ways:

1. Deriving the endmembers directly from the observed dataset
2. or from a reference database.

When utilizing a reference database, the challenges are that the database spectra and the spectra of the observed dataset are rarely acquired under the same conditions [PMPP04], e.g. different lighting conditions, different wavelength range or different FWHM-characteristics

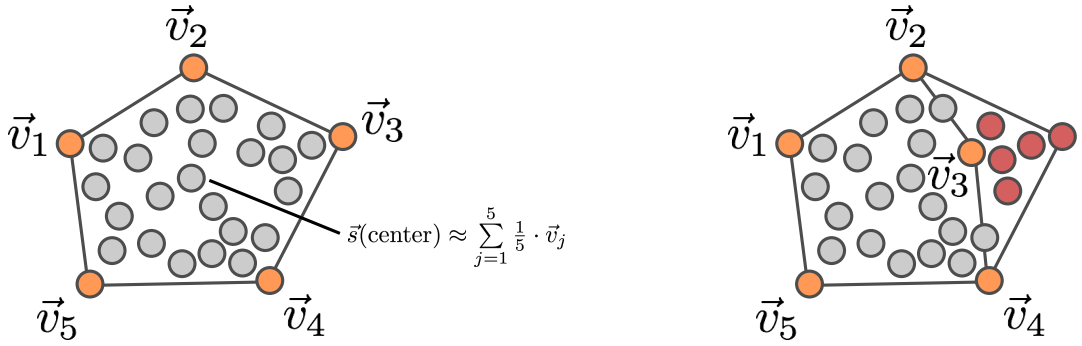

Figure 1.7: Two-dimensional example illustration of the linear mixture model, which is based on the endmembers $\vec{v}_j$. The quality of the reconstruction mainly depends on the correctly estimated set of endmembers, which define the convex hull of the dataset (left). In case of FCLSU, i.e. convex combination, it is obvious that a not optimal estimated set of endmembers (right) lead to insufficient reconstructions (red points).

of applied filters. These challenges are avoided when the search of constituents is directly done in the observed data. In the following an overview of manual and automatic endmember selection methods are shown.

Manual Endmember Selection Early endmember determination approaches were based on the expert knowledge of humans, for instance the prior knowledge about the contents of the imaged terrain was used to select some candidate endmember spectra from a reference database [VG08]. But this task can be quite challenging, as already seen above. Furthermore, reference databases also can be incomplete [BC93]. Therefore, especially in cases of new application domains, the determination of endmembers within the observed dataset is a very important analysis task. Bateson and Curtiss [BC93, BC96] have presented a method for manual selection of endmembers, that is based on PCA and parallel coordinate plots (PCPs) [ID90]. Initially, the dataset is projected into the space of the first two principal components. The extremes, i.e. points on the convex hull, of the resulting scatter plot can be interactively added to the set of endmembers. Consequently, the visualization is 2D for the first three selections and 3D of the fourth selection, which gets cluttered in high-dimensional space. Here, a PCP is applied to overcome this visualization shortcoming. According to the authors [BC93, BC96], the main weaknesses of this method are:

- The requirement of human intervention time in order to judge the endmember set.
- The possibility that different analysts can achieve somewhat different endmembers.

More information about the mentioned visualization techniques are provided in the upcoming section 1.2.3 .

Endmember Extraction Algorithms Many algorithms can be found in the literature that perform an automatic search for the constituent spectra of a dataset. Complementary to the

representation of data as convex combination of endmembers, there are methods based on vector space quantization by data centroid assignments [Gra84], including specialized data metrics [KV11]. Here, we focus on the more widespread use of endmembers for the spectral unmixing procedure. Over the past decade several endmember extraction algorithms have been developed [PMPP04]. These algorithms roughly can be categorized into **spectral-**, **spatial-spectral-** and **heuristic-based** algorithms [PMZ09, VG08].

heuristic-based: Pixel Purity Index (PPI) algorithm [BKG95] is one of the most commonly applied endmember extraction approaches [PMPP02]. PPI considers the spectra as n-dimensional vectors and generates a large number of random n-dimensional unit vectors, where n is the number of spectral bands. These random vectors are also referred as skewers. Each pixel spectrum is then projected onto each skewer. After the projection of all pixels onto each skewer, the most extreme projections (minimum and maximum) are selected. Next, the PPI scores are computed by counting the number of times a pixel has been selected as extreme. Pixels with a score equal or higher than a user defined threshold are finally considered as endmember candidates. The rationale of this approach is that random projections are asymptotically distance-preserving, thus, frequent mappings of given vectors to extreme scalar values also indicate boundary positions in the original high-dimensional space.

spatial-spectral-based: The Automated Morphological Endmember Extraction (AMEE) algorithm [PMPP02] is a prominent example in this category of methods. Inspired by mathematical morphology, i.e. the definition of multispectral dilation and erosion operators, the neighborhood around each pixel (x,y) is searched for the most spectrally pure $\vec{p}$ and most highly mixed pixel $\vec{m}$ [PMP*10]. To do so, for each pixel in the neighborhood the cumulative distance is calculated

$$D\left(\vec{s}(x,y),K\right) = d\left(\vec{s}(x,y),\vec{s}(s,t)\right),\ \forall(s,t) \in K, \tag{1.2}$$

where, d is a distance measure, e.g. SAD, and K is the kernel that defines the neighborhood around each pixel. The calculated cumulative distances then are used to determine $\vec{p}$ and $\vec{m}$, where $\vec{p}$ is the spectrum of K with the maximum distance and $\vec{m}$ is the spectrum with the minimum distance. Subsequently, the distance between $\vec{p}$ and $\vec{m}$ is calculated, for example by using again SAD. The resulting distance is then assigned as score to a score-map at the corresponding pixel position of $\vec{p}$. This score is referred to as morphological eccentricity index (MEI). The size of the neighborhood K is increased iteratively and at each iteration the scores of the found pure pixels are updated as described above. The procedure results in a two-dimensional score-map, with equal spatial resolution as the multispectral data, where maxima correspond to endmember candidate pixels [VG08].

spectral-based: Orthogonal Subspace Projection (OSP) [HC94] is a very popular hyperspectral imaging technique that has become a standard and can be used in many different applications [Cha05]. This algorithm recursively selects the maximum projection in the

orthogonal subspace which is linearly spanned by the already discovered endmembers [PMP*10]. Usually the spectrum with the maximum length of the data is considered as the first endmember $\vec{v}_1$ and defines the first column of the matrix U. Based on U, a $n \times n$ orthogonal projection matrix $P^{\perp}$ is calculated

$$P^{\perp} = I - UU^{+} \text{ with } U^{+} = (U^T U)^{-1} U^T \tag{1.3}$$

where U^{+} is the pseudo inverse of U, I is the identity and n is the number of bands. By applying $P^{\perp}$ to each pixel, the dataset is projected into an orthogonal subspace, where the endmember signatures, which are represented by the columns of U, are eliminated. Then, the maximum absolute projection, i.e. residuum, is selected as the second endmember $\vec{v}_2$ which is added as second column to U. Considering the modified U matrix, $P^{\perp}$ is recomputed to find the third endmember in the same manner as described above. This process is repeated until a desired number of endmembers is identified. Note that, because of the orthogonality of OSP, the number of endmembers found by this approach is limited to the number of spectral bands n.

The Vertex Component Analysis (VCA) [ND04] makes use of the concept of orthogonal subspace projections. The VCA algorithms exploits that endmember are vertices of a simplex and that the affine transformation of a simplex is also a simplex [PMP*10]. Thus, VCA models the data as a positive cone, which is then projected onto a properly chosen hyperplane. The result of this projection, again, is a simplex, whose vertices are considered as the endmembers. After the identification of the simplex, VCA projects the data to a random direction and selects the largest projection as the first endmember. Next, the data are iteratively projected onto the direction that is orthogonal to the subspace spanned by the already determined endmembers.

The N-FINDR [Win99] algorithm inflates a simplex inside the data in order to discover the set of spectra with the largest possible volume [PMP*10]. Initially the algorithm begins with a random selection of pixels, which defines the initial volume. In order to refine the estimate of endmembers, every pixel of the image must be evaluated in order to find the set of pixels that maximize the volume. Finally. the pixels that define the maximum volume are selected as endmembers.

Since these algorithms typically only extract a single standard endmember spectrum for each endmember class, they usually do not incorporate the spectral variability within an endmember class (see Fig. 5.16), which has been identified as one of the most profound sources of error in the estimation of abundances [SZPA12]. The recent literature presents solutions to improve the abundance estimation, e.g. the multiple endmember spectral mixture analysis (MESMA) [RGC*98] algorithm, see the review of Somers et al. [SATC11] for further approaches and details. However, the premise of these solutions is the availability of a spectral library that allows the modeling of the endmembers variability, thus introducing limitations when measurements are not available or incomplete [SZPA12]. Furthermore, experimental

results comparing different endmember variability reduction techniques are very scarce making it hard to identify the most robust and most effective technique to build an understanding of how to match application and endmember reduction strategies [SATC11].

Moreover, there is still the general question of unsupervised multispectral data analysis: how many endmembers are present in the data? Here, many methods can be applied as preprocessing to estimate the number of endmembers. Conceptually they are comparable to the above mentioned noise reduction methods, e.g. based on the variance or the SNR of the data. Thus, they typically also require a robust parameter estimation to achieve good estimation results. Here, the proposed method of Chang and Du [CD04], called virtual dimensionality (VD), tries to automatically estimate good thresholds for variance- and SNR-based methods, but likewise needs a parameterisation for the configuration of false-alarms. The hyperspectral signal subspace identification by minimum error (HySime) approach were presented by Bioucas-Dias and Nascimento [BDN08] and has the goal to be parameter free. After an initial estimation of the signal and noise correlation matrices, the algorithm selects the first eigenvectors that contain the most of the data information [BDN08].

Moreover, as mentioned in Sec. 1.2.2, a dataset also can consist only of mixed spectra. This challenge recently was addressed by an approach of Eches et al. [EDT10]. Based on the assumption that the spectra of the data are linear combinations of an unknown number of random endmembers, the authors propose a semi-supervised hierarchical Bayesian algorithm to estimate the mixture coefficients as well as the number of endmembers.

As there are circumstances where the automatic estimation is very challenging, the results of these algorithms should be considered as a first guess of a preprocessing step. Therefore, the estimated number of endmembers is subject to change and has to be verified in the subsequent data analysis.

1.2.3 Visualization

Creating visual representations to provide insights to multispectral image data is not a straightforward issue, since it is difficult to visualize all aspects of a spectral image in one picture [PvdH01]. Thus, different visualization techniques typically are combined by multiple linked views, e.g. scatterplots and image-based representations. Here, typically the user can specify a subset of interest by brushing, i.e. drawing selections onto the visual representation of a view [FH09]. In general, each visualization technique has own pros and cons, therefore the final aim of the multiple linked views is the best possible compensation of the respective drawbacks of the used visualization techniques. The common visualization techniques roughly can be grouped into three categories:

- Image-based visualization of spatial relationships,
- Plot-based visualization of spectral characteristics, and
- Feature-based representation to group similar spectra.

Examples for each categories are discussed in the following paragraphs.

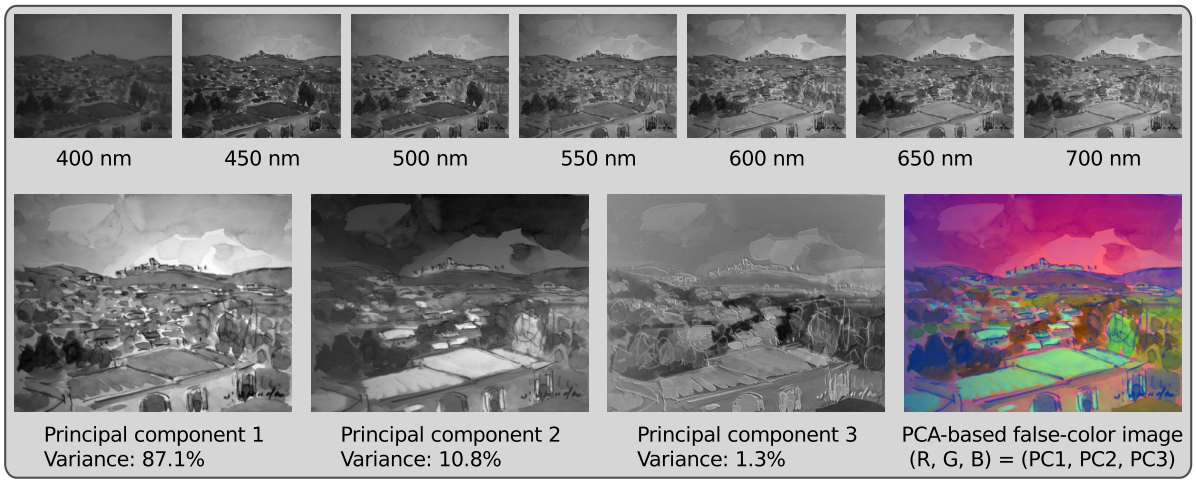

Figure 1.8: Example of a PCA-based false-color image, based on the dataset *Watercolors* (see Appendix A). The top row shows some single spectral bands of the dataset. The bottom row shows the first three principal components, in total representing a variance of 99.2%, and the corresponding false-color representation.

Image-based Visualization One of the most simplest techniques to visualize a multispectral image, is to scroll through the spectral bands one by one, or to select three spectral bands to map these bands to the color primitives R, G, and B to achieve a false-color interpretation. However, a meaningful manual selection of three bands in terms of the best describing variance of the multispectral data is very time consuming. Thus, it is common to apply dimensionality reduction methods like PCA and then to map the resulting principal components to the color primitives. Figure 1.8 shows an example for such a typical false-color image. In addition, also weighting functions, which describe the chromatic response, can be applied to spectra in order to transform them to color primitives. Typically, such a weighting achieves also a false-coloring. But, when the spectra cover the visible range, then the CIE standard observer color matching functions, see Appendix B.3, can be applied to achieve a true color image [PvdH01].

Yet, the aim of the methods were to assign colors to spectra in a meaningful way to discriminate distinct spectra. However, it is also very common in multispectral data visualization to first apply multispectral data analysis approaches and then to utilize the analysis result to achieve a more classification-based visualization, like in [AGDJ09] . Conceptually, the visualization works as follows. First, an unique color is assigned to each found class, e.g. cluster, of the initial data analysis step. Then, each pixel of the dataset is colored according to the class it belongs to in order to achieve a classification/segmentation result.

One observation in multispectral data visualization is, that different features can be found at different resolutions in different spectral bands. Therefore, many approaches can be found in the literature that aim a multiresolution fusion, i.e. the combination of relevant information

of several bands in one single image. The basic principle of all fusion methods roughly can be described by three steps:

1. Perform a hierarchical image decomposition for each band.
2. Apply a fusion scheme at each decomposition level to combine the respective contributions.
3. Generate a single image based on the different fused levels.

Having this three steps in mind, the main differences of several fusion algorithms focus on the first two steps. On the one hand, the choice of the image decomposition method in the first step, e.g. based on wavelet transforms [LMM95], Laplacian pyramids [SW02], Markov random fields [Mig10], or MDS [LAK*11] and on the other hand the corresponding criteria to rank the contributions of the bands in the second step. Commonly, multiresolution fusion methods typically perform best, when the spectral dimensionality is relatively low, a maximum of about ten bands.

In summary, all image-based visualization methods provide good opportunities to get insights into spatial relationships, but, it is obvious that they provide no access to the spectral distribution of the data.

Plot-based Visualization The visualization of a spectrum typically is achieved by using a two-dimensional plot, spectral bands verses the absorbance or reflectance values [PvdH01]. Typically, such a plot represents only one spectrum, or relative few spectra, thus provides only limited insights into the spectral distribution of the complete data. To get a more complete overview of the spectral characteristics, also multivariate visualization techniques like PCP [ID90] can be used. In the line with usual two-dimensional plots, the parallel vertical lines in a PCP represent the spectral bands. Plotting all, spectra in one PCP typically results in a cluttered representation, which can be improved by clutter reduction methods, e. g. [ED07], [ZYQ*08], in order to gain better insight into the spectral characteristics.

Furthermore, Radviz [HGM*97] can be used to place the n-dimensional spectra in a planar radial plot of equal dimensionality. This means, that each spectrum $\vec{s}(x,y)$ is represented by a 2D-point $\mathbf{p}(x,y)$ in the Radviz plot. To do so, the Radviz plot makes use of spring constants, where n springs are attached with one end to the respective dimensions. The remaining ends are connected to a point $\mathbf{p}(x,y)$ and the spring constants K_i are defined by corresponding attribute values of $\vec{s}(x,y)$ (cf. Fig. 1.9). Here, the attributes of $\vec{s}(x,y)$ usually are normalized to have values in the range $[0,1]$. The position of $\mathbf{p}(x,y)$ can be computed with

$$\mathbf{p}(x,y) = \frac{\sum_{\lambda=1}^{n} \hat{d_\lambda}\, \hat{s}(x,y,\lambda)}{\sum_{\lambda=1}^{n} \hat{s}(x,y,\lambda)}, \tag{1.4}$$

where $\hat{d_\lambda}$ is a vector that points from the center of the plot to the position of the respective dimension on the circle. At the final position of $\mathbf{p}(x,y)$ the sum of all spring forces is zero.

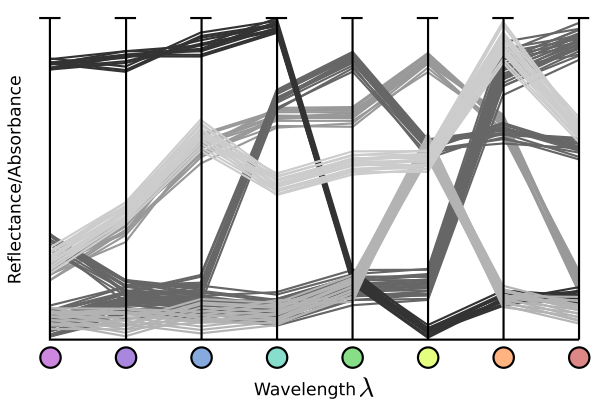

Parallel coordinate plot

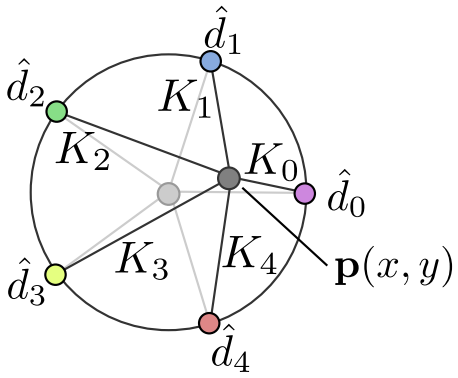

Radviz plot

Figure 1.9: Conceptional illustrations of two multivariate plotting techniques: PCP in the left and the Radviz mapping in the right.

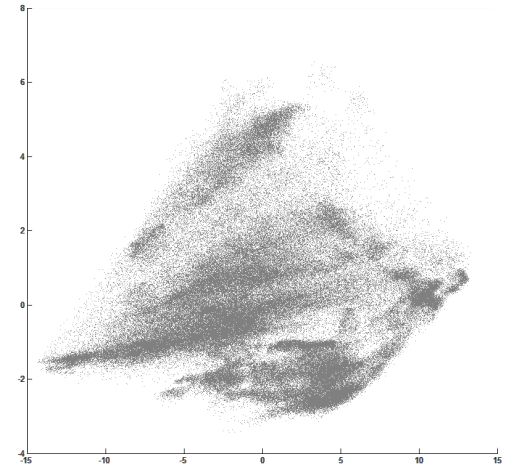

Scatter plot of the first two principal components

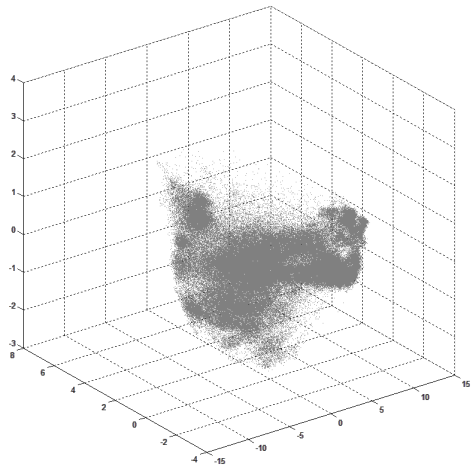

Scatter plot of the first three principal components

Figure 1.10: Example of PCA-based scatter plots, again based on the dataset *Watercolors* (see Appendix A). The left 2D scatter plot is based on the first two principal components and the 3D scatter plot additionally uses the third principal component.

Compared to PCP the spectral characteristics are getting lost again. But, Radviz allows the intuitive exploration of spectral similarities, since similar spectra should appear close to each other.

While such plotting techniques allow to gain insights into the spectral characteristics or spectral similarities, at the same time the spatial relationship is lost. Thus, typically a spectral plotting technique in combination with a supplementary visualization technique, like image-based visualizations, is used to compensate this major drawback.

Feature-based Visualization As seen before, dimensionality reduction methods, like the popular PCA, are applied to facilitate the visualization of high-dimensional data, e.g. by composing a false-color image based on three principal components. In addition, the high-dimensional data elements also can be represented as points in a lower-dimensional scatter plot, where the coordinates are defined by features, e.g. found principal components. Here, similar elements are close to each other (cluster) and are apart from other clusters which are defined by dissimilar elements, see Fig. 1.10 for an example. The dimensionality of these plots typically is limited to two, or three dimensions [PvdH01]. Thus, a meaningful selection and combination of the features is required to achieve good discriminating scatter plots.

Chapter 2

Design Goals – Requirements and Challenges

In the introduction of this thesis, the main aim of this dissertation was already presented, which is the proposal of visual analysis methods to facilitate the generic analysis of multispectral image data. Moreover, also fundamental challenges of multispectral image processing will be discussed, like the influence of blur in multispectral image analysis. In order to conclude in design goals of this thesis, this chapter presents an general overview of requirements and challenges for software solutions. Here, the overview is oriented on the distinct stages of the before presented processing pipeline. The structure of this chapter is divided into four sections, whose subjects are as follows.

The first section presents a brief overview of applications fields. Here, the overview has two aims. First, to present the variety of applications in order to underline the necessity of generic analysis approaches. Second, the applications scenarios should present impressions about some typical processing tasks to provide some background information.

Having the overview of some applications in mind, the requirements and challenges of the abstract multispectral processing pipeline are pointed out and discussed in the second section.

Following the discussion of challenges and requirements, the third section presents the prior work to finally conclude in a conceptional discussion of design goals for visual analysis methods within the scope of this thesis.

2.1 Application Scenarios

As mentioned before, due to the ability of performing a very deep analysis of materials or scene characteristics multispectral sensors are very popular in many application fields. In the following, a brief overview of exemplary chosen application scenarios is given to provide some background knowledge for the upcoming discussions.

Remote Sensing The development of multispectral sensors for remote sensing has improved the capability of ground-based data collection in many fields [BDP10]. Beside mineralogy

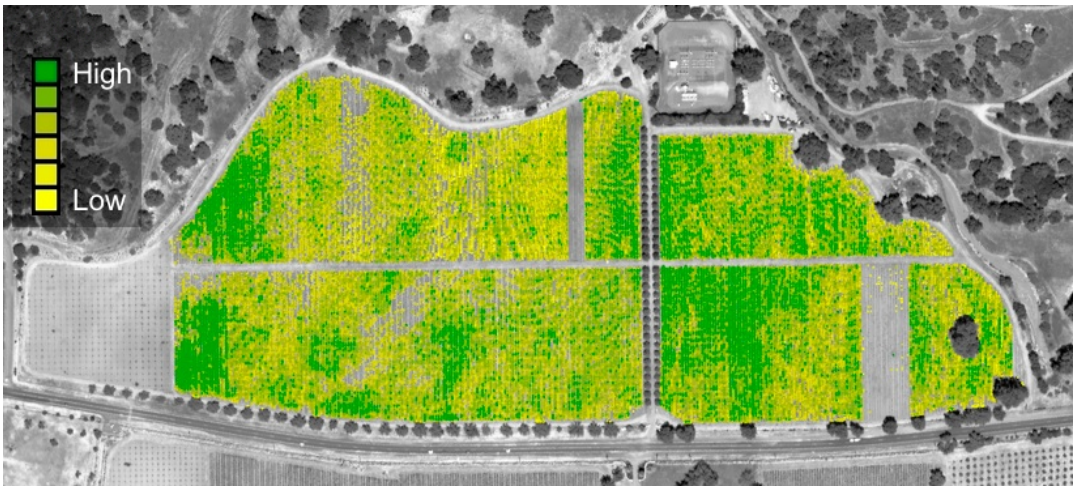

Realtive leaf water content of trees

Figure 2.1: Example application for agriculture. The realtive leaf water content of trees by the analysis of the absorbance is shown. Adapted from [Spe12].

[KBH03], surveilance [SBH*02], one popular application field is the analysis of vegetative health and agriculture. Here, the multispectral imagery allows the identification, classification and detection of vegetation phenomena [Spe12]. For instance, Fig. 2.1 shows a results of the analysis of the relative leaf water content of trees by the analysis of the absorbance.

Recycling Another application field is recycling. Since many different materials can be distinguished by their spectral characteristics, multispectral imaging is used to improve the quality and efficiency of automatic sorting of the different materials [KEG*13]. In this context, Fig. 2.2 shows an example of a dataset with different materials, e.g. glass, plastics, paper, and the associated classification map. As can be seen, also the two bottles in the bottom left and bottom right of different plastics can be distinguished by their spectral characteristics.

Dataset

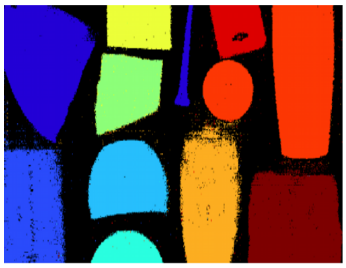

Classification map

Figure 2.2: Example application for recycling. The left image shows a color image of the used dataset and the right image illustrates the classification result. Adapted from [KEG*13].

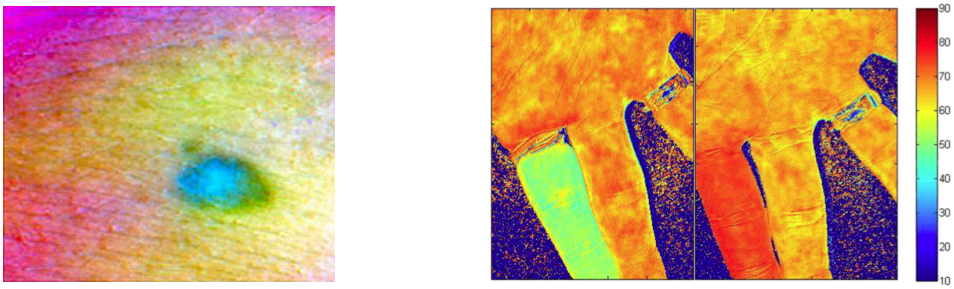

Detection of melanoma (cyan) Oxyhemoglobin in blood (in %)

Figure 2.3: Examples for medical applications. The left image image shows a false-color image of skin where a melanom was identified, retrieved from [Pho09]. The right image shows the oxyhemoglobin in blood for both, with temporarily restrict blood flow in a finger and released restriction that caused a hyperfusion, retrieved from [ZFS*08].

Medical Multispectral imaging has become affordable, reliable and usually noninvasive method for many medical tasks. Beside others, during the recent years many studies have applied multispectral imaging for the early detection and diagnostics of cancer [AUK*11]. Also the distinction of melanoma from other skin diseases is in the focus of research, as exemplarily shown in Fig. 2.3 [Pho09]. Moreover, the concentration of oxyhemoglobin in blood can be analyzed by the utilization of multispectral imaging, e.g. to assist surgeons [ZFS*08]. A simple example of the detection of oxyhemoglobin concentration is shown in Fig. 2.3.

Food Quality The potential for material analysis of multispectral image data also has been studied for the analysis of food quality. The potential of multispectral imaging has been analyzed for a huge variety of foods, e.g. the ripeness of tomatoes [PVdHY02] or the quality of meat and fish [Sun12] and so on. For instance the sugar distribution of melons is visualized in Fig. 2.4 by utilizing the strong inverse correlation of the sugar concentration and the absorbance of band 676 nm [Sun12].

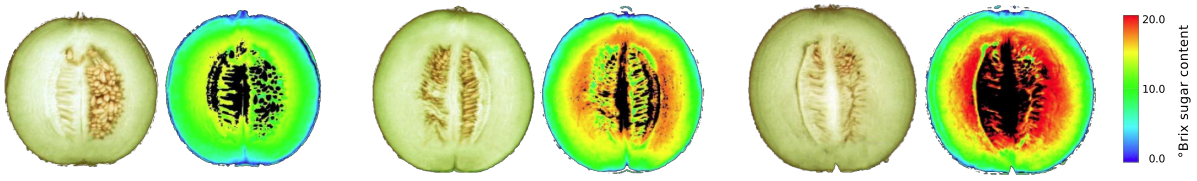

Unripe Mature Fully mature

Figure 2.4: Examples for food quality inspection. The °Brix sugar concentration of melons of different ripeness are shown together with their color images [Sun12]. Adapted from [Sun12].

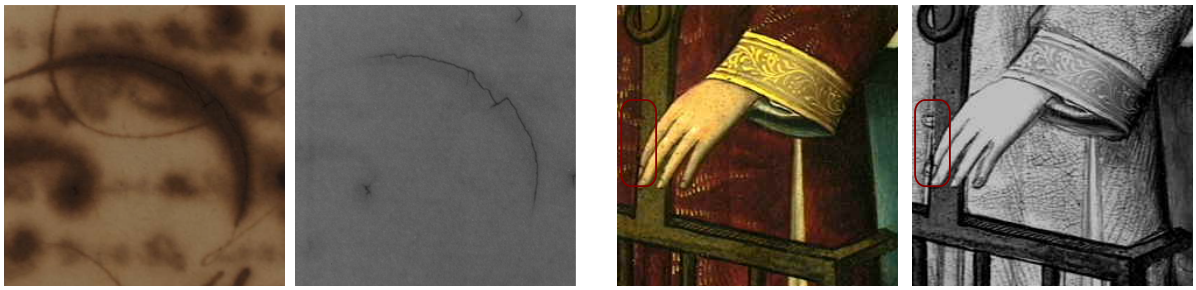

Original image | Revealed tear at 1050 nm | Original image | Near-IR reveals underdrawings

Figure 2.5: Example for analysis of arts. In the left, a tear gets visible in the near-IR image which is quite difficult to observe in the original image, retrieved from [KZD*10]. The right images show the potential to examine design changes (marked regions) and strokes of the artist by the use of near-IR, adapted from [AI08].

Analysis of Arts The visualization of high resolution images of different wavelengths allows to examine information and details of paintings or historical documents at different levels of depth. Moreover, the nowadays digital images contain more details that an artist would be able to see, because the color accuracy of the digital images contains more color levels than the human eye is able to see [CPLP06]. Multispectral imaging for instance can be used for forensics of arts to e.g. reveal damages like tears (see Fig. 2.5) [KZD*10]. Furthermore, this imaging technique can be applied to perceive subtle information on the painter's technique, e.g. by viewing of underdrawings (again see Fig. 2.5) [CPLP06].

Document Verification The verification of documents is also a popular application domain of multispectral imaging. One reason of this popularity is the ability of noninvasive capturing of documents. One famous example out of the everyday life is the verification of banknotes. For instance, the euro banknote incorporates several security features to verify its genuineness.

The front (left) and the back (right) of a five euro banknote under infrared light

Figure 2.6: Example for document verification. Some security features of banknotes are only visible under specific light, e.g. infrared light. The images of the banknotes are adapted from [Eur13].

Figure 2.7: Example for application field of biometrics. A conventional TIR image is compared to a composed multispectral fingerprint image of one finger. As can be seen, fine structures are visible throughout the multispectral image. Adapted from [RNB08].

Beside features that can be simply felt or seen, there are also additional features that are getting visible under specific illumination, e.g. see Fig. 2.6 to see a five euro banknote under infrared light [Eur13].

Biometrics Nowadays, multispectral imaging can be used to compensate uncontrolled conditions, like insufficient illumination or low scanning resolutions, to improve the detection of features in biometrics [BLGK11]. In the field of fingerprint acquisition, typically total internal reflectance (TIR) sensors are used that acquire the points of optical contact between sensor platen and material. Comparing this conventional sensors to a multispectral based sensor reveals that fine structures of fingerprints are visible throughout the multispectral image (cf. Fig. 2.7) [RNB08].

2.2 Requirements and Challenges

Having some application domains in mind, this section presents subtle requirements and challenges of the distinct steps of the introduced multispectral processing pipeline with respect to the main aims of this dissertation. Here, the main aims are the proposal of visual analysis methods to facilitate the generic analysis of multispectral image data and the discussion of more fundamental challenges when processing multispectral image data in general.

Acquisition Many applications require a reliable determination of spectral characteristics, e.g. to identify cancers in medical applications. However, analysis results do not solely depend on the capabilities of the analysis methods, they partly also depend on the quality of the acquired image data, e.g. from SNR. For this reason, although the main scope of this thesis is the analysis of the data, the acquisition of multispectral images will be roughly addressed. As seen in the fundamentals, many multispectral data suffer from noise, but also other reasons for image degradation, like outlier and blur, can frequently be found in such data. Therefore,

such imaging-based issues have to be considered in particular for applications which have high requirements on the precision of the analysis, e.g. in medical applications.

Data Analysis As introduced in the fundamentals 1.2.2, the complexity of the data poses significant challenges for its analysis. Compared to nowadays hardware capabilities, the data reduction with the goal to better meet the hardware limitations of past decades has faded out of the spotlight of research. Here, the new trend is to process the full data with the help of recent hardware developments, like parallelization on a graphics processing unit (GPU). Although this avoids wrong results because of incorrect data reductions, the general challenge of high-dimensionality, e.g. the choice of similarity measure, remains.

As seen in the brief overview of the applications there exist several goals that are desirable to be achieved. Here, one major goal is the discovery and understanding of relationships, e.g. the inverse correlation of the °Brix sugar content and the absorbance of a specific band (676 nm) in case of melons. But before an understanding of relationships can be extracted, typically it is the first and very important goal to determine the primary constituent spectral characteristics of a dataset. Here, constituent spectral characteristics can be both, a spectrum itself as spectral signature of a material, or specific wavelength ranges to discriminate different materials. Beside the general challenge to identify the primary spectral characteristics of the high-dimensional data, another challenge is the popularity of these data. Because of this popularity, there is a high demand for generic solutions to enable a user to get access to the spectral characteristics for a large variety of application domains. Therefore, it is a central requirement to gain insight and knowledge of the data in a universal manner, especially, to support research in new application domains.

Beside the analysis of the data itself, another central challenge is the presence of imperfections, e.g. noise, outliers, or blur, as seen in the previous section. These imperfections can harm the results of automatic data analysis or in worst cases, can lead to useless analysis results. As discussed in the fundamentals 1.2.2, when analyzing data that are subject to imperfections typically a preprocessing step is applied in order to reduce the influence of imperfections. Thus, to achieve better results by improving the conditions for the automatic data analysis. But, preprocessing methods very often are subject to parameterization, that mostly depends on the application domain. Moreover, a wrong parameterization also can corrupt the information. For instance, noise reduction often is achieved by smoothing of specific bands, but the question is how much should a band smoothed without loosing information by destroying spectral characteristics, e.g. spectral peaks. Therefore, another requirement is an effective and universal preprocessing in order to enhance the quality of the data without loosing information.

In summary, the analysis part has to pay attention to several points:

- Influences of image degradations have to be considered in data analysis strategies in general.
- Preprocessing has to enhance the quality of the data in order to improve the robustness of analysis approaches, without destroying spectral characteristics.

- The data analysis itself has to be capable of determining desired spectral characteristics and relationships in high-dimensional space. While the high-dimensionality itself poses already significant challenges, like the choice of similarity measures and it consequences for the analysis, the challenge is further intensified by the claim of determining sophisticated results for a wide variety of applications.
- Since it is desired to process the full-data, it is important to consider the computation time, especially in the context of user-based analysis.

Visualization In general, visual analysis has the goal to incorporate the human in the data exploration process, which has proven to be a high value in exploratory data analysis [Kei02]. Moreover, these approaches are especially useful when the initial knowledge about the data is quite low and the exploration goals are vague. However, to get insight into the data it is vital to first present the data in an appropriate visual form that enables a user to interact with the data or analysis results. But, as discussed before, mutlispectral images contain much more bands than can be displayed on a usual three channel display, which requires the projection to a lower dimensional space, typically RGB color space [CRHW09]. However, this down projection usually leads to an information loss. Since it is hard to visualize all spectral aspects in one image, different visualization techniques typically are combined by multiple linked views in order to mutually compensate each pros and cons, as already seen in the fundamentals 1.2.3. Considering this visualization challenge and the recent literature, the main requirements for multispectral data visualization are summarized by Jacobson and Gupta [JG05] which have formulated two questions:

- What is a good visualization of multispectral data to enable the best interaction?
- How can the information loss of the down projection in the visualization process be judged?

2.3 Prior Work

This section focuses on the discussion of the prior work to overview the state-of-the-art solutions also with respect to the challenges and requirements that were discussed in the previous section 2.2.

One central requirement is the ability to process multispectral datasets in a generic way to allow the analysis of a large variety of application domains. But, most of the available visualization solutions mainly present approaches for specific domains. Beside earth observation data [KLB*93, CRHW09, JG05], some other examples are analysis of paintings [CPLP06], astrophysical data [LFH08], hyperspectral data of historical documents [KZD*10], biological related visualization of spectrometry data [BvL05] and color visualization of hyperspectral data in general [Mig10]. Beside, these visualization solutions, there are also analysis toolboxes available. Here, the Hyperspectral Image Analysis Toolbox (HIAT) [Cen05] is a common example and provides a collection of functions that build upon MATLAB and extends

its functionality in terms of image processing methods for multispectral data. Some features of HIAT are classifiers, feature extraction and selection, as well as pre- and post-processing algorithms.

Beside, these solutions, software for analysis and visualization is mainly available for multispectral datasets from the field of remote sensing.

Here, one of the most popular commercial tool is the software ENvironment for Visualizing Images (ENVI) [EXE13] from EXELIS Visual Information Solutions. Combining advanced spectral image processing and geospatial analysis technology, and based on the extensible modular software design, ENVI is one of the leading solutions, especially for the field of remote sensing. In excerpts, some analysis opportunities are: time depended change detection in images, anomaly detection, feature extraction, measurement of relative water depth, registration of images to maps, and many more.

Another commercial tool is Geomatica [PCI13] from PCI Geomatics, which especially addresses the field of remote sensing, like Synthetic Aperture Radar (SAR) images. Beside, data enhancement capabilities, like atmospheric corrections, the software provides accelerated workflows by using 64-bit and parallelization.

Beside, these commercial solution, several freely available software solutions can be found. Here, MultiSpec [BL02] is a very popular tool and a good representative of analysis software for multispectral remote sensing data. It provides means for classification, e.g. by clustering methods, whose results can be overlaid on a grayscaled single band of the multispectral image cube. Furthermore, the spectrum of a pixel can be plotted. When more then one pixel is selected, the mean, standard deviation and minimum and maximum of the selection is plotted.

Developed by the U.S. Army Geospatial Center, Hypercube [U.S12] is another freely available software that addresses geospatial processing tasks. For instance Hypercube enables spectral classifications using both imagery and spectral libraries. Moreover, it provides the functionality to e.g. filter, warp, photogrammetrically project multispectral data.

The DS9 [JM03] is a complete astronomical imaging and data visualization application that is provided by the Smithsonian Astrophysical Observatory. This very popular application provides 2D as well as also 3D views, and comes with many advanced features that are focused and designed for astrophysical data.

As shown in the fundamentals 1.2.2, Linear spectral unmixing (LSU) is a very popular analysis method to get a holistic understanding of a multispectral image. Recently, Jimenez et al. [JMP12] developed a comprehensive open-source tool, called HyperMix, that allows performing all steps of the LSU chain for remotely sensed multispectral data. The authors implemented several popular algorithms, e.g. OSP or AMEE, and allow to do a quantitative comparison of the implemented algorithms based on both, using reference spectral libraries and common metrics like RMSE.

A overview of the mentioned solutions is provided in Table 2.1. As can be seen, many of the solutions come with the ability to enhance the data by preprocessing. While only some approaches provide means to analyze subpixel details, allmost all tools provide solutions for segmentation, i.e. classification, or extraction of spectral characteristics. Several of the ap-

proaches are also surveyed by Jordan and Angelopoulou [JA10]. According to the overview, the authors certify that the current state-of-the-art solutions, on the one hand, visualize multispectral data and/or provide comprehensive methods to analyze them, but, on the other hand, have a lack in universality. To overcome these lacks, they propose their generic open-source framework, Gerbil [JA10]. Gerbil is highly interactive with combined viewports, PCP for spectral distribution and spectral gradient distribution views as well as a spatial view of a single wavelength image. Beside the combined viewports, Gerbil provides possibilities for labeling the data using supervised and unsupervised image segmentation. In the domain of multispectral image analysis, yet, Gerbil is the only tool which can be treated as a visual analysis approach. However, Gerbil unfortunately does not provide means to analyze subpixel details of multispectral image data.

		HIAT	ENVI	Geomatica	MultiSpec	Hypercube	DS9	HyperMix	Gerbil
Application domain		RS	RS	RS	RS	RS	A	RS	U
Freely available		✓	×	×	✓	✓	✓	✓	✓
Analysis	Preprocessing	✓	✓	✓	×	✓	n.a.	×	×
	Segmentation	✓	✓	✓	✓	✓	✓	×	✓
	Subpixel details	✓	✓	✓	×	×	n.a.	✓	×
Visualization		◯	✓	✓	◯	◯	✓	◯	✓
Visual Analysis		×	×	×	×	×	×	×	✓

Table 2.1: Overview of the capabilities of the prior work. The abbreviations and symbols have the following meaning: RS=remote sensing, A=astronomy, U=universal, ✓=yes, ×=no and ◯=slightly.

2.4 Discussion of Design Goals

Based on the previous sections of this chapter, the following discussion should reveal final design goals and requirements that have to be considered in this thesis.

Software that processes multispectral data has a long history and mainly focuses on remotely sensed or astronomical data, as seen before (cf. Table 2.1). For these application domains, the current state-of-the-art solutions are already remarkable. However, many of these solutions focus more on analysis algorithms and less on a intuitive and comprehensive visualization. Jordan and Angelopoulou [JA10] also reported some restrictions of the visualization opportunities, e.g. MultiSpec [BL02] does not provide a spectral distribution view, Hypercube [U.S12] provides a user to mainly scroll through the spectral bands, even the popular ENVI [EXE13] is restricted to viewing single bands or false-coloring images. So far, as mentioned above, Gerbil [JA10] is the only tool which can be treated as a visual analysis approach in the domain of multispectral data analysis. Here, Gerbil mainly focuses on the

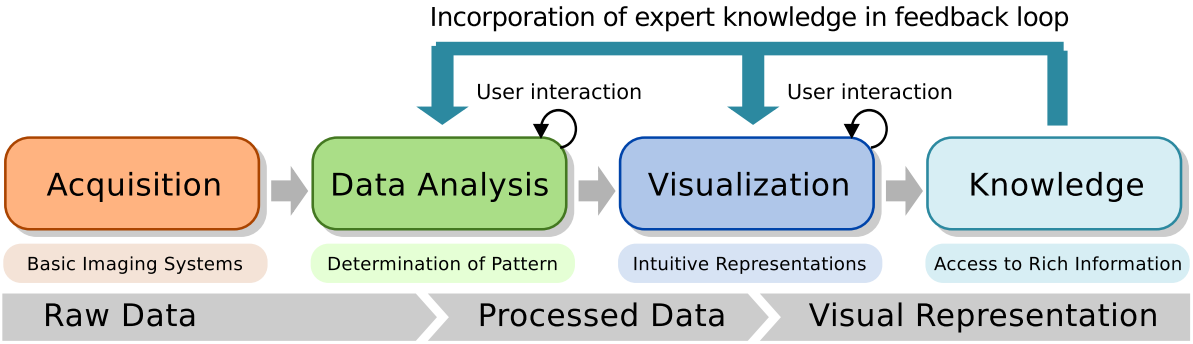

Figure 2.8: Conceptional overview of the proposed extension of the abstract processing pipeline.

exploration of topological and spectral information and provides means to achieve a segmentation of a multispectral image. Moreover, because of the highly interactive design it allows a domain independent exploration of multispectral data. However, apart from unsupervised segmentation methods, like the Mean Shift [CM02] algorithm, Gerbil would benefit from more comprehensive user guidance, e.g. by emphasizing of predetermined constituent spectra or the display of deviations in single clusters.

Taking together, it shall be the **general aim** to use successful analysis concepts of well known application domains and to combine them with intuitive and comprehensive visualizations methodologies in order to achieve more generic, but powerful, visual analysis solutions. Here, the visualization mainly shall enable a user, as an domain expert, to judge the quality of the analysis result and to reveal hidden information in an intuitive and flexible manner. Here, the visual feedback shall provide user guidance in the analysis and evaluation process in order to allow focused analysis. Since the user shall hold the key role in the analysis process, the analyst shall be enabled to make adjustments or corrections in the distinct stages of the pipeline to achieve a refined result. In this manner, as shown in Fig. 2.8, a visual analysis cycle shall be achieved which is terminated by the user when a proper result is found.

This thesis presents two generic visual analysis methods for two popular multispectral data analysis areas, which are on the one hand the **linear spectral unmixing** and on the other hand the **multispectral image segmentation**.

Linear Spectral Unmixing As discussed in the fundamentals and in the previous section, the LSU is a very popular analysis method to get a holistic understanding of a multispectral image, because this concept allows the understanding of subpixel details. Although LSU is very popular and its results provide a comprehensive overview of the observed data, yet, the concept has not achieved a comparable popularity in the context of user-based visual analysis of multispectral data. Even though, as seen in the previous section, HyperMix [JMP12] already allows to perform all steps of the LSU-chain, it focuses on the comparison of results of different algorithms and not on the interactive analysis. One reason for the restrained usage of

the concept in interactive solutions is that the runtimes for the endmember extraction and/or the inverse unmixing operations can be very high, as discussed later on. Moreover, when considering the common literature, it gets obvious that the major research focus for LSU was the development and comparison of automatic algorithms, e.g. for endmember determination, mainly for the field of remote sensing. Anyway, the usage of LSU in a visual analytics approach sounds very promising, since the analysis potential meets the requirement of very detailed understanding of the data to reveal information and relations. Thus, it is worth to identify and discuss the corresponding challenges and benefits of LSU in the context of interactive approaches. The detailed discussion of this topic and the proposal of a system design is presented within the major parts of chapters 4 and 5.

Multispectral Image Segmentation Gerbil [JA10] has shown a successful realization of an exploration concept, based on PCP, for the interactive segmentation of multispectral image data. Taking this successful solution as inspiration, the utilization of other multivariate visualization techniques, like Radviz (cf. Sec. 1.2.3), shall be discussed to reveal new opportunities or challenges in the context of multispectral image segmentation. The discussion of such a system concept is presented in Sec. 5.3.

Finally some general design remarks are presented with respect to the previously identified requirements:

- As seen before, the preprocessing of multispectral data, in term of removing imperfections to enhance the analysis, often is necessary. Here, the visualization shall provide means for an analyst to ensure that no spectral characteristics are destroyed by the current parameterization.
- The quality of determined analysis results shall always be visually represented to allow an analyst to judge the quality. Moreover, the proposed methods shall provide further assistance tools to deeper explore and finally to correct the results, if necessary. Here, the assistance tools shall follow an intuitive and problem specific design concept to enable the best incorporation of user-based expert knowledge.
- Because of the typical high-dimensionality of the data, the user guidance in the exploration process is very important to achieve a focused exploration.
- Moreover, very time-consuming methods, e.g. data analysis algorithms, shall be parallelized, if applicable, to achieve a faster response for an user to again keep him focused.

Taking together, it is the overall goal to involve the user as good as possible in the analysis process by visual feedback and exploration tools to incorporate the expert knowledge, e.g. to fine-tune paramterizations, correct automatic results, and to finally reveal rich information for various applications.

Finally, apart from the main scope of this thesis, the fundamental aspect of blur in multispectral data, due to limitations of imaging devices, will be addressed to at least give some

impressions of eventual consequences for the data analysis in general. This discussion is provided in the upcoming chapter.

Chapter 3

Blur in Multispectral Image Data

This chapter discusses the observation that multispectral image data often consist of spectral bands which are blurred. This distortion mainly is due to chromatic aberration, which is the failure of a lens to focus in the full spectral range of an imaging system. While a detailed discussion of this topic is beyond the scope of this thesis, the main aim of this chapter is more a fundamentally discussion to point out some related challenges and to finally provide a conceptional proposal for compensating the blur of filter-based multispectral imaging systems. The structure of this chapter is subdivided into two sections, whose subjects are as follows.

The first section provides further details of the problem by discussing general reasons of the blur in multispectral data. Moreover, a qualitative evaluation is presented to discuss the consequences of the blur in the context multispectral data analysis.

The last section presents a conceptionally proposal for the compensation of image artifacts, e.g. blur, in multispectral imaging by means of computational photography.

---

*Publications: The set of computational photography techniques has been presented by Heide et al. [HRH*13]. Here, the discussion of the deblurring process is focused on degraded RGB images when using simple lenses instead of highly complex lens systems. This work is an advanced result, whose general idea basically stems from the master thesis of Felix Heide [Hei11] at the University of Siegen.*

3.1 Problem Discussion

First the discussion of reasons for blur in multispectral images is provided, which starts with the description of the utilized multispectral imaging system. The next section is dedicated to a qualitatively evaluation of consequences of blurred images in the context of multispectral data analysis.

3.1.1 Blur in Multispectral Imaging

In this section, the Nuance EX imaging system from Perkin Elmer [Per13], former Cambridge Research & Instrumentation (CRi), is used. The system is a filter-based plane scanner (see Sec. 1.2.1) imaging device that uses a LCTF as bandpass filter that operates with a FWHM of 10nm in the spectral range from 450nm to 950nm. Here, the Sony ICX285 CCD sensor (2/3-inch) with 1.4-megapixel (1392×1040) is used for the capturing. Moreover, this sensor is cooled to minimize thermal noise. As lens, a standard consumer Sigma 30mm F1.4 EX DC HSM is used. This lens is optimized for the visible wavelength range. But, as will be seen in the following, also in the optimized range blurring artifacts will get visible. Therefore, more complex optimized lenses, especially including the non-visible range, are not considered in the following.

Typically, a large variety of different image degradations can appear, e.g. thermal noise, out of focus blur, or illumination-based over-exposures, and many more. But, by neglecting all this different variations, mainly one source of aberration can be identified which in particular affects filter-based multispectral imaging. Due to the fact, that the imaging system covers a wide spectral range, which is sequentially captured by adjusting the LCTF, mainly dispersion-based blur occurs. Moreover, since all different wavelengths will not be equally focused on the sensor, the blur will vary over the spectral range. This type of aberration is frequently also called chromatic aberration. Based on the illustrative measurement setup depicted in Fig. 3.1,

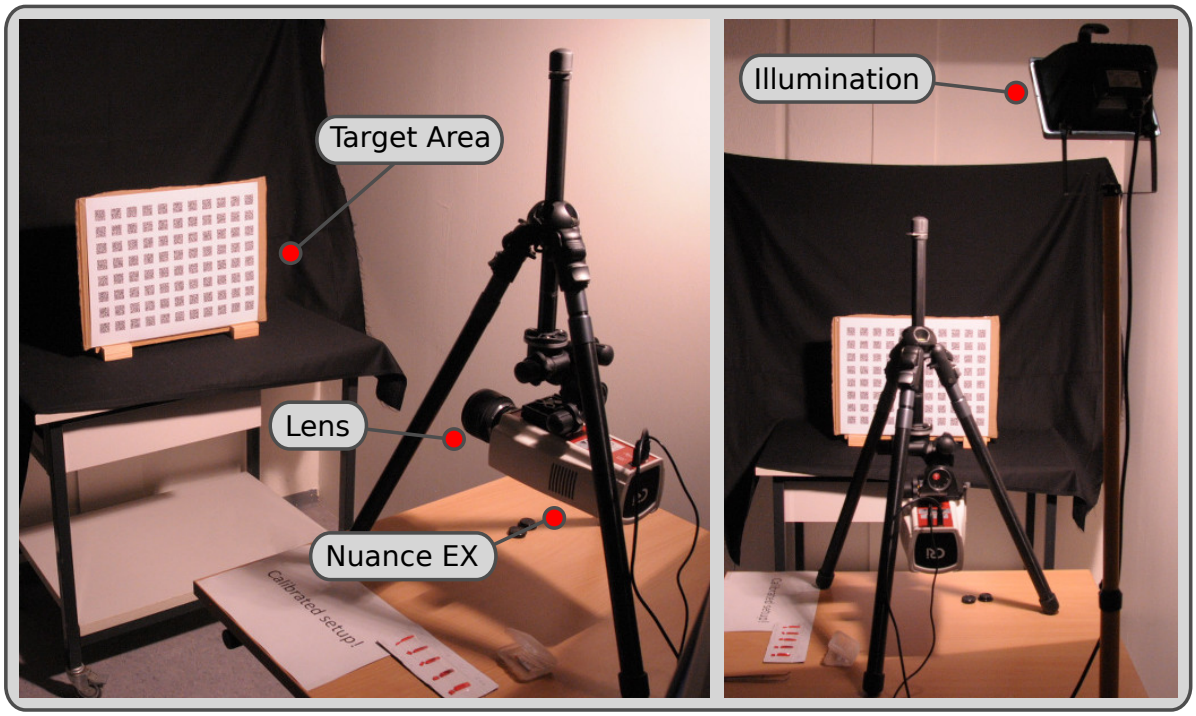

Figure 3.1: The basic illustration of the used measurement setup in this chapter.

multispectral images of a resolution chart were acquired to show this effect. Roughly the measurement process works as follows:

1. One spectral band is selected to focus the lens.
2. Then the sequential capturing of all bands starts.

In this test, the middle band, i.e. 700nm, were used to focus the lens and based on the FWHM of 10nm image cubes with 51 bands were acquired in the range of the LCTF. Moreover, measurements for four different apertures were made, resulting in four image cubes. The cubes are represented by close-ups, showing the bands of the two most extreme ends as well as the middle band of the whole range, see Fig. 3.2. The varying sharpness in the spectral range can be seen, when comparing the images for 700nm to the corresponding two extreme ends of the range, for all apertures. Here, as mentioned above, it also gets visible that the 450nm bands, which are in the optimized range of the lens, are blurred.

Comparing the close-ups of 700nm among themselves, reveals spatial blur with respect to the selected aperture, due to lens aberrations. Here, also close-ups for the center of the resolution chart are depicted (blue) for the focused band in order to better represent this observation. Moreover, also when the lens is stopped down to F16 in order to reduce the aberration of the lens to a minimum, it can be seen that the blur in the two correspondingly shown bands still is present.

Beside the observation of spatial blur with respect to the different apertures, it also can be observed long acquisition times, especially for the aperture F16 (cf. Fig. 3.2). This behavior is due to the high loss, about the half, of transmittance by the utilization of the LCTF, as seen in Sec. 1.2.1. Thus, requires higher exposure times in the acquisition process to compensate the lost of transmittance.

3.1.2 Qualitative Evaluation of Consequences for Analysis

While the previous section has revealed the presence of aberration in multispectral data, which are mainly caused by chromatic aberration, the following discussion provides a qualitative evaluation of the consequences of the blur for multispectral data analysis.

For this evaluation, two multispectral datasets, the *Egyptian statue* and the *Balloons* are considered. As can be seen in the appendix A, these datasets are taken from a multispectral image database and are also acquired by the usage of an LCTF. Although these datasets were acquired for the visible spectral range and when assuming that a lens that is optimized for the visible range was used, these datasets are also affected by blur, which strengthens the previous discussion independently from the previous test. Two blur channels of both datasets are exemplary shown in Fig. 3.3. In the case of the *Balloons* dataset, the blur is easily noticeable, for instance by considering the letters. In case of the statue the blur is not that obvious, therefore the middle band (550nm) is also included for comparison.

However, in the following these data are artificially blurred in different magnitudes in order to examine the consequences for the data analysis. Here, the artificial blurring is done by pixel-based applying a circular averaging filter in the following way, which also is illustrated

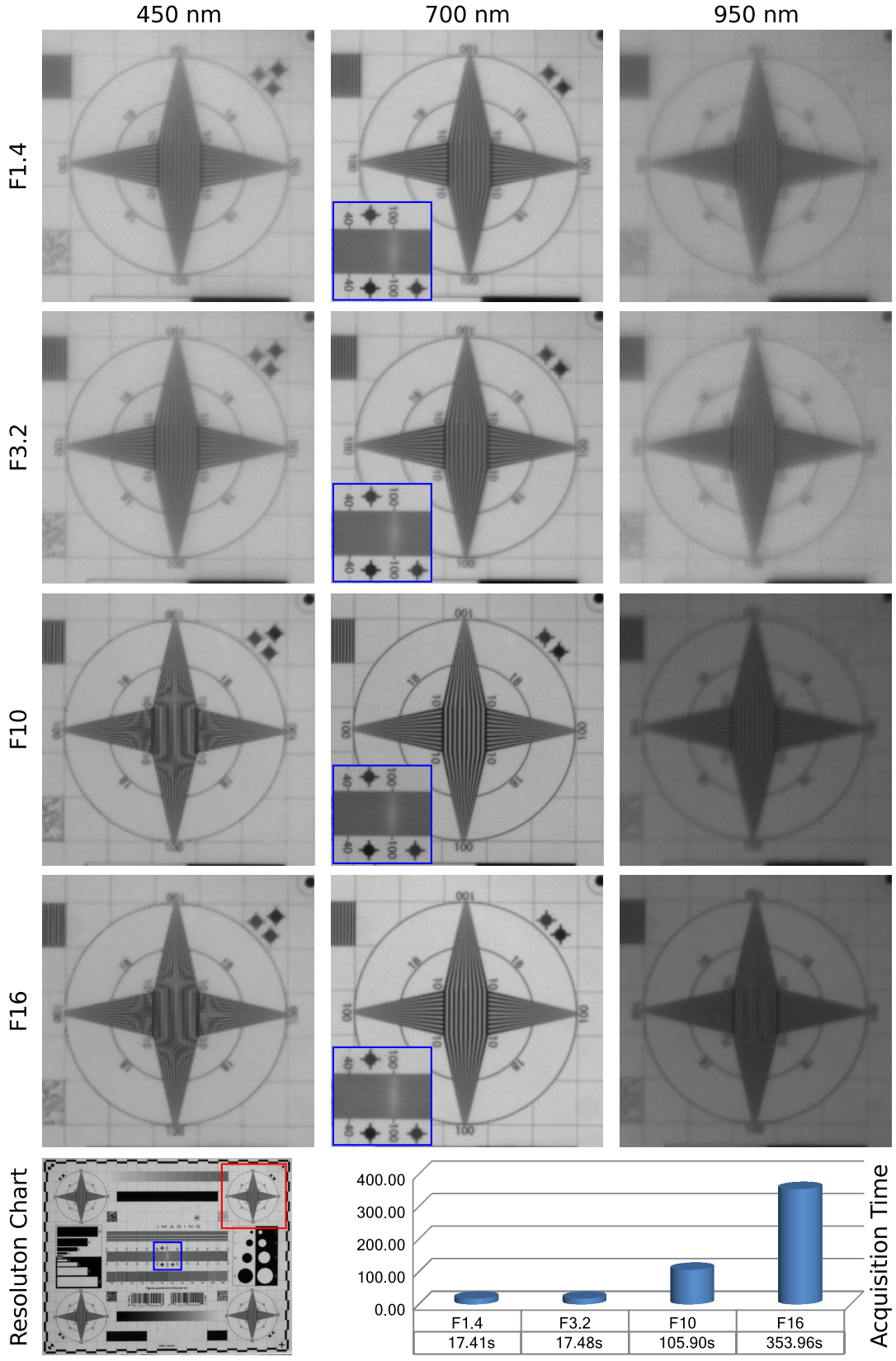

Figure 3.2: Resolution charts and acquisition times for different wavelength and apertures.

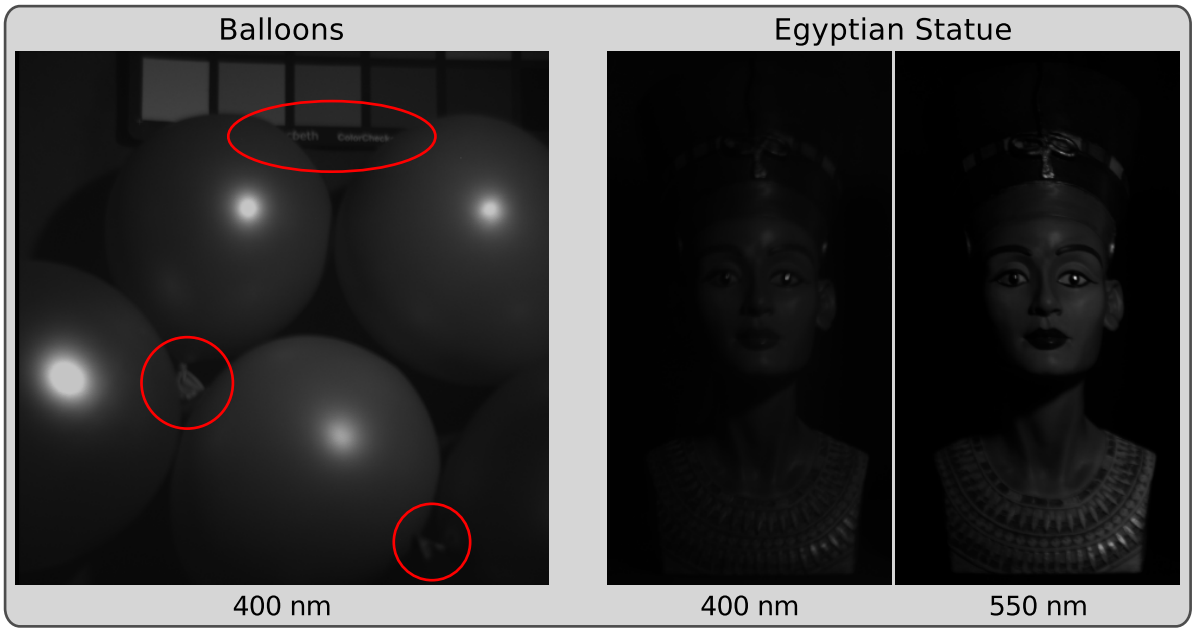

Figure 3.3: Illustration of the blur in the used datasets.

in Fig. 3.4. The middle band of a dataset is assumed as focused, where no artificial blur is added. Based on the middle band, then in both directions all other bands are blurred. Here, the radius of the blur kernel linearly is interpolated with respect to the distance between the current band and the middle band. Starting from zero at the middle band up to a defined maximal blur radius, which defines the magnitude. The artificial blur was added in both datasets and for four different radii (1.0, 1.5, 2.0, and 2.5) in order to achieve the test data.

Now, two analysis strategies are applied to both type of test data. One is the nonparametric Mean Shift algorithm to achieve a cluster-based segmentation result and the other one is the technique of LSU. In case of LSU, OSP was applied to determine the constituents of the dataset in a more objective way, since this algorithm requires no user-based thresholding of

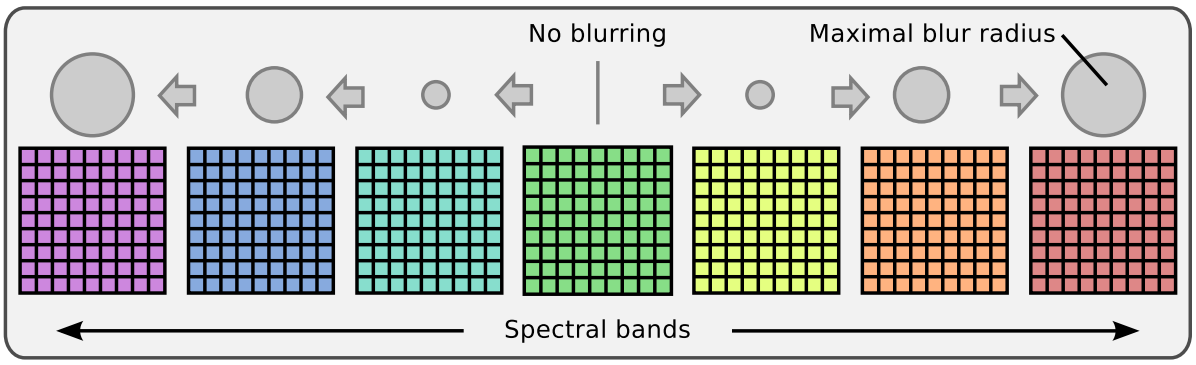

Figure 3.4: Illustration of the artificial blurring process.

a score map to determine the final constituents. The results for both types of test data, the *Egyptian statue* and the *Balloons* are shown in figures 3.5 and 3.6, respectively. For the results of the LSU, the pixels of determined endmembers are marked in the corresponding average image of the image cube in order to illustrate differences between the results. Moreover, the residual error, based on NED, is depicted to show the reconstruction qualities of the unmixing process. For both types of data, remarkable residual errors can be observed, also in the case when no artificial blur was added. Note, also an increasing of the corresponding limitations of OSP to more than ten endmembers would not dramatically improve the results. The discussion of reasons for those deviations, e.g. presence of high absorbance spectra which is although true in these cases, is provided in the upcoming chapters of this thesis and therefore are not in the focus of this discussion. Thus, the evaluation focuses on the qualitative differences of the results in order to draw initial conclusions.

Egyptian statue Considering first the results of the *Egyptian statue*, the following observations can be made. When comparing the first column to the second column it mainly gets visible that the lips are not represented in the second case. Because of the spectral similarity of the lips and the skin (face, neck, and right ear), this issue therefore introduces higher errors in these areas too. Beside this degradation, however, two spectra were found in the lower part of the statue, which is not the case in the first column. Although this leads to an improved representation of the lower part, still high error values can be noted, which were not present in the first column. Considering the color image of the statue in the appendix, it gets obvious that these areas are colored red. Thus, the reason for this failure is due to the drop of the constituent of the lips. Regarding the lips it can be observed, that these are only found in the first and third column. Considering the third column in more detail, it can be seen that here only one constituent was found in the lower part. Additionally, the spectrum of the left eye was not determined in this column, which is also true for the upcoming columns four and five. The results of the last two columns are relatively equal. Compared to the other columns it can be seen, that here the first time a constituent of the skin (ear) was found and again two spectra were determined in the lower part.

The results of the Mean Shift can not be evaluated that comprehensively as the LSU-results, because the automatic color-coding may lead to wrong impressions, due to comparable color levels or the change of cluster-colors between the columns. However, it can be observed that the number of determined clusters is varying with respect to the different blur levels.

Taking together the observations of the first test case, it gets obvious that especially endmembers within finer spatial structures suffer most by the presence of blur, for instance consider the determined constituent of the lips. Since the concept of LSU provides the capability to describe subpixel details, also the presence of an endmember, for instance in blurred fine structures, i.e. mixture, is not problematic, as long as redundant information for the endmember are available from corresponding larger more homogeneous areas. Certainly this assumption is only true for spatially equally distributed blur, which is not always the case as seen in the previous section.

Such mixed pixels can not be distinguished that easily by methods which are not con-

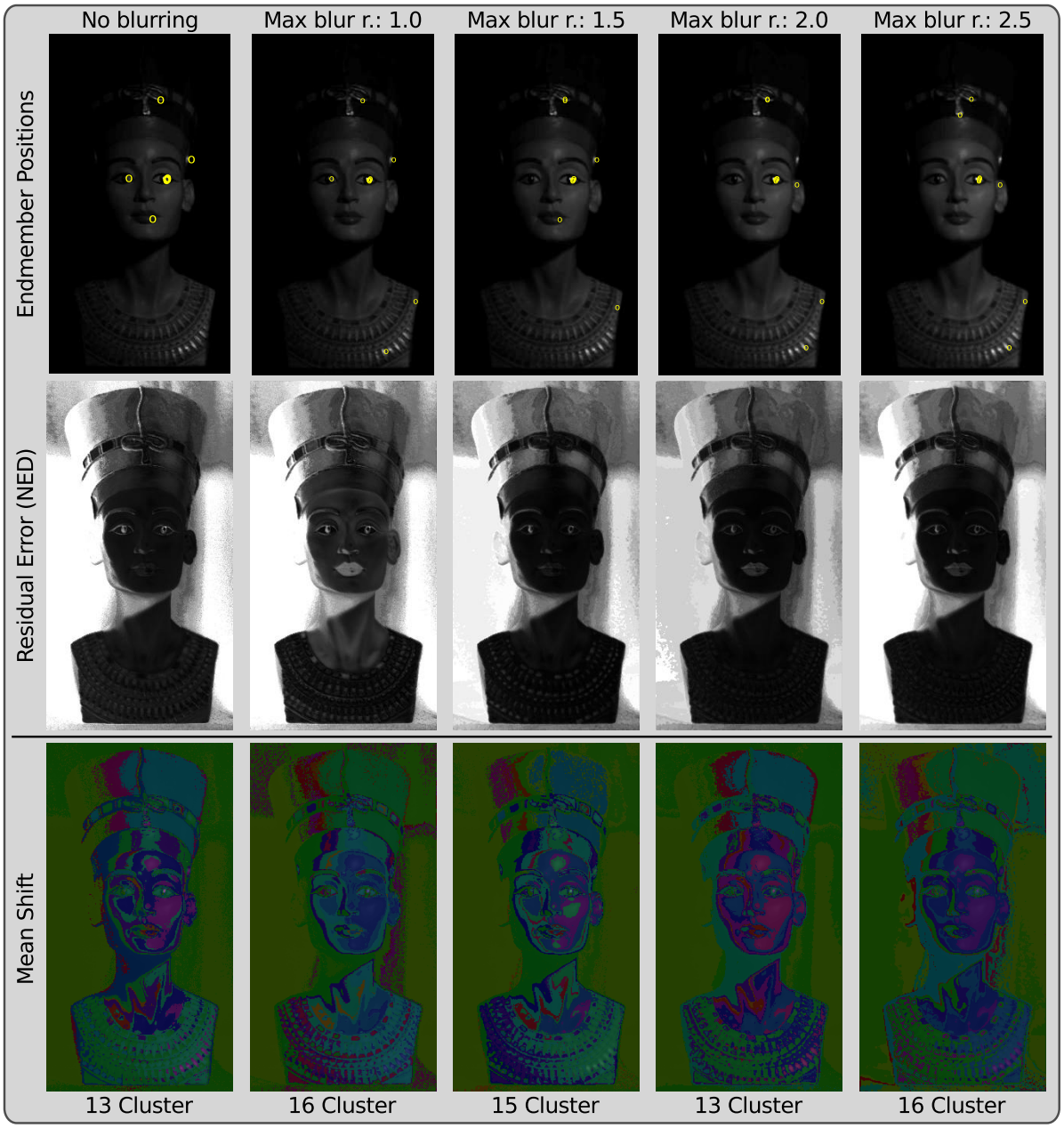

Figure 3.5: Egyptian statue: Qualitative comparison of analysis results based on different blur levels. The endmembers were determined by OSP, which was limited to 10. Moreover, the number of determined clusters by the Mean Shift algorithm is provided.

sidering subpixel information, like the Mean Shift. As consequence, mixtures are typically considered as distinct clusters. Moreover, small areas can get lost by the assignment to an other cluster.

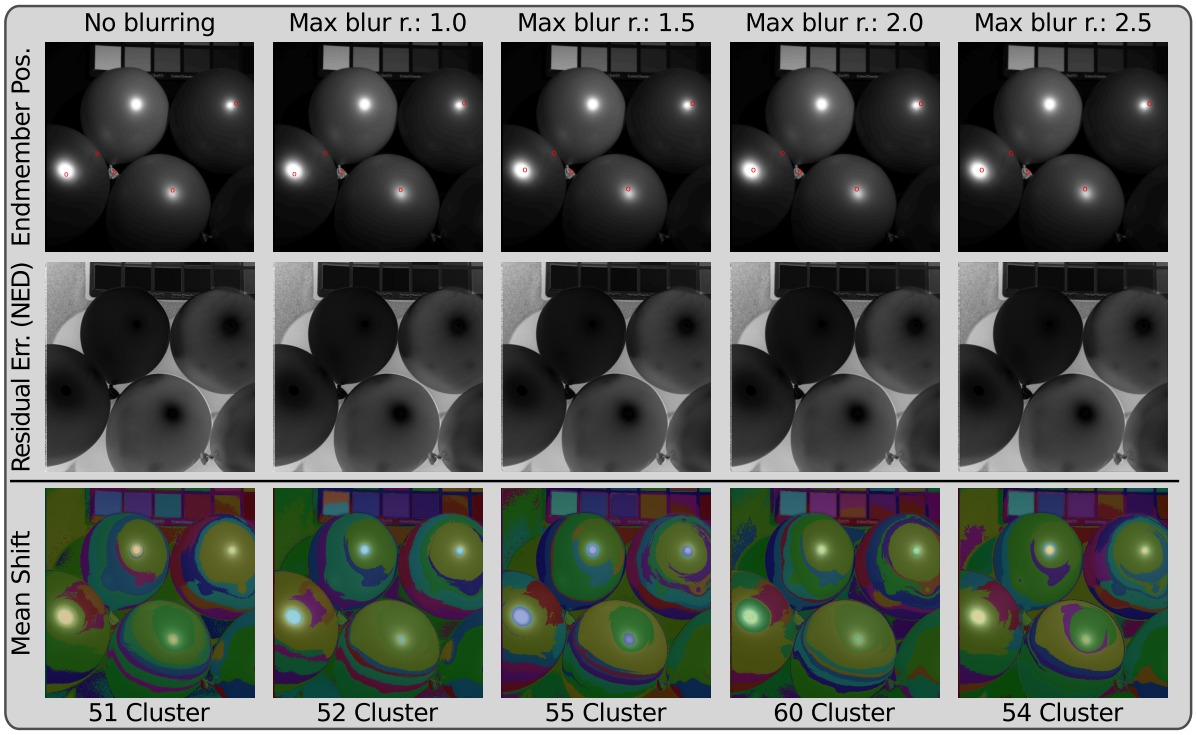

Figure 3.6: Balloons: Qualitative comparison of analysis results based on different blur levels. The endmembers were determined by OSP, which was limited to 5. Moreover, the number of determined clusters by the Mean Shift algorithm is provided.

Balloons Considering the second, i.e. *Balloons*, test case, these previous assumptions are getting confirmed. Comparing all the achieved LSU-results, especially the positions of the determined constituents, does not reveal any noticeable changes. This is due to the fact that this dataset contains less finer structures the the previous one. When considering the specular highlights of this dataset, which are much larger than in the other test case, then the relation of spatial area and the determination of the endmembers gets obvious. The results of the Mean Shift are not as constant as the results of theLSU, because of the lack to express subpixel details.

It can be concluded that blur can have influences with respect to the data analysis. In particular, it has been observed that the influence has a strong relation to details of targets, e.g. fine structures seems to suffer more. Certainly, the presence of blur has a strong influence when matching measured spectra against reference spectra of different measurement setups, which is in particular true for instance when using reference libraries. Yet, a more detailed final statement of the influence can not be given and needs more research of this particular problem, which would exceed the scope of this thesis.

3.2 Conceptional Proposal of a Deblurring Approach

The here discussed proposal is based on the set of computational photography techniques that has been presented by Heide et al. [HRH*13]. The discussion of Heide et al. is focused on the deblurring process of RGB images that are degraded, because of the utilization of simple lenses instead of highly complex lens systems (optics). The involving aspects for multispectral imaging systems are only marginally discussed and are part of joint future work. Thus, the following explanation focuses on a conceptional overview of the proposed, but already promising, deblurring approach. Since, as seen above, the chromatic aberration of optics is a major reason for blur in multispectral images, the main aim of this approach is to achieve a more lens independent image acquisition.

Starting with the discussion of the related work, the second section gives an rough overview of the approach, including also the underlying image formation model. The next two sections describe the two main elements of the computational photography tool set. The last section presents a first result of this proposed approach and discusses current shortcomings, which are part of joint future work.

3.2.1 Related Work

The idea of image deblurring is not new and a lot of recent work exist to compensate aberrations in images. Beside the common way to compensate these aberrations by designing increasingly complex optics with dozen individual optical elements [MM91], also post-processing methods exist which remove the aberrations after the capturing. This post-processing step typically is known as **image deconvolution**. Several convolution approaches can be found in the literature. Here, the most basic approaches include frequency-space division and the Wiener filter [WWM*64], which however have their difficulties with frequencies that are suppressed by the blur kernel. Motivated to compensate blur in optical systems for astronomy, the classical iterative method Richardson-Lucy [Ric72, Luc74] was developed. In the recent years, this approach has been often extended in many ways, including residual deconvolution [YSQS07] and Bilateral Richardson-Lucy [YSQS08]. Typically the image deconvolution problem can be assumed as ill-posed. Therefore, recently a lot of work has been done in order to incorporate prior knowledge of images in the deblurring process to better cope with large blur kernels and the complete loss of frequencies. Such image priors include both, convex and non-convex regularization terms. Common convex methods are total variation [CKG*11] and total curvature [GC11], which are guaranteed to converge to a global optimal solution in the optimization. Although non-convex techniques are not guaranteed to converge to a global optimum, they typically produce state-of-the-art results in practice. Here, two well-known methods are for instance the Iteratively Reweighted Least Squares [LFDF07, JZSK09] and a Hyper-Laplacian prior which was introduced by Krishnan and Fergus [KF09].

All previously mentioned deconvolution methods are so-called *blind* deconvolution methods which have no knowledge about the blur kernels. However, the best deblurring results can be achieved with *non-blind* deconvolution methods, i.e. when the underlying blur kernels

are known. Therefore, several approaches exist to estimate the PSFs which describe the blur kernels, including spectral methods [GB00] and estimation from edge-based [JSK08] or noise-based patterns [BSA10] or image pairs [YSQS07]. Moreover, recently Schuler et al. presented an approach which estimates PSFs that are constrained to a class that exhibits the generic symmetry properties of lens blurs by creating a suitable orthonormal basis [SHHS12]. As mentioned by Schuler et al. [SHHS12], the proposed image prior is content specific and is only suitable for natural scenes.

Non-blind deconvolution methods are recently applied to compensate spatially varying PSFs [KPCW11] and to remove chromatic aberrations [CKS09, JZSK09] for images taken with complex optical systems, thus typically having quite small PSFs. Joshi et al. [JZSK09] proposes a color prior that encourages color gradients that are linear blends of two base colors. But, since large-area color fringing is typically composed of several segments that are linear mixtures of different base colors, the proposed prior has difficulties to remove color fringing from chromatic aberration. Especially designed to remove color fringing in images, Kang [Kan07] proposes a method which is based on edge-detection. Thus, intrinsically requires images that do not suffer from large blur kernels. Cho et al. [CJZ*10, CZJ*12] propose a deconvolution method that uses locally learned gradient statistics for content-aware image restoration [CJZ*10] and for restoring mid-frequency textures [CZJ*12]. By working in the YUV color space, Schuler et al. [SHHS11] present a Hyper-Laplacian prior to avoid color artifacts stemming from PSFs with relatively sparse features and thin structures. However, this prior suffers from the lack of global convergence and is not sufficient to avoid artifacts in the presence of large disk-like blurs such as the ones produced by spherical and chromatic aberrations.

In contrast to all these methods, the following conceptional discussion of the approach presented by Heide et al. [HRH*13] uses a convex cross-channel prior for multi-channel images that can be implemented efficiently and with guaranteed global convergence. As a result, it can produce excellent image quality even in the presence of very large blur kernels.

3.2.2 Overview

As seen before, many variations and reasons for blur in images can appear in an optical system. Typically, a linear and general image formation model is assumed in order to describe the process of blurring as well as of the deblurring. In the notation of [HRH*13], this model consists of four quantities:

J	The acquired blurred image.
B	The blur kernel that describes the PSF.
I	The underlying sharp image.
N	The additive image noise.

With respect to the image resolution $n \times m$, all these quantities are $\in \mathbb{R}^{n \times m}$. When considering $\mathbf{B}, \vec{j}, \vec{i}$ and $\vec{n}$ as the corresponding quantities in matrix-vector form, the linear model can be

formulated as

$$\vec{j} = \mathbf{B}\vec{i} + \vec{n}. \tag{3.1}$$

Based on this formulation and when neglecting $\vec{n}$, the blur of an image solely depends on $\mathbf{B}$. Thus, the process of image deblurring tries to solve the inverse problem of Eq. (3.1) in order to achieve $\vec{i}$. As already seen above, the deblurring process is called *non-blind* when $\mathbf{B}$ is known, otherwise the process is called *blind* deblurring.

In the following, a proposal of a *non-blind* deblurring process is presented. Therefore, the process roughly can be seen as a two step approach, consisting of

1. a calibration step to estimate $\mathbf{B}$, i.e. the PSFs, and
2. the final non-blind deblurring step to achieve the sharp image.

Both steps are discussed in the upcoming two subsections. Since the aim of this section is the conceptional discussion of this deblurring approach in order to present the big picture, the following technical explanations and the discussion of the prior work are reduced to a minimum. Readers, who are interested in an in-depth discussion, therefore are referred to the based work [HRH*13].

3.2.3 Estimation of Point Spread Functions

The estimation of the PSFs is a fundamental requirement of the non-blind deblurring. Here, it does not matter if a PSF was measured in a laboratory situation, or any other existing estimation method was used. Since, PSFs typically are spatially varying, a calibration pattern based approach is used. Based on the discussion of noise targets in [BSA10], the calibration pattern consists of several random white-noise patches, where each patch will generate one PSF in the estimation. Figure 3.7, in the top left, shows an example of a calibration pattern. Here, white borders help to achieve physically correct boundary conditions. It is important, that the patches have a flat spectral reflectance in the applied spectral range.

Considering the image formation model in Eq. (3.1), when both images, $\vec{j}$ and $\vec{i}$, of the calibration pattern are known, then the PSF estimation can be proposed as an inverse optimization problem in order to achieve $\mathbf{B}$. While it is trivial to achieve the blurred image $\vec{j}$ of a calibration pattern, the corresponding sharp image can be achieved by stopping the lens down to an almost pinhole aperture in order to avoid lens aberrations, as also was done in Fig. 3.2. In the context of multispectral imaging, this means, that $\vec{i}$ of the pattern is acquired for the focused band. Whereas the usual acquisition of a complete image cube of the calibration pattern leads to a dataset, where each band is considered as a $\vec{j}$. Now, the PSFs for each band can be estimated by solving the minimization problem, which in more details is discussed in [HRH*13]. Exemplary, the Fig. 3.7 shows the estimated PSFs for three spectral bands, where the spatial dependence of the PSFs can be well noticed, especially for the 950nm band.

The PSF estimation typically has to be done once as preprocessing step in order to achieve a calibrated setup. Then the typically acquired multispectral image data can be deblurred with respect to these PSFs.

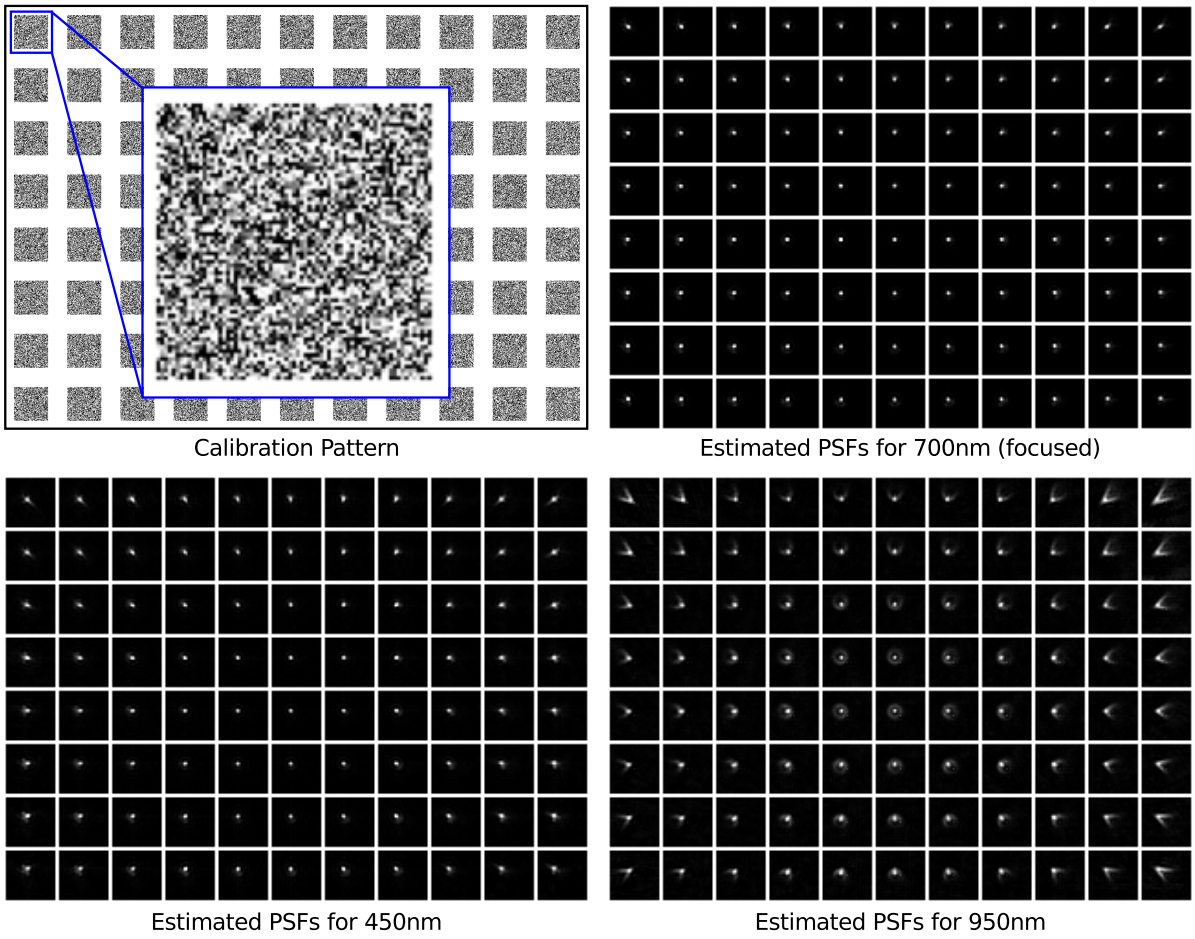

Figure 3.7: Calibration pattern, consisting of several white-noise patches, and corresponding exemplary estimated PSFs of the measurement setup depicted in Fig. 3.1. The 700nm band was focused in this example.

3.2.4 Non-Blind Deblurring

Now, assuming that the PSFs are already given, the deblurring process itself is the focus of the explanation. As mentioned before, the rational of the deblurring process of Heide et al. [HRH*13] is the incorporation of cross-channel information. Here, the authors have mainly focused on RGB images which were acquired by the usage of simple lenses. Compared to complex lenses, simple lenses only have very limited abilities to compensate chromatic aberration in the capturing process. This is due to fact, that typically one channel is significantly better focused than the other two channels. Because of this behavior, the here imposed problem is quite comparable to the observed blurring problem of the multispectral imaging in Sec. 3.1.1.

The case of RGB is assumed in the following. The independent deblurring of color channels $\vec{j}_{\{1\ldots3\}}$ based on their corresponding PSFs $\mathbf{B}_{\{1\ldots3\}}$ has revealed that this procedure does

not in general produce acceptable results. Since, frequencies in some channels may be distorted beyond recovery. By the proposal to share information of channels in the deblurring process, successfully preserved frequencies in a channel should help to recover lost frequencies in another channel. Based on two assumptions,

1. edges in images appear in the same place in all images and
2. hue changes are sparse throughout the image,

the cross-channel gradient prior

$$\nabla\vec{i}_k/\vec{i}_k \approx \nabla\vec{i}_l/\vec{i}_l \;\Leftrightarrow\; \nabla\vec{i}_k \cdot \vec{i}_l \approx \nabla\vec{i}_l \cdot \vec{i}_k \tag{3.2}$$

is defined. Here, both operators, multiplication and division, are pixel-wise applied with respect to a channel pair l,k. By the usage of this prior, the following optimization problem can be formulated

$$(\vec{i}_c)_{opt} = \underset{\vec{i}_c}{\operatorname{argmin}} \left\| \mathbf{B}_c\vec{i}_c - \vec{j}_c \right\|_2^2 + \alpha_c \sum_{a=1}^{5} \left\| \mathbf{H}_a\vec{i}_c \right\|_1 + \sum_{l\neq c} \beta_{cl} \sum_{a=1}^{2} \left\| \mathbf{H}_a\vec{i}_c \cdot \vec{i}_l - \mathbf{H}_a\vec{i}_l \cdot \vec{i}_c \right\|_1 \tag{3.3}$$

for a single channel, where the first term is a standard least-squares data fitting term, the second term is a image prior, and the last term is the presented cross-channel prior. As can be seen, for both priors an l_1 norm is used to ensure that the optimization problem is convex. Moreover, $\mathbf{H}$ defines convolution matrices, where $\mathbf{H}_{\{1,2\}}$ are corresponding to the first derivatives and $\mathbf{H}_{\{3\ldots5\}}$ are corresponding to the second derivatives. Additionally, both priors, the image prior and cross-channel prior, are weighted by $\alpha_c, \beta_{c,l} \in \mathbb{R}$, where for RGB $c,l \in 1\ldots3$. In case of multispectral imaging, the cross-channel prior is applied for all pairs of spectral bands.

Readers that are interested in the implementation of the minimization of Eq. 3.3, are referred to Heide et al. [HRH*13], where the minimization algorithm is discussed in full detail.

3.2.5 A first Result for Multispectral Imaging

The application domain of this approach mainly was intended for the compensation of aberration in RGB images, which were acquired by the usage of simple lenses. While the results for RGB are already discussed in many details and are, with good success, compared to other state-of-the-art deblurring methods in the underlying work, the evaluation for multispectral imaging has not achieved the same level up to the finalization of this thesis. Although, first results are looking quite promising, as exemplary depicted in Fig. 3.8, this should not hide the fact that further research is needed. Because, the assumption of fixed PSFs for each spectral band is often violated. For instance, the assumption can fail to properly reconstruct metamers which will have different blur kernels and therefore will lead to errors in the data fitting term of Eq. (3.3).

However, the presented computational photography tools show a first step into the direction of a more lens independent and proper acquisition of multispectral image cubes. Which,

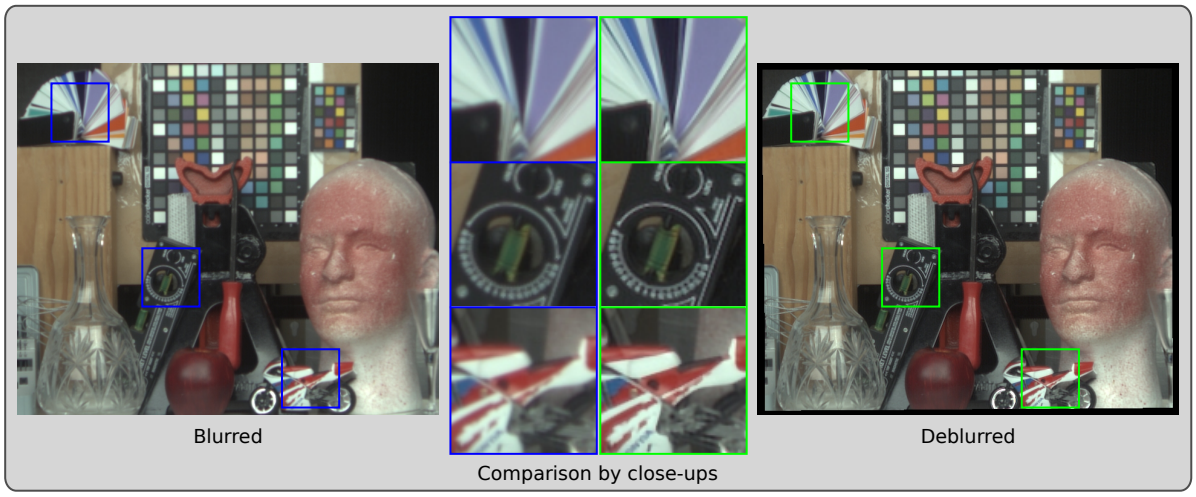

Figure 3.8: A first deblurring result for multispectral imaging after mapping to sRGB.

beside the improved sharpness, also have high potential to achieve reduced acquisition times, since the utilization of slowed down apertures, to achieve sharper images, fades into the background.

3.3 Summary

This chapter has mainly discussed the presence of aberrations in multispectral images by focusing on plane-based multispectral imaging. Instead of providing a full detailed discussion of this topic, the main aim of this chapter was a more fundamentally overview.

The first section has provided a problem discussion, that had revealed issues for blurred multispectral data and furthermore has presented a qualitative discussion of noticeable consequences for the data analysis. Here, the qualitative evaluation of the consequences was based on artificially blurred datasets and was exemplary done for the Means Shift clustering algorithm and the technique of LSU.

The last section has presented a conceptional proposal of a two step multispectral imaging approach, that allows the compensation of blurring. Here, the main goal was to acquire images more independently from limitations of lenses. The presented first result already achieved good deblurring result, but, assumes fixed PSFs for each spectral band, which is not true for all cases, e.g. in case of metamers.

Taking together, although an influence of blur with respect to the data analysis is noticeable, yet, a final statement about the consequences in data analysis can not be provided and mainly depends on further developments and evaluations of the proposed deblurring process. However, the analysis results of the LSU have shown easily noticeable residual errors in all cases. Among others, this fact is a key aspect that is further discussed within the following main scope of this thesis, which mainly presents a concept of visual analysis to verify and optimize LSU-results in general.

Chapter 4

Multispectral Data Analysis

As mentioned in section 2 the analysis of multispectral data is a challenging task due to a variety of defiances, e.g. imperfections, or the high-dimensionality in general. This chapter presents and discusses several aspects of multispectral data analysis, but mainly focuses on challenges of the analysis concept of LSU and the possibilities for visual analysis approaches. The structure of this chapter is subdivided into four sections, whose subjects are as follows.

The first section addresses the assessment of high-dimensional vector attribute variability to determine the minimum transformation effort, when transforming one vector to another one. Although the presented method is applied to multispectral image data, the here addressed question regarding distance metrics in high-dimensional data spaces is answered in a more fundamental way.

The second section deals with the first part of a visual analysis system, whose aim is the generic determination of constituent spectra based on the analysis concept of linear spectral unmixing. This approach introduces a generic workflow that combines automatic analysis approaches and user interaction to semi-automatically find an optimal set of endmembers.

Multispectral analysis results in general and results of endmember extraction algorithms in particular can be dramatically influenced by imperfections, like outliers, as described in section 2. This third section of the chapter therefore introduces a modular outlier masking scheme to improve the robustness of automatic endmember extraction algorithms.

The calculation of abundances in LSU commonly involves non-negative inverse methods, which can be computationally very expensive by itself [VG08]. Since, LSU is also utilized in interactive approaches, for instance in the second section, this section covers methods to enhance the calculation speed of the inverse operations, thus, achieving a better utilization of

LSU in a visual analysis approach.

Publications: The generalized similarity assessment of high-dimensional vectors has been developed by Marc Strickert and was presented in [SLKV11, SLB11]. The generic determination of constituent spectra, as well as the outlier masking and progressive unmixing scheme, including also the prediction of coefficients, has been subject in [LBK12]. In the context of efficient coefficients calculation in spectral mixture analysis the general coefficient estimation method has been presented in [LK13].

4.1 Similarity Measure in High-Dimensional Space

This section presents a general method for the assessment of data attribute variability, which plays an important role in initial screening of high-dimensional datasets. The here addressed key question is how much each data attribute contributes to an optimum transformation of vectors for reaching maximum similarity. This question is formalized and solved in a mathematically rigorous optimization framework for each data pair of interest. Instead of the commonly used second centralized moment, known as variance, the proposed method allows a mathematically rigorous characterization of attribute sensitivity given not only Euclidean distances but partial data comparisons by general similarity measures. Applied to multispectral image data, different spectral features are getting highlighted in dependence of the choice of measure, this way creating new image segmentation aspects.

Starting with some background information in section 4.1.1, section 4.1.2 introduces a method for the assessment of attribute variation of two high-dimensional vectors. Based on this method, two ways for the attribute variance assessment are presented in Sec. 4.1.3. Results of this generalized method, applied to multispectral image data, are shown in section 4.1.4.

4.1.1 Background

Multispectral image data provide a wealth of data that impose challenges on the analysis, because of the size, the complexity, and the typically non-Euclidean nature of spectral datasets [Cha07]. Recent work allows to effectively address the size problem by employing multi-central processing unit (CPU) or GPU-accelerated computing [TNI*10]. Non-Euclidean nature is addressed by general data similarity measures like Minkowski distances [KWH06], matrix metrics [SBS*10], Pearson correlation [SSVS09], or its descendant, the SAD, or, recently, divergence measures [VHS*10].

Depending ultimately on data measures, the nearest neighbor search is one of the most important operations in data processing models, such as hierarchical clustering [Joh67], vector quantization [Gra84], endmember detection [VG08, PMP*10, BDPD*12] or morphological operations [HR98]. In supervised scenarios, the selection of the 'right' measure can be alleviated by data-driven adaptive metrics. For example, weighting factors of the adaptive Euclidean distance can be learned from the data for scaling individual data attributes according

to optimizing features such as class discrimination [HV02]. Other examples include learning a matrix metric [SKS*09], or adaptive Pearson correlation [SSS*06].

Initial data exploration in unsupervised scenarios of yet unknown or unlabeled high-dimensional datasets often starts with the calculation of basic statistics of the dataset attributes, e.g. histograms or statistical moments e.g. mean, variance, skewness and kurtosis. Relationships between attributes are usually characterized by the covariance matrix which is also the main ingredient for PCA, one of the most widely utilized dimension reduction methods, as also seen in the fundamentals. Along with variance and covariance quantities come normalization methods like z-score transformation, i.e. mean-centered attribute divided by attribute variance, and whitening, i.e. linearly de-correlated attributes with identity covariance matrix, thus, enforcing statistical independence. All these concepts are based on the implicit assumption of underlying Euclidean data spaces. Particularly, the growing popularity of alternative similarity measures requires a reconsideration of variance quantification. The main reason is consistency of the analysis pipeline. For example, if clustering based on Pearson correlation similarity is desired, it might be adverse to choose standard PCA for data preprocessing, or z-score normalization of spectral data might be prohibited if the main processing part utilizes a divergence measure.

In the following, a very general variational approach is presented for unsupervised assessment of attribute (co-)variability (sensitivity) for differentiable metrics (similarity measures) taking real-valued vectors as arguments.

4.1.2 Assessment of Attribute Variation

In the following, metrics, divergence measures, and dissimilarities will be addressed as distances in the non-mathematical intuitive way. Generally, if two vectors $\vec{x}, \vec{w} \in \mathbb{R}^n$ from a dataset are given, the key idea here is to measure the minimum efforts needed to transform the variable vector $\vec{w}$ into a representation of maximum similarity with the target vector $\vec{x}$. Such an optimum transformation typically poses two challenges,

1. cancellation by potential vector symmetry and
2. optimum paths of point to point measures can be different,

both challenges are illustrated in Fig. 4.1. The optimum paths for the transformations $\vec{x} \to \vec{w}$ and $\vec{w} \to \vec{x}$ in a given space can be different. Moreover, their line integrals may be equal or different. Motivated by these two challenges, here it is the goal to record the minimum transformation effort by measuring

1. **magnitudes** of channel changes and
2. the variational path **integration**

during the optimum transformation. This procedure to traverse the optimum path and to measure the minimum transformation effort is called distance pursuit (DP). The DP is formalized and solved for each data pair of interest in a mathematically rigorous optimization framework in the following.

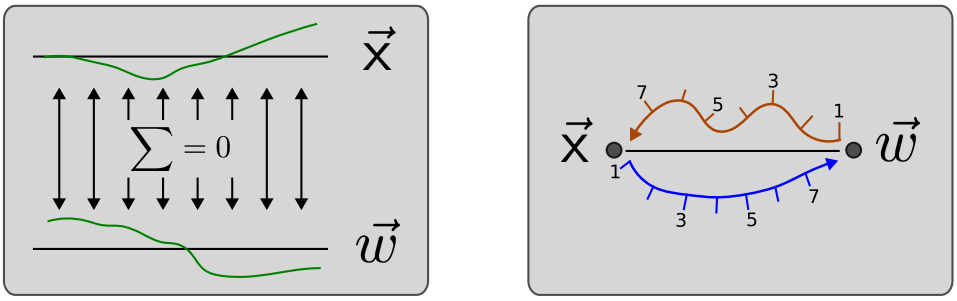

Cancellation by vector symmetry — Optimum paths can be different

Figure 4.1: Illustration of two challenges of an optimum transformation in high-dimensional space.

Algorithm 1 distance pursuit $\mathrm{DP}_{\{\vec{b},g\}}(\vec{x},\vec{w},t)$

```
// input x⃗ target vector; w⃗ source vector; t number of steps
g ← 0; b⃗ ← 0⃗_n // Initialize target variables
// Visit distance sequence elements, excluding m_0
for m ← m_1 to m_t do
    v⃗ ← arg min_{w⃗*} |m − d(x⃗, w⃗*)| // optimum vector at m, starting at w⃗* = w⃗
    Δ⃗ ← v⃗ − w⃗ // differential displacement
    w⃗ ← w⃗ + Δ⃗ // move on to identified location w⃗ = v⃗
    b⃗ ← b⃗ + Δ⃗ // integrate changes per attribute
    g ← g + √⟨Δ⃗⟩² // line integral
end for
return g, b⃗
```

Distance pursuit A pragmatic solution to traverse the optimum path between a source vector $\vec{w}$ and a target vector $\vec{x}$ can be formulated in an iterative manner. This iterative procedure is outlined in Algorithm 1 and in principle is illustrated in Fig. 4.2.

First, a monotonic distance sequence $\vec{m} = \{m_0 = \mathrm{d}(\vec{x},\vec{w}),\ldots,m_t = \mathrm{d}_{target}\}$ from the initial vector distance m_0 to the maximum possible degree of similarity d_{target} is created with $\mathrm{d}_{target} = 0$ for metrics and divergence measures and $\mathrm{d}_{target} = 1$ for Pearson correlation. An equidistant sampling of $t = 10$ sub-intervals, such as done in this work, is pragmatic but not mandatory. The vector $\vec{w}$ moves along the minimum path following increasing steps of similarity towards the target vector $\vec{x}$. During the transformation of $\vec{w}$, the two quantities are collected:

1. g, the overall line integral summing up path fragment lengths and
2. $\vec{b}$, the integrated differential attribute vector.

Thus, a piecewise linear approximation in n-dimensional Euclidean space is conducted to effectively assess attribute properties of the data under the distance measure of interest.

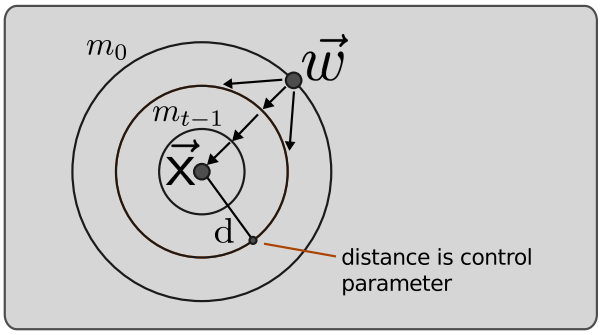

Figure 4.2: Euclidean illustration of the distance pursuit principle.

Line 5 of the Algorithm 1 provides the important identification of the next position of vector $\vec{w}$ for getting a bit more similar to vector $\vec{x}$. Gradient-based optimization methods can be used for minimizing the distance discrepancies between the current position and the next step of the target distance imposed by line 4. For distances $\mathrm{d}(\vec{x}, \vec{w}^*)$, the Minkowski distance (B.7), the Pearson correlation (B.9), and the γ-divergence (B.11), see Appendix , are utilized in this method. The gradient of the arg min operation, required for optimization, is

$$\delta = -\mathsf{sign}(s - \mathrm{d}(\vec{x}, \vec{w}^*)) \cdot \partial \mathrm{d}(\vec{x}, \vec{w}^*) / \partial \vec{w}^* \,. \tag{4.1}$$

Alternatively, a least squares expression can be employed in line 5, but it tends to generate numerical underflows during convergence.

Common gradient-based methods find zero discrepancy solutions desired in line 5. Yet, since optima for reaching a given similarity s are not unique, only minimum norm results for Δ are valid to get minimum path lengths. Else, for example with Minkowski metrics usually two points along the search line would yield valid optima at distance s to the target vector $\vec{x}$. Possible oscillations would be integrated out in line 8 for attribute variability, but the line integral in line 9, based on repeated calculations of $\langle\vec{\Delta}\rangle^2 := \langle\vec{\Delta}, \vec{\Delta}\rangle$, would be over-estimated.

Different gradient-based optimizers were tried using a reference implementation of Minkowski metrics with line integrals being standard Euclidean distance and attribute variability being standard variance, irrespective of the choice of the metric order p. Memory-limited Broyden-Fletcher-Goldfarb-Shanno (BFGS) turned out to provide the best mix of speed, memory requirement, and accuracy, in comparison to full BFGS, conjugate gradients, and steepest gradient descent.

4.1.3 Generalized Partial Covariance

The result of the distance pursuit algorithm is used as building block in a general formula for measuring the attribute variability of a dataset $\mathsf{X} = (x_{lk})_{l=1\ldots m,\, k=1\ldots n}$ with m data vectors (in rows) containing n attributes. Considering the reformulated text book term of standard

variance

$$\sigma_k^2 = \frac{1}{m-1} \cdot \sum_{l=1}^{m} (x_{lk} - \mu_k)^2, \tag{4.2}$$

where μ_k is the mean value of the k-th attribute and x_{lk} is the entry of the k-th attribute in the l-th data vector x_l. This common notation of variance quantifies the quadratic deviation of the k-th attribute from its mean. Alternatively, the expansion of $\mu_k = \frac{1}{m} \cdot \sum_{j=1}^{m} x_{jk}$ could be used for deriving a double sum notation of the variance visiting all pairs of data. Here, a double sum expansion of σ_k^2 avoids the explicit calculation of the mean value μ_k

$$\frac{1}{2 \cdot m \cdot (m-1)} \sum_{i=1}^{m} \sum_{j=1}^{m} (x_{ik} - x_{jk})^2. \tag{4.3}$$

Generally, pairwise attribute contributions, i.e. covariance, can be quantified via the partial derivatives for data relationships defined by either all pairs of data vectors or by a subset of pairs. Let $\mathscr{I}^i$ be the set of indices of data vectors connected to a data vector $\vec{\mathsf{x}}_i$, then the double sum notation can be transformed into the generalized partial covariance expression

$$Q_{kl} = \frac{1}{G} \cdot \sum_{i=1}^{m} \sum_{j=1}^{|\mathscr{I}^i|} \mathsf{DP}_{b_k}(\vec{\mathsf{x}}_i, \vec{\mathsf{x}}_{\mathscr{I}_j^i}, t) \cdot \mathsf{DP}_{b_l}(\vec{\mathsf{x}}_i, \vec{\mathsf{x}}_{\mathscr{I}_j^i}, t), \quad k,l = 1 \ldots n, \tag{4.4}$$

where the values Q_{kl} quantify the overall attribute contribution of all desired pairs of data vectors. Thus, Equation 4.4 quantifies attribute variability given data connectivity and distance measure. Here, the DP algorithm (cf. Algorithm 1,) is called with a resolution of t steps to calculate the integrated attribute derivative vectors $\vec{b}$ of which the k-th and l-th components are taken.

The normalization constant $G = 2 \cdot (-z + \sum_{i=1}^{m} |\mathscr{I}^i|)$ is twice the number of pairwise comparisons, excluding the number z of non-contributing self-comparisons $i = \mathscr{I}_j^i$. For all pairs of data $\mathscr{I}^i = \{1 \ldots m\}$ for $i = 1 \ldots m$ this leads to $G = 2 \cdot (-m + m^2)$ which yields an unbiased estimation of the variance $\sigma_k^2 = Q_{kk}$ of the k-th attribute for the Euclidean distance. This case allows a connection to Eq. (4.2), because the DP algorithm yields the simple difference $\vec{b} = \vec{\mathsf{x}}_i - \vec{\mathsf{x}}_j$.

The partial generalized covariance matrix Q is necessarily symmetric due to the commutative calls to DP in Eq. (4.4). This matrix can be used to calculate the partial generalized correlation matrix R according to the formula

$$R_{kl} = Q_{kl} / \sqrt{Q_{kk} \cdot Q_{ll}}. \tag{4.5}$$

If only R is of interest, the factor G in Eq. (4.4) is canceld out and does not need to be calculated. Thus, for data living in Euclidean space, these values are exactly the values much more efficiently can be calculated by Eq. (B.9). But, the benefits of the presented approach are custom data connectivities and similarity measures. Moreover, Euclidean assumptions like mean values $\mu_{\vec{\mathsf{x}}}$ of data vectors are not needed, because distance-specific centers of gravity are implicitly computed by the double sum. Thus, this approach is suitable for non-Euclidean measures too.

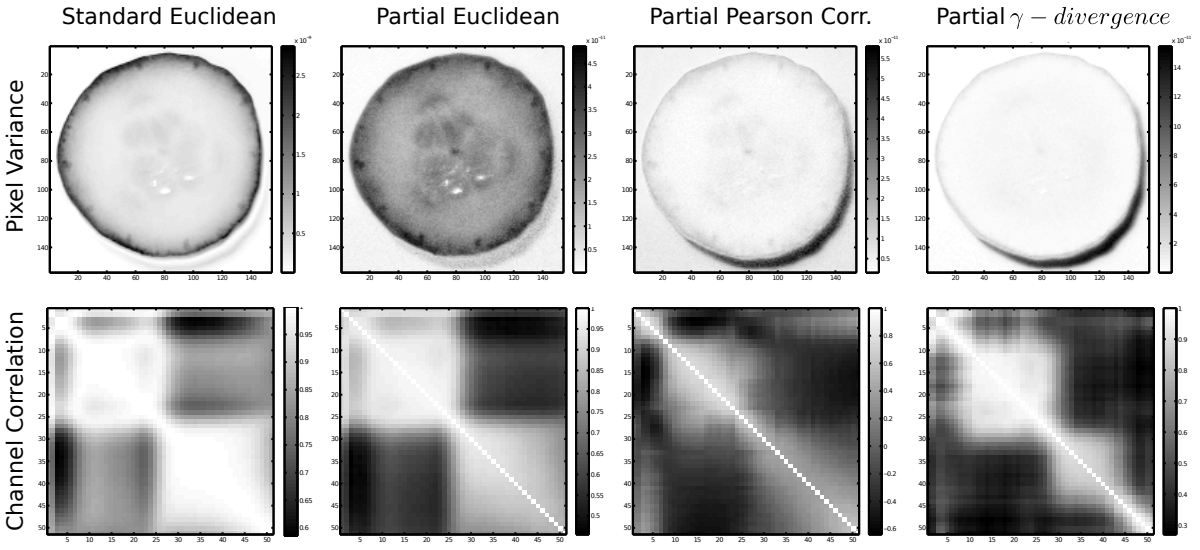

Figure 4.3: The top row shows the pixel variance and the bottom row shows the frequency channel correlation of the *Cucumber* dataset (cf. Appendix A) for different distance measures: From left to right, standard (all pairs) Euclidean distance and partial (adjacent data pairs) Euclidean distance, Pearson correlation, and γ-divergence for $\gamma = 0.1$ (brighter means higher).

4.1.4 Application to Multispectral Image Data

Food analysis is important for quality control and nutraceutics, thus, a representative multispectral image of a sliced *cucumber* fruit (see Appendix A) is taken as analysis target. The two targeted complementary perspectives for partial generalized attribute variance assessment are: per **pixel variance** involving pairs of channels and frequency **channel correlations** involving pairs of pixels.

Pixel variance is assessed for adjacent channels using the index set $\mathscr{I}^i = i \pm 1$ clipped to valid indices. This requires DP for 100 pairs of channels represented by one of the 51 frequency-specific monochrome image layers, resulting in an image of partial generalized variance per pixel. Involving adjacent channels uses only local differences for detecting more subtle relative changes than by global comparisons of distant and different frequency channels. As a consequence of the localized view, the analysis gets more sensitive to changes in else highly correlated channels. This is shown in the first two images in the top row of Fig. 4.3 changing from standard (i.e. global) to partial (i.e. local) variance. For Pearson correlation and γ-divergence the shadow cast rather than the cucumber peel or the background gets emphasized. This is, because both measures are β-scaling invariant to vectors $\beta \cdot \vec{\mathsf{x}}$ and thus optimally aligned with respect to scaling, i.e. being able to highlight variability in non-alignable structures like noise-containing shadows, which is useful for filtering different aspects. Note,

that in this particular case the background is white, which leads to a much better SNR in the background as in the shadow.

Channel correlations are assessed in the first local neighborhood of each pixel ij with $\mathscr{I}^{ij} = (i,j) + \{(-1,-1),(-1,0),(-1,1),(0,-1),(0,1),(1,-1),(1,0),(1,1)$ as index set. The resulting partial generalized correlation matrices of all pairs of 51 channels are shown in the bottom row of Fig. 4.3. Generally, there are two major clusters split in the middle (at about channel 25), and the first two channels are a bit outstanding. The range for partial Euclidean correlation (0.45–1) is a bit larger than for global correlation (0.59–1). Even richer are the partial correlation patterns for Pearson correlation (range: -0.6–1) and for γ-divergence (range: 0.29–1) which reveals four clusters along the diagonal line (two large, two small).

The application to multi-spectral data has shown the ability to provide richer partial covariance structures by utilizing local comparisons. Furthermore, data invariance properties of Pearson correlation and γ-divergence allowed to identify shadow areas rather than interior fruit segments being highlighted by Euclidean distance. Thus, due to different similarity impressions, the choice of similarity measure strongly depends on the analysis task itself, e.g. identification of shadows. Unsupervised and supervised data analysis tasks along data processing pipelines with other than Minkowski distances will benefit from the proposed method, because the measure-specific assessment of attribute variability is a very fundamental requirement. Several tightly connected methods like generalized whitening operation and PCA are yet to be exploited in future research.

4.1.5 Summary

This section has presented an approach for the assessment of attribute variability when transforming one vector into a representation of maximum similarity with a target vector. Here, the typically posed challenges of cancellation by vector symmetry and that the optimum paths of point to point measures can be different were addressed by a progressively distance pursuit algorithm. This algorithm measures the magnitudes of attribute changes and the variation path integration to address the two main challenges. For large datasets, the current implementation requires extraordinary runtime, because multiple nonlinear optimizations are required for each compared vector pair. Thus, in the context of this dissertation, has a rather more fundamental aspect. What can be learned fundamentally from this approach and the application to multispectral data, presented in section 4.1.4, is that the similarity assessment of high-dimensional vectors, i.e. spectra, strongly depends on the chosen metric, e.g. different similarity impressions, and the analysis task, e.g. detection of shadows. The general aspect of different similarity impressions of different similarity measures are revisited in the context of section 5.2.

4.2 Generic Determination of Constituent Spectra

The SMA requires the complete knowledge of the image endmembers, whose determination, on many practical occasions, may not be realistic [DRC03]. One reason is that every different endmember extraction algorithm has its own merits and no single approach is optimal and applicable to all cases [QFMSP12]. Moreover, as introduced in Sec. 1.2.2, the presence of pixels that represent pure substances depends on the acquisition device, e.g. sensor resolution or the chromatic aberration of a lens, as seen in Sec. 3.1.1. Consequently, there are possible situation where certain algorithms determine mixed pixels instead of the desired pure pixels [PMPP04]. Additionally, Plaza et al. [PMPP04] point out the increasing number of endmember identification methods and the resulting necessity of a standardized strategies to evaluate the quality of selected endmembers.

In this section, a visual analysis approach is presented to close the gap between limitations of automatic algorithms and an optimal set of endmembers of an observed multispectral dataset. The strength of the presented approach is the utilization of automatic extraction algorithms in an interactive approach to combine the benefits of both, manual and automatic endmember selection. This approach consists of two steps:

1. In a first step automatic algorithms and user-based parameter fine-tuning are combined in a semi-automatic endmember extraction part to determine a good initial set of endmembers.

2. As second step, the initial set of endmembers is manually refined in a visual analysis cycle, where analysts can bring in their expert knowledge.

First, a conceptional overview of the approach, including both steps, is presented in section 4.2.1. After the overview, the first part of this approach, the semi-automatic endmember extraction, is explained in section 4.2.2. Since, the aspects of the second part of the approach are mainly related to the visualization of multispectral data, the details of this part are discussed in the visualization chapter (see section 5.1) later on.

4.2.1 Conceptional Overview

This section gives an overview of a generic and problem-adopted way to extract endmembers of a dataset. In unsupervised multispectral data analysis, as discussed in the fundamentals 1.2.2, there is no a priori knowledge about the data available, e.g. about the number of endmembers. Moreover, often automatic algorithms for instance suffer from low SNR or outliers. Therefore, this analysis approach focuses on visual feedback to enable the user to assess the quality of an endmember set and to optimize it, if necessary, to finally achieve an application specific optimal set of constituent spectra.

A conceptional overview of the processing pipeline is depicted in Fig. 4.4. As can be seen, this process brings together the concepts of automatic and manual endmember selection. Therefore, the process can roughly be subdivided into two parts: **semi-automatic endmember extraction** and **manual refinement of the endmember set**. Before the workflow

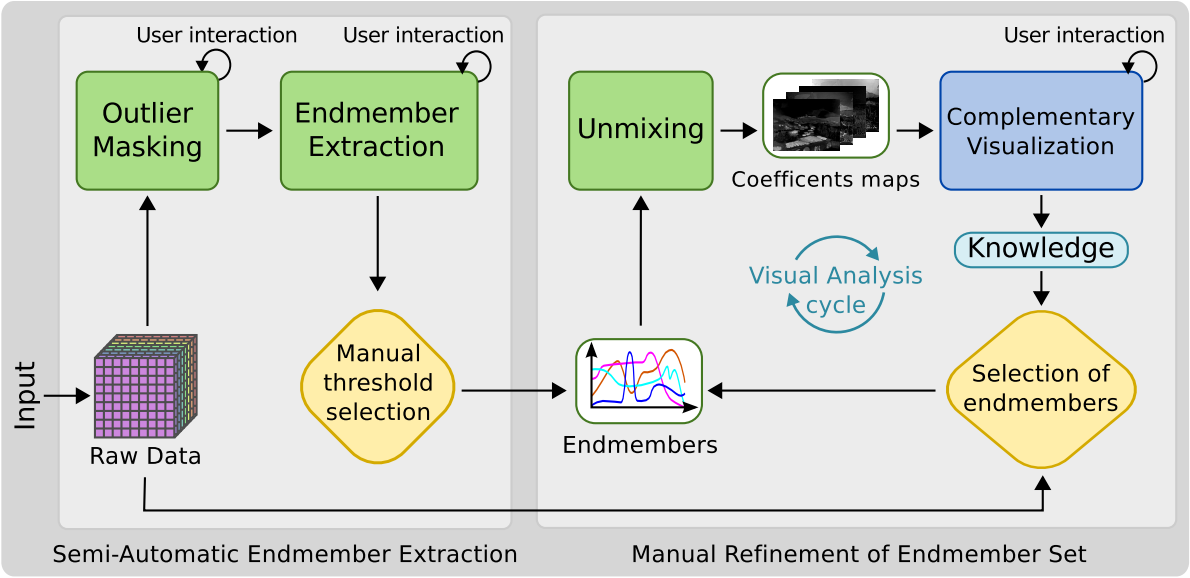

Figure 4.4: The exploration process is divided in two parts. First, semi-automatic endmember extraction and second, manual refinement of the endmember set within the visual analysis cycle. The rhombuses represent the main stages where analysts can refine the result and visualization. The complementary visualization is the main feedback and enhances the application specific information content in order to gain knowledge. In the case that data contain uncertainties, an optional outlier detection can be applied in order to improve the robustness of the endmember extraction.

and analysis part of the pipeline is discussed in more detail, first an overview of the four key components is presented:

1. *Outlier masking:* The outlier detection is an optional step in order to improve the robustness of the endmember extraction algorithms (see Sec. 4.3.2).

2. *Endmember extraction:* Endmember extraction algorithms are applied for automatic data analysis in order to find an initial set of characteristic spectra (see Sec. 4.2.2).

3. *Unmixing:* In the unmixing step, the coefficients are computed and a binary unmixing is done by computing the nearest neighbors for each endmember (see Sec. 4.4).

4. *Complementary visualization:* The two results of the unmixing step are visualized with two views, where each view is enhanced by an associated error image view. Furthermore, the four views are extended by several exploration options for deeper insights. More details of these four views are discussed in Sec. 5.1.

The workflow description of the pipeline is as follows:

Semi-Automatic Endmember Extraction The initial set of endmembers is discovered by applying *endmember extraction algorithms* as a first step. The parameters of the algorithms, if necessary, can be fine-tuned till a convincing initialization is found. In the case of uncertainties in the raw data, e.g. in the presence of outliers, the optional *outlier masking* can be applied before the endmember extraction step in order to improve the robustness of the automatic analysis. Based on the set of endmembers, the linear spectral unmixing coefficients and the nearest neighborhood (NN) for each endmember are calculated subsequently in the *unmixing* step.

Manual Refinement of the Endmember Set. After the initialization, the unmixing results are visualized by four *complementary views*, two views for the calculated results and two for the associated unmixing error images. Additionally, the user has means to further explore the results, thus to enhance the knowledge about the data. Whenever the user modifies the set of endmembers (select, deselect or add endmembers), the dataset is instantaneously unmixed and the views are updated immediately in order to ensure an adequate visual feedback. Furthermore, the principle of modification underlies an interactive exploration process where the analysts can bring in their domain-based expert knowledge in a visual analysis cycle. Based on their expert knowledge, the users should be enabled to confirm their expectations and to discover the unexpected [KAF*08]. Finally, when a good set of endmembers is found, the error images usually show no or negligible deviations for the whole spatial area or for regions of interest.

4.2.2 Semi-Automatic Endmember Extraction

As discussed above, the generic extraction of the constituents of an observed multispectral dataset utilizes common endmember extraction algorithms to find an initial set of endmembers, which afterwards interactively can be verified and optimized by the user. However, the high dimensionality of multispectral image data makes it necessary to reduce the visual complexity for the user in an interactive exploration approach. Thus, the reduction to a small number of constituents by automatic algorithms also can be regarded as a reduction of visual complexity in order to allow meaningful visualization and exploration methods. Since the current section focuses on the determination of the initial endmembers set, for the moment it is enough to know that these visualization and exploration methods provide the user with comprehensive tools to evaluate as well as to enhance the quality of a discovered set (details are provided in Sec. 5.1).

When applying endmember determination algorithms in the context of an interactive analysis approach mainly three challenges can be identified:

1. These extraction algorithm are usually rather time-consuming.
2. For some algorithms the parameters have to be manually fine-tuned.
3. The presence of imperfections in multispectral datasets.

The corresponding approaches for these challenges are discussed in the following paragraphs.

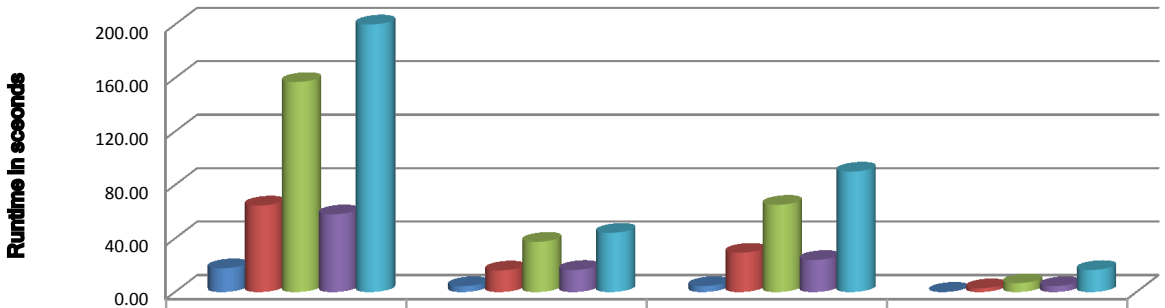

	Diamond (512x512x510)	Graphene (256x256x510)	Cuprite (614x512x192)	Glass tiles (512x512x31)
OSP CUDA	17.63	4.26	4.30	0.09
PPI CUDA	64.58	16.00	29.29	2.68
AMEE CUDA	157.00	37.41	65.12	6.52
OSP Matlab	57.98	16.41	23.88	4.30
PPI Matlab	204.92	44.16	89.95	16.37

Figure 4.5: Runtime comparison of some endmember determination algorithms for four datasets (cf. Appendix A). Here, the runtimes of the CUDA-based implementations of AMEE, PPI, and OSP are compared. Moreover, the runtimes of optimized Matlab implementations of OSP and PPI are listed for further comparison. In each case, OSP was limited to 10 endmembers, PPI has used 5000 skewers, and AMEE has executed 100 iterations. Note: Compared to all other methods, the CUDA-based implementation of AMEE is one of the slowest. Since the runtime of an alternative Matlab implementation of AMEE is even longer, this alternative implementation was excluded in this test scenario. The test system was equipped with an Intel Core i7 2.67GHz CPU, 12GB main memory and a NVIDIA GeForce GTX 480 (1536MB) graphics card and the used version of Matlab was R2010b (64-bit).

Time-consumption Commonly, a huge amount of data has to be processed in order to find the set of endmembers. This is a rather time-consuming operation. Recent works [SPT*07, SPTT08, SP10, SMP10] have shown the performance improvements that can be achieved with GPU-based implementations in the context of multispectral data processing. Therefore, after studying the literature in terms of accuracy and speed as well as based on own investigations, one popular method for each category of the endmember extraction algorithms (see Sec. 1.2.2) have been selected and implemented in CUDA to exploit the parallelization of a GPU. Here, the following algorithms were selected: AMEE, PPI, and OSP. For PPI an existing CUDA-based implementation of Sánchez and Plaza [SP10] was utilized.

In Fig. 4.5, the runtimes of the implemented algorithms are compared for four datasets. As can be seen, the runtimes of all methods depend very much on the spatial- and spectral resolution. In all cases, the CUDA-based implementation of OSP has achieved the lowest runtime, especially for the dataset *Glass tiles*. However, by comparing to all results, none of the implemented algorithms achieves interactive runtimes in each case, especially not for

datatsets that have both, high spatial and high spectral resolution. Therefore, its proposed to utilize these algorithms in the manner of a preprocessing step in a visual analysis approach.

Parameter fine-tuning In case of PPI and AMEE, the number of resulting endmembers strongly depends on user-based parameterisation, e.g. the thresholding of corresponding score maps. For these algorithms, the first unrefined set of endmembers thus is considered as a set of endmember candidates, which in most cases includes subsets of very similar spectra. Traditionally, the final set of endmembers is derived by calculating the mean of similar spectra or by choosing one representative spectrum of each group. In this context Plaza et al. [PMP*10] suggests to use OSP to further reduce the set of candidate spectra. In order to not belatedly introduce orthogonal restrictions to PPI and AMEE the decision was not to utilize OSP for this task. Moreover, the calculation of a mean spectrum can change the characteristics of a spectrum in case of incorrect grouping of spectra, e.g. by wrong thresholding in the spectral matching. Consequently, the focus is on the selection of a representative spectrum for each group in order to bypass changes of the spectral characteristic that may occur when calculating the mean. Yet, the challenge of grouping similar spectra by spectral matching is not solved. But, through the integration of immediate visual feedback that expresses the effects of parameter-changes, the user is visually guided in the parameter fine-tuning process in order to find the best possible initialization result. Fig. 4.6 shows simple examples for the parameter fine-tuning. Here, the corresponding error images can be considered as a simple example for the visual feedback. Moreover it can be seen, that the modification of parameters is mainly focused on the choice of common similarity measures (cf. Sec. 1.2.2) and the fine-tuning of thresholds.

Presence of imperfections As mentioned in the fundamentals (cf. Sec. 1.2.2) the endmember extraction algorithms typically search for the extreme spectra that generate the convex hull of a dataset. Therefore, these kind of common algorithms are sensitive against outliers. So if a dataset contains outliers, with a high probability these are identified as endmembers, which can lead to a unsatisfying result, as presented in the upcoming result section. In such cases, the usage of the optional preprocessing (see Sec. 4.3.2) is proposed to mark outliers, which then are not processed by endmember extraction algorithms in the following.

4.2.3 Usage Examples

In the following, results for two datasets, *Lemons* and *Graphene*, are discussed (cf. Appendix A).

Lemons The Fig. 4.7 illustrates the parameter fine-tuning of PPI, where the case with the 19 endmembers depicts the best result that was achieved with PPI. Since OSP was the most successful algorithm in the example with artificial dataset (cf. Fig. 4.6), a result of the OSP was depicted too. As can be seen, in this case the result of OSP is not as good as the best PPI-result, although OSP was configured to search for 31 endmembers, which is the maximum

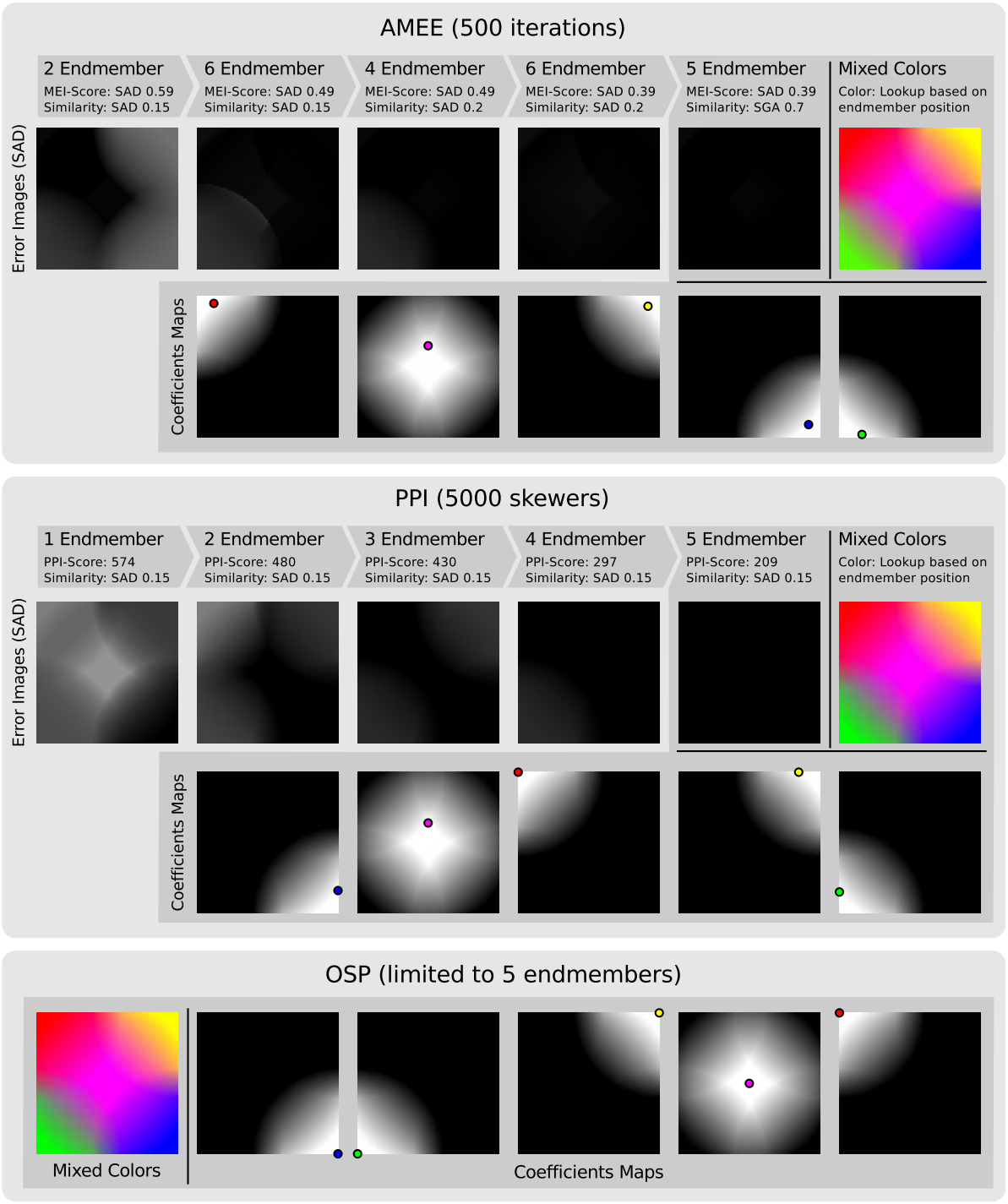

Figure 4.6: Examples for parameter fine-tuning in the semi-automatic endmember extraction for an artificial dataset *Five Endmembers* (cf. Appendix A). The parameter fine-tuning for AMEE is depicted in the top and the middle illustrates the fine-tuning process for PPI. For both approaches the applied paramterisations (score map threshold and similarity threshold) are depicted. For the sake of completeness, also the result of OSP is depicted. All determined endmembers are good representatives for this simple dataset. However, OSP was the only algorithm which was able to find the exact positions for each endmember (found positions are marked in corresponding coefficients maps).

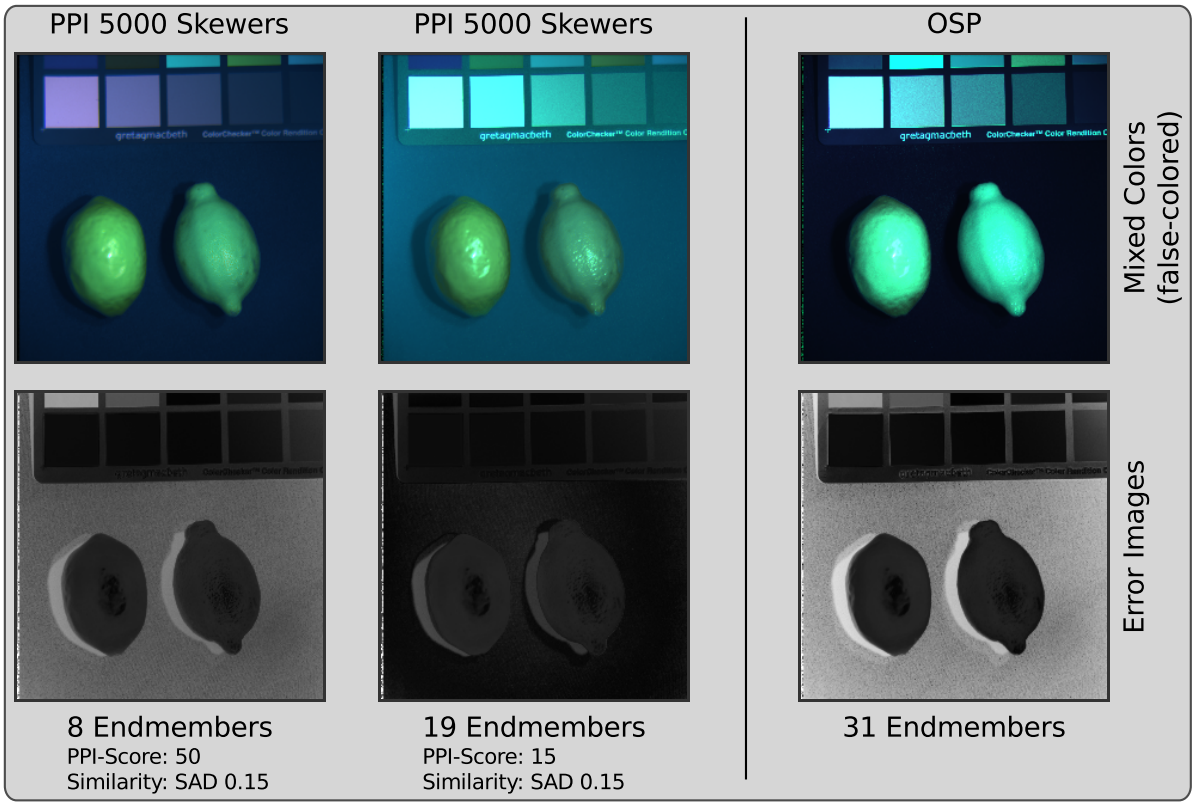

Figure 4.7: PPI-results are shown to illustrate the parameter fine-tuning in the semi-automatic endmember extraction for the *Lemons* dataset (cf. Appendix A). The PPI-results are compared to OSP, which was the most successful algorithm in the example with the artificial dataset (cf. Fig. 4.6). As can be seen, here the results are not as comparable as in the case with the artificial dataset. Especially OSP has high deviations in the background area.

for this dataset. While the representation of the Lemons look comparable for both, PPI and OSP, especially the background area is not as good represented in the OSP-result. However, also the PPI-result has still some deviations left which a user easily can notice. Thus, a user based verification and refinement of the endmember set, as discussed in Sec. 5.1, in general is highly recommended.

Graphene While the results of the previous case are not perfect, but already quite acceptable, the results for the *Graphene* dataset are throughout unsatisfactory, see Fig. 4.8. The reason for these inaccurate results is due to the presence of imperfections in the data. Especially OSP, which is a greedy algorithm, suffers from such circumstances. As discussed before, in such cases the usage of a preprocessing is supposed to enhance the robustness of automatic analysis results. Therefore, this challenging dataset is reconsidered in a usage example in the upcoming explanation of the supposed outlier masking scheme (Sec. 4.3.2).

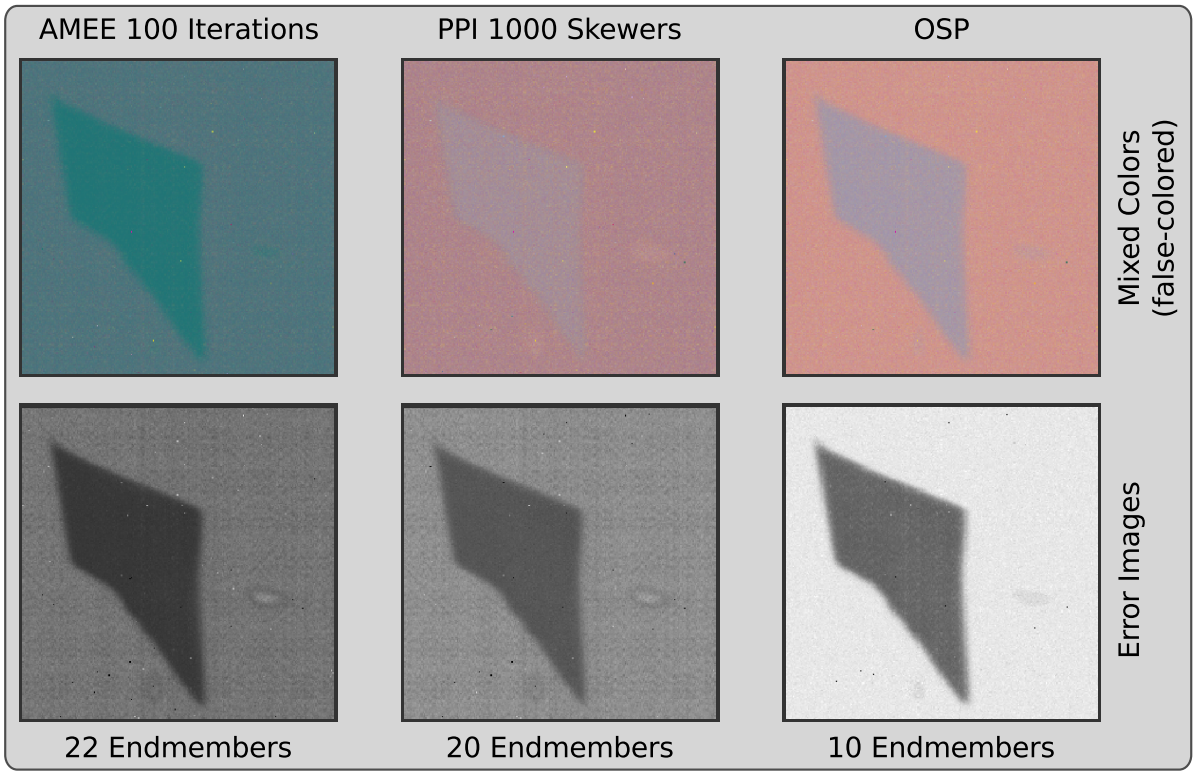

Figure 4.8: Three results that have been achieved with the semi-automatic endmember determination are compared. As can be seen, the reconstruction quality of AMEE (left), PPI (middle), and OSP (right) is quite comparable. But, in all cases the reconstruction quality is not fully satisfying, since all error images still reveal high error values.

4.2.4 Summary

This section has presented the first part, the semi-automatic endmember extraction, of the proposed visual analysis approach for the generic identification of constituent spectra. The here discussed first part mainly has addressed the challenge to achieve a proper parameterisation for endmember extraction algorithms, if necessary. Without discussing details of the visualization of the second part, the discussed usage examples have already shown the general potential of visual feedback to find the best initial endmember set by parameter fine-tuning. The details of the second part, the manual refinement of the endmember set, are subject in section 5.1.2, thus, to mainly tackle cases where these algorithms are not able to determine a reliable set of constituents. Beside these quality aspects of a set, also the runtimes of the endmember extraction algorithms for datasets with different spatial as well as spectral resolution were discussed. This discussion has turned out that these algorithms can be rather slow, therefore should preferably used as preprocessing in a visual analysis approach.

Moreover, this section already has revealed one major circumstance, i.e. outliers, in the

data, which can prevent a reliable automatic extraction result. Beside the user-based correction in a post-processing step, the next section proposes a outlier masking scheme as preprocessing to improve the robustness of these algorithms. Thus, to improve the initially found result to consequently reduce the refinement effort of a user in the second part.

4.3 Outlier Masking for Endmember Extraction

Since endmember extraction algorithms (see Sec. 1.2.2) are searching for extremes in a dataset, outliers can dramatically harm the resulting constituent set, as seen before. This section therefore discusses a preprocessing scheme to handle outlier in data and to consequently improve the robustness of automatic endmember extraction algorithms.

Starting with an overview to provide background information about imperfections in multispectral data (Sec. 4.3.1), next, an outlier masking scheme for multispectral data is described in Sec. 4.3.2. Exemplary results are shown in Sec. 4.3.3.

4.3.1 Background

The task of endmember extraction algorithms is the determination of spectra that are physically meaningful, which in itself is challenging enough. However, this challenge is compounded by the fact that these algorithms also have to perform for environments having limited and imperfect information [Kes03]. In contrast to statistical techniques like PCA, endmember extraction techniques are capable of also determining spectra with a relatively low spatial distribution in the dataset. Therefore, also pixels that contain imperfections which may arise by atmospheric phenomena or sensor artifacts may be extracted as endmembers. As a consequence, these algorithms perform best with data that are free from artifacts that can create spurious results [Kes03].

In many applications, multispectral data are preprocessed to reduce impurities to improve the analysis result (cf. Sec. 1.2.2). For instance in the application domain of confocal Raman microscopy, the datasets typically are preprocessed to smooth the spectra, remove the fluorescence background or remove atmospheric phenomena, e.g. cosmic rays that result in high peaks, usually, in single spectral band in a single pixel (see Fig. 4.9). Still, it is challenging to find a suitable parameterization in the preprocessing without losing too much spectral Raman information [DHT10]. Therefore in general it is recommended that any spectroscopic software allow the preview of the resulting spectrum to judge the current parameterization by an expert [DHT10].

4.3.2 Outlier Masking

As presented in the background information, the preprocessing of multispectral datasets can be necessary when data contain imperfections which prevent good analysis results. But, the search for a proper paramterization in the preprocessing typically is a balancing act between

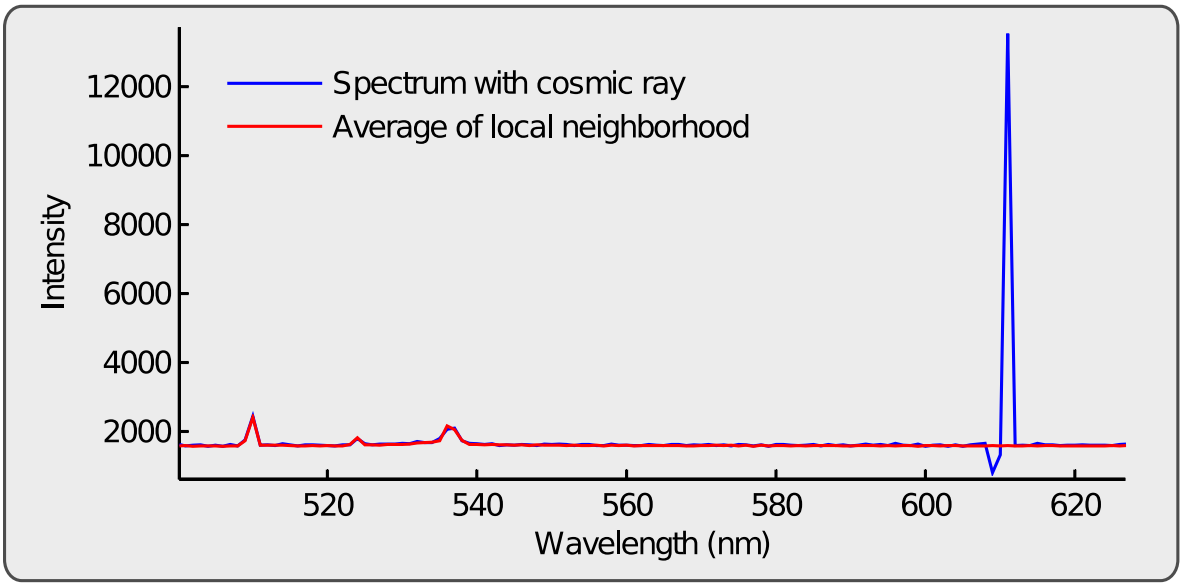

Figure 4.9: This plot shows spectra of the *Graphene* dataset (cf. App. A). Here, the wavelength range is limited to the interesting spectral bands. The blue line is a spectrum that contains a cosmic ray at wavelength 616nm (the negative peak is because of integer overflows in the sensor). Compared to the average spectrum of the corresponding local neighborhood (red dashed line) it is noticeable that a cosmic ray affects only a single pixel.

good data enhancement and loosing of spectral characteristics, e.g. due to too much smoothing. Therefore, the here presented preprocessing scheme has the aim to improve the robustness of the automatic analysis in cases where the data contain outliers, without loosing any information.

This aim is achieved by the use of a two-dimensional binary lookup-table (LUT), where aberrant pixel (x,y) are marked as outlier. The LUT is referred to as outlier mask (OM) in the following. In the automatic analysis, the OM is used to check if a pixel should be processed. In the case of an outlier, the associated pixel is skipped. Note that these outlier pixels are only skipped in the automatic endmember extraction. In subsequent calculation, e.g. to determine the reconstruction quality, the unfiltered dataset is used. By the subsequent processing of the whole dataset, no information can get lost, since this non-destructive editing has the advantage that false selections consequently lead to high values in the error images so that the analyst can directly react (see Sec. 4.2.1).

In general, the outlier masking follows a modular design and allows the usage of application specific methods for outlier detection, like centroid-based outlier detection in multivariate data [EM98] or support vector data description [TD04]. In the following, an example for outlier detection in the context of confocal Raman microscopy [DHT10] is shown. Here, as mentioned above, cosmic rays are one of the impurities frequently encountered in multispectral datasets, i.e. confocal Raman datasets. As can be seen in Fig. 4.9, an outlier spectrum, caused by a cosmic ray, significantly differs from its local spatial neighborhood, at least at one spec-

Algorithm 2 Pseudocode of an outlier detection module for cosmic ray identification

```
Initialize outlier mask (OM)
OM[X, Y] // X and Y are the spatial resolution of the source image
→ initialize OM with FALSE
Search for deviations to determine outlier
for each pixel(x,y) do
  for each wavelength do
    numDeviations = 0
    // Proof the local 3 × 3 neighborhood
    for each adjacent neighbor do
      // Difference of the current wavelength intensities
      curDist = abs(curPixel-curNeighbor)
      // T_user is a user defined threshold
      if curDist > T_user then
        numDeviations = numDeviations+1
      end if
    end for
    if 3 ≤ numDeviations then
      OM(x,y) = TRUE
    end if
  end for
end for
```

tral channel. Due to its relatively simple characteristic, a straight forward algorithm can be applied to identify cosmic rays. The approach (see Alg. 2) checks the 3×3 neighborhood of each pixel and marks a pixel as outlier, i.e. $\mathrm{OM}(x,y) = \mathrm{TRUE}$, if, in at least three spectral bands, intensity variations can be perceived which are larger than a user-defined threshold T_{user}.

4.3.3 Usage Example

Confocal Raman microscopy (CRM) is a combination of confocal microscopy, delivering a sharp 3D image of semi-transparent materials, and Raman spectroscopy, which provides multispectral data in high spatial resolution. The main application for CRM is the determination of the chemical composition of the specimen. Here, the main goal of analysts is the identification of the constituents in the dataset. In this section the robustness improvement of automatic analysis by the presented outlier masking scheme is exemplary discussed for CRM. The following results are achieved by using the *Graphene* dataset, which mainly consists of graphene and silicon as substrate. Here, graphene appears in two different layer thicknesses, a thicker, larger flack and two smaller, thinner flacks at the bottom and the right of the dataset, which have different spectral characteristics. See the Appendix A for further details about this dataset. Applying a PCA directly reveals the major challenges in confocal Raman datasets

(see Fig. 4.10): A sensor specific "noise" pattern (here in the first principal component) and cosmic rays dominate the dataset.

The importance of proper preprocessing is demonstrated by applying automatic endmembers extraction with and without outlier masking. As shown in Sec. 4.2.3, the automatic endmember extraction algorithms PPI, AMEE and OSP yield comparable reconstruction qualities. Since, OSP suffers most from the presence of outliers, the result of OSP (limited to 10 endmembers) is considered (see Fig. 4.11, left) in this test scenario to best possible show the effect of the outlier masking. Based on the OSP-result, the two most influencing constituent spectra are manually selected. Furthermore, the colors have been exchanged for easier subsequent comparison to the result with enabled outlier masking, later on. In both cases without outlier masking the associated error images entirely show large error values, especially for the substrate silicon. Actually, all detected endmembers are severely influenced by cosmic rays, thus are no good representative spectra. Yet, the poor distinction of graphene and silicon is only possible because of the lucky circumstance that dominating cosmic rays are present in both materials of interest. If this would not be the case, for instance when assuming that outliers are only present in one material, e.g. silicon, then the automatic determination would not find graphene until at least all dominating outliers have been found before. This is a worst-case scenario, but shows the high-influence of outliers in the automatic determination of constituents and also the importance of visual feedback in order to allow an analyst to judge the quality of the determined result.

Applying the outlier masking technique in combination with automatic endmember extraction, the resulting initial set of endmembers contains all relevant spectra, i.e. the silicon substrate and both, the thicker (colored red) and two thinner graphene flacks (colored green). Selecting these characteristic spectra achieves the final result in Fig. 4.11, right, without any further manipulation of the set of endmembers, except from the exchange of representative colors. The skipped outliers can still be seen in the error images as bright pixels. Thus, the analyst can still examine the spectra of these single pixels, e.g. to confirm the exclusion or to perform corrections if necessary. Finally, Fig. 4.12 shows the quality difference between non-preprocessed (left) and preprocessed results in terms of the coefficient maps of the corresponding endmembers.

4.3.4 Summary

This section has discussed an outlier masking scheme that is capable to improve the robustness of automatic endmember extraction algorithms. While the focus of the discussion was laid onto the detection of cosmic rays for CRM, the modular design of this scheme also allows the integration of application specific outlier detection methods. Beside the major aim, the improvement of robustness, the second aspect of this scheme is that no information can be lost in a visual analysis approach. Applied to the challenging *Graphene* dataset, this usage example has shown, in comparison to the result of Sec. 4.2.3, that the automatic algorithms were able to determine a reliable set which needs no further refinement by a user.

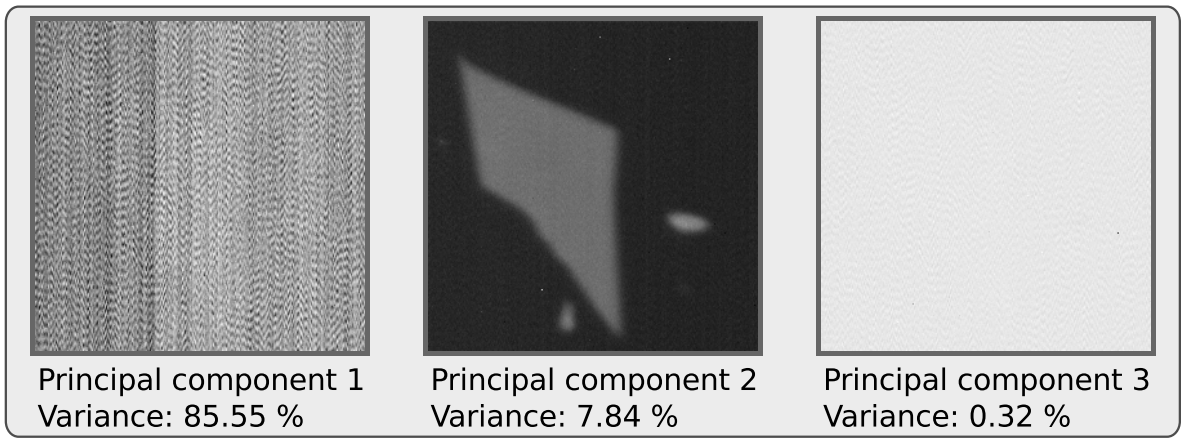

Figure 4.10: The high noise level of the *Graphene* dataset is shown with the help of the first three principal components in an increasing order *(from left to right)*.

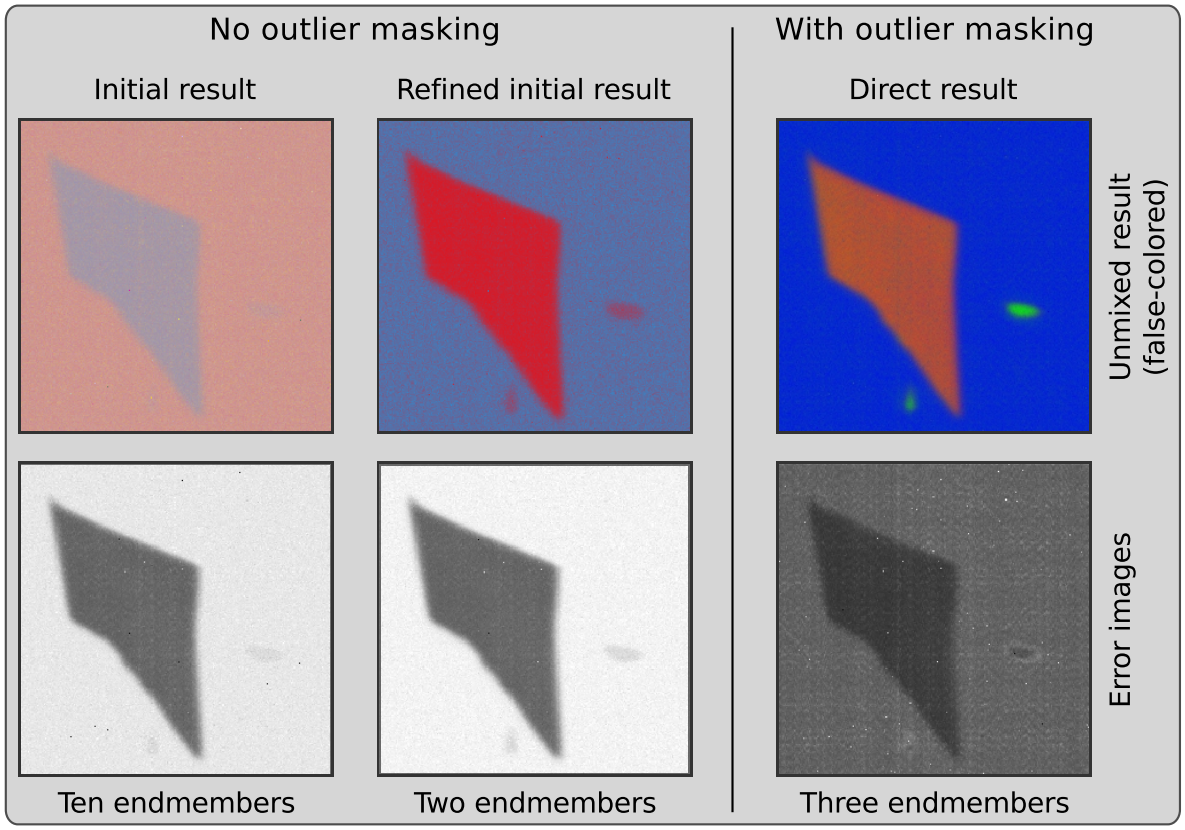

Figure 4.11: Result for the *Graphene* dataset. Initialization result with ten endmembers *(left)*, manual refinement and color selection of initial endmembers without outlier masking *(middle)* and after applying the proposed outlier masking *(right)*. The red (and green) areas belong to graphene while blue represents the silicon as substrate *(middle and right)*.

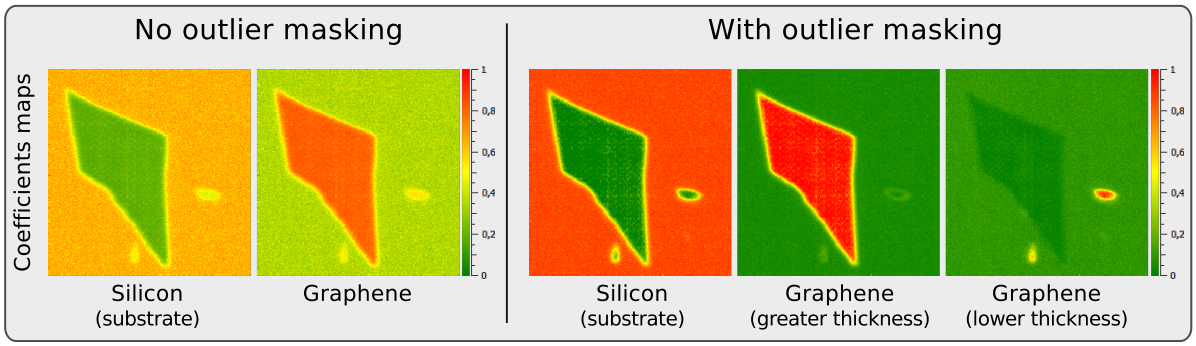

Figure 4.12: The coefficient maps for both, without *(left)* and with outlier masking *(right)*. All images are normalized. The lower values, that are poor representations of the selected material, are represented by green, while high values, indicating proper material assignments, are colored red.

4.4 Unmixing Coefficients for Interactive Applications

Beside the important determination of a proper set of endmembers, the LSU reconstruction requires an inversion process in order to achieve the necessary coefficients $\alpha_j(x,y)$ for the endmembers $\vec{v}_j$ in each pixel. As seen in Sec. 1.2.2, typically both physical constraints, ANC and ASC, are enforced to achieve physical plausibility. In this case, the calculation of the coefficients typically can be very expensive, especially for complex high-dimensional multispectral data with a large set of endmembers [SL11]. Therefore, interactive applications should utilize the LSU as preprocessing and focusing on the exploration of the static results. But, when the exploration leads to the result that a modification of the endmember set is necessary, then an analyst is interested in getting a fast response when modifying the set. Typically, modifications on a set of endmembers are done in a progressive way, which implies a frequent usage of inverse operations. Thus, this section presents three approaches that allow a more efficient utilization of LSU in interactive applications, i.e. visual analysis-based approaches.

Starting with an overview of the related work in section 4.4.1, the next section discusses a progressive utilization of the inversion step. The section 4.4.3 shows a method for the prediction of new coefficients in case of modification of the endmember set and section 4.4.4 discusses an efficient OSP-based solver for the computation of ANC coefficients. Results of the last two approaches are presented in section 4.4.5.

4.4.1 Background

Applying UCLSU, e.g. using least-squares methods like Moore-Penrose pseudoinverse, achieves fast results, but do not incorporate the physical plausibility as when impose ANC and ASC. UCLSU can result into negative coefficients which consequently lead to unnatural negative endmembers. But, as discussed above, if the non-negativity constraint is

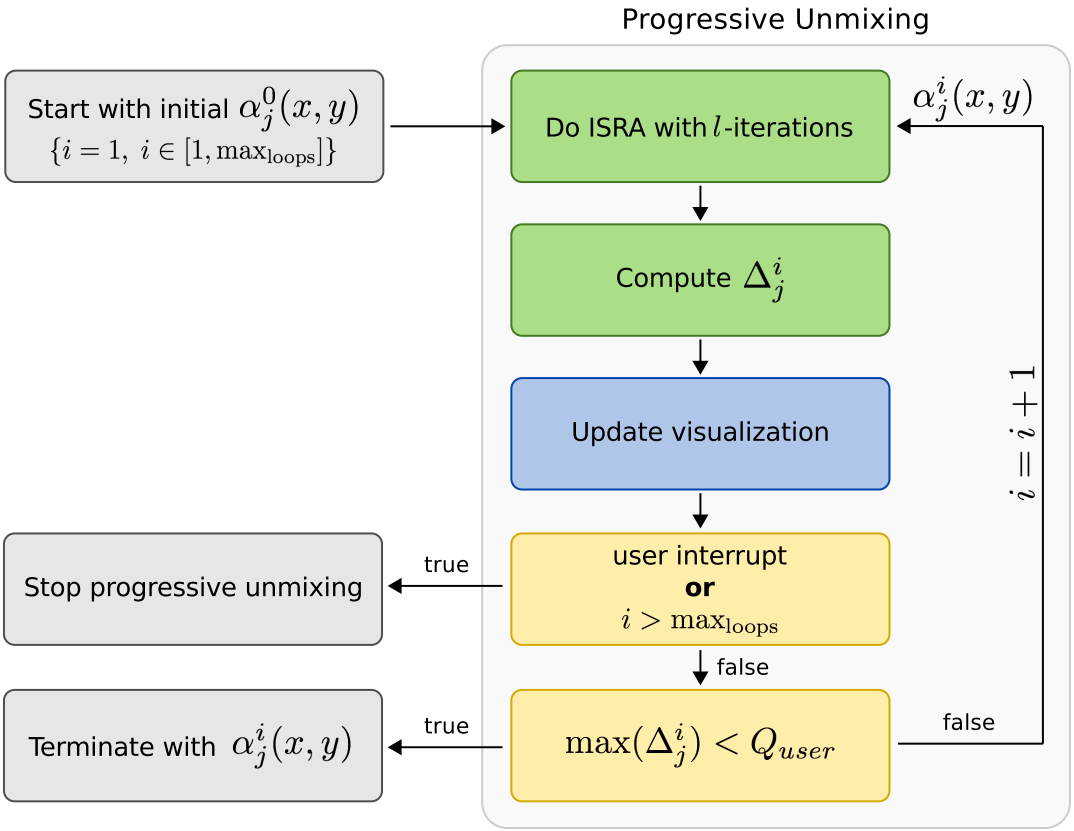

Figure 4.13: The workflow of the progressive unmixing, where Q_{user} is a quality threshold for the averaged relative l_2-error Δ_j^i.

claimed, non-negative methods, e.g. [CH00, HCIC01], are involved which can be computationally very expensive by itself [VG08]. Furthermore, ISRA Eq. (B.13) [DWM86, DP93], which guarantees convergence in a finite number of iterations, can be applied. Recently, Sánchez et al. [SMPC10] presented a CUDA-based implementation of ISRA that has turned out to be a great improvement in terms of runtime. In a test scenario, the authors gained a significant speedup of the GPU version (∼126 sec) compared to a sequential CPU implementation (∼3351 sec). But in terms of an interactive exploration, it is far too slow.

4.4.2 Progressive Unmixing Scheme

In interactive applications, a key-factor is the visual feedback which has to enable a user to sufficiently steer the application and to extract the significant information. However, when a set of endmembers V is found or an existing set is modified the unmixing has to be applied in order to update the visual feedback, e.g. the complimentary visualization described in Sec. 5.1. But, as discussed before, the inversion step for NCLSU as well as FCLSU typically is too time consuming for interactive approaches. Therefore, a progressive unmixing scheme

is presented where a user is able to trace the evaluation of the unmixing in order to proceed with the analysis or stop the time consuming calculation, when modifications on V are getting necessary (see Fig. 4.13). Due to the iterative operating principle of ISRA (see Appendix B.2), the implementation of Sánchez et al. [SMPC10] can be utilized very well in the progressive unmixing scheme that is discussed in the following.

Since this optimization algorithm works in an iterative manner, a termination criterion is recommended in order to avoid unnecessary iterations. Therefore, the computation is stopped after a defined number of iterations l and for each endmember the averaged relative l_2-error Δ_j^i, which is a measure for convergence, is computed:

$$\Delta_j^i = \frac{1}{X \cdot Y} \cdot \sum_{x=1}^{X} \sum_{y=1}^{Y} \delta_j^i(x,y) \text{ with } \delta_j^i(x,y) = \frac{\|\alpha_j^i(x,y) - \alpha_j^{i-1}(x,y)\|_2}{\|\alpha_j^i(x,y)\|_2} \tag{4.6}$$

Here, α_j^i are the coefficients of $\vec{v}_j$ where i is the number of executions ($i \leq \max_{\text{loops}}$) and X as well as Y represent the spatial resolution in x- and respectively y-dimension. The algorithm terminates when all Δ_j^i are smaller as a user-defined quality threshold Q_{user}, i.e. $\max(\Delta_j^i) < Q_{user}$ with $0 \leq j \leq q$, where q is the number of endmembers in V. Whenever the algorithms stops for this termination check the associated visualizations are updated. Thus, the user can follow the progressive refinement of the LSU-result and has the option to stop the inverse calculation, e.g. to further modify the endmember set.

4.4.3 Prediction of New Coefficients for Refined Endmember Sets

At the beginning of the coefficients calculation by ISRA, all coefficients are usually initialized to one. Typically, the unmixing is restarted whenever a new set of endmembers is to be applied. This is also necessary, when only minor modifications on V have been applied, e.g. when one endmember has been added, in an interactive approach. The idea of this prediction approach is to make use of prior unmixing results and the fact that the altered set of endmembers typically only differs by a single spectrum, that has been added or removed. Therefore, two cases are distinguished in the prediction: the **removal of an endmember** and the **insertion of a new endmember**. In the following explanation, the set of endmembers V is notated as $V^m = \{\vec{v}_1^m, \vec{v}_2^m, \ldots, \vec{v}_q^m\}$.

Removal of an endmember In this case, the new set of endmembers is

$$V^{m+1} = V^m \setminus \{\vec{v}_k^m\}, \tag{4.7}$$

where $\vec{v}_k^m$ is the removed endmember. Based on V^{m+1}, the formulation

$$\left\| \vec{v}_k^m - \sum_{j \neq k}^{q} \beta_j \vec{v}_j^m \right\|_2^2 \rightarrow \min \tag{4.8}$$

is optimized with a singular value decomposition-based least squares method. Thus, the weight β_j resembles the best approximation of V^{m+1} to the skipped spectrum $\vec{v}_n^m$,

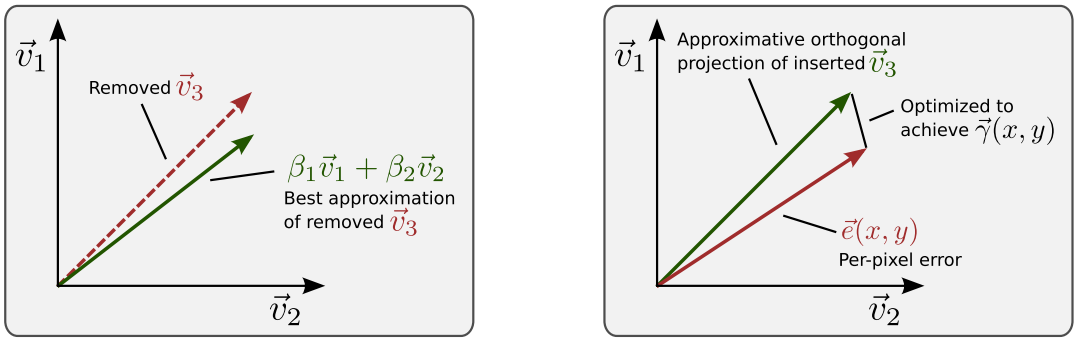

Removal of an Endmember | Insertion of an Endmember

Figure 4.14: Conceptional illustration of the idea of the coefficient prediction for both, the removal (left) and the insertion (right) of an endmember.

see Fig. 4.14. The estimated weights β_j are then used for the prediction of the new initialization values by distributing α_n^m to the remaining endmembers

$$\alpha_j^{m+1} = \alpha_k^m \beta_j + \alpha_j^m, \; j \neq k \tag{4.9}$$

with respect to the removed endmember $\vec{v}_n^m$. Note, that the β_j's are computed once for the whole dataset and the prediction is applied to all individual pixel using Eq. (4.9).

Insertion of an endmember The set of endmembers is considered in the same manner as before, but now the new set is defined as

$$V^{m+1} = V^m \cup \left\{\vec{v}_{q+1}\right\}, \tag{4.10}$$

where $\vec{v}_{q+1}$ is the inserted endmember. The main idea here is to reduce the current per-pixel error with respect to the prior set of endmembers, i.e.

$$e(x,y) = \vec{s}(x,y) - \sum_{j=1}^{q} \alpha_j^m(x,y)\vec{v}_j^m, \tag{4.11}$$

where $\vec{s}(x,y)$ is the source spectrum and the convex combination is the current mixed spectrum with respect to V^m.

The assumption is, that, in average, the best correction can be achieved in the direction of the projection of the newly introduced endmember $\vec{v}_{q+1}$ with respect to the prior set of endmembers. Therefore, first the approximate orthogonal projection of $\vec{v}_{q+1}$ is calculated by solving the following least squares problem

$$\left\| \vec{v}_{q+1} - \sum_{j=1}^{q} \beta_j \vec{v}_j^m \right\|_2^2 \to \min. \tag{4.12}$$

Based on the per-pixel error $e(x,y)$ and the calculated weights β_j, now, the equation

$$\left\| e(x,y) - \gamma(x,y)(\vec{v}_{q+1} - \sum_{j=1}^{q} \beta_j \vec{v}_j^m) \right\|_2^2 \rightarrow \min \tag{4.13}$$

can be optimized in order to achieve the per-pixel correction coefficient $\gamma(x,y)$, see Fig. 4.14. Finally, the previous coefficient values α_j^m are adjusted as follows

$$\alpha_j^{m+1}(x,y) = \alpha_j^m(x,y) - \gamma(x,y) \cdot \beta_j, \quad j = 1,\ldots,k \tag{4.14}$$

$$\alpha_{q+1}^{m+1}(x,y) = \gamma(x,y). \tag{4.15}$$

For performance reasons, in both cases non-constrained least squares methods are used. Non-constrained methods may lead to undesired negative coefficients of some pixels. In such cases the resulting coefficients are clamped to a value close to zero. Here, it is important to not clamp to zero to allow the subsequent coefficient calculation in ISRA (cf. App. B.2). Beside ISRA, the presented prediction method can be applied for all solvers which assume initial coefficients.

4.4.4 OSP-Based Coefficient Estimation

With the main goal to avoid the need of a previous unmixing result, this section presents a method for the direct estimation of endmember coefficients. The here discussed method estimates the coefficients based on residuals which are achieved by applying the principle of OSP. While the original aim of OSP was the endmember extraction, Du et al. 2003 [DRC03] have shown that OSP and constrained energy minimization are closely related. Different from the aim to determine a full set of endmembers, the goal of the constrained energy minimization is to detect a desired target signature within an unknown image. Here, the close relation between both approaches is based on the fact, that OSP eliminates undesired spectral signatures by applying orthogonal projections (cf. Eq. (1.3)). This principle of OSP is also the rationale of the here discussed method, therefore, this method is referred to as Orthogonal Subspace Projection based coefficient estimator (OSPCE) in the following.

Assuming that the determined endmember matrix U, where endmembers are column-wise, contains the significant endmembers V of the dataset. Then the general idea of the approach is, that the influence, i.e. coefficients, of an endmember $\vec{v}_j$ can be computed by projecting the dataset into the orthogonal space that is based on all determined endmembers except $\vec{v}_j$. Thus, the coefficient calculation of a $\vec{v}_j$ is always based on a reduced endmember matrix

$$U_j^- = U \setminus \{\vec{v}_j\}, \tag{4.16}$$

where $\vec{v}_j$ was removed from the originally determined U. Concerning LSU, Eq. (1.1) can be reformulated into

$$\vec{s}(x,y) = \alpha_j(x,y)\vec{v}_j + \sum_{i \in F \setminus j} \alpha_i(x,y)\vec{v}_i + \vec{n}(x,y) \tag{4.17}$$

where $F = \{f_1, f_2, \ldots, f_q\}$ is the set of all endmember indices. Now, the orthogonal subspace projector $P_j^{\perp}$ is computed according to Eq. (1.3) with U_j^-. When projecting Eq. (4.17) with $P_j^{\perp}$ and the noise is neglected the following equation is achieved

$$\vec{s}^{\perp}(x,y) = \alpha_j(x,y)\vec{v}_j^{\perp} + \sum_{i \in F \setminus j} \alpha_i(x,y)\vec{v}_i^{\perp} \tag{4.18}$$

$$\text{with } \vec{v}_i^{\perp} = P_j^{\perp}\vec{v}_i = 0 \text{ for } i \in F \setminus j. \tag{4.19}$$

The endmember signatures $\vec{v}_i$ are eliminated in the subspace orthogonal to U_j^- and therefore the remaining signal of $\vec{s}^{\perp}(x,y)$ is due to $\vec{v}_j^{\perp}$ so that

$$\vec{s}^{\perp}(x,y) = \alpha_j(x,y)\vec{v}_j^{\perp}. \tag{4.20}$$

Based on this, the coefficient $\alpha_j(x,y)$ is estimated with

$$\alpha_j(x,y) = \left\langle \vec{s}^{\perp}(x,y), \vec{v}_j^{\perp} \right\rangle / \left\langle \vec{v}_j^{\perp}, \vec{v}_j^{\perp} \right\rangle \tag{4.21}$$

where $\vec{v}_j^{\perp}$ and $\vec{s}^{\perp}(x,y)$ are the projected current endmember $\vec{v}_j$ and the current spectrum $\vec{s}(x,y)$ of a pixel (x,y)

$$\vec{v}_j^{\perp} = P_j^{\perp}\vec{v}_j,\ \vec{s}^{\perp}(x,y) = P_j^{\perp}\vec{s}(x,y). \tag{4.22}$$

Thus, the coefficient $\alpha_j(x,y)$ lies in $[0,1]$, as long as the underlying estimated set of endmembers V is reasonable. There are issues when spectral vectors are falling outside the convex hull generated by V, due to wrong endmember determination. For instance, when a $\vec{s}(x,y)$ of the data is spectrally equal to a $\vec{v}_j$ but the intensity level is higher, then the estimated $\alpha_j(x,y)$ is greater than one. Since there is no active enforcement of the ANC, in the most unfavorable case it may happen that when significant endmembers $\vec{v}_j$ are missing in V that the achieved $\alpha_j(x,y)$ gets negative. Thus, preventively a negative $\alpha_j(x,y)$ is clamped to a positive value close to zero at the end of the calculation. Here, again it is not clamped to zero to allow the subsequent coefficient calculation when the OSPCE method is combined with ISRA (cf. App. B.2), see below. Note, the incompleteness of V is a general problem in the solving process and not a specific challenge of OSPCE. For instance, the inversion method ISRA itself guaranties positivity, also when the set of endmembers is incomplete, but, the reconstruction then is also not satisfying, i.e. correct.

The coefficients for both, the other pixels and remaining endmembers are calculated in the same way. So far, the coefficients are non-negativity constrained. In addition, the calculated abundances α^V of all endmembers can be normalized in order to achieve fully constrained coefficients.

As sown in Algorithm 3, the whole approach is divided into two parts, the calculation of the orthogonal projectors and the coefficients. This division is due to the facts, that the orthogonal projectors (cf. Eq. (1.3)) are on the one hand constant for the whole process as well as for all pixels and on the other hand can be computed fast on the CPU. The remaining calculations for all pixels are calculated in parallel by using CUDA which results in a decreased runtime.

Algorithm 3 OSP-based Coefficient Estimation

Calculate orthogonal projectors

for each endmember $\vec{v}_j$ **on CPU do**
  generate U_j^- (Eq. (4.16))
  compute the orthogonal projector $P_j^\perp$ (Eq. (1.3))
end for

Compute coefficients

for each pixel (x,y) **in parallel do**
  for each projector $P_j^\perp$ **in parallel do**
    compute $\vec{v}_j^\perp$ and $\vec{s}^\perp(x,y)$. (Eq. (4.22))
    compute coefficients $\alpha_j(x,y)$ (Eq. (4.21))
    preventative clamping of $\alpha_j(x,y)$
  end for
  normalize coefficients $\alpha^V(x,y)$ of all endmembers
end for

As can be seen in the upcoming section 4.4.5, the coefficients of the OSPCE method are already quite accurate and the iterative ISRA has a longer runtime to achieve comparable results. However, by combining both methods the general results can be improved in terms of both, accuracy and performance. Here, as also discussed in section 4.4.3, it is again the aim to achieve a faster convergence of ISRA by a proper initialization of the coefficients. Therefore, the calculated coefficients of OSPCE can be used to initialize the coefficients for ISRA. Doing so, the number of iterations for ISRA decreases while still maintaining results of the same quality.

4.4.5 Results

This section presents the results of the prediction approach for refined endmember sets (cf. Sec. 4.4.3) and of the OSPCE (cf. Sec. 4.4.4). Therefore, the section is divided into two corresponding subsections: the **Prediction of New Coefficients for Refined Endmember Sets** and the **OSP-Based Constraint Unmixing**. Since the first approach requires a previous unmixing result and is especially designed for the prediction of new coefficients when a single endmember was inserted or removed, the results are presented for modification scenarios. Different from the first approach, the second approach directly estimates the coefficients independently without a previous unmixing result, thus the results focus on the comparison to ISRA. In both subsections, the test system again was equipped with an Intel Core i7 2.67GHz CPU, 12GB main memory and a NVIDIA GeForce GTX 480 (1536MB) graphics card.

Prediction of New Coefficients for Refined Endmember Sets

The results of the presented coefficient prediction approach are shown by the usage of ISRA, where both coefficient initialization methods, default with one and the predicted coefficients,

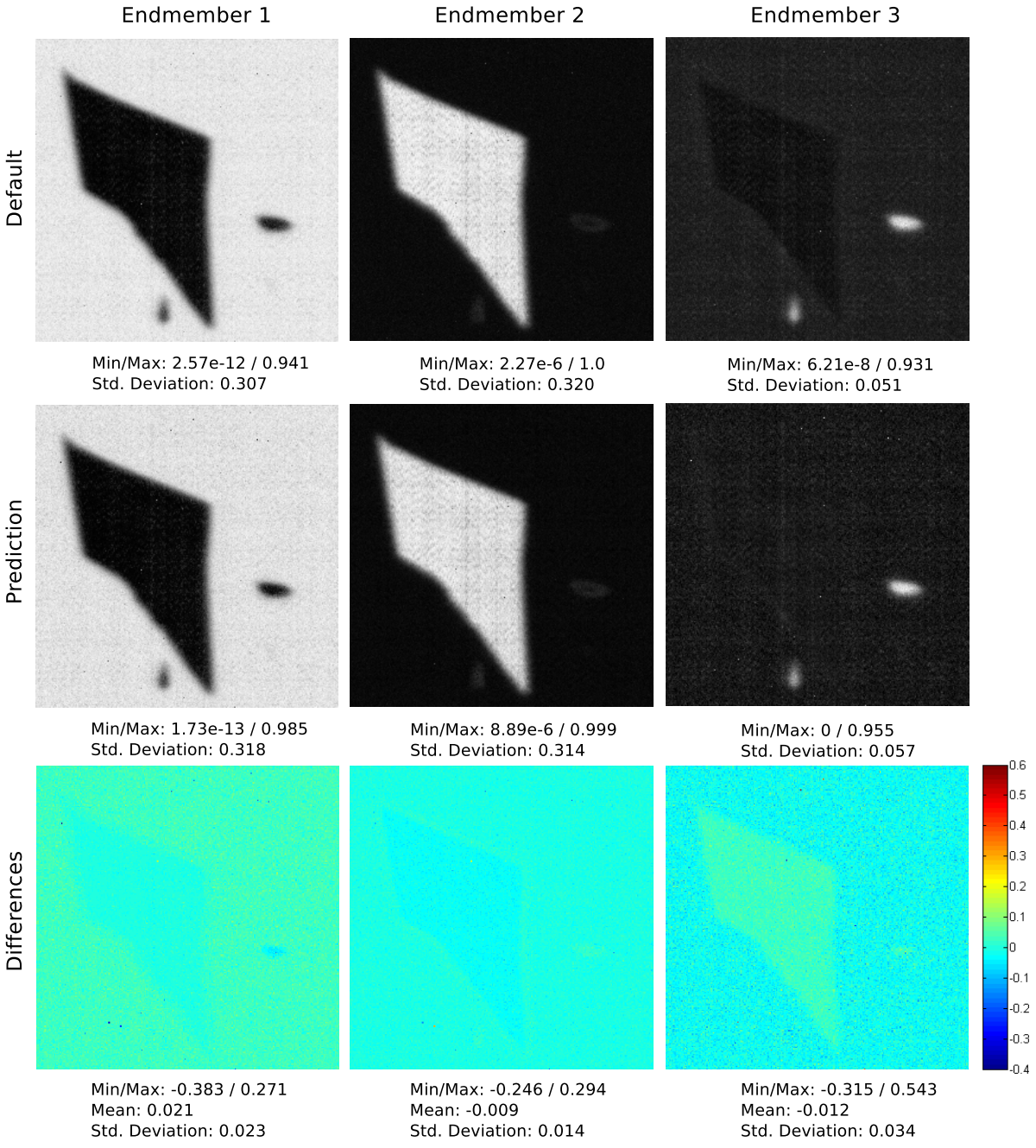

Figure 4.15: This illustration shows the quality of the coefficients for the three final endmembers. The first two rows show the final normalized coefficient maps for the default initialization *(top)* and the initialization with prediction *(middle)*. The bottom row shows the associated difference images of the coefficient maps (default minus prediction). This test scenario was based on the *Graphene* dataset (cf. App. A) and the quality threshold Q_{user} was 0.1.

are discussed in comparison. For both initialization approaches, two test scenarios are done to reflect the results, first focusing on the quality, i.e. difference of the final coefficients, and second discussing the speedup.

Quality-focused Evaluation In this first test scenario, the *Graphene* dataset (cf. App. A) was used, which already is known from Sec. 4.3.3. At the beginning of this test, three endmembers were already selected. During the test, first two endmembers were removed and then two new endmembers were added.

As we can see in Fig. 4.15, the coefficient maps of the three endmembers are quite comparable for both approaches. Especially the difference images of the coefficient maps (prediction subtracted from default) show that there are a few small areas which are not as good as in the default case. The reason for this is that ISRA typically terminates earlier in the case of the prediction, although some smaller areas need more optimization iterations, especially, when some endmembers have a high influence in huge parts of the data, since the averaged relative l_2-error value is used for the termination check. Nevertheless the results are quite comparable.

Speedup-focused Evaluation In the second test scenario, for five datasets, the runtimes were measured and the quality was compared to the default initialization. The scenario was as follows: Initially, ten endmembers (EM) were already selected for each dataset. During the time measurement endmembers were removed (-) and added (+) by following a constant scheme that can be seen in the header of Table 4.1. This Table shows the time consumption of each action, the complete- and averaged runtimes. In some cases, the prediction was slower as the default initialization. But, by considering the total time consumptions, the prediction method overall was faster than the default initialization. Based on this scenario, an average speedup of about 24% was measured. Furthermore, the quality difference of both initializations of this scenario is shown in Table 4.2. As can be seen, the maximum absolute difference values of this comparison are in some cases quite high, while the standard deviation and mean values are quite low for all tests. The reason for this effect is already discussed above in the first test scenario.

OSP-Based Coefficient Estimation

The results of the OSPCE are presented in comparison to the results of ISRA from Sánchez et al. [SMPC10]. ISRA computes ANC coefficients and FCLSU is achieved by the normalization of the coefficients. The methods are applied to three datasets, first for the field of remote sensing and second for artificial datasets. The Appendix A gives some details on the selected datasets.

Remote Sensing Here, the very common *Cuprite* dataset was used. The endmembers in this test have been extracted directly from the data by applying the OSP algorithm, limited to ten endmembers.

Initialization	Data	-EM0	-EM5	-EM9	+EM0	+EM5	-EM8	+EM9	+EM8	∑	Ø
Default	Lemons	4.5s	3.1s	3.0s	3.5s	5.2s	4.5s	5.3s	6.1s	35.2s	4.4s
Prediction	Lemons	2.4s	4.1s	2.5s	3.4s	4.3s	2.2s	4.7s	5.4s	29.1s	3.6s
Default	Glass tiles	6.0s	5.2s	4.2s	4.8s	6.5s	5.2s	6.0s	6.8s	44.7s	5.6s
Prediction	Glass tiles	7.6s	1.5s	2.8s	7.4s	8.2s	1.9s	5.7s	6.1s	41.3s	5.2s
Default	Flowers	5.1s	4.3s	3.4s	5.7s	7.3s	5.2s	6.0s	8.8s	45.8s	5.7s
Prediction	Flowers	2.0s	2.1s	1.9s	4.6s	5.9s	5.1s	5.0s	5.8s	32.4s	4.0s
Default	Graphene	6.3s	4.9s	3.8s	4.9s	7.3s	4.9s	7.3s	10.5s	50.0s	6.3s
Prediction	Graphene	1.0s	2.5s	1.2s	4.1s	4.2s	1.6s	3.1s	5.2s	23.0s	2.54s
Default	Peppers	3.2s	2.6s	2.6s	3.8s	4.6s	3.5s	4.2s	5.5s	30.1s	3.8s
Prediction	Peppers	1.4s	4.3s	2.2s	2.9s	4.2s	2.6s	3.9s	5.0s	26.7s	3.3s

Table 4.1: Measured runtimes of the second test scenario. Initially ten endmembers (EM) were already selected by OSP. During the time measurement endmembers were removed (-) and added (+) by following a constant scheme. The quality threshold Q_{user} was 0.1 in each case. See Appendix A for more details about the used data.

Data	Values	EM0	EM1	EM2	EM3	EM4	EM5	EM6	EM7	EM8	EM9	Ø
Lemons	$\max \lvert d \rvert$	0.60	0.10	0.09	0.14	0.10	0.14	0.54	0.39	0.93	0.26	0.33
	mean	-0.01	0	0	0	0	0	0.01	0.02	0.03	0.01	0.01
	std	0.06	0.02	0.01	0.01	0.01	0.01	0.05	0.05	0.10	0.04	0.03
Glass tiles	$\max \lvert d \rvert$	0.43	0.42	0.23	0.88	0.42	0.36	0.45	0.62	0.84	1.95	0.66
	mean	-0,01	0	0	0	0	0	0	0.01	0.02	0.02	0.002
	std	0.03	0.01	0,02	0.04	0.04	0.01	0.03	0.05	0.05	0.06	0.04
Flowers	$\max \lvert d \rvert$	0.16	0.15	0.02	0.12	0.19	0.10	0.11	0.08	0.14	0.15	0.12
	mean	-0.01	-0.01	0	-0.01	0	0	0.01	0	0.01	0.01	0
	std	0.02	0.01	0	0.01	0.01	0.02	0.01	0.01	0.01	0.02	0.01
Graphene	$\max \lvert d \rvert$	0.62	0.46	0.25	0.46	0.47	0.72	0.97	0.43	0.68	0.79	0.59
	mean	0	-0.02	0	0.02	-0.01	0.01	0.05	0.01	0.02	0.02	0.01
	std	0.03	0.07	0.01	0.07	0.03	0.04	0.16	0.04	0.06	0.07	0.06
Peppers	$\max \lvert d \rvert$	0.62	0.30	0.11	0.19	0.59	0.24	0.37	0.58	0.75	0.48	0.42
	mean	0	-0.01	0	0.01	0.03	-0.01	0.02	0	0.03	0.03	0.01
	std	0.03	0.05	0.01	0.02	0.11	0.03	0.07	0.03	0.06	0.07	0.05

Table 4.2: Based on the differences of the coefficients (prediction subtracted from default), the values of the maximum absolute difference $\max |d|$, mean and standard deviation are mentioned to show the quality of the second scenario. See Appendix A for more details about the used data.

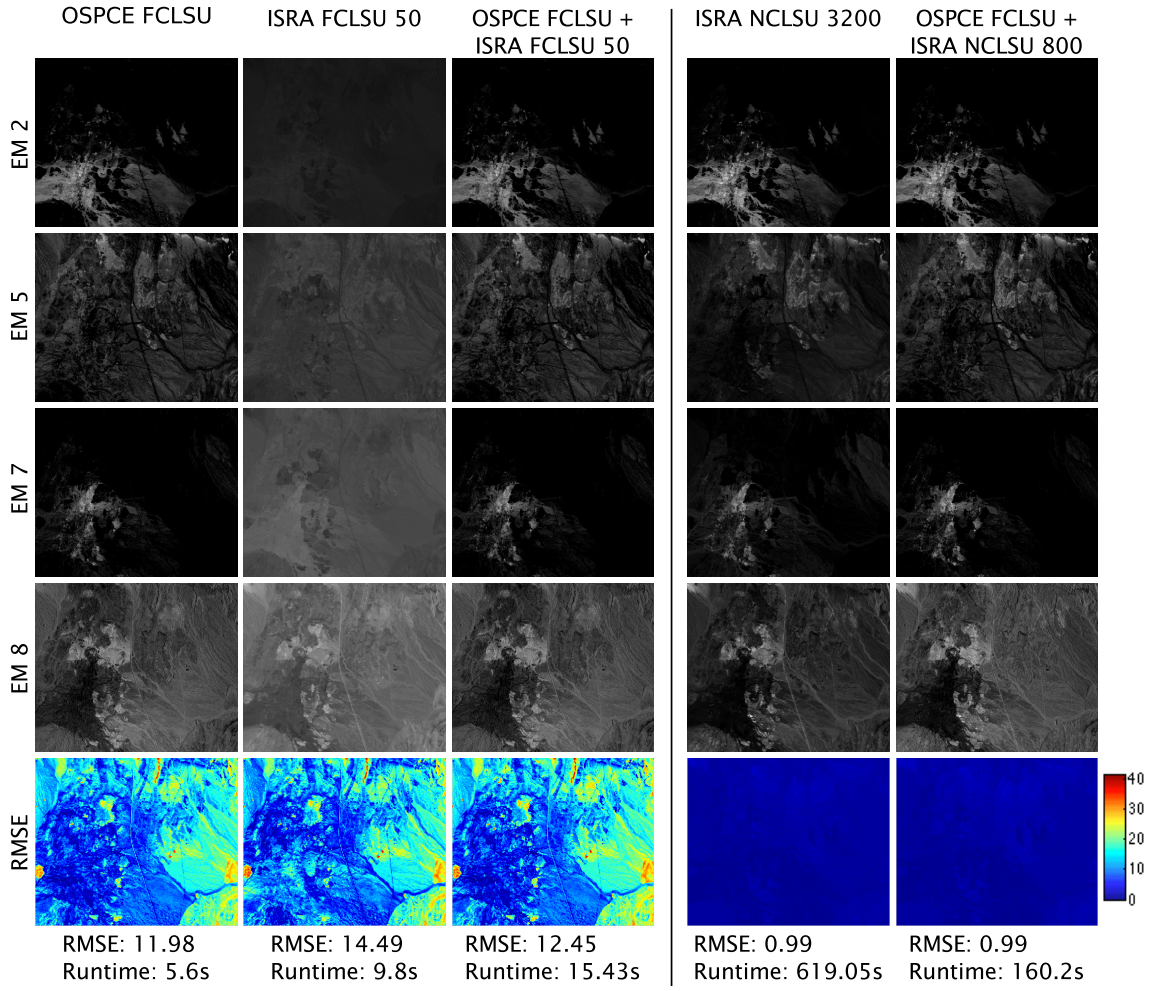

Figure 4.16: The quality of the applied methods is shown by the coefficients-maps of four selected endmembers and corresponding RMSE reconstruction errors (in percentage). On the left side, the OSPCE method is compared to ISRA and to the combined version OSPCE+ISRA, all fully-constrained. Comparing column 1 and 2, it can be seen that OSPCE achieves more accurate results with a lower runtime than ISRA with a low number of iterations. Column 3 shows improved ISRA-results when combined with OSPCE. On the right, a comparison of the combined version OSPCE+ISRA and ISRA alone is shown for NCLSU. As can be seen, the combined version achieves results comparable to ISRA alone, but needs fewer iterations.

In comparison, the results of OSPCE-FCLSU and ISRA-FCLSU are shown in the left part of Fig. 4.16. As can be seen, the result of OSPCE-FCLSU is accurate and the runtime is shorter as ISRA with 50 iterations. Moreover, the combination of OSPCE and ISRA shows that the initialization of ISRA with the estimated coefficients of OSPCE improves the ISRA result. Here, the number of iterations was chosen low intentionally in order to demonstrate the influence of the combination and to give a feeling for the runtimes. In the following, this combination is called OSPCE+ISRA and is evaluated also for higher iteration numbers of

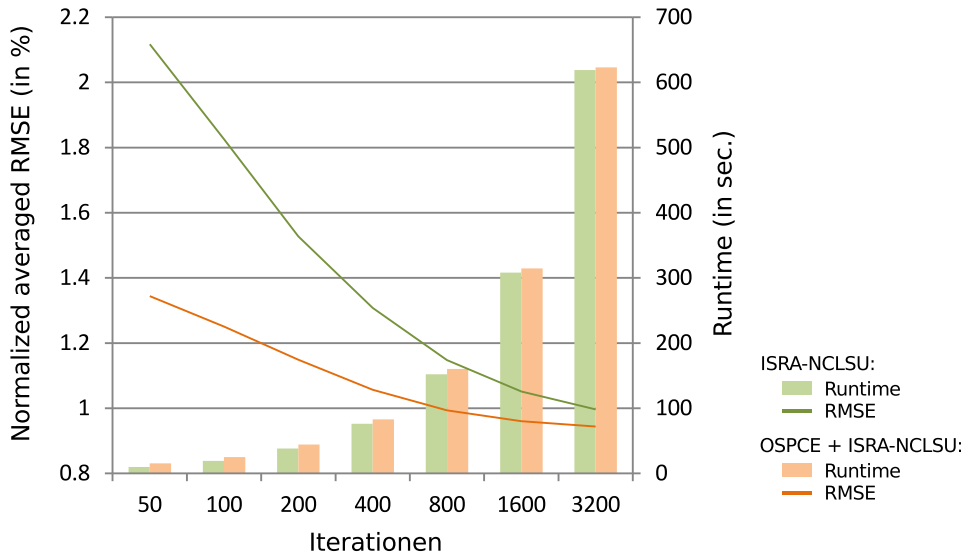

Figure 4.17: This diagram shows, based on the *Cuprite* dataset, the normalized averaged RMSE reconstruction error trend and the runtimes for ISRA and the combination of OSPCE+ISRA. OSPCE has a runtime of 5.6 seconds.

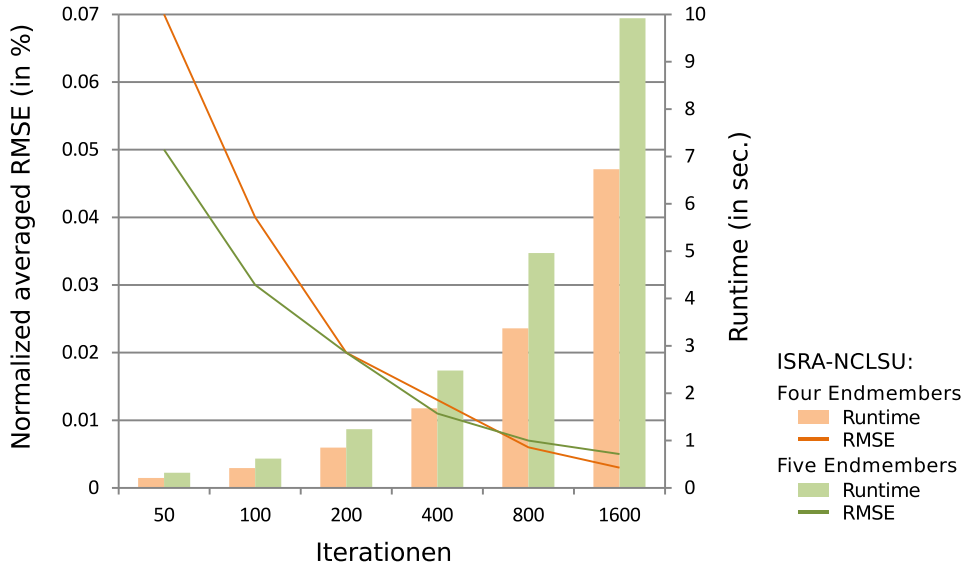

Figure 4.18: This diagram shows the normalized averaged RMSE reconstruction error trend and the runtimes for ISRA-NCLSU for two artificial datasets, four and five endmembers. OSPCE-NCLSU achieves, after a runtime of 0.45 seconds, an averaged RMSE of 0.0004 for the dataset with four endmembers. Moreover, for the other dataset an averaged RMSE of 0.006 is achieved after 0.56 seconds.

ISRA-NCLSU. In Fig. 4.17, the runtimes and normalized RMSE reconstruction error trends of ISRA and OSPCE+ISRA are compared. As can be seen, the OSPCE-based initialization of ISRA decreases the RMSE-values. For instance, with 800 iterations (160 sec.), OSPCE+ISRA achieves a comparable result as the typical usage of ISRA with 3200 iterations (610 sec.). This also can be seen in the right part of Fig. 4.16. Also the combination of OSPCE-NCLSU and ISRA has been tested. But it has turned out, that the differences of the coefficients regarding OSPCE-FCLSU and OSPCE-NCLSU are to small to have noticeable impact with respect to accuracy and performance.

Artificial Data The results for two artificial datasets, four endmemberss and five endmembers, are shown in the following. Since the number of constituents and exact positions are known for these two datasets, errors caused by an improper endmember set are impossible. Moreover, these data are free from noise. In order to prevent reconstruction errors due to the scaling of the coefficients in order to achieve FCLSU, in all upcoming cases ISRA as well as OSPCE are applied to achieve ANC coefficients. Thus, deviations between the raw data and its corresponding reconstruction are mainly due to the applied inversion process in the following.

The ISRA error trend is depicted in Fig. 4.18. As can be seen, all RMSE-values are very low. However, compared to OSPCE, the achieved values with ISRA are all greater. In detail, OSPCE achieves, after a runtime of 0.45 seconds, an averaged RMSE of 0.0004 for the dataset with four endmembers and for the other dataset an averaged RMSE of 0.006, after 0.56 seconds. Since the error trends are focused on averaged values, also the resulting coefficients maps are depicted in Fig. 4.19 in order to provide a better impression of the quality. Here, the results of ISRA with 50 and 1600 iterations are shown in comparison to OSPCE.

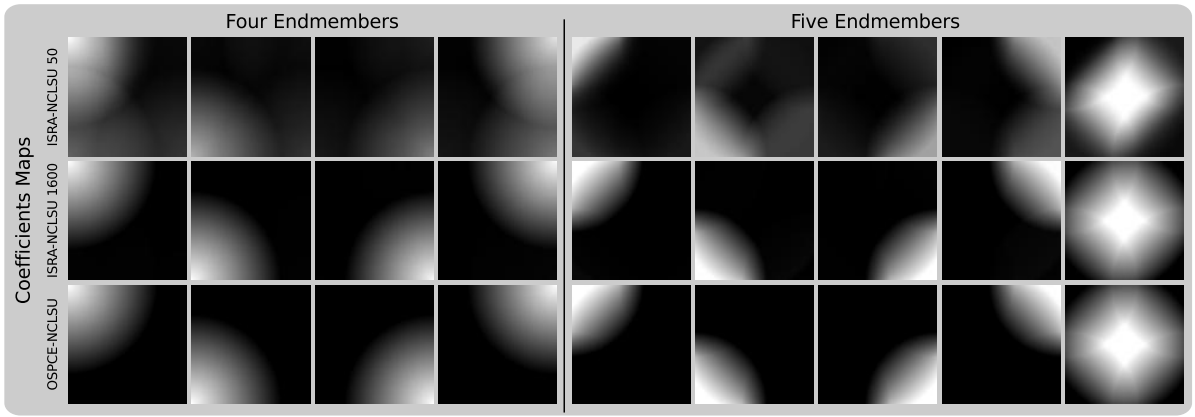

Figure 4.19: Comparision of coefficients maps for OSPCE and ISRA in case of two artificial datasets.

4.4.6 Summary

This section has proposed several methods to more efficiently utilize inverse unmixing methods for interactive applications, especially when ANC is enforced. Beside a progressive utilization of ISRA combined with a termination criteria to achieve a better integration in the explorative workflow, mainly two methods are presented to speedup the coefficient computation.

First, a method that utilizes previously calculated coefficients to predict coefficients in case of modifications on the set of endmembers. Here, it was proposed to utilize these predicted coefficients as initialization of ISRA to achieve a faster convergence. The shown results, in comparison to ISRA, have proven a good quality of the predicted coefficients and in a test scenario this method had achieved a speedup of 24%.

Second, the OSPCE method was proposed, that estimates the coefficients of each endmember by successively eliminating all other endmembers, based on the OSP-principle, from the spectra to determine the respective endmember influence. Compared to the prediction-based method, the OSPCE has the advantage that it needs no previous unmixing result to estimate the coefficients. Since, potential inaccuracies in results of OSPCE, e.g. based on orthogonal restriction, are corrected and ISRA certainly needs less iterations to achieve good results, this combination has turned out to be a general improvement in terms of runtime and accuracy.

4.5 Summary

This chapter has discussed several aspects of multispectral data analysis. Beside the more fundamental aspect of the similarity measure in high-dimensional space, the reminder of the chapter was focused on analysis aspects with respect to interactive analysis concepts in the context of LSU. Here, mainly three challenges have been identified.

First, it has turned out, that it cant be guaranteed that endmember extraction algorithms for each circumstance or application will find a reliable set of constituents. Thus, a visual analysis concept was proposed for the verification and refinement of the determined result. Moreover, it has been shown that the resulting set of constituents often depends on a good parameterization, whose fine-tuning greatly benefits from visual feedback.

Second, outliers in multispectral data can prevent automatic algorithms to find good representative constituents of datasets. The usage of the proposed outlier masking scheme has been proven to be capable to improve the robustness of these algorithms in such cases, without the risk that any information can be lost within the proposed visual analysis concept.

Finally, the often time-consuming inverse operations of the LSU were addressed in this chapter. Beside a progressive scheme, mainly two methods were presented to speedup the calculation of the coefficients for interactive applications.

Taken together, the presented approaches and concepts provide means to utilize the LSU in a visual analysis approach. Thus, to achieve reliable set of constituents for a broad variety of application domains and also for datasets that suffer from imperfections by incorporating the

expert knowledge of an analyst. Here, an adequate visual feedback implicitly was assumed as key aspect to ensure a proper verification or refinement, but, the discussion of the visualization aspects was skipped. Therefore, the next chapter discusses the open aspects and challenges from the visualization point of view.

Chapter 5

Multispectral Image Visualization

Creating visual representations in order to provide insights to multispectral image data is not a straightforward issue, since it is, in general, impossible to visualize all aspects of a spectral image in one picture [PvdH01]. The following sections mainly cover visualization means which are embedded in visual analysis approaches to purposefully enable users to get insights into the essential spectral characteristics of an image. The chapter is structured in three sections, where the first two sections address challenges in the domain of LSU and the last section discusses a semi-automatic segmentation approach.

The first section addresses the complementary visualization for the evaluation of the completeness of endmember sets. This visualization and the therewith introduced exploration means together build the second part of the approach for **Generic Determination of Constituent Spectra** presented in section 4.2.1.

The second section presents global expressive spectral error visualizations in order to provide user guidance in a visual analysis approach to finally enhance the results of spectral mixture analysis. The presented visualization methods improve the user guidance on the one hand, by enhancing the interpretation of typical distance measures and on the other hand, by discriminating spectral errors in different error classes.

The last section of the chapter deals with a multispectral image segmentation approach, that is based on a common multivariate visualization technique. This approach achieves the segmentation in a semi-automatic manner and in general allows a user to get insights into the spatial topology of multispectral image data.

Publications: The complementary visualization as well as the associated exploration methods have been published in [LBK12], while the expressive spectral error visualization-based visual analysis approach for enhanced spectral mixture analysis was subject in [LUK13]. The Radviz-based multispectral image segmentation has been presented in [LPK13].

5.1 Complementary Visualization

This section discusses a juxtaposed complementary visualization for the evaluation of the completeness of endmember sets, which was already mentioned before in Sec. 4.2.1. The complementary visualization consists of two views for the calculated results of the unmixing as well as two additional views for associated distance-based error images. The details of these views are presented in Sec. 5.1.1. Additionally, supplemental exploration tools ensure that analysts are able to utilize their exploration experiences as well as their expert knowledge to evaluate and refine an endmember set, if necessary. This exploration possibilities are presented in Sec. 5.1.2.

5.1.1 Visualizations

The assessment of the reconstruction quality of LSU is an important step for judging a set of endmembers V. In this context, a complementary visualization is introduced in order to provide a more comprehensive quality visualization than by using a typical single error image, as discussed later on. As shown in Fig. 5.1, this visualization is composed of four views that are arranged in a matrix like style and provide the main feedback for an analyst.

The columns represent the reconstruction results of the LSU Eq. (1.1), based on the computed coefficients (see Sec. 4.4), and of a **binary unmixing** step which computes the NN of each endmember. In detail, the binary unmixing is performed by computing the distance of a spectrum $\vec{s}(x,y)$ to all endmembers of the current set V.

$$\mathrm{dist}_{\mathrm{NN}}(x,y) = \min_{\vec{v}_i \in V} d(\vec{s}(x,y), \vec{v}_i) \tag{5.1}$$

$$\mathrm{map}_{\mathrm{NN}}(x,y) = \arg\min_{\vec{v}_i \in V} d(\vec{s}(x,y), \vec{v}_i) \tag{5.2}$$

The endmember with the shortest distance, i.e. the nearest neighbor, is then assigned to the currently observed pixel. In addition, the associated distance is stored as well. For the distance measurement d the user can choose between the distance metrics that are listed in the Appendix B.1. This nearest neighbor selection is done for all pixels of the multispectral data and leads to a labeling based on the set of endmembers.

The top row of the complementary visualization shows the reconstruction based on false-color representations, while the bottom row shows the distance between the raw data and the respective reconstruction. Details of both visualizations are discussed in the following.

Reconstruction views Note that each endmember has an assigned color which is used for the graphical representation. This means on the one hand that in the LSU visualization the colors of the endmembers are mixed for each pixel according to the calculated coefficients. In the NN-based visualization, the color of the closest endmember is assigned to a pixel when the stored distance $\mathrm{dist}_{\mathrm{NN}}(x,y)$ is below a user defined sensitivity threshold. When the distance is too large, black is assigned. By adjusting this threshold, the user easily can explore the spatial distribution of the endmembers depending on the

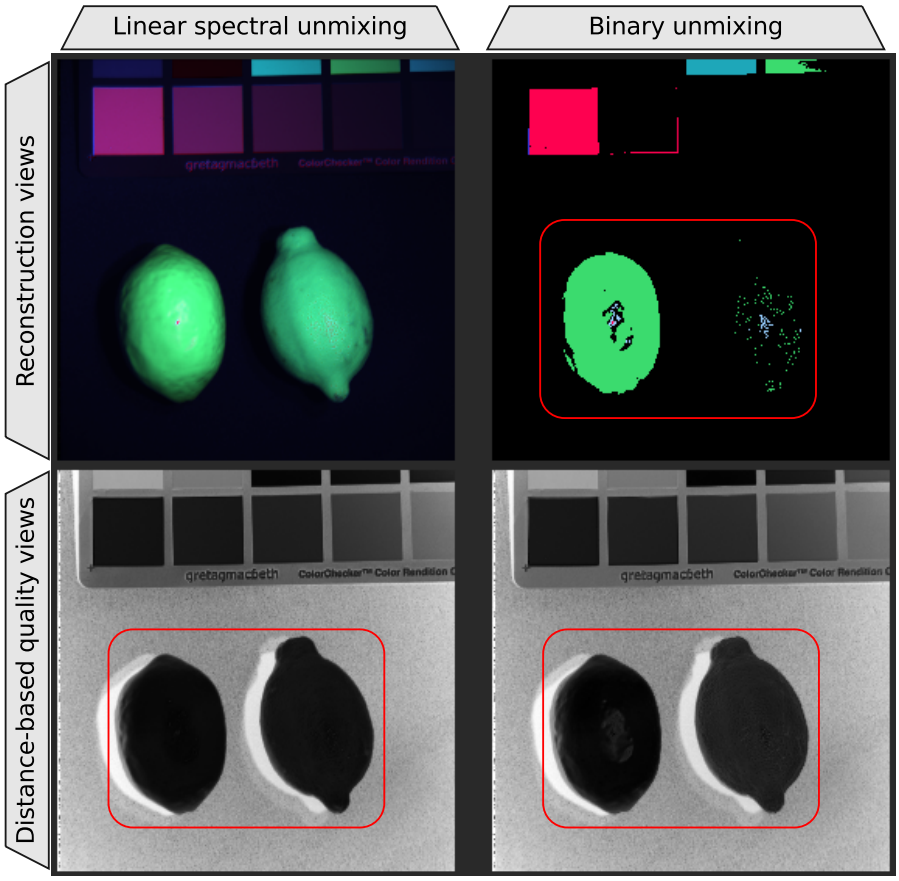

Figure 5.1: Overview of the complementary visualization which consists of four views: The results of the LSU and of the binary unmixing, each with the associated distance-based quality view beneath. In this example the *Lemons* dataset was utilized (cf. App. A). Together, the three marked areas reveal that the right lemon is not represented that well by the endmembers as the left lemon. This is not that clearly reflected in the LSU-based visualization alone.

distance. Thus, the resulting visual representation is quite comparable to cluster-based segmentation results.

One general problem is the initial choice of colors for the endmembers, directly after the endmember extraction. Here, the aim is to achieve a color setting, that already resembles spectral similarities, thus supporting the user to identify possibly redundant endmembers. A first idea would be to transform the endmembers to RGB by applying the color matching functions, see Appendix B.3. But, this is only meaningful for spectra that are in the domain of the matching functions. A second idea, which is used here, is to determine the initial colors on the basis of the PCA-based false-color image of the corresponding dataset (cf. Sec. 1.2.3). Since the spatial resolutions of the PCA-based false-color image and the multispectral image are the same, the initial colors assigned to the endmembers are given by selecting the false-color at the corresponding pixel of

the endmember position (x,y). Apart from the resembling of the spectral similarity, the main advantage of this color selection method is that the PCA-based false-color coding is a standard technique in multispectral data visualization, thus the resulting unmixing result is directly comparable to this standard.

Distance-based quality views The associated grayscale distance images show the current distances, i.e. errors, between the reconstructed data and the raw spectrum. In case of the binary unmixing the distances are already given by dist_{NN}. The distances of the LSU are computed between the reconstructed spectra and the raw spectra, i.e. $d(\vec{s}(x,y), \sum \alpha_j(x,y)\vec{v}_j)$. Like in the binary unmixing, the applied metric can be chosen from the methods presented in Appendix B.1. These error images guide the user directly to insufficiencies in the current set of endmembers, e.g. missing characteristic spectra.

The strength of this kind of visualization is, that the four single views are supplementary to each other. Thus, compared to a single error image, it gives a more widespread impression of the completeness of the endmember set, e.g. spatial distribution of endmembers. Consider again the example of Fig. 5.1. Beside the more obvious shortcomings, like the representation of the background or the color-checker, also minor deviations are noticeable when taking together all views. For instance, the three marked regions reveal that the right lemon is not that well represented compared to the left one. This consequently reveals that both lemons are at least slightly different. Such an issue can be noticed very well by a user, which now can verify or modify the set of constituents by utilization of exploration tools, as discussed in the upcoming section.

5.1.2 Exploration Methods

In order to support a user to reveal information, the rationale of a visual analysis approach is a meaningful visualization, which is combined with intuitive exploration possibilities. Here, the exploration means must enable a user to directly apply the perceived information e.g. to refine the visualization, or to change the parameterization of algorithms. Therefore, this section presents exploration methods which are able to supplement the previous presented complementary visualization in order to ensure that the determined set of endmembers can be meaningfully evaluated and modified, i.e. removal and insertion of endmembers. Thus, to improve the reconstruction quality, if necessary. This aim is achieved by three exploration widgets:

1. **Residual error segmentation** for the identification of pixels with a similar error behavior.

2. **Spectrum exploration widget** for the estimation of the capability of a selected spectrum $\vec{s}(x,y)$ to serve as additional endmember.

3. **Endmember set exploration widget** for the evaluation of the influence of each endmember.

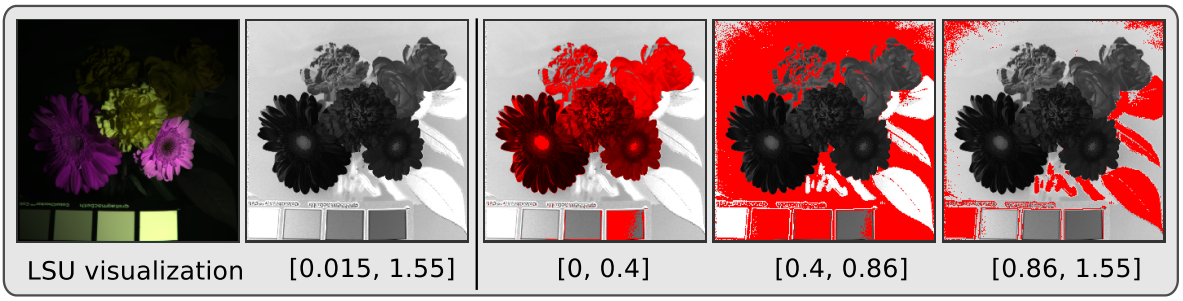

Figure 5.2: These illustrations are based on the *Flowers* dataset (cf. App. A). The LSU visualization and the associated residual error image is shown on the left. Next, different parts of the image are segmented (red) by defining distinct ranges of interest with respect to the residual error. From left to right, the flowers, the background and the leafs are segmented. The chosen distance metric was the spectral correlation angle (see Appendix B.1)

As more detailed explained in the following, these views ensure that analysts are able in order to comprehensively utilize their expert knowledge to evaluate a set of endmembers and to refine it, if necessary.

Residual error segmentation As pixels with similar residual error very frequently are belonging to the same object or material, the distance-based quality views can be used for explicit object and/or material segmentation. Therefore, the user can define a range of interest with respect to the residual error. A color overlay is applied to the pixels with distances that are within the range of interest. Based on this color overlay, pixels with similar error behavior are getting highlighted to ensure a more focused exploration of a user. Fig. 5.2 illustrates this simple, yet very efficient segmentation approach. However, this approach strictly ignores the fact that the resulting residual scalar values of distance measures have the potential to be ambiguous. Thus, a specified error range can result in the segmentation of objects of distinct materials. Moreover, their is the chance that no specific error range exists that results in a clear disjoint grouping of objects. When considering Fig. 5.2, it can be observed that different objects are segmented in one error range, e.g. leafs and parts of the background (right). Anyway, the idea of grouping pixels with similar error behavior has revealed high potential in order to further guide a user in the exploration process. Therefore, based on the discovered observations, a more advanced and expressive spectral error visualization is presented in Sec. 5.2 to tackle these issues, thus to further minimize the user interaction by a more improved guidance.

Spectrum exploration widget At the beginning of the exploration, the set of endmembers V consists of the result of the endmember extraction analysis (see Sec. 4.2). As described before, the aim of the complementary visualization is the proper reflection of the reconstruction quality and to guide a user to spectra that have potential to improve the reconstruction, if necessary. A spectrum that has high potential of improving the result typically has a high error value in at least one of the distance images, or has no assigned endmember in the NN-based

visualization. Thus, these indications are used to purposefully draw the attention to such interesting pixels. A mouse click on an interesting pixel in one of the four views launches an exploration widget (see Fig. 5.3) to evaluate the selected spectrum $\vec{s}(x,y)$, e.g. to reveal its potential to decrease the residual error. The widget mainly contains a spectral plotter in order to show the spectral distribution of $\vec{s}(x,y)$ and a corresponding distance image that shows the distances between $\vec{s}(x,y)$ and all other pixels, i.e. spectra. The spatial impact of the selected spectrum $\vec{s}(x,y)$ in the grayscaled distance image can be further explored by adjusting a similarity threshold value to explore how much $\vec{s}(x,y)$ is related to the other pixels. By this predictive evaluation of the influence, unnecessary inverse unmixing calculation are prevented which can be very time-consuming (as discussed in Sec. 4.4).

Furthermore, the plot of the current spectrum allows experts to interpret the spectral characteristics and to directly compare them to the current set of endmembers V. Here, the visualization of all endmember provides the opportunity to examine the spectral distribution of V at the same time in comparison to the currently selected spectrum. Thus, an analyst can see how different the distributions are, e.g. to see if they partly converge or diverge. Focusing on the current selection, an analyst easily can see which endmember resembles the current spectrum best. Or the other way around, it can be seen how distinct the current spectrum is compared to V. Thus, to see how good it can serve as a new endmember. Finally, when $\vec{s}(x,y)$ fits the users requirements, it can directly be added as a new endmember to V.

Endmember set exploration widget So far, the evaluation of the current set of endmembers V was out of the focus. Thus, in order to more carefully reveal the influence of an endmember in the LSU result, a more detailed evaluation of V is achieved by another widget that contains a list of all endmember, active and inactive (see Fig. 5.4). Here, inactive declares endmember that were active in previous LSU runs. These are kept to easily reactivate them in case of a misapprehension of a user.

By choosing one of the endmembers, the properties of the selected element are presented. Here, the properties view mainly contains the coefficients map and a spectral plot. The coefficient map gives a very good overview of the influence of the selected endmember at each image location. Thus, inappropriate endmembers , i.e. endmembers whose coefficients are very low or concentrated on one pixel, e.g. in case of an outlier, can be detected. In conjunction with the spectral distribution in the plot, users can get a quick and broad overview. As in the spectrum exploration widget, the single spectrum again can be compared to the spectral distribution of all current endmembers at once, by plotting them combined in the same manner as in the spectrum exploration widget. Doing so, the user can check if and how distinct the endmembers are and identify wavelength ranges which are most interesting for the application.

Furthermore, the properties view contains text fields for both, the name of the endmember and user notes. Thus, the analysts can exchange the name of the element and/or add additional notes to record observations and hypotheses. This is necessary in order to keep track of increasing or bigger endmember sets. Finally, it is possible to exchange the color or directly disable endmembers for the upcoming update cycle.

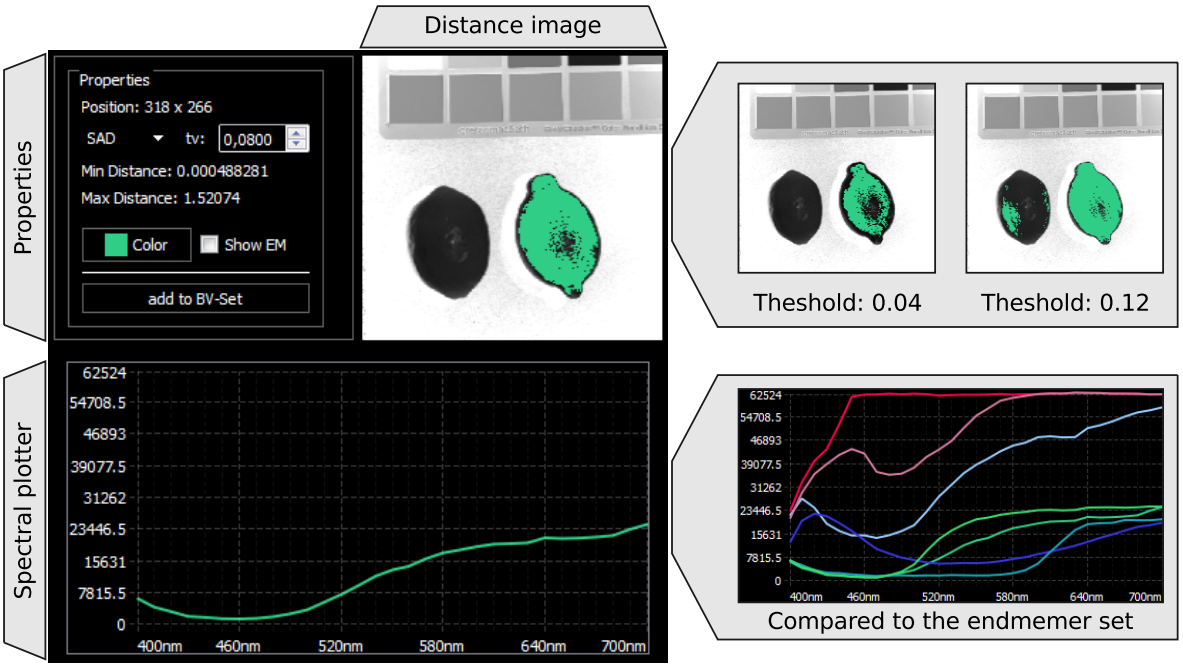

Figure 5.3: The spectrum exploration widget for the evaluation of a selected pixel, i.e. spectrum. Additional distance images are depicted for different distance thresholds to exemplarily show the spatial impact evaluation. By modification of the threshold, the similarity of the current spectrum compared to all other pixels can be explored. Furthermore, the spectral plot allows to interpret the spectral characteristics, also compared to the endmember set.

5.1.3 Usage Examples

The presented visualization approach is capable of evaluating the completeness of endmember sets and if needed to refine the set. The interactive analysis approach is applied to three datasets from three different applications in order to show that the technique can be applied to a broad variety of data exploration problems. Here, in each case only ANC is enforced in the inverse operation of the unmixing to avoid issues that are imposed by the variability in an endmember class. The aspect of endmember variability in LSU is discussed in more details in Sec. 5.2 later on.

In the first example, the multispectral dataset *Lemons* with comparably low spectral dimensionality is reconsidered. The second scenario shows a result for the very high spectral dimensional confocal Raman dataset *Diamond*. Next, the *Washington DC Mall* dataset from the field of remote sensing is analyzed. Details about these datasets again can be found in the Appendix A. Finally, the usage examples closing with a discussion of technical and general limitations of this approach.

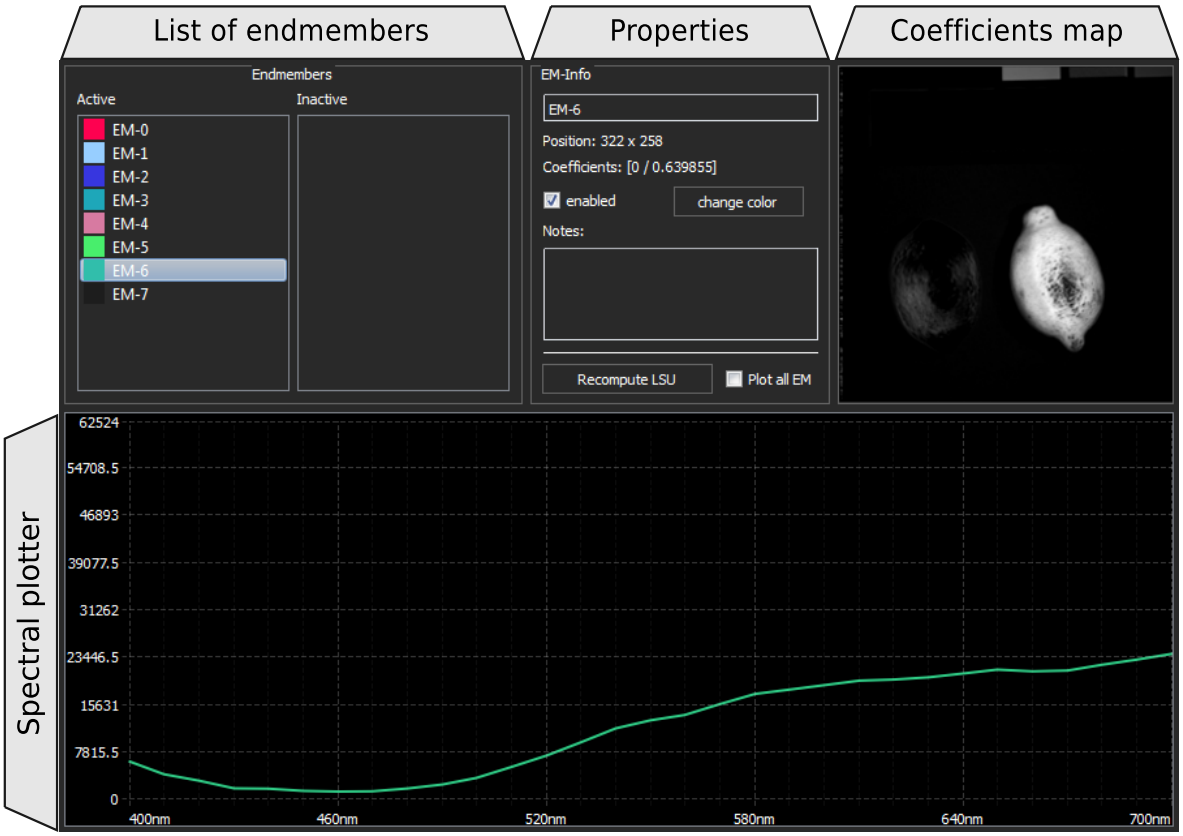

Figure 5.4: The screenshot shows the widget for the exploration of the endmembers. The endmembers are listed in two lists, distinguishing active and inactive endmembers. By selecting one endmember, the analyst can mainly examine the corresponding coefficients map and the spectrum. Again, the spectrum also can be compared to the spectral distribution of all active endmembers (cf. Fig. 5.3).

Multispectral Imaging

The *Lemons* dataset mainly contains a real and an artificial lemon placed at the right and left, respectively (see Appendix A). The utilization of this dataset in the usage examples of the Semi-Automatic Endmember Extraction (see Sec. 4.2.3) already has shown, that here the PPI algorithm performs better than the OSP. However, both have in common that they are fail to distinguish these two lemons. Therefore, it is the goal to more carefully identify the characteristic spectra of the two lemons. In order to stress the visualization approach, the more inaccurate result of PPI, consisting of eight endmembers is considered as the initial result (cf. Fig. 4.7).

In the result of the automatic endmembers extraction, two major deficiencies can clearly be observed, i.e. the background component has not been identified, as shown in the error image, and the characteristic spectra of the lemons, especially of the real lemon, are not well captured, as can be seen in the NN-visualization and in the error images. The background has

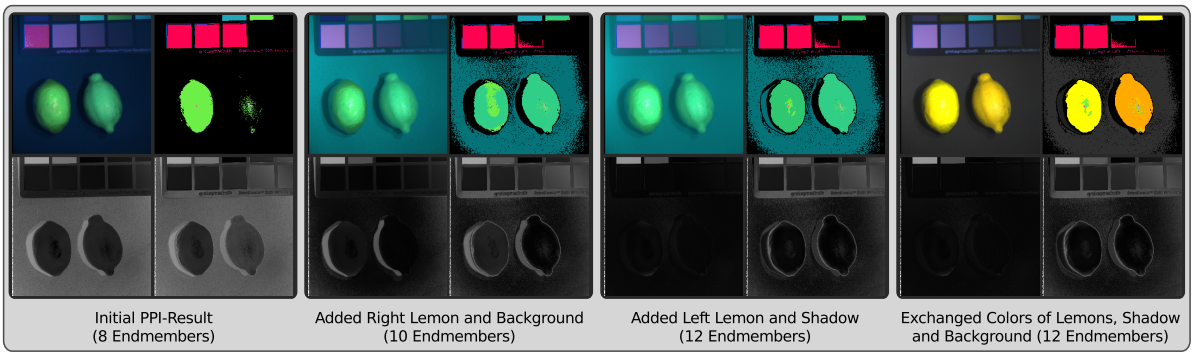

Figure 5.5: The images show the different intermediate exploration results of the *Lemons* dataset as follows: The initialization result with eight endmembers and initial colors from the false-color image *(left)*. By examining the initial set, it can be seen that the background and the lemons are not well represented by the initial endmembers. Therefore missing endmember were manually added to the set: First, spectra for both, the left lemon and the background (second image from left). Second, a better constituent for the left lemon and also on representative for the shadows were added (third image from left). Finally, the initial colors were manually exchanged to achieve an easier distinction of both lemons. The dark shades (low values) in the error images indicate the modeling success.

a high absorption almost over the whole wavelength range, which leads to low intensity values. Consequently, the background is hard to identify for endmember extraction algorithms, which search for extremal spectral values. As seen in Sec. 4.2.3, PPI was able to find the background with an other parameterization. But, when reconsidering this result, also PPI was not able to determine a good representative for the shadowed areas, which are also consisting of low intensity values. Anyway, applying the interactive visual analysis approach to the initial result, both types of defects can easily be removed by adding the appropriate spectra to the set of endmember. The refinement success can be followed in Fig. 5.5. First, a representative spectrum for the real lemon and also for the background were added (second image from left). A more detailed analysis of the left lemon furthermore reveals, that the automatically identified endmember mainly represents the specular highlights of the lemon. Thus, adding another, non-highlight spectrum to the set of endmembers, yields the intermediate result (third image from left). Here, in addition, also one representative for the shadowed areas were added. Finally, the colors of the new endmembers were exchanged to mainly allow an easier differentiation of both lemons. Since the focus of this analysis was achieving a better representation of the lemons, the refinement of the color-checker was not addressed. However, when requested, the refinement would continue in the same manner as presented. As can be seen by this example, an analyst is also able to focus on specific analysis task to reveal the desired information.

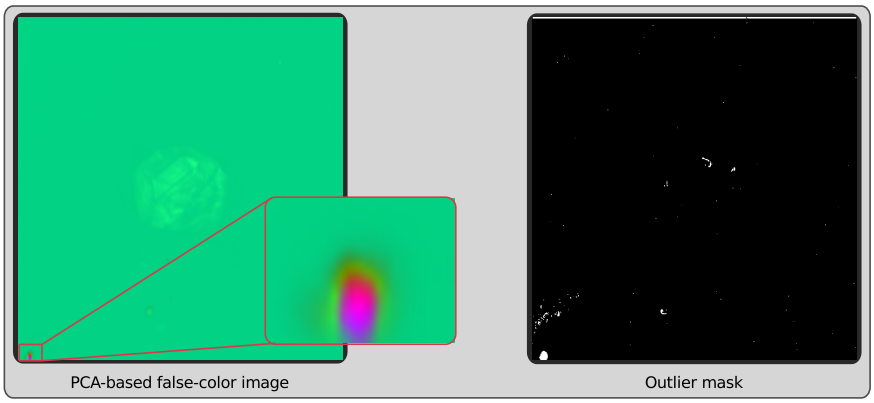

Figure 5.6: The *Diamond* dataset is dominated by a small region with high fluorescence intensity (close-up), which is shown by the PCA-based false-color image *(left)*. The right image depicts the outlier mask, beside the high fluorescence, potentially attributed to noise and small imperfections of the probe.

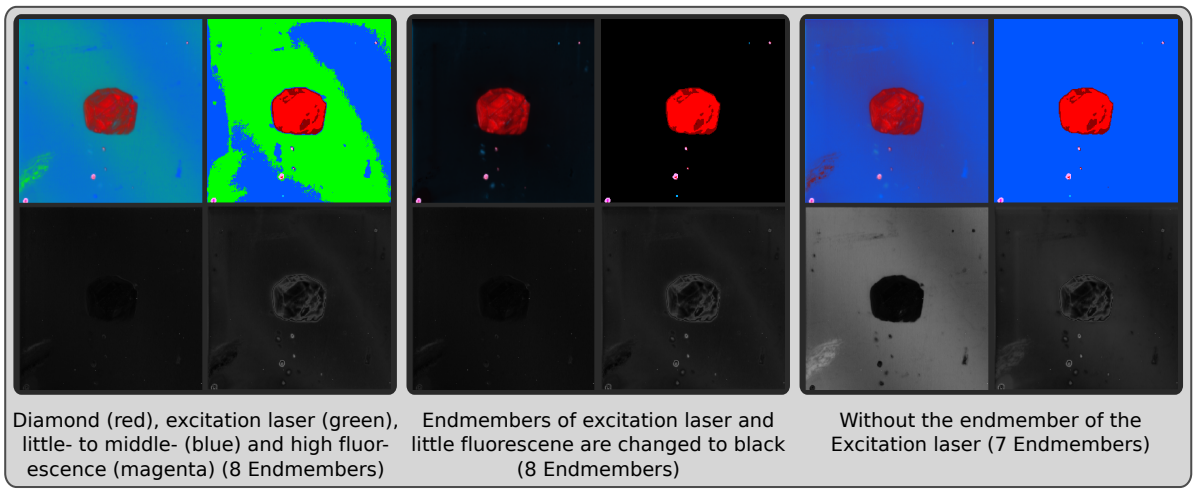

Figure 5.7: Results of the proposed method for the *Diamond* dataset. The left and middle images show the representation of the data based on eight endmembers. In the left, red is the diamond (two endmembers), magenta are areas of high fluorescence intensity in the mid of the wavelength range (three endmembers), blue are mainly the regions which contain little to average fluorescence intensity (two endmembers), and green represents regions where the spectrum of the excitation laser is very prominent (one endmember). The middle image shows exactly the same set of endmembers, but the colors of the two endmembers which are corresponding to the excitation laser and little fluorescence intensity are changed to black in order to emphasize the regions with the laser and middle fluorescence intensity as well as the diamond endmembers. The right image depicts the same set of endmembers, but without the endmember of the excitation laser.

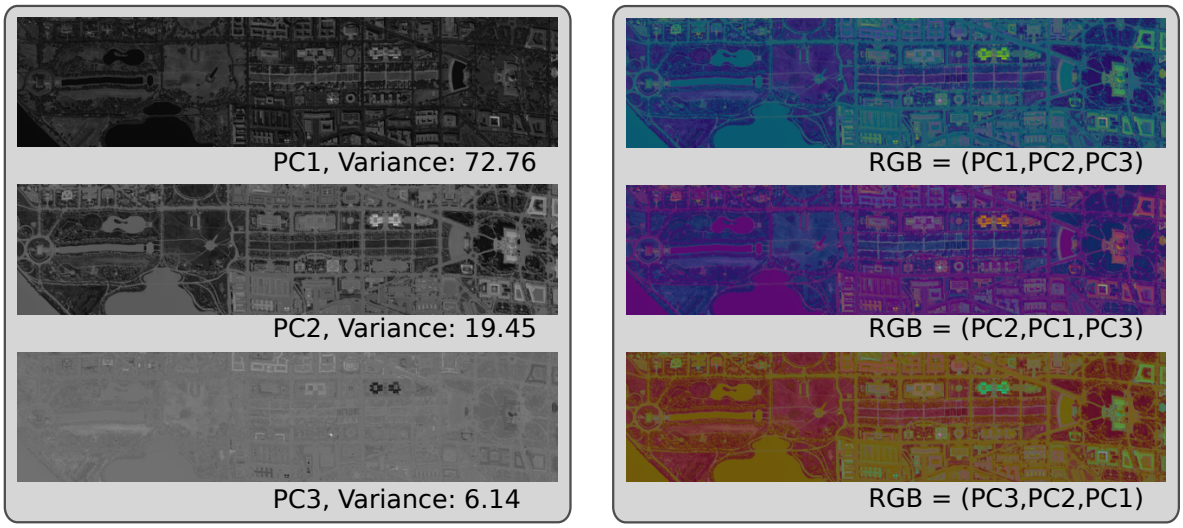

Figure 5.8: The first three principal components of a PCA for the *Washington DC Mall* dataset (see Appendix A) are shown in the *left column*. Furthermore, the *right column* shows three composed false-color images that are permutations of the three principal components.

Confocal Raman Microscopy

The *Diamond* dataset mainly consists of a diamond and some imperfections, i.e. some isolated dust particles, causing high amplitude peaks, and an area with high fluorescence illumination in the lower left corner (possible resulting from a human finger print). Both artifacts create considerable challenges to the spectral analysis since they dominate the dataset.

The dominant influence of these fluorescence effects are getting clearly visible in the PCA-based false-color image, see Fig. 5.6 (left). Consequently, the endmember extraction algorithms mainly find endmembers in the set of outliers, as also seen for the *Graphene* dataset in Sec. 4.3.3. Thus, applying the preprocessing improves the result of the automatic endmember extraction. Pixels that are skipped for the endmember extraction can be seen in the outlier mask (see Fig. 5.6, right). Based on the initial set of endmembers, computed with the OSP method (limited to 10 endmembers), eight prominent spectra were selected manually (see Fig. 5.7). Different color codings are applied in order to emphasize several meaningful endmembers, e.g. the diamond or excitation laser. Furthermore, the error images of the linear spectral unmixing, in case of eight endmembers, are only containing negligible values, indicating that the current set of endmembers is a good representation of the whole dataset.

Remote Sensing

Remote sensing datasets usually have a high spectral dimensionality. A main task of this application field is the identification of geological and urban structures at the sensed region of the earth. In this section, the results for the *Washington DC Mall* dataset are shown in comparison to the work of Landgrebe [Lan02]. In his work Landgrebe shows an example

analysis of the test dataset, based on the MultiSpec Software [BL02]. This example analysis results in a thematic map that shows seven classes, which are *Roofs*, *Road*, *Gras*, *Trees*, *Trail*, *Water* and *Shadow*. The goal is to achieve comparable results with the presented interactive visual analysis system.

Since utilizing PCA is very common in the application of remote sensing in order to get a first impression of the data, also a comparison to PCA-based false-color images is provided in Fig. 5.8. The left column shows the first three principal components of the test data, whereas the right column shows three composed false-color RGB-images that are samples of three permutations of the three principal components. Especially the first two principal components give a good overview of the structures of the data. These structures are further emphasized by the composed false-color images. However, there is no explicit relation between single principal components and specific structures, like water, grass or roofs.

In contrast to the CRM example before, non of the automatic endmember extraction algorithms was able to deliver an initial set of endmembers that includes all relevant structures. For example, OSP was applied four times, delimited to 10, 20, 30 and 50 endmembers, and in all initializations no proper representation for the classes *shadow*, *road*, *tree* and *water* was present. One reason is, that that some classes exhibit quite similar spectral characteristics, furthermore, classes like water have a high absorption (similar to the background in the *Lemons* dataset). Both effects make it extremely hard, if not impossible, to automatically select all relevant spectra as endmember.

Based on the initial set of automatically extracted endmembers, as given in Fig. 5.9 (initialization result), the complementary visualization directly draws the user's attention towards the missing characteristic spectra. Refining the initial set of endmembers by applying the presented approach, yields the result as presented in Fig. 5.9 (manual refined result). Note, the distinguished endmembers (classes) are colored in a similar fashion as in [Lan02] to make the results comparable.

Fig. 5.10 presents a close-up around the "Lincoln Memorial". Both, linear spectral unmixing and the nearest neighbor images, show detailed structures. However, it can be discovered, that the unmixing of the road around the "Lincoln Memorial" and the roof of the Memorial exhibits a too strong influence of the *shadow*-endmember, i.e. it gets comparably high coefficients in the convex combination of the corresponding pixels. However, also the used reference image has shortcomings. For instance, some pixels around several trees are classified as water. This is also the case for some of the pixels in the presented LSU-result. These shortcomings are due to the similarity of these classes, e.g. shadows, roads, and water are all classes with high absorbance. Thus, this issue goes back to the general problem of similarity measure in high-dimensional spaces.

Discussion

As shown by the usage examples above, the visual analysis approach allows the user to assess and to progressively refine an endmember set. Here, the complementary visualization and the proposed exploration means allow an analyst to incorporate his expert knowledge to achieve

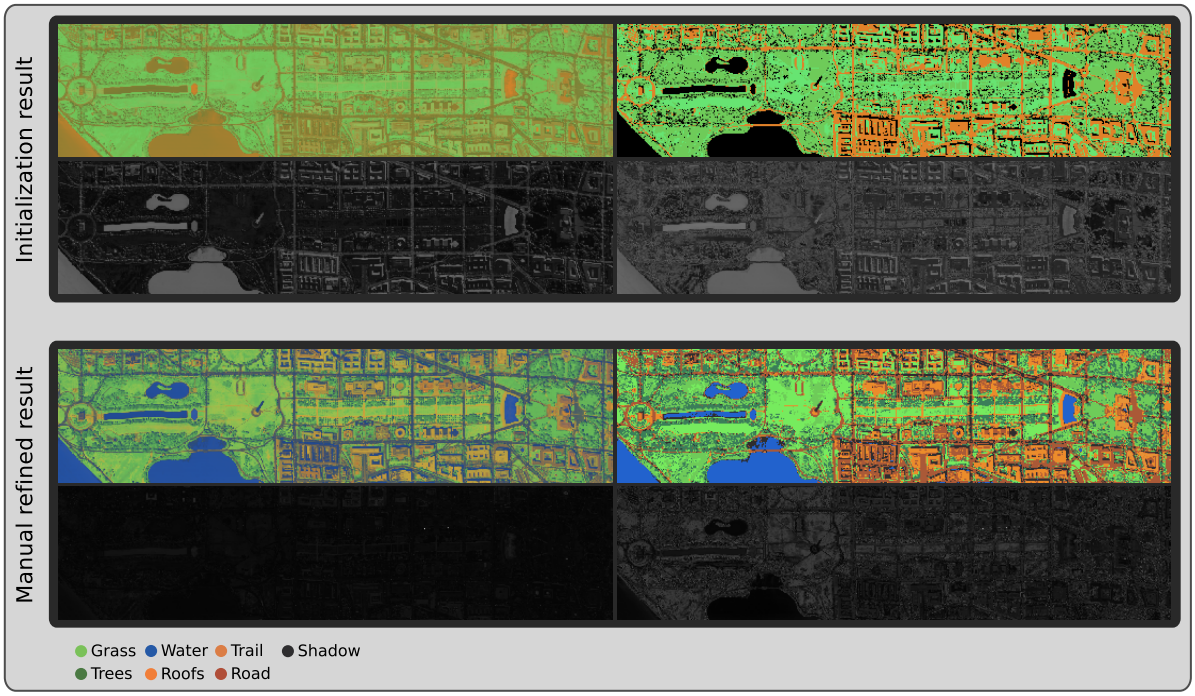

Figure 5.9: The result of the presented approach for the *Washington DC Mall* data (see Appendix A). The columns show the result of the linear spectral unmixing and nearest neighbor visualization for the initial result, based on OSP limited to 10 endmembers, *(top)* and the manual refined result *(bottom)*. Both results are shown with corresponding grayscaled error images respectively beneath.

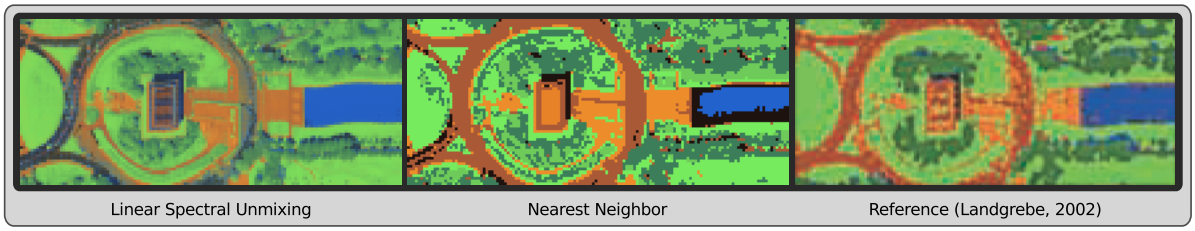

Figure 5.10: This figure shows a close-up of the final result around the area of the "Lincoln Memorial". Compared to the nearest neighbor visualization *(middle)*, smooth and detailed structures are visible in the linear spectral unmixing *(left)*. Furthermore, it is obvious that the corresponding endmember of *shadow* has too high influence in the convex combinations for the road and the roof of the Memorial. For comparison, also a close-up of the corresponding area of the result from [Lan02] is shown in the *right*.

the best possible application specific result. However, the approach is subject to some general technical limitations:

- The number of endmembers in general is limited by the number of spectral bands.
- The stability of the LSU-coefficients naturally depends on the independence and completeness of the set of endmembers; see Fig. 5.10.
- Endmembers with comparable spectral characteristics or with comparably low spectral intensities are hard to be identified in automatic processes.

Beside these general technical limitations, also some limitations of the presented approach can be identified which prevent a more sophisticatedly incorporation of an analyst in the exploration process.

Distance images The usage example presented with the *Lemons* dataset shows that different residual errors can lead to indistinguishable ambiguous scalar values in the distance images, as also discussed in Sec. 5.1.2. Consider the error values of the two distinct lemons in the almost left image of Fig 5.5, which are indistinguishable at all. Thus, these distance images alone do not allow the distinction of both lemons. Although the NN-based visualization is capable to reveal the difference of both lemons, the shortcoming of the grayscaled distance images offers good potential for improvements.

Reconstruction quality The proposed approach mainly relies on low deviation values in the distance images. However, so far their is no opportunity to evaluate the reconstructed spectra more carefully in comparison with the raw spectra. Thus, does not allow an analyst to judge deviations comprehensively, e.g. to see if a deviation is due to a constant magnitude or a narrow peak. For instance, a narrow peak in total can lead to a comparable low error value. But, since a peak can be characteristically for a specific material, the deviation should be proved by an expert to ensure a reliable endmember set. This would not be the case, when only looking for high deviation values.

Sequentially presentation of information The evaluation of a set of constituents can be done by the proposed endmember set exploration widget (cf. Sec. 5.1.2). The rationale of this widget is the selection of a single element, i.e. constituent, to examine its properties. Although it is possible to compare the currently selected spectral characteristics to the spectral distribution of the complete set of constituents, the instantly comparison of other properties, e.g. coefficients maps, takes place in a sequential order. Thus, leads to an non intuitive exploration process, e.g. when revealing in which area which endmember has influence.

5.1.4 Summary

This section has presented a visual analysis approach for interactive exploration, verification and optimization of LSU-results, which defines the second part of the process for generic

identification of constituents spectra, see Sec. 4.2. Based on a complementary visualization, containing views for the LSU, the NN visualization and respective distance images, an analyst is enabled to verify the completeness of an endmember set. Several exploration tools allow an analyst to incorporate his expert knowledge to further assess or refine the set of constituents, if necessary. The benefits of the interactive exploration approach has been demonstrated for various application domains. Finally, also limitations of the here discussed concept have been discussed, which are subject of the upcoming section.

5.2 Expressive Spectral Error Visualization

The previous section has presented an visualization approach to assess the quality of an endmember set. The rationale of the visualization mainly relies on low deviation values in the supplementing distance images. However, as the discussion of this approach as revealed, this concept has two major shortcomings that have potential for improvements, which are mainly the possible ambiguity of distance values and a more detailed verification of the reconstruction of a spectrum. Therefore, this section introduces expressive spectral error visualization concepts in order to enhance and supplement typical distance measures.

The remainder of this section is organized as follows. The problem statement is discussed in more details in section 5.2.1. Then the conceptional overview of the approach is presented in Sec. 5.2.2, while the details of the expressive spectral error visualizations are subject in the upcoming two sections 5.2.3 and 5.2.4. The section 5.2.5 shows the general means and exploration possibilities of the supplemented visual analysis approach which embeds the expressive visualizations. The results are presented by usage examples for multispectral imaging and CRM in Sec. 5.2.6.

5.2.1 Problem Statement

SMA has been a very active research field in recent years [JMP12]. Here, the quality of the final result, i.e. the residual error between the raw and the reconstructed data, strongly depends on the selected endmembers and automatic endmember extraction algorithms can fail to determine a complete set of endmembers as seen before. Additionally, one of the most profound source of error in LSU lies in the lack of the ability to account for sufficient temporal and spatial spectral variability [SATC11]. An example of this variability is shown in Fig. 5.16, where a multiplicative scaling effect is clearly evident in the spectra, but the shape of the spectra itself is nearly invariant [Kes03]. Thus, manual intervention, in terms of more precise identification of constituents, can be mandatory in many applications in order to improve the unmixing, as already shown in sections 4.2 and 5.1. But, manual intervention leads to the requirement of efficient user guidance and visual exploration methods, for example to identify missing endmember candidates, i.e. missing materials, that have high potential to improve the quality of the unmixing.

Spectral error evaluation can be done by comparing the results to accurate ground truth references, when available. But typically the accuracy of LSU is mainly quantified based on

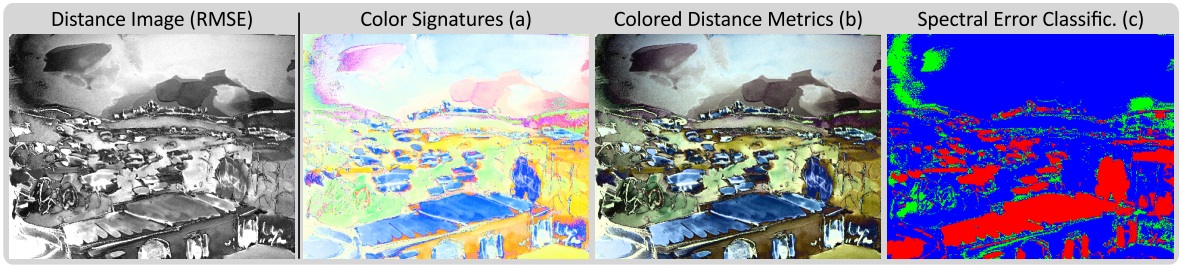

Figure 5.11: A typical distance image that expresses the quality of a LSU-result and which can be used as basis for a refinement of an endmember set is shown (left) and compared to the contributions of the here presented approaches (right). Distinct residual errors are easier distinguishable with the **color signatures**, which can be combined with common distance images and then are called **colored distance metrics**. Additionally, a **spectral error classification** discriminates pixels in terms of missing endmembers (red), variability error (blue) and neglectable deviations (green).

the fit between the reconstructed data S_{LSU}, obtained by using Eq. (1.1), and the raw data S_{RAW} [SATC11]. Here, several metrics (cf. Appendix B.1) can be applied in order to evaluate the quality by pairwise computation of the distances between $\vec{s}_{RAW}(x,y)$ and $\vec{s}_{LSU}(x,y)$ for each pixel, resulting in a distance image. Keshava and Mustard [KM02] state, that it is still unclear what combination of physical and mathematical modeling can optimally extract information from hyperspectral signals and as consequence they see no single distance metric that is useful in all circumstances. Thus, different metrics can lead to different quality impressions. Moreover, the common distance metrics lead to a single scalar error value per pixel. This mapping results in severe information loss, since different spectral residual errors may lead to the same, i.e. ambiguous, scalar error. Manual inspection of individual spectral residual errors, on the other hand, is extremely time-consuming and does not provide global information about the distribution of the spectral error. Only a few approaches exist in the literature that are aiming the evaluation of spectral unmixing quality in a comprehensive way. Beside the presented approach in Sec. 4.2, the most recent approach is HyperMix [JMP12], as discussed in Sec. 2.3. However, both approaches map the spectral residual errors to single scalar error values, incorporating a significant loss of information, and do not allow detailed local (spectral) explorations. Therefore, this section presents a visual analysis approach which enhances LSU-results by expressive spectral error visualizations in order to efficiently guide a user to specific spectra for local exploration. These visualizations consist of a qualitative coloring scheme, called **color signatures**, for easier differentiation of distinct errors by visually grouping in a global sense. **Colored distance metrics**, the combination of **color signatures** and typical distance images, are used to reduce the ambiguity of scalar error values, see Fig. 5.11 (a, b). The **colored distance metrics** also can be interactively modified by the design of transfer functions to freely highlight or determine error regions of interest. Beside the coloring, also a **spectral error classification** is presented to mainly provide the distinction between residual errors caused by endmember variability or by missing endmembers, see Fig. 5.11 (c).

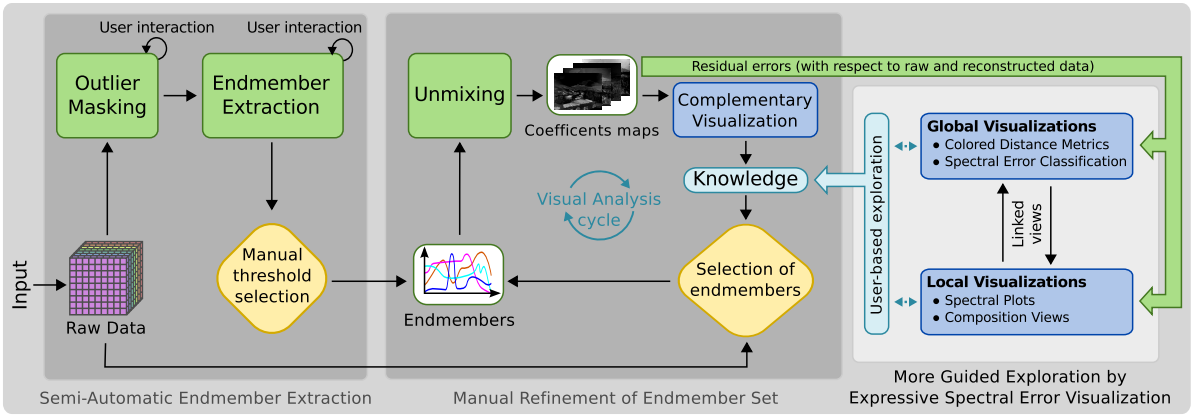

Figure 5.12: Conceptual overview of the proposed extension of the previous visual analysis approach (dark gray in the left). The analysis starts from the current LSU-result. In the guided exploration process the global **expressive spectral error visualizations** sophisticatedly guide an analyst to pixels of interest for local verification and exploration of the reconstruction quality of a spectrum. All visualizations are linked to allow effective knowledge extraction. If necessary, the set of endmembers can be instantly refined in the same manner as presented before.

5.2.2 Conceptional Overview

A conceptual overview of this approach is depicted in Fig. 5.12. As can be seen, this approach supplements the pipeline of the generic determination of constituent spectra (cf. Sec. 4.2). Compared to the before presented approach, here, it is vital to examine and understand the influence of each endmember for both, the complete dataset (global) and also single pixels (local), e.g. to compare $\vec{s}_{RAW}(x,y)$ and $\vec{s}_{LSU}(x,y)$, thus, to address and compensate the main limitations of the complementary visualization (cf. Sec. 5.1.3). In addition, beside the verification of the quality, this approach also allows the more comprehensive interactive exploration of the LSU-result in order to facilitate the knowledge gathering process of previously unknown datasets, e.g. to explore the distribution or the influence of endmembers in mixed spectra.

Starting from the current LSU-result, endmembers and corresponding coefficients maps, the exploration process is driven by local and global visualizations. While the applied local visualizations allow the detailed examination of the reconstruction quality and the composition of a spectrum, the global views provide visual guidance by **expressive spectral error visualizations** in order to sophisticatedly guide an analyst to pixels of interest. All visualizations are linked to allow effective knowledge extraction. If necessary, the set of endmembers can be refined in the same manner as presented before.

As a simple example, consider a typical LSU-result: Usually the unmixing quality is proved by applying similarity measures, which can lead to different quality impressions and the results can be ambiguous since different spectral errors can lead to same error values (see Sec. 2.3). Moreover, errors based on endmember variability can lead to conspicuous distance values. In a typical distance image, these distance values can not be distinguished

from distance values that are originate from missing endmembers. Therefore, endmember variability can compromise the detection of endmembers. In the worst case this would require an analyst to explore all pixels in order to validate the unmixing result. Hence, in order to encounter these challenges and to reduce the interaction effort, mainly two global **expressive spectral error visualizations** are presented.

Colored Distance Metrics enhance the typical distance images to achieve a visual grouping of pixels with a similar error behavior. Thus, it reduces the ambiguity of distance values by coloring.

Spectral Error Classification is done in order to classify pixels in three terms: neglectable spectral errors and spectral errors that are caused by endmember variability or by missing endmembers.

Based on these global impressions, the analysts sophisticatedly can identify pixels of interest for comprehensive local validation. The details of both global visualizations are presented in the following two sections.

5.2.3 Colored Distance Metrics

Focusing on typical distance images, the differentiation of error values is improved by a proposed qualitative coloring of residual spectral errors, so-called **color signatures**, to visually group comparable residues, thus, to reduce the ambiguity of the scalar values. In Fig. 5.13, a typical challenge of grayscaled distance images can be seen. Due to ambiguous distance values, distinct residual errors are indistinguishable. In contrast, the proposed **color signatures** allow a qualitative distinction of the residual errors by their colors. In order to best possibly express the distinct residual errors by a color, the variance of the residuals is used to achieve optimal color distribution and saturation. An enhanced distance image, where residual errors with same error behavior are visually grouped, is achieved by weighting a **color signature** with a common distance image.

In the following the calculation of the **color signatures** is discussed. Based on both, $\vec{s}_{RAW}(x,y)$ and $\vec{s}_{LSU}(x,y)$, the residual error $\vec{r}(x,y)$ and the absolute residuum $\vec{r}_{abs}(x,y)$

$$\vec{r}(x,y) = \vec{s}_{RAW}(x,y) - \vec{s}_{LSU}(x,y) \text{ and } \vec{r}_{abs}(x,y,\lambda) = |\vec{r}(x,y,\lambda)| \text{ for all } \lambda \tag{5.3}$$

are calculated for each pixel (x,y) of an image with the spatial resolution X and Y. Then the $\vec{r}_{abs}(x,y)$ is considered as a spectrum and transformed into a *RGB*-color. Here, one of the goals is an intuitive interaction concept. Therefore, a spectrum transformation is presented, which is intuitive and allows a user to estimate a residual characteristic from its color. The *RGB*-values are computed

$$B = \frac{1}{n_{u_B}} \sum_{\lambda=1}^{u_B} \vec{r}_{abs}(x,y,\lambda),\ G = \frac{1}{n_{u_G}} \sum_{\lambda=u_B+1}^{u_G} \vec{r}_{abs}(x,y,\lambda),\ R = \frac{1}{n_{u_R}} \sum_{\lambda=u_G+1}^{u_R} \vec{r}_{abs}(x,y,\lambda) \tag{5.4}$$

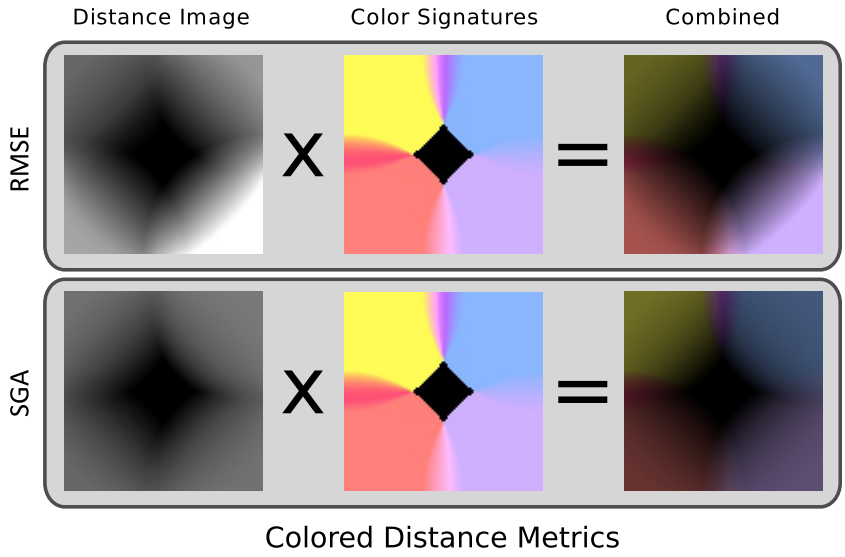

Figure 5.13: Based on the artificial dataset *Five endmembers* (cf. Appendix A), the benefit of the proposed **colored distance metrics** is exemplary depicted for two metrics. In this example, only the centered endmember was selected. Thus, the four missing endmembers lead to distinct residual errors. While the residuals are indistinguishable in the typical grayscale images, they are easily distinguishable in the **color signatures** enhanced distance images (combined).

by splitting the whole residual spectrum $\vec{r}_{abs}(x,y)$ in three intervals to correspond with the *RGB* color model. Here, the intervals are defined by three boundary values $u_{\{B,G,R\}}$. The deviations of each interval are summed up and averaged in order to achieve the *RGB*-values. In order to achieve the maximum brightness, the color values R, G and B are normalized by dividing through the maximal component value

$$\bar{R} = \frac{R}{\max(R,G,B)}, \; \bar{G},\bar{B} \text{ analog.} \tag{5.5}$$

In order to achieve the best possible color distribution and saturation, the boundaries $u_{\{B,G,R\}}$ are selected in the way that the standard deviations σ_λ of the spectral bands

$$\sigma_\lambda = \sqrt{\frac{1}{X \cdot Y} \sum_{x=1}^{X} \sum_{y=1}^{Y} \left(\vec{r}_{abs}(x,y,\lambda) - \mu_\lambda\right)^2}, \text{ where } \mu_\lambda = \frac{1}{X \cdot Y} \sum_{x=1}^{X} \sum_{y=1}^{Y} \vec{r}_{abs}(x,y,\lambda) \tag{5.6}$$

are consistent in all three intervals

$$\frac{1}{3} \sum_{\lambda=1}^{n} \sigma_\lambda \approx \sum_{\lambda=1}^{u_B} \sigma_\lambda \approx \sum_{\lambda=u_B+1}^{u_B+u_G+1} \sigma_\lambda \approx \sum_{\lambda=u_B+u_G+1}^{u_B+u_G+u_R+1=n} \sigma_\lambda. \tag{5.7}$$

Based on the **color signatures**, a user can intuitively estimate from the colors in which of the three intervals the error occurs, e.g. red color means last third or magenta means error

in the first and third range. Errors in nearly the complete range will lead to white, while a black color will mean, that the reconstruction error is low in all ranges. The **color signatures** are computed for all pixels, leading to an color signature image that element-wise can be weighted by arbitrary distance images, resulting in a **colored distance metric**. Figure 5.13 shows a simple example, based on a synthetic dataset. Since different metrics can lead to different quality impressions of results, this approach also allows an analyst to simultaneously overview the distance images of all implemented metrics as well as the **color signature** image at the same time allowing an intuitive combination, see example in Fig. 5.14.

Modification of Color Signatures by Transfer Functions So far the result of the **color signatures** depends on the variance-based sizes of the three intervals R, G and B. Sometimes it is desired to freely highlight or determine residual error characteristics of interest. Moreover, since light emission often is not uniform and sensors provide smaller intensity values in the infrared range, an adjusted weighting is useful in order to manually compensate such issues.

Based on residual statistics, that illustrate the error trend, a global view is proposed that allows the interactive design of transfer functions (TF) to fine-tune the initial intervals of R, G and B, see Fig. 5.15. Moreover, **color signatures** also can be completely changed, since the number of TFs is not limited to three. The error trend view shows the current residuum $\vec{r}(x,y)$ as well as several global average residual errors. In detail, the average residual error $\vec{r}_{avg}$ and also the average positive $\vec{r}^{\,+}_{avg}$ as well as average negative $\vec{r}^{\,-}_{avg}$ residual error are included. The averages are computed

$$\vec{r}_{avg} = \frac{1}{X \cdot Y} \sum_{x=1}^{X} \sum_{y=1}^{Y} \vec{r}(x,y) \text{ and } \vec{r}^{\,+}_{avg} = \frac{1}{P^+} \sum_{x=1}^{X} \sum_{y=1}^{Y} \vec{r}^{\,+}(x,y),\ \vec{r}^{\,-}_{avg} \text{ analog} \tag{5.8}$$

with respect to all pixels, where

$$\vec{r}^{\,+}(x,y,\lambda) = \max\{\vec{r}(x,y,\lambda),0\} \text{ and } \vec{r}^{\,-}(x,y,\lambda) = \min\{\vec{r}(x,y,\lambda),0\}. \tag{5.9}$$

Here, P^+ and P^- are the number of positive and negative error values, respectively. Furthermore, for each band, also the min- and maximum error value is depicted to show the maximum variance at the same time. The TFs can be defined via trapezoids and are related to the bands. Here, the width and the height of a Trapezoid defines the wavelength interval and the weighting factor, respectively. Based on the user-defined TFs $\mathrm{tf}_1(\lambda),\ldots,\mathrm{tf}_h(\lambda)$ and their corresponding colors $RGB(\mathrm{tf}_i)$, the new RGB-values are composed by

$$R(x,y) = \sum_{i=1}^{h} \left(\sum_{\lambda=m_i}^{n_i} \vec{r}(x,y,\lambda) \cdot \mathrm{tf}_i(\lambda) \cdot d\lambda \right) \frac{R(\mathrm{tf}_i)}{\vec{r}^{\,max}_{abs} \cdot \Delta\lambda_i} \text{ , with } \Delta\lambda_i = m_i - n_i \tag{5.10}$$

$G(x,y)$, $B(x,y)$ analog,

where h is the number of TFs, m_i and n_i define the corresponding interval $[m_i,n_i]$ of a $tf_i(\lambda)$ and $\vec{r}^{\,max}_{abs}$ is the maximal absolute error value of a all residual values.

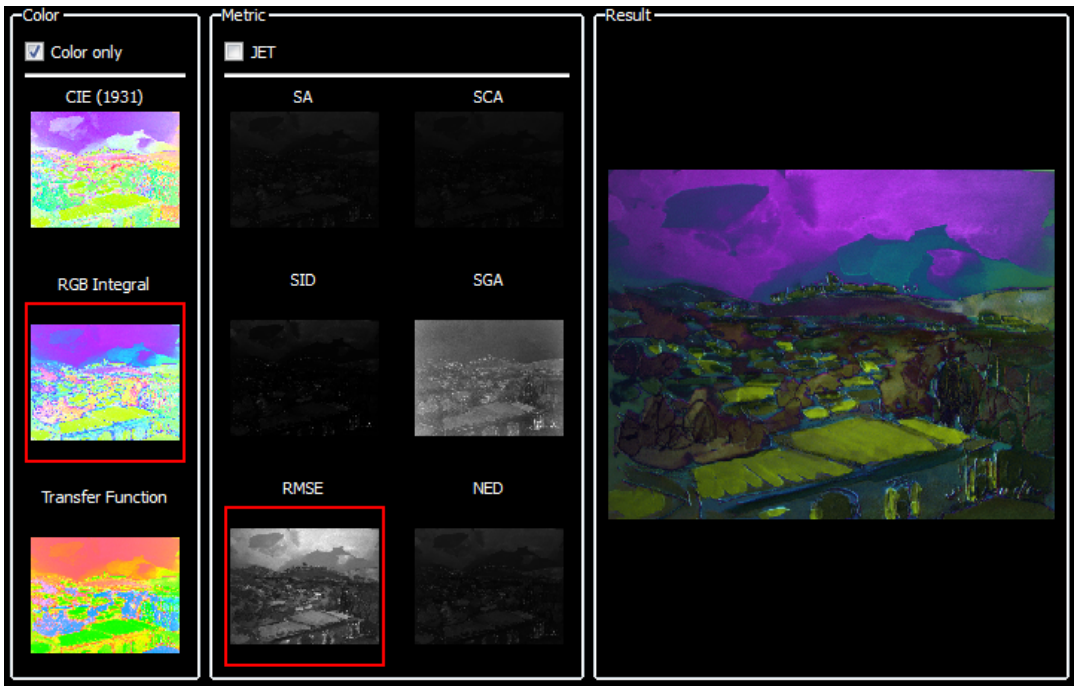

Figure 5.14: The simultaneously overview of different distance images simplifies the process of distance metric selection. Beside the usual grayscaled images, also the possibility of jet-coloring is provided. Moreover, the metrics can be combined with the results of the color signatures, achieving a colored distance metric, to emphasize comparable distances. A close-up of the current selection (combination) is always shown on the right.

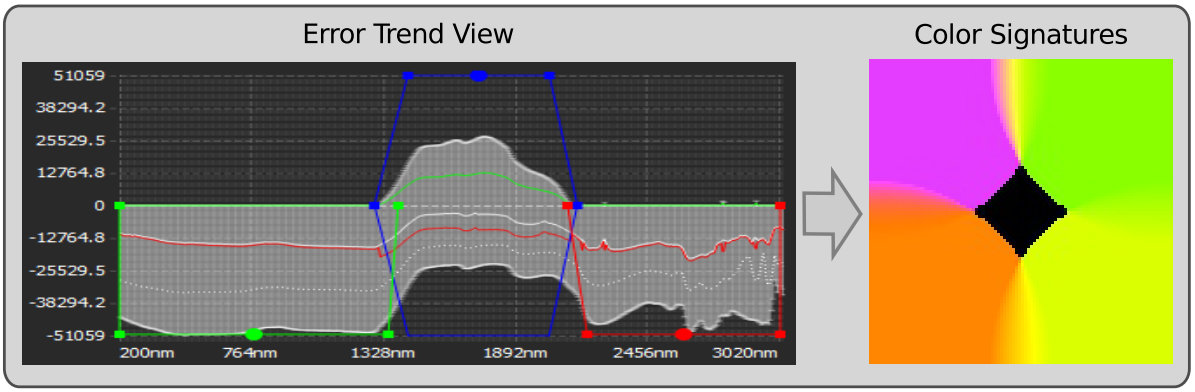

Figure 5.15: The error trend view, where the white line is the average residuum, the green and red line represents the positive and negative averages of the residues. The dashed white line represents the local residuum of the current pixel. Here, the TFs of the **color signatures** of Fig. 5.13 are modified.

5.2.4 Spectral Error Classification

While the aim of the **colored distance metrics** is the qualitative grouping of comparable residual errors, the aim of the **spectral error classification** is to mainly distinguish errors introduced by endmember variability form errors due to missing endmembers, to more purposefully guide an analyst to missing endmembers.

Beside missing endmembers, as mentioned in Sec. 5.2.1, the endmember variability also is one of the most profound sources of error in the estimation of abundances [SZPA12]. The reason for this is, that typically FCLSU is applied to achieve a physically reasonable result. But, for instance, when in a pixel low coefficient values $\alpha_j(x,y) < 1$ are necessary because of the variability and the sum of all coefficients is not one, then the enforced ASC introduces errors in the abundance estimation. An example of this issue is illustrated in Fig. 5.16 (right), where an optimal $\sum \alpha_j(x,y)$ is 0.72. But, because of the ASC in FCLSU the individual $\alpha_j(x,y)$ are scaled to sum up to one, which leads to an error that is introduced by the variability. As can be seen, when only ANC is enforced the reconstructed spectrum $\vec{s}_{LSU}(x,y)$ is comparable to $\vec{s}_{RAW}(x,y)$. This circumstance serves as idea to identify errors based on endmember variability. In detail, the **spectral error classification** is based on two results of LSU, i.e. NCLSU and FCLSU. Since the fully constrained coefficients can be obtained directly from the NCLSU-coefficients by scaling the coefficients to fulfill the ASC, the computational effort is comparable to the typical FCLSU calculation. Based on both results, two corresponding RMSE-values are computed for each pixel

$$d^{NC}(x,y) = RMSE(\vec{s}_{RAW}(x,y), \vec{s}_{NCLSU}(x,y)) \tag{5.11}$$

$$d^{FC}(x,y) = RMSE(\vec{s}_{RAW}(x,y), \vec{s}_{FCLSU}(x,y)). \tag{5.12}$$

The two calculated deviation values are used to classify the type of deviation:

$$sec(x,y) = \begin{cases} \text{Neglectable deviation} & \text{if } 0 \leq d^{NC}(x,y),\ d^{FC}(x,y) < v \\ \text{Variability deviation} & \text{else if } 0 \leq d^{NC}(x,y) < v \\ \text{Missing endmember} & \text{else,} \end{cases} \tag{5.13}$$

where v is a user defined quality threshold. When both deviation values are smaller than v, a pixel is classified as neglectable deviation, while in all other cases $d^{NC}(x,y)$ is used to distinguish the remaining types of deviations. Applying $sec(x,y)$ to all pixels generates a classification image SEC, see Fig. 5.17 for an example. Moreover, SEC can be weighted resulting in SEC_w

$$sec_w(x,y) = \begin{cases} sec(x,y)\frac{d^{NC}(x,y)}{\max(d^{NC}(\text{all pixels}))} & \text{if Neglectable deviation} \\ sec(x,y)\frac{f(x,y)}{\max(f(\text{all pixels}))} & \text{else} \end{cases} \tag{5.14}$$

$$\text{with } f(x,y) = \text{abs}\left(1 - \sum_{j=1}^{q} \alpha_j^{NC}(x,y)\right) \tag{5.15}$$

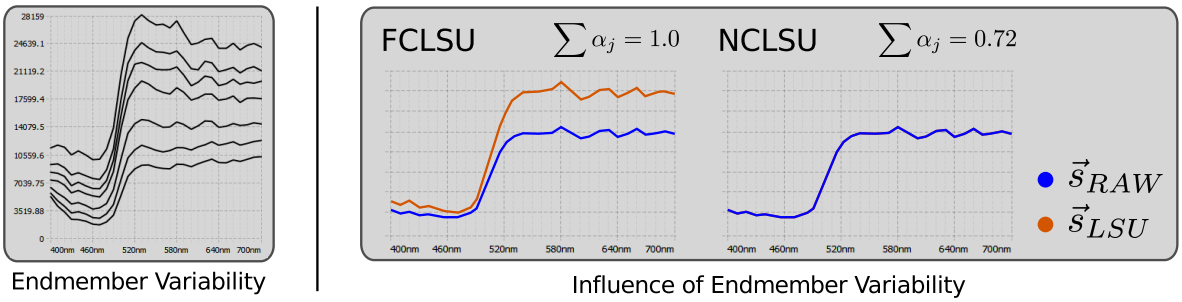

Figure 5.16: The left figure shows an example for the variability in an endmember class. The variability based abundance estimation error in FCLSU is illustrated on the right, in comparison to NCLSU.

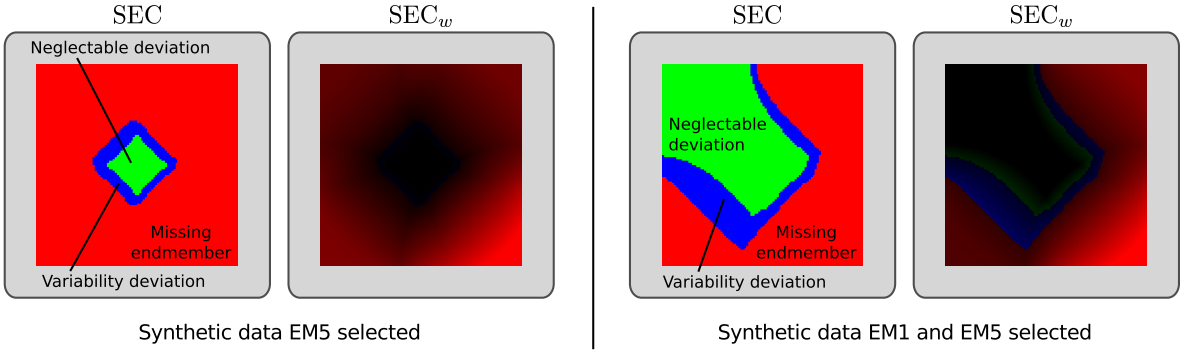

Figure 5.17: Two examples of the proposed spectral error classification. Here, the first example is based on the LSU-result already presented in Fig. 5.13 (left). Moreover, a second scenario is depicted in order to better illustrate the weighting in SEC_w

in order to easier discover pixels that have major deviations. Here, q is again the number of endmembers and for a pixel that is classified as *missing endmember*, the normalized $d^{NC}(x,y)$ is used as weighting factor for $sec(x,y)$. In all other cases, the endmember variability is expressed in $sec_w(x,y)$ by the difference between the sum of the coefficients of the endmembers of the NCLSU $\alpha_j^{NC}(x,y)$ and the FCLSU, which is one. Consider again Fig. 5.17 for an example of this weighting scheme.

5.2.5 Interactive Exploration

The graphical user interface of this supplemented visual analysis approach is shown in Fig. 5.18 and consists of several linked views. Beside several 2D data visualizations, e.g. sRGB color representation by the usage of CIE standard observer color matching functions (see Appendix B.3), the global visualizations mainly consists of the two proposed **expressive spectral error visualizations** for global guidance to identify pixels for further local investigations. The local visualizations allow the analysts to explore the currently selected pixel to validate the reconstruction, e.g. by exploring the composition of a mixed spectrum. In the reconstruction and composition views, the white line shows the raw spectrum $\vec{s}_{RAW}(x,y)$ and the

blue line/area represents the reconstruction $\vec{s}_{LSU}(x,y)$. The visualization of the residual error $\vec{r}(x,y)$ helps to determine the wavelength range in which errors occur and which quantity they have, if present.

Compared to the previous endmember set exploration widget (cf. Sec. 5.1.2), with its weak point of sequential exploration, here the properties of the endmembers are presented simultaneously in one view. Here, the view shows all coefficients maps at once to give an overview in which region which endmember has influence and to what extent. Each map is colored in the respective color of the corresponding endmember, which can be modified and is consistent in all proposed views. Moreover, an endmember instantly can be activated and deactivated within the properties of the corresponding coefficients map. Additionally, the current pixel position can easily be moved to the position of the dataset where the endmember was found by clicking onto the pin icon of a coefficient map. By this, the spectrum of an endmember can be easily found for further exploration in one of the other views. Finally, the visual complexity of this view can be reduced by showing only information, e.g. coefficient maps, of endmembers which have influence in the currently observed pixel.

All visualizations allow zooming into details and are linked. Thus, zooming or clicking on a pixel in a global view leads to an direct update in all views. In each global view, the current pixel position is highlighted. The user can visually explore the LSU-result step-by-step to gain insight. Based on this supplementing insights, the user is able to get a more comprehensive impression of the reliability of the current endmember set and can be more focused in the refinement. Thus, a user can directly use the perceived knowledge in case of wrong or incomplete sets in order to refine the LSU-result, by removal or insertion of an endmember.

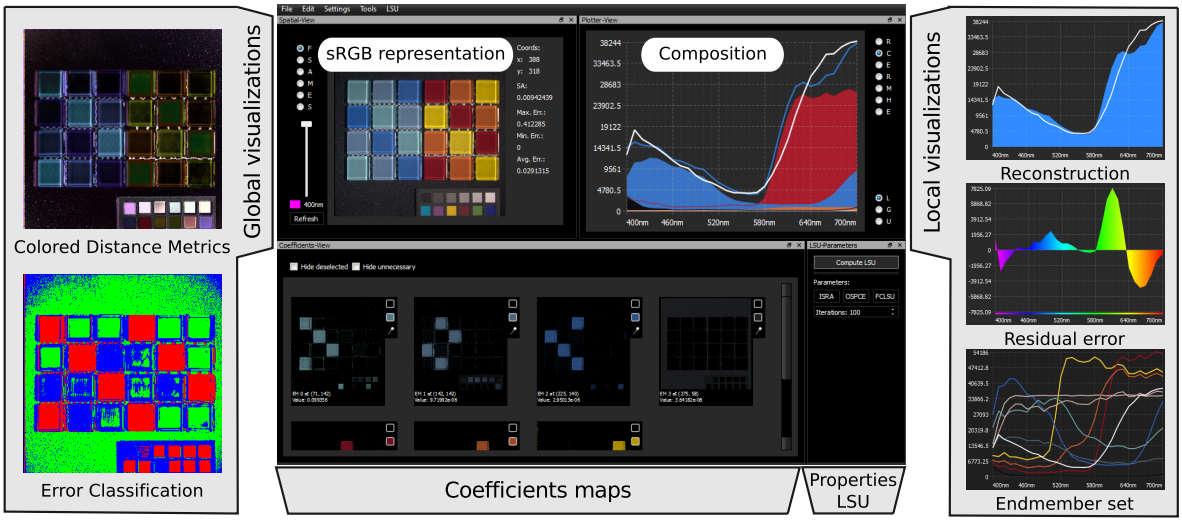

Figure 5.18: Overview of the graphical user interface, that focuses on several linked views, achieved coefficients maps, global spectral error views and per-pixel views for detailed local investigations.

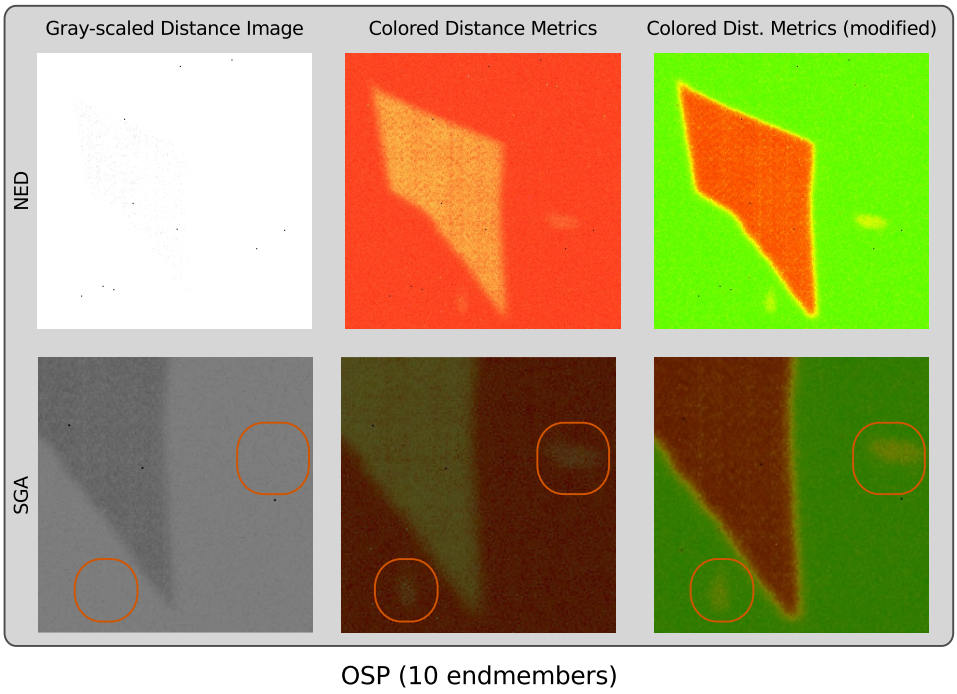

Figure 5.19: The OSP-result for the *Graphene* dataset. Compared to the usual distance images, error values are easier distinguishable in the proposed **colored distance metrics** (SGA images are zoomed in). Moreover, the two different layer thicknesses of graphene can be distinguished in the modified colored distance metrics.

5.2.6 Results

At first usage examples of the presented approach are shown for two domains, CRM and multispectral scene data. Before the limitations are discussed, first, the evaluations of domain experts are reflected.

Usage Examples

Since, the focus is the validation of LSU-results and not the endmember detection algorithms itself, details of the detection process are omitted. Mainly two common methods, OSP and PPI, are utilized in the following. The inverse operation is done by using the implementation of the image space reconstruction algorithm of Sánchez et al. [SMPC10].

Graphene: As already discussed in Sec. 4.3.3, the *Graphene* dataset (cf. Appendix A) contains some imperfections, e.g. peaks because of cosmic rays, that are quite challenging for automatic algorithms. Here, the usage of the proposed outlier masking already allows the direct determination of the constituent spectra. Thus, further interactive refinement by the user can be omitted. However, when assuming that their is no preprocessing available, then the initial result of this dataset is a kind of worst-case scenario for the interactive refinement. As shown

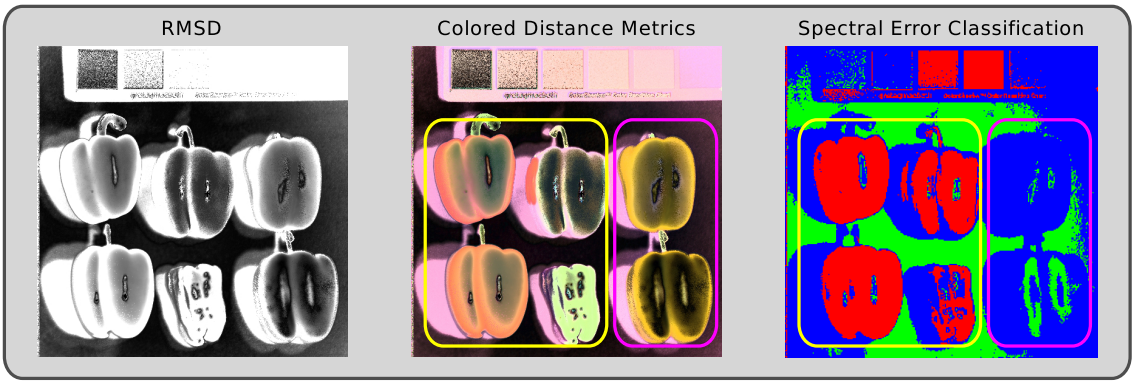

OSP (25 endmembers + added background)

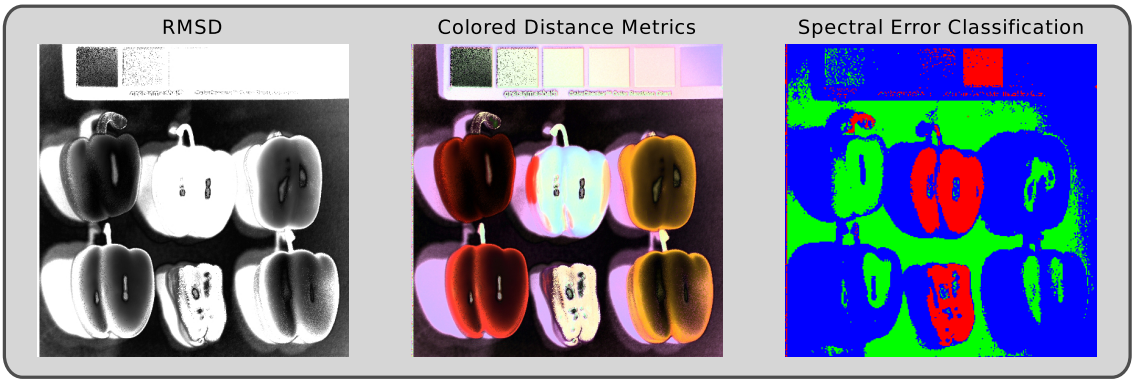

PPI (23 endmembers + added background)

Figure 5.20: Results of OSP and PPI for the *Peppers* dataset, both with an added background spectrum. The interpretation of the results is facilitated by the two proposed global visualizations, **colored distance metrics** and **spectral error classification**, in terms of both, easier discriminability of different residual errors and easier identification of missing endmembers.

in Fig. 5.19, all distance images present high error values, especially for the NED. While two error regions are already distinguishable in the distance image of the SGA, the NED-image reflects a worst-case, where no errors are distinguishable. Anyway, the interpretation of both distance images are improved by the combination with our proposed **color signatures**. As a result of this, different error regions are getting visible in all **colored distance metrics**. Also two other small error parts, see marked areas of SGA, are now noticeable. So far, the two different thicknesses of the graphene are not distinguishable with the default **color signatures**. But, this issue can be addressed by modifying the **color signatures** by transfer functions, also shown in Fig. 5.19. By means of the expressive spectral error visualization, the shortcomings of the automatically estimated set of endmembers (applying OSP) can be easily noticed. Thus, the result can be refined from ten to only three spectra. The quality improvement of this refinement was already shown in Sec. 4.3.3 in the context of the outlier masking.

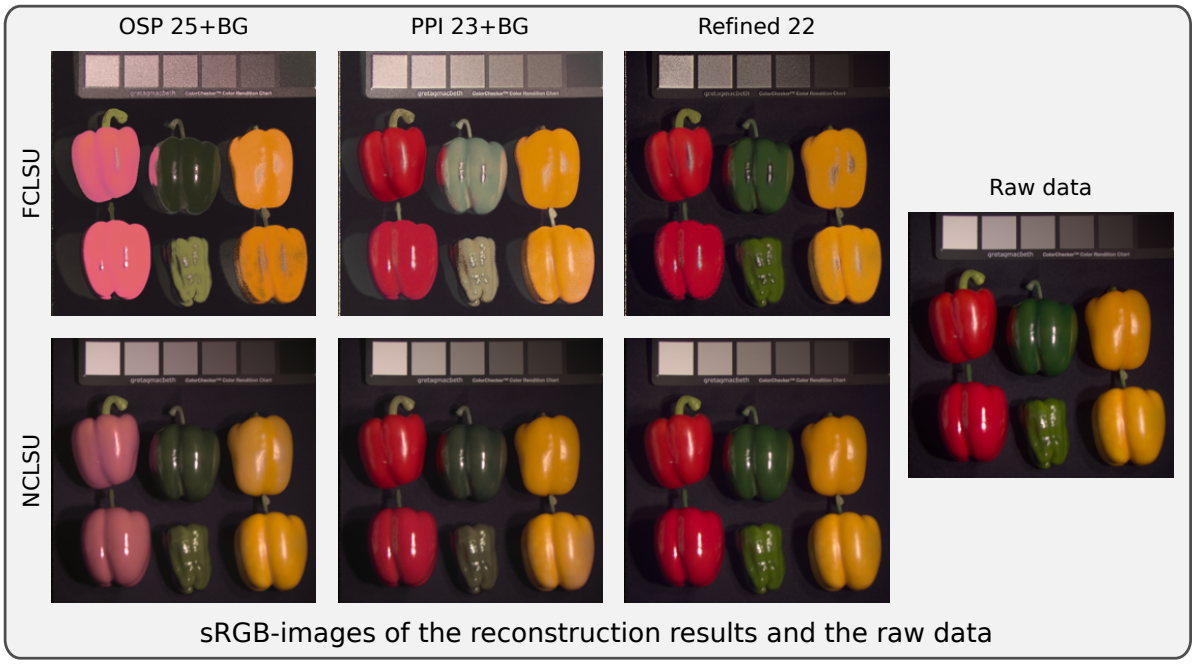

Figure 5.21: The reconstruction quality is shown by sRGB-transformed datasets of the respective results and the raw data. As can be seen, mainly the green peppers are not well represented in the initial results of OSP and PPI. In case of OSP, also the red peppers are not satisfactorily reproduced.

Peppers: The *Peppers* dataset (cf. Appendix A) mainly consists of two red, two green and two yellow peppers. For each color, one artificial pepper was used. Figure 5.20 shows the initial reconstruction quality for both algorithms, PPI and OSP. Note, in both cases, the algorithms have not found the dark background. In order to facilitate the upcoming explanation of the verification process, a corresponding background-spectrum was manually added to the set of endmembers. In both depicted results the discriminability of the error values is improved by the proposed **colored distance metrics**. Moreover, the spectral error classification view supports the analyst in the determination of missing constituent spectra. Comparing the marked areas of the OSP-result, it is getting obvious that not all high error values are missing endmembers. On the one hand, the magenta colored area shows error values that are quite high, but the reason for this is the endmember variability and not a missing constituent. On the other hand, the errors in the yellow area are due to missing endmembers, which are distinguishable in the **colored distance metrics**. The quality of the reconstructions, based on the OSP-, PPI- and the refinement, are illustrated in Fig. 5.21 by showing the sRGB transformed reconstructed multispectral datasets. In order to judge the quality, also the sRGB-image of the raw data is included.

Evaluation

The approach has been demonstrated to four experts from the domains of multispectral data processing and sensor development. Here the approach was applied in the context of three application areas, multispectral scene analysis, remote sensing and CRM. Each expert was asked to judge the functionality and usability of our approach to verify the completeness of endmember sets and to indicate areas that need further research. Their comments are summarized in the following paragraphs by pointing out the pros and cons.

The evaluation of the reconstruction quality of the spectral unmixing focuses on the completeness and quality of an endmember set. Furthermore, there are also questions about the inverse operation itself, when for instance the reconstructed spectrum differs only in a constant magnitude from the raw spectrum, e.g. in case of endmember variability. The domain experts stated, that such issues can be perceived very well by the guided and simultaneous exploration of local and global views.

In general, the experts like the opportunity to see the several distance metrics juxtaposed to instantly compare them. Also, the emphasizing of similar distances with **color signatures** has proven to be helpful in the exploration process. Moreover, the definition of transfer functions to focus on errors of interest has also been rated as good.

Additionally, most of the experts like the consistent coloring of the endmembers, which facilitates the insight, e.g. to be able to see in which area which endmember is present. However, some experts would be interested in a stronger quantification by numbers to see how much influence an endmember has with respect to the entire dataset. But, since the common distance metrics have problems to achieve comparable quantification results, up to now, it is an open question how this can be solved. Also, the sparsity of coefficient maps cannot be used meaningfully, since materials also can be present only in a comparably small area of the data.

Limitations

As shown before, the common grayscaled distance images can be improved with our proposed **color signatures** in order to achieve **colored distance metrics**. Here, residues are roughly subdivided into three intervals. It may happen that different errors can produce comparable colors, when e.g. one error has deviations in the first part of an interval and another error has deviations in the second part of the same interval, while the remaining parts of both errors are comparable. The analyst can still notice the wavelength range of interest, but can not distinguish the different errors so easily. Here, the manually modification of the **color signatures** by TF design in the error trend view can be used to enhance the analyzes and highlight the affected bands separately. However, a complete change of TFs may result in a less intuitive color representation, especially when mixed colors are applied as representative TF-colors.

5.2.7 Summary

This section has introduced two global **expressive spectral error visualizations** in the context of SMA to addresses the limitations of the complementary visualization, see Sec. 5.1. Thus,

to mainly improve the efficiency of the guidance process in order to more focused identify specific spectra for local exploration. **Color signatures** are used to enhance common distance metrics, so-called **colored distance metrics**, in order to reduce the ambiguity of distance values by coloring. Furthermore, the **color signatures** are freely adjustable by the design of transfer functions, based on residual statistics. In addition, the global error impressions are facilitated by a **spectral error classification** view. All these means help to make correlations visible, thus guide a user more focused to interesting pixels for detailed local investigation. The benefits of the introduced expressive error visualization concepts have been demonstrated by usage examples of two domains. Moreover, a discussion of limitations and an evaluation of domain experts that state the pros and cons of the approach have been included.

5.3 Radviz-based Multispectral Image Segmentation

Different from the previous discussion of visual analysis methods in the field of SMA, this section presents another visual analysis concept which has the aim to achieve segmented multispectral images in a semi-automatic manner in order to get insights into the topology of the data. Here, the analysis concept is mainly based on the multivariate visualization Radviz [HGM*97] (cf. Sec. 1.2.3).

The remainder of this section is organized as follows. Sec. 5.3.1 presents the problem statement. A conceptional overview of the approach is presented in Sec. 5.3.2, while the technical details are discussed in the sections 5.3.3 and 5.3.4. The results are presented by usage examples for multispectral imaging in Sec. 5.3.5.

5.3.1 Problem Statement

The aim of the here discussed approach utilizes, as Gerbil [JA10] (see Sec. 2.3), a multivariate visualization technique in order to achieve a segmented multispectral image, thus to get insights into its topology. But, in contrast to Gerbil [JA10], the here presented method utilizes the multivariate visualization Radviz [HGM*97] instead of PCP [ID90]. As described in the fundamentals 1.2.3, Radviz is a lossless visualization, which is conceptional comparable to PCP. The main difference is that in Radviz the n-dimensional attributes of the dataset are equidistantly placed on a circle instead of a straight coordinate. A n-dimensional element of a dataset then is represented by a 2D-point in the space of the circle. Comparable to PCA, similar elements should appear close to each other, thus will form clusters. According to Hoffman [HGM*97] this method preserves certain symmetries of the multidimensional dataset and allows an intuitive representation. Therefore, the intrinsic clustering of comparable spectra in a Radviz plot is utilized in the here discussed approach to achieve a **semi-automatic segmentation** of a multispectral image. However, Hoffman states that clusters with dissimilar characteristics can, partially, overlap which can harm the interpretation of a multivariate visualization. Furthermore, for high-dimensional datasets, huge numbers of projections are possible which can lead to a stunning evaluation task in interactive analysis [AEL*10]. In this context, Albuquerque et al. [AEL*10] recently have proposed a quality measure to achieve

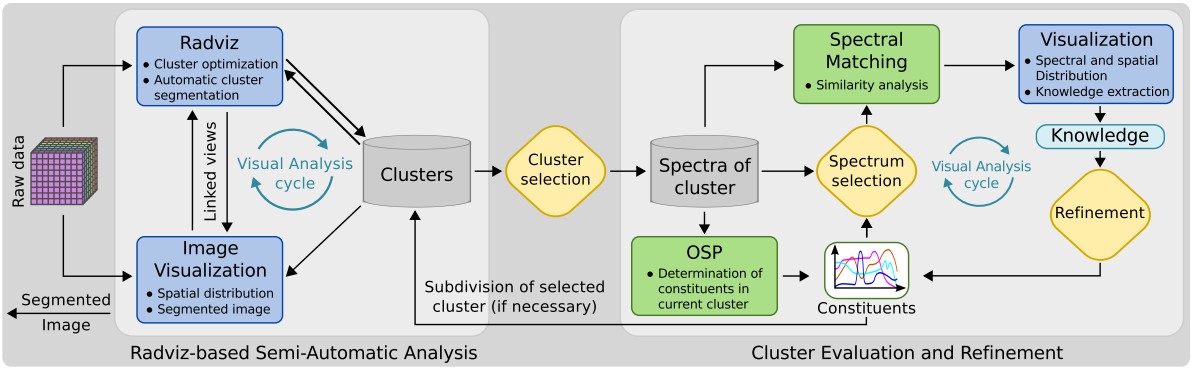

Figure 5.22: Conceptional overview of the Radviz-based image segmentation approach.

improved placements of elements for multivariate visualizations like Radviz. The here discussed approach also utilizes this proposed method in order to initially achieve a good cluster distribution. But, since automatic methods may fail, additionally, also a **cluster evaluation view** is presented in order to manually examine and to refine the clustering, i.e. the segmentation, of the image. Here, the visual complexity is a major challenge, thus an initial reduction of the complexity is required in order to reduce the amount of user interaction. Since the complexity depends on the number of spectra in an observed cluster, it is the goal to provide a user with a first selection of constituents of a cluster. As discussed previously in the context of SMA, prominent algorithms that determine the constituent spectra of a multispectral dataset are endmember extraction algorithms, see fundamentals 1.2.2. Therefore, the here explained approach applies OSP in the cluster evaluation in order to determine the set of constituents in a observed cluster, thus to reduce the visual complexity by the initial selection of constituents. Note, that OSP is only be applied to get an assisting guess and not to achieve an unmixing result later on.

5.3.2 Conceptional Overview

The aim of the here presented approach is to assist a user with the interactive evaluation and segmentation of multispectral images in order to provide easier access to the wealth of information. The visual complexity of multispectral data initially is meaningfully reduced by automatic cluster segmentation in the Radviz plot to provide a good starting point for the user based evaluation part. An overview of the whole approach is illustrated in Fig. 5.22. As can be seen, the approach is divided into two parts:

1. *Radviz-based Semi-Automatic Analysis:* A Radviz plot is linked with an image-based visualization. Where the image shows the connection between individual pixel areas [PvdH01]. Beside manual brushing of pixels in both views in order to show corresponding elements, also an automatic segmentation of clusters in the Radviz view is included.

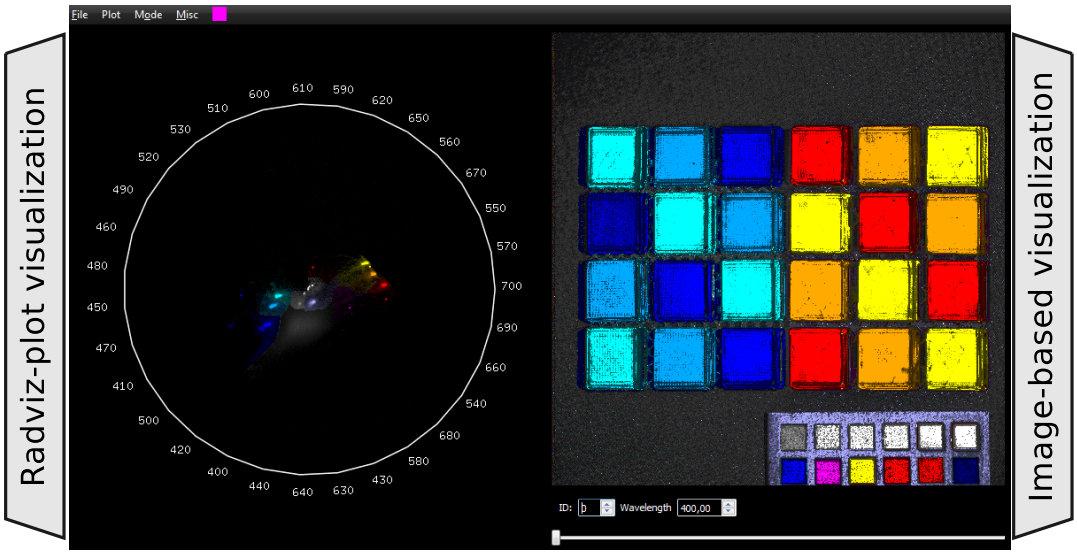

Figure 5.23: Overview of the graphical user interface of the first part consisting of two juxtaposed and complementary views: a Radviz plot and a image-based visualization.

2. *Cluster Evaluation and Refinement:* The cluster evaluation view shows automatically determined constituent and/or freely chosen constituent spectra of the cluster in a spectral plot. Furthermore, the nearest neighborhood of each constituent can be evaluated in order to show spectral correlation in the spatial area.

The workflow description is as follows: The first part gives an overview of the cluster-based segmented multispectral image. Furthermore, it is possible to express the standard deviation of the clusters by the color-coding to draw the attention of a user to particular clusters of interest. Desired clusters can be evaluated meaningfully and refined to improve the segmentation of the dataset. The details of both parts are discussed in the upcoming two sections.

5.3.3 Radviz-based Semi-Automatic Analysis

As described before, this part consists of two juxtaposed and complementary views: a Radviz plot and an image-based visualization (cf. Fig. 5.23). Here, the focus is the initial segmentation of a multispectral image. Before the two associated main issues are discussed, consisting of segmentation and the coloring of the pixels and clusters, first the details of the Radviz generation are explained.

Radviz plot The Radviz plot is generated as explained in the fundamentals 1.2.3. But, in addition to the common way, the recently presented method of Albuquerque et al. [AEL*10] is applied to best possibly reduce the overlap of clusters in an automatic manner. The authors propose a greedy incremental optimization to improve the placement of elements in Radviz (see Alg. 4). Since this process is a greedy method and the maximum intensities of a spectrum have the most influence in the placement of the points $\mathbf{p}(x,y)$, the dimensions of the dataset are

sorted according to the maximum intensities before the optimization. Therefore, the sorting ensures that the dimensions with higher influence are processed first.

Algorithm 4 Optimized placement of spectra in Radviz

```
Initially a plot is created based on the first three dimensions
while not all dimensions are processed do
    Take the next dimension
    Extend the previous plot
    Create all possible plots
    Keep the plot with the highest number of clusters
end while
```

Segmentation of the dataset is achieved by brushing in the Radviz plot or in the image-based visualization. Furthermore, an automatic segmentation of clusters based on the Radviz view is allowed. Here, the Radviz plot is subdivided into a virtual grid in order to determine clusters by the evaluation of the corresponding point densities of the grid cells. All grid cells are sequentially processed in order to determine the clusters of the Radviz plot (see Alg. 5). Tests have shown that the resolution of the virtual grid should have twice the image resolution in order to achieve good clustering results. For instance, when an image has the resolution 128×128 then the proposed resolution of the virtual grid is 256×256.

Algorithm 5 Cluster-detection in the Radviz plot

```
for all virtual grid cells do
    if density of cell (i, j) > user threshold then
        Consider the first local neighborhood of (i, j)
        if neighbors are related to a cluster then
            Select the neighbor with the most comparable density value to (i, j)
            Assign (i, j) to the cluster of the selected neighbor
        else
            Define a new cluster
            Assign (i, j) to the new cluster
        end if
    end if
end for
```

Coloring is achieved by brushing or assignment of default colors to already determined clusters. As default, the intensity of colored segments (pixels/points) represent the corresponding cell density (number of $\vec{s}(x,y)$ in a cell). Moreover, the density scale can turned off to focus on the segmented regions which may be hard to perceived because of a lower cell density. The coloring also can be applied to single bands or the average image of the cube.

Beside the coloring of the segments, also two more coloring methods, variance- and PCA-based, are made available:

Variance-based coloring is appropriate when clusters are already found. Here, the aim is that a user easily can determine clusters of major interest by the visualization of the standard deviation of each cluster. Therefore, for each cluster j the standard deviation of the enclosed spectra is computed

$$\sigma_j = \sqrt{\frac{1}{m_j}\sum_{i=1}^{m}\left\langle \vec{s}_{j,i}^{\,\delta}, \vec{s}_{j,i}^{\,\delta}\right\rangle} \tag{5.16}$$

$$\text{with } \vec{s}_{j,i}^{\,\delta} = \vec{s}_{j,i} - \vec{s}_j^{\,avg} \text{ and } \vec{s}_j^{\,avg} = \frac{1}{m}\sum_{i=1}^{m}\vec{s}_{j,i},$$

where $\vec{s}_{j,i}$ are the corresponding spectra and m_j is the number of spectra in cluster j. The resulting σ_j are color coded in an overlay-map, where green and red means low and high standard deviation, respectively. The colors for the σ_j values between the extremes are appropriately interpolated between red and green, e.g. a value of the middle range appears in a yellow tone (cf. Fig. 5.26).

PCA-based coloring can be applied in addition to the techniques described above and for two reasons. First, to provide an initial overview of the data, when users want to segment the dataset mainly by brushing. Second, to assess the result of the clustering in comparison to this default multispectral visualization technique, that already resembles the spectral similarities of the data. To do so, both views are colorized based on the PCA-based false-color image, which is generated in the same manner as described before (cf. Sec. 5.1.1).

5.3.4 Cluster Evaluation and Refinement

The second part of this approach is dedicated to the detailed evaluation of the individual clusters, e.g. clusters with a high standard deviation. This evaluation is introduced for two reasons: First, to gather more local knowledge of the data, i.e. spectral and spatial distribution in the cluster. Second, to refine clusters by subdivision, where the automatic optimization of the Radviz clustering has failed. In the following, the main aspects of this view,

- automatic reduction of visual complexity,
- spatial and spectral distribution of constituents,
- and refinement by subdivision,

are described.

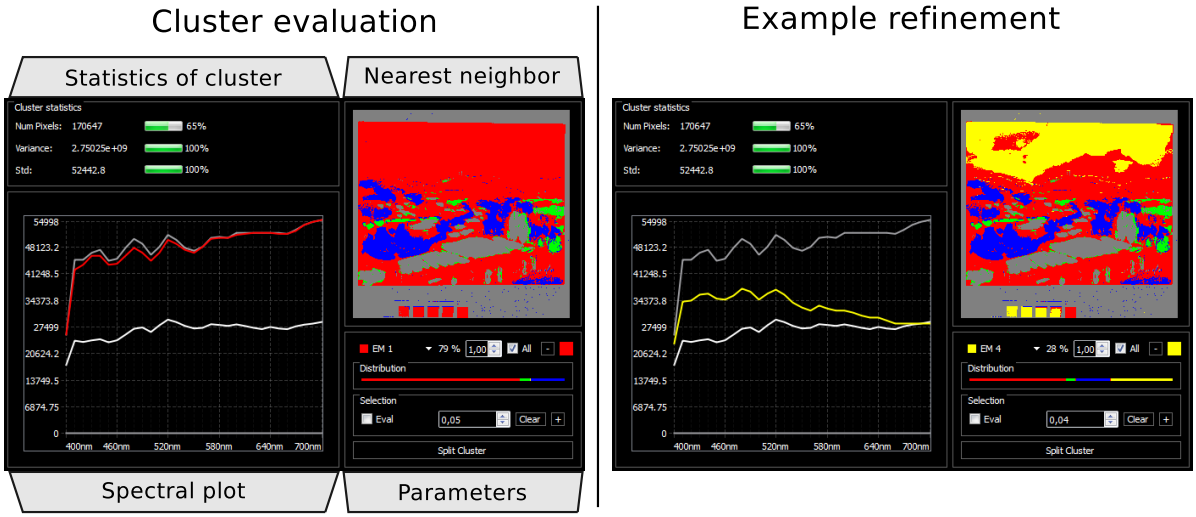

Figure 5.24: Overview of the cluster evaluation view. This example shows the aforementioned problem that distinct spectra can lead to overlapping clusters in the Radviz plot, which consequently are considered as one single cluster. As can be seen in the left image, in such a case a proper automatic segmentation of an image is prevented. However, the proposed cluster evaluation view allows the subsequent evaluation and refinement of such a cluster. Here, the evaluation is supported by the reduction of visual complexity based on the determined constituents of the cluster (highlighted in red, green and blue), thus presents a first guess. Note, pixel that do not belong to the current cluster are gray-colored in the nearest neighbor view. In the right image the initial set of constituents was refined by the manually selection of an additional constituent spectrum (yellow). At the end of the evaluation, the current cluster can be subdivided into subclusters in order to achieve a more precise segmentation result.

Automatic reduction of visual complexity: Constituent spectra of the selected cluster are automatically determined by an endmember extraction algorithm (see fundamentals 1.2.2). As mentioned before, such a search for endmembers is comparable to determine the spectra that define the convex hull. Here, OSP is applied to the spectra of the currently observed cluster and the algorithm terminates when the maximum residuum converges or the number of found spectra is equal to the number of bands n. The discovered constituents are the basis of the detailed evaluation in this view and achieve a first visual reduction of visual complexity to sophisticatedly guide the user in this view.

Spatial and spectral distribution: The **spatial distribution** is visualized by the NN of each constituent, which is achieved by spectral matching (cf. fundamentals 1.2.2) in the same manner as presented in the complementary visualization in Sec. 5.1. In detail, the spectral similarity for each constituent to each spectrum of the cluster is computed, e.g. by applying SAD. For each spectrum of the cluster the constituent with the highest similarity is then assigned as nearest neighbor. Thus, achieving a labeling based on the set of constituents in or-

der to show the spatial distribution within the observed cluster (see Fig. 5.24 nearest neighbor area). For easier comparison of the quantitative influence, i.e. number of nearest neighbors, of each constituent, a distribution bar plot (see Fig. 5.24 parameters area) is displayed which also allows the intuitive selection of constituents. Furthermore, the shortest distance for each spectrum and nearest neighbor pair is stored for subsequent evaluation of the spatial distribution based on user-defined thresholding of the applied similarity range.

A **spectral plot** shows the currently chosen constituent spectrum. For further orientation, additionally, the average, the minimum, and the maximum intensity values are shown in this plot. Especially, the extreme lines (minimum and maximum) are helpful for the comparison of the spectrum of interest directly with the intensity range of all cluster-spectra (see Fig. 5.24).

Refinement by subdivision: With the goal to improve the segmentation of the image by the refinement of clusters where the automatic optimization of the Radviz clustering has failed, i.e. clusters with a high standard deviation, a subdivision approach is used that relies on the determined set of constituents. The determined set of constituents of a cluster can be manually refined by removing constituents or adding freely chosen spectra as new constituents. Here, the decision making process is supported by the means which are described above, e.g. by considering the spatial distribution. After the evaluation, the user decides if subdividing the cluster leads to improved results and should be finally performed. For instance, when the high standard deviation is based only on spectral variability, then a subdivision will not be as significant as when distinct spectral features are mixed in one cluster. When the user comes to the conclusion that a refinement of the cluster is necessary, then the cluster is subdivided into subclusters. Here, the subclusters are defined by the determined set of constituents. In details, each constituent and its associated nearest neighborhood defines one subcluster, thus the subdivision of the initial cluster leads to a refined segmentation of the image. The Radviz plot and the linked image-visualization are immediately updated after the subdivision.

5.3.5 Usage Examples

The Radviz-based visual analysis approach was applied to a RGB test image and two multispectral scene data, *Flowers* and *Watercolors* (see Appendix A). A third result (*Glass tiles*) is already shown in Fig. 5.23.

RGB: A RGB test image was used to present a simple result in Fig. 5.25. Since white and black lead to the same position in the Radviz plot, the initial clustering does not allow to differentiate both colors. Thus the standard deviation of the corresponding cluster is very high. By using the proposed subdivision approach both colors can be separated.

Flowers: In Fig. 5.26, the refined result is compared with the initial- and PCA-based coloring. Comparing the PCA- and both segmentation results, it can be seen that the different flowers, the leafs, the background and the color-checker are segmented more precisely with

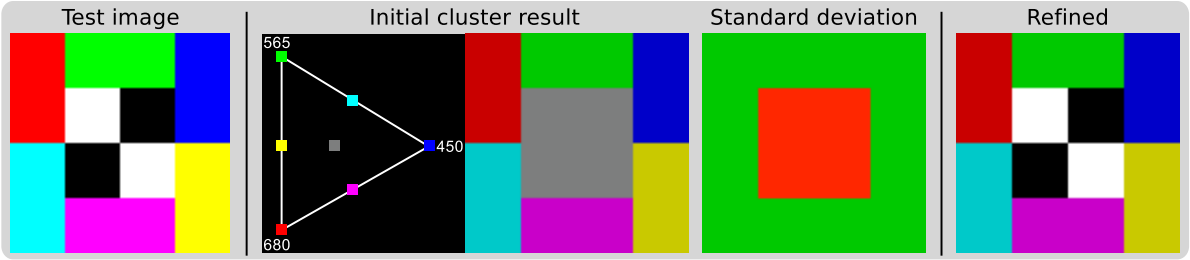

Figure 5.25: The initial and refined result for a RGB test image.

the proposed method. In general, the segmentation of the flowers image is very challenging due to spectral variability, e.g. by shading effects of the flowers.

Watercolors: This example shows another comparison of an initial and refined result. As shown in Fig. 5.27, the details of the watercolors-painting are finer separated in the refined result. Furthermore, the big cluster that represents the frame of the color-checker and the background has been visually merged.

5.3.6 Summary

This section has presented a Radviz-based approach to segment multispectral images in a semi-automatic manner. To achieve a reliable segmentation, the approach enables users to get insight into the spectral topology of multispectral image data, i.e. spatial distribution of spectra. As main part of the approach a meaningful cluster evaluation view was introduced to gain insight to the spectral distribution of a cluster. Based on this views an analyst is enabled, on the one hand, to explore clusters, and on the other hand to refine the clustering (segmentation) by subdivision, if necessary. The usage of the interactive approach was demonstrated with three datasets.

5.4 Summary

In this chapter mainly interactive visualization methods have been presented with the aim to assist analysts in the knowledge gathering process in order to get insights to the essential spectral characteristics of a multispectral image. The main challenge to get access to the wealth of information in multispectral data is the high-dimensionality of the data, which usually prevents to visualize all aspects of the data in one visual representation. Thus, beside automatic analysis algorithms, e.g. for dimensionality reduction, typically an analyst has to steer the visualization process in order to set the focus of the exploration and to reveal the information. Here, focusing on both, SMA and multispectral image segmentation, challenges were discussed and solutions were proposed.

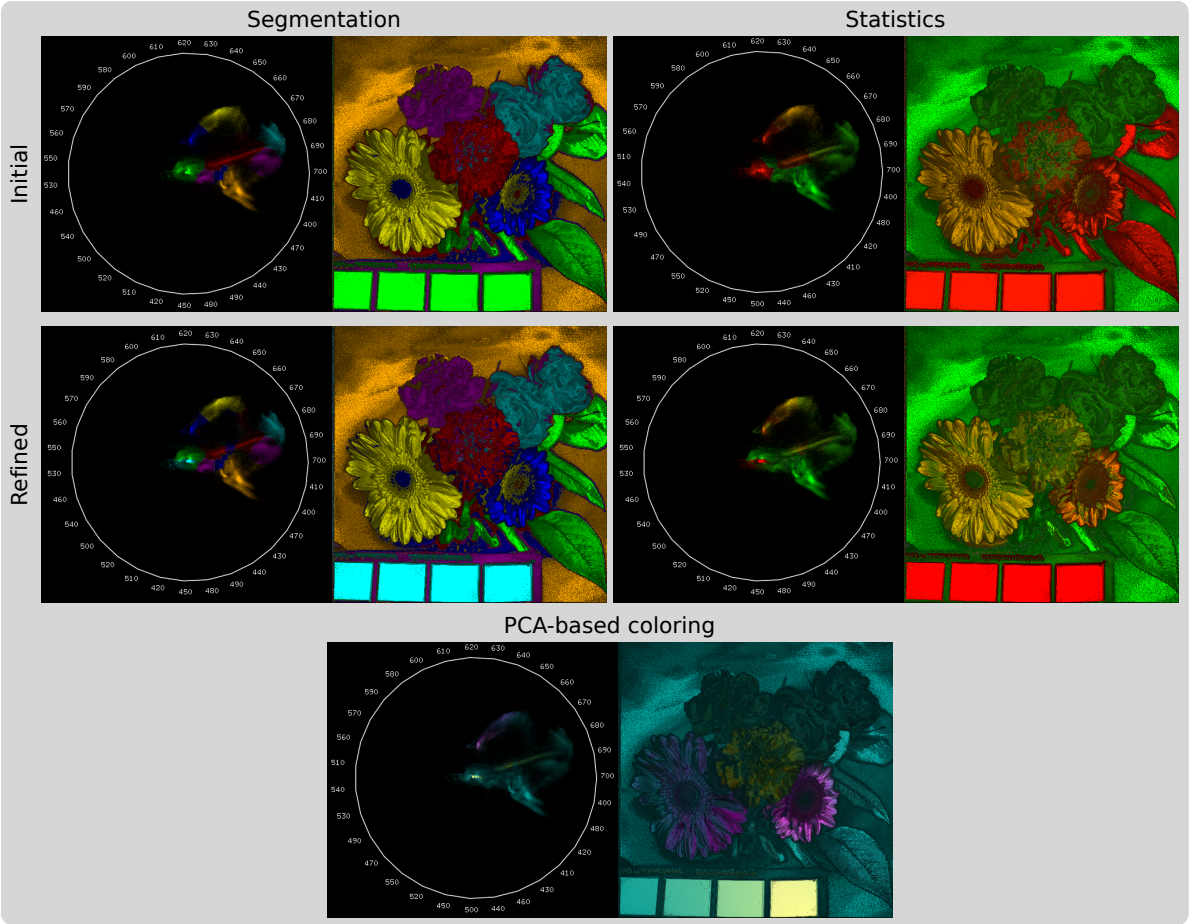

Figure 5.26: Results for the *Flowers* dataset: PCA-based coloring and the initial as well as the refined segmentation result. The remaining deviations are due to different intensity levels of the spectra, i.e. spectral variability.

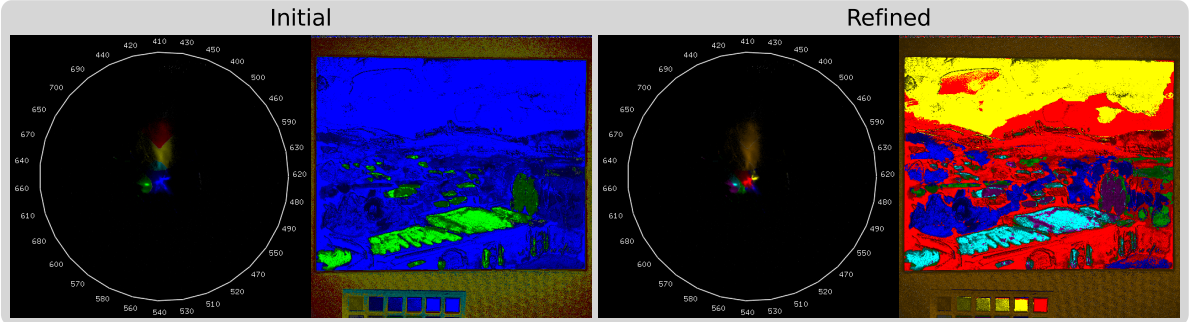

Figure 5.27: Results for the *Watercolors* dataset: the initial and refined result, where the details of the watercolors-painting are finer separated.

In the context of SMA it was shown, that the reliability of an automatically determined set of endmembers can be easily verified by an analyst with proper visualization methods. More essential, it has been shown that there can be circumstances which prevent automatic algorithms to determine a fully reliable set and that in such cases the presented visualization means assist analysts to achieve an improved set of constituents by refinement. Thus, to finally allow a reliable and holistic exploration of multispectral datasets in order to get a very deep understanding, also of subpixel details. Finally, based on these visualization means, the concept of SMA can be applied to a huge variety of application domains.

With the focus to achieve a segmentation of a multispectral image, it was shown that the intrinsic clustering of comparable spectra in a Radviz plot can be utilized to achieve a segmented multispectral image. Again, visualization means help to reveal clusters that can profit by a user-driven refinement of the segmented area in order to progressively enhance the complete segmentation result.

Taking together, the presented visualization means and exploration concepts provide comprehensive and generic tools for the user-driven exploration of multispectral image data. Altogether, both presented approaches make it possible to understand multispectral image data. However, compared to the SMA approach, the insights by the segmentation approach are very limited because of the missing possibility to view and analyze subpixel details.

Chapter 6

Application Example

The search for a specific target spectrum in multispectral datasets is a very common analysis task in multispectral data analysis. This search is done, for instance, to see whether the target signature is present in the data or not. Moreover, when a signature is contained in the data, then an analyst typically is interested in which areas the target is present and with which magnitude.

Before different analysis strategies are demonstrated in the following application scenario, the section first describes the used data and the analysis goal.

6.1 Application Scenario

In this application example, an domain expert was interested to see in which areas of a measured dataset the energetic material RDX is present. Here, the dataset and a reference spectrum of RDX were acquired by the utilization of THz time-domain spectroscopy, see [FG88] for more details about this acquisition method. The dataset has a spatial resolution of 26×26 and covers a frequency range of 0.23–1.92 THz (~156–1289μm) with 30 bands. Moreover,

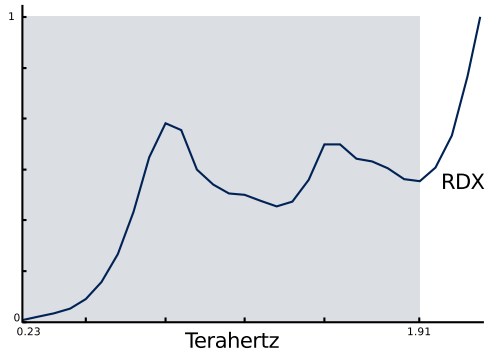

Figure 6.1: The measured reference spectrum of the energetic material RDX. The marked region shows the characteristic area.

the dataset mainly consists of a substrate and a sample of RDX. For the substrate, a polymethacrylimide rigid foam was used, which is very common, since it has remarkable dielectric properties, e.g. an extremely low refractive index and a low absorption in the range from 0.1 to 2.0 THz [RIS*04]. The reference spectrum of the RDX can be seen in Fig. 6.1, which is based on the measurement of a RDX sample that was not embedded in a substrate, but, was created by a pressing process to achieve a plane parallel surface.

Spectral Matching Since the task was to determine in which areas RDX is presented in the dataset, first the spectral similarity between the reference and each pixel of the dataset was computed. The results for SAD and SID are shown in Fig. 6.2. In this particular case, the expectations of the domain expert were not fulfilled by the results of the spectral matching. Because, surprisingly, the lower distance values correspond to the substrate, instead to the RDX. Further analysis with the domain expert have revealed several issues for this behavior:

1. The peaks of the RDX in the dataset are more narrow than in the reference.
2. The peaks are slightly shifted.
3. In large parts of the dataset, the RDX-spectra are mixed with the substrate. Also compare with the PCA-result in Fig. 6.2, where the third principal component shows a quite homogeneous result.

While the shift of the peaks could be manually corrected, the other two issues prevented a successful spectral matching. Beside the general challenge of matching spectra of different measurements (cf. Sec. 1.2.2), e.g. based on reference libraries, this example mainly shows the importance of expert knowledge during the analysis. Without this knowledge, an analyst may assume that RDX is not present in the data. Anyway, it was decided to analyze the dataset in the following without the reference spectrum. Since one of the reasons is the mixture of the substrate and the RDX the focus of the following discussion is on the SMA. But, before this discussion, first a short overview of multispectral image segmentation results is given to provide a complete impression.

Multispectra Image Segmentation In Fig. 6.3 the results of the before presented Radviz-based approach for multispectral image segmentation are shown. As can be seen, the initial result of the plot does not allows to discriminate both materials as good as in the plot with the optimized ordering of the bands. The close-ups with different colorings show the successful distinction of both materials. The reliability of this differentiation is confirmed by the variance-based image, which shows no major deviations in the both clusters. Comparing to the PCA-result of Fig. 6.2 and the PCA-based coloring of the plot, reveals the positions of the pixels (yellow and cyan colors) which are corresponding the corona like ring structure, which is visible in the second principal component. According to the domain expert this structure is due to refraction of the light on the border of both materials. The bottom row of the figure shows the automatic segmentation results for both, with and without weighting by the cell

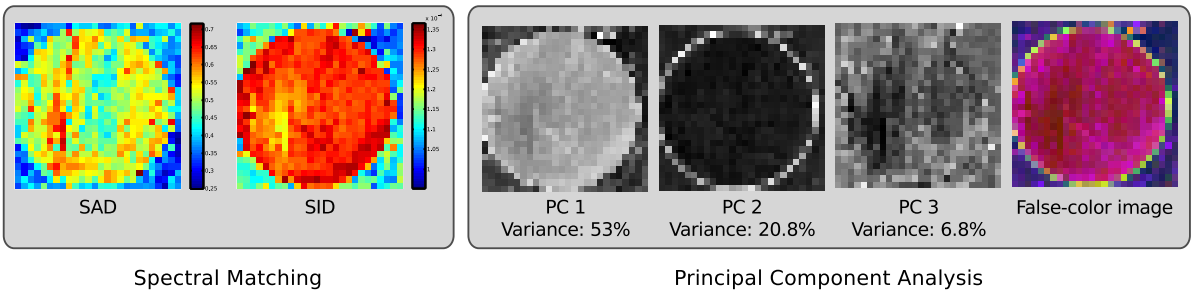

Figure 6.2: Results of the spectral matching and PCA.

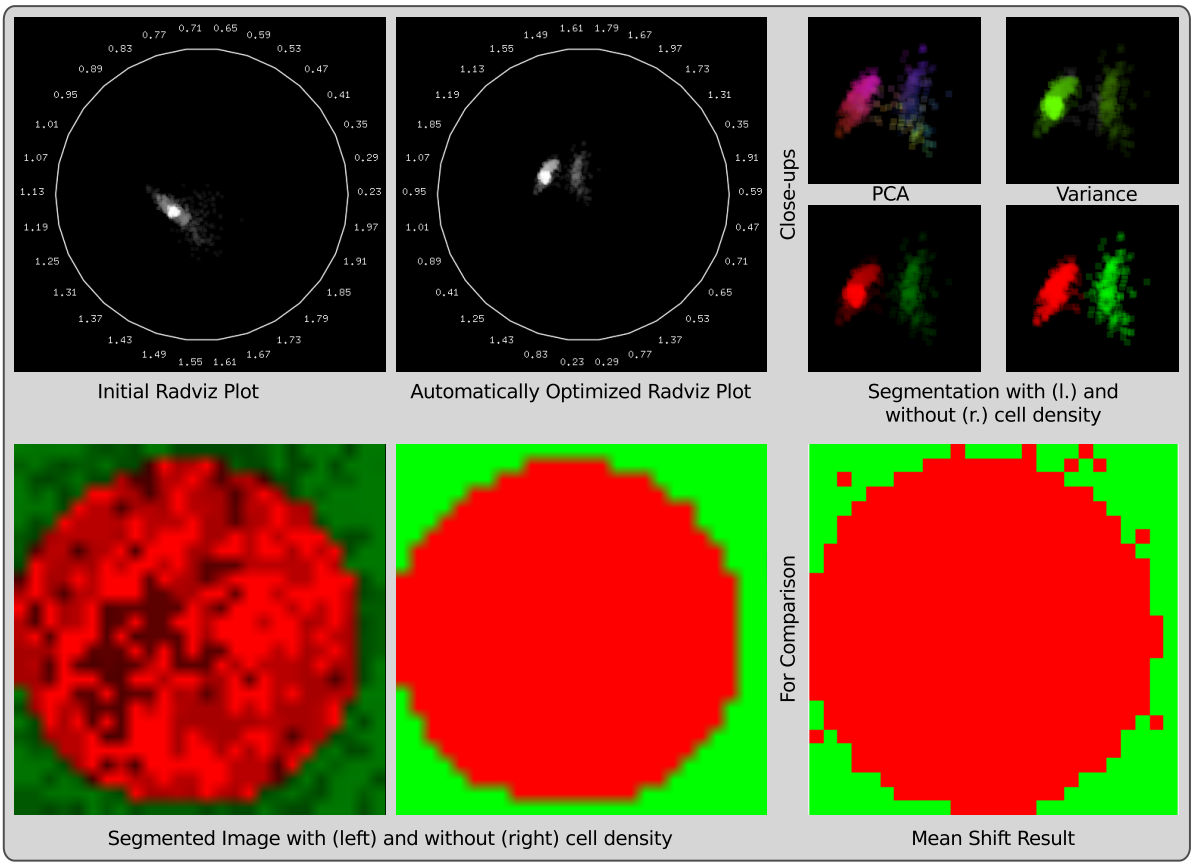

Figure 6.3: Radviz-based segmentation result in comparison to the result of the Mean Shift algorithm in the bottom row. The corresponding Radviz plots are in the top row and demonstrate the influence of the optimization for the placement of elements. Moreover, different colorings are shown as close-ups.

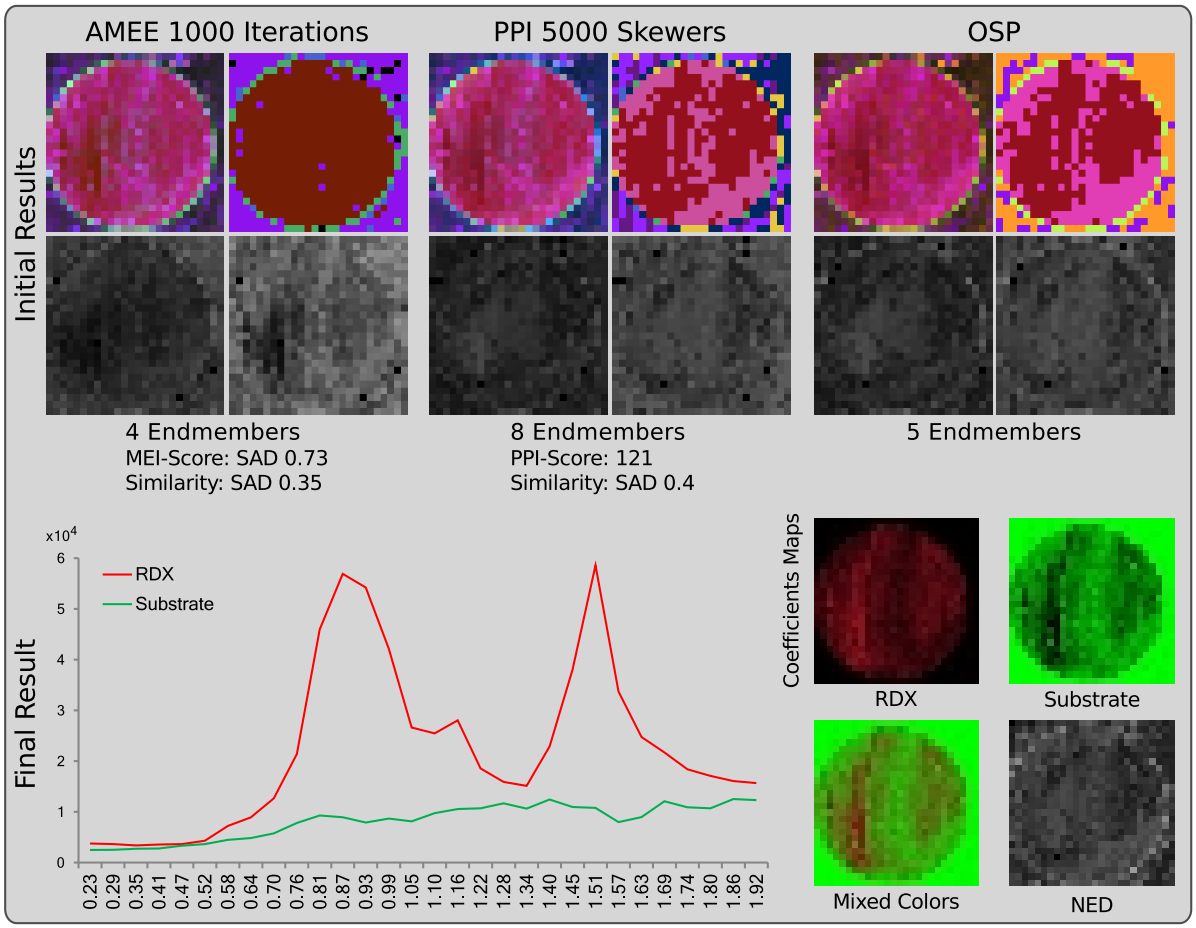

Figure 6.4: LSU results. The top row shows a comparison of the achieved initialization results of AMEE, PPI, and OSP by their corresponding complimentary visualizations. Below the final LSU-result is depicted, which was achieved by manual refinement and based on the expert knowledge.

density (cf. Sec. 5.3.3). As can be seen, the activated cell density reveals areas with lower density, which show some similarities to the results of the spectral matching and the PCA-result in Fig. 6.2. Finally, the Radviz-based segmentation result is compared to a unsupervised result of the nonparametric Mean Shift algorithm (cf. Sec. 1.2.2).

Spectral Mixture Analysis As mentioned before, large parts of the RDX-sample are mixed with the substrate. Thus, after discussing the results of the multispectral image segmentation, now the results of the LSU are presented to achieve a deeper knowledge about the proportion of each material in each pixel. Based on the complementary visualization, Fig. 6.4 shows the best achieved initial results of the three implemented endmember extraction algorithms, AMEE, PPI, and OSP. In comparison to the other algorithms it can be seen, that PPI requires the biggest set of endmembers in order to achieve a proper representation by the constituents.

Note, all distance images are based on NED, where the black pixels are corresponding to the determined positions of the endmembers. The remaining errors are mainly due to noise in the data. As can be seen, all results are capable to represent the corona like ring structure. Anyway, some of the determined constituents are quite redundant and were selected because of noise-based deviations. Moreover, the positions of the constituents are not consistent, but quite comparable. Compared to the before shown PCA-result, which serves as color initialization of the endmembers, the result of PPI resembles the false-color image the best. This is mainly due to the fact that a better representation of the substrate was found. Additionally, especially in the NN-visualization it can be seen, that the substrate is not well represented in the result of the OSP. In summary, the results are quite comparable, but all have their own merits, e.g. AMEE has the lowest number of endmembers. Finally, based on the presented exploration means, the best representatives for the substrate and the RDX were determined by manual exploration and refinement, based on the knowledge of the domain expert. The achieved result of the refinement is illustrated in the bottom row of Fig. 6.4. The proportions of the RDX and the substrate can be seen in the corresponding coefficients maps. Based on the coefficients maps and the resulting mixed colors, the before mentioned mixture of RDX and the substrate is now more obvious. Moreover, the before mentioned difference of the RDX-peaks between the reference and the dataset are getting visible when comparing the plot of the final result and the plot in Fig. 6.1.

6.2 Summary

This chapter has discussed an application scenario where a domain expert was interested to see in which areas of a measured dataset the energetic material RDX, whose signature separately was measured, is contained. Typically for such tasks, first spectral matching was used to compute the distances between the measures reference spectrum and the pixels of the dataset. Due to the expectations of the domain expert, the results were classified as failure. Thus, the dataset itself was analyzed without the reference spectrum in the the following. While the applied segmentation approaches were able to differentiate both materials, the result of the LSU also had revealed subpixel details, i.e. the proportion of each material in each pixel.

Taking together, this application example has shown the importance of expert knowledge during the analysis. Moreover, the domain expert was able to focused explore the dataset to reveal the information of interest.

Summary and Conclusions

Multispectral imaging mainly originates from the domain of remote sensing, but nowadays is applied for various applications, like recycling, medical, food quality, analysis of arts, document verification, biometrics and many more. Due to the high popularity of this imaging technique, there is a high demand for generic solutions to enable the user to get access to relevant information, e.g. constituent spectra, for a large variety of application domains. But, due to the typically high-density of spectral information, usually the interpretation on the one hand, is complex for humans and on the other hand, is time-consuming for computers. Thus, the challenging task of interpretation consequently requires efficient data analysis algorithms and intuitive visualization methods to support the understanding of the data and to finally make use out of them.

This thesis proposed the usage of visual analysis methods which are efficient, intuitive and generic to address the identified challenges. Thus, the main aim of the presented work was to demonstrate that the involvement of the user in the analysis process is possible and feasible in order to achieve good analysis results and to facilitate the interpretation.

For the development of such visual analysis methods, beside the discussion of processing speed, the challenges mainly were posed in two parts, the data analysis and the visualization. Taking together all the discussions, two novel exploration methods were introduced:

Generic Determination of Constituent Spectra Based on the popular multispectral analysis technique LSU, a concept was presented in order to find the best application specific parameterization of endmember extraction algorithms and consequently to explore, assess, and refine the set of endmembers. The exploration and assessment of the results are driven by various assisting visualizations, mainly a complementary visualization and an expressive spectral error visualization for better user guidance. Moreover, the robustness of the automatic algorithms can be improved by an optional outlier masking scheme and the calculation time of inverse unmixing operations can be reduced by the introduced coefficients estimation methods.

Radviz-based Multispectral Image Segmentation With the focus to achieve a segmentation of a multispectral image, it was shown that the intrinsic clustering of certain symmetries in a Radviz plot can be utilized to achieve a segmented multispectral image. As main part of the approach, a cluster evaluation view was introduced in order to gain insight to the spectral distribution of a cluster and to subdivide it, if necessary. Again,

visualization means assist a user to reveal clusters that can profit by such a subdivision in order to progressively enhance the segmentation result.

Moreover, also rather fundamental challenges and concepts of the multispectral data processing are discussed to provide a further understanding of processing in general. Here mainly two aspects were discussed:

Blur in Multispectral Image Data By focusing on plane-based multispectral imaging, reasons for the blur were revealed and a qualitative discussion of noticeable consequences for the data analysis was provided. Moreover, a conceptional proposal for a two step multispectral imaging approach was discussed to compensate the blur in multispectral images.

Similarity Measure in High-Dimensional Space A distance pursuit algorithm was discussed in order to assess the attribute variability, when transforming one vector into a representation of maximum similarity with a target vector. By the consideration of this general method in the context of multispectral images the influence of different similarity measures have been demonstrated. Which has turned out, that the similarity assessment of spectra strongly depends on the chosen metric and the analysis task itself.

Taking together the main aspects of this thesis, the presented visual analysis methods provide comprehensive and generic means for an expert knowledge-driven and guided exploration of multispectral image data. In particular, when achieved automatic analysis results are insufficient because of both, challenging datasets that suffer from imperfections and/or specific analysis tasks, e.g. when an expert is interested in specific information.

Especially the LSU-based visual analysis has turned out to achieve a holistic understanding of observed data. Moreover, based on the resulting constituents, an expert is enabled to more easily identify spectra and spectral characteristics of interest for further research. Certainly, this approach is only able to determine pure constituents in data, when the data contain pure spectra. Here, it may is also worth to consider a subsequent unmixing of the determined constituents based on reference libraries in the future, but, which itself is a challenging task as exemplary can be seen when considering the aspect blur in multispectral imaging or also has been shown in the application example (see Chapter 6).

Another challenge that needs further investigations, also for the domain of library based unmixing, is the possibility of ill-posed mixtures. For instance, consider a spectrum with two peaks. It is unclear, if this spectrum is a constituent or if it is a mixture of two corresponding spectra. Such cases can be meaningfully handled only by experts. Thus, future work should be dedicated to reveal such issues and provide means to constrain the upcoming inverse unmixing operations.

Finally, the here presented methods suggest a generic usage to mainly achieve an unsupervised understanding of multispectral datasets. It has been shown, that the methods successfully can be applied in the context of various application domains, i.e. remote sensing, CRM, typical scenes and also in the terahertz domain. However, the means of these presented approaches may can support from specialized methods for specific applications. For instance, to

include prior knowledge of a specific application domain to initially determine more sufficient sets of constituents.

Appendix A

Datasets

Multispectral Scene Data

Balloons

Spatial: 512×512
Spectral: 31 bands
Range: 400nm–700nm
Device: LCTF

Source: CAVE

sRGB-image

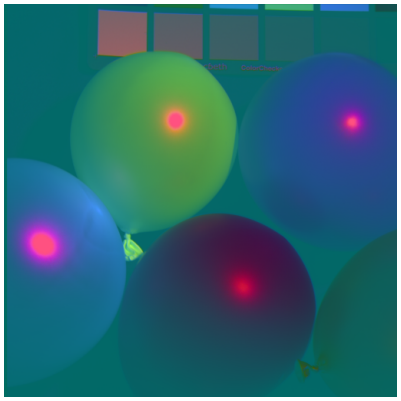

PCA-based false-color image

Cucumber

Spatial: 416×408
Spectral: 51 bands
Range: 450nm–950nm
Device: LCTF

Source: CGMM

sRGB-image

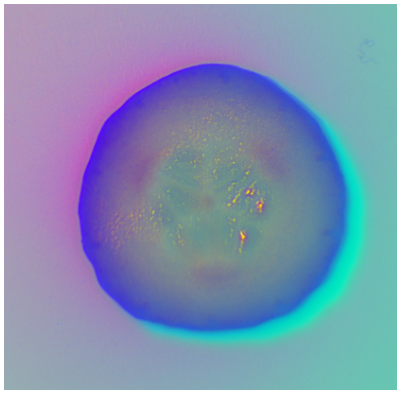

PCA-based false-color image

Egyptian statue

Spatial: 240×450
Spectral: 31 bands
Range: 400nm–700nm
Device: LCTF

Source: CAVE

Note: The dataset was cropped to the area of the statue.

sRGB-image

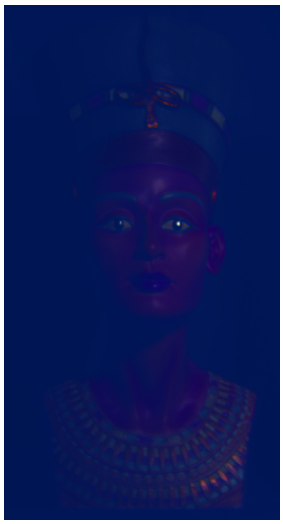

PCA-based false-color image

Flowers

Spatial: 512×512
Spectral: 31 bands
Range: 400nm–700nm
Device: LCTF

Source: CAVE

sRGB-image

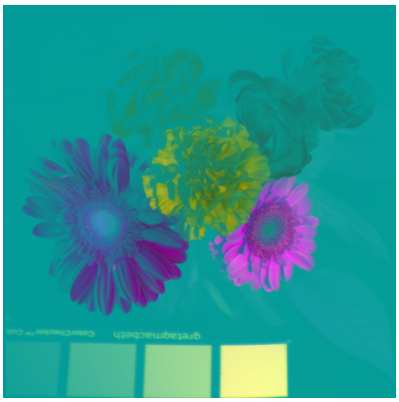

PCA-based false-color image

Glass tiles

Spatial: 512×512
Spectral: 31 bands
Range: 400nm–700nm
Device: LCTF

Source: CAVE

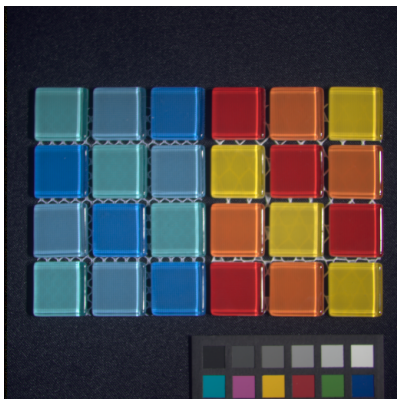

sRGB-image

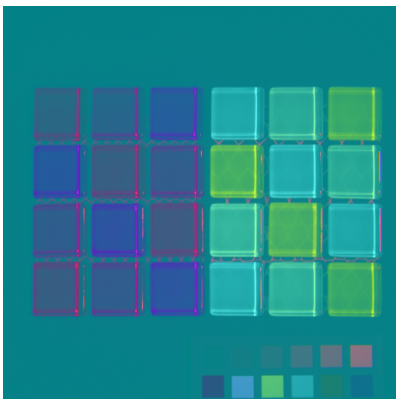

PCA-based false-color image

Lemons

Artificial *(left)* and real *(right)* lemons

Spatial: 512×512
Spectral: 31 bands
Range: 400nm–700nm
Device: LCTF

Source: CAVE

sRGB-image

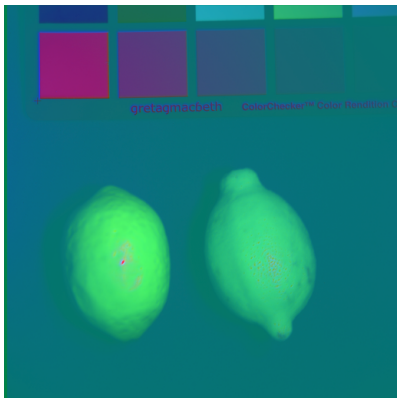

PCA-based false-color image

Peppers

Artificial and real peppers

Spatial: 512×512
Spectral: 31 bands
Range: 400nm–700nm
Device: LCTF

Source: CAVE

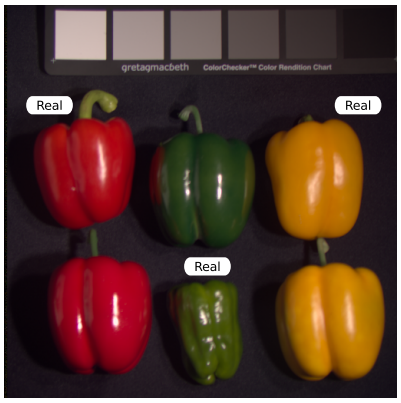

sRGB-image

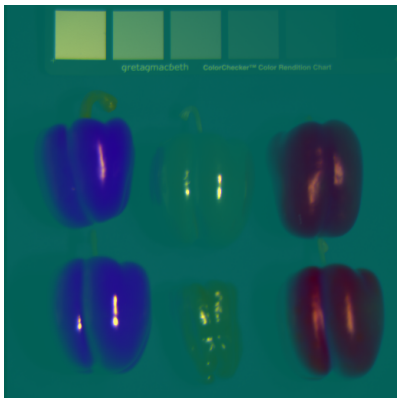

PCA-based false-color image

Watercolors

Watercolors painting

Spatial: 480×376
Spectral: 31 bands
Range: 400nm–700nm
Device: LCTF

Source: CAVE

Note: The dataset was cropped to the area of painting.

sRGB-image

PCA-based false-color image

Remote Sensing

Cuprite

Patch: f970619t01p02_r02_sc03.a.rfl

Spatial: 614×512
Spectral: 224 bands
Range: 370nm–2506nm
Device: AVIRIS

Source: NASA

Note: Bands were reduced to 192, by removing 19 channels that only contain zero data.

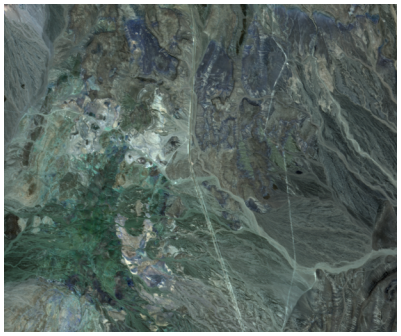

RGB-image

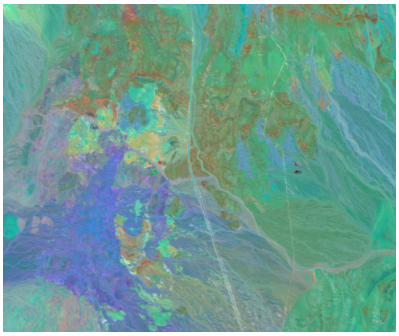

PCA-based false-color image

Washington DC Mall

Spatial: 1280×307
Spectral: 191 bands
Range: 401nm–2473nm
Device: HYDICE

Source: MultiSpec

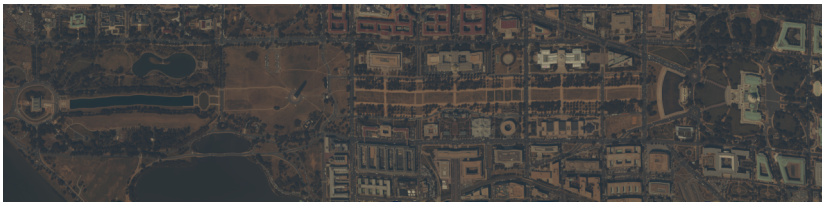

RGB-image

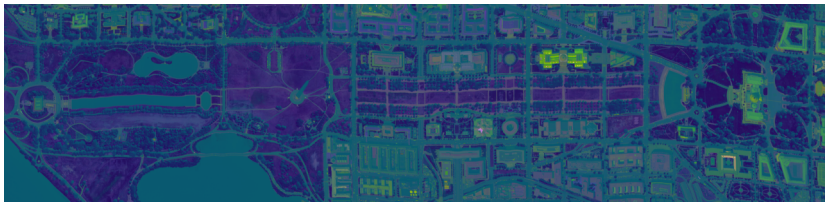

PCA-based false-color image

Confocal Raman Microscopy

Diamond

Diamond and small areas with high fluorescence

Spatial: 512×512
Spectral: 510 bands
Range: 322nm–870nm
Device: CRM

Source: HiFreq

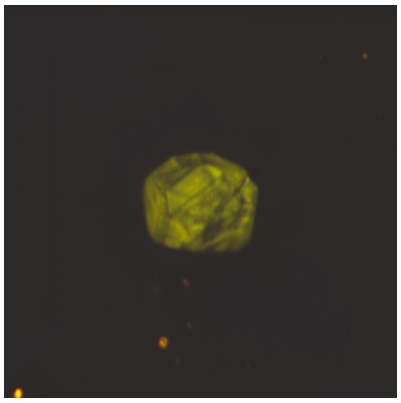

sRGB-image

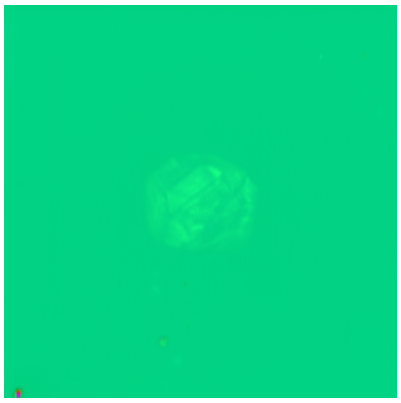

PCA-based false-color image

Graphene

Graphene and silicon as substrate

Spatial: 256×256
Spectral: 510 bands
Range: 322nm–870nm
Device: CRM

Source: HiFreq

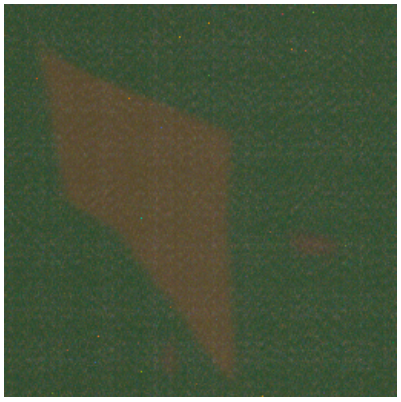

sRGB-image

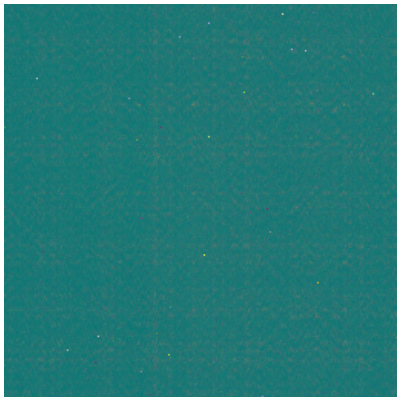

PCA-based false-color image

Artificial Datasets

Concept: Five constituent spectra, i.e. *actinolite, barite, calcite, datolite, dry grass*, were taken from the U.S. Geological Survey (USGS) mineral library and placed at particular positions in the spatial domain. Then, the influence of each constituent was linearly decreased away from the particular position, resulting in a linearly mixed multispectral image cube.

Five Endmembers

Spatial: 100×100
Spectral: 473 bands
Range: 200nm–3000nm

Source: USGS

Note: Four constituents were placed at the four corners and one constituent was placed at the center position.

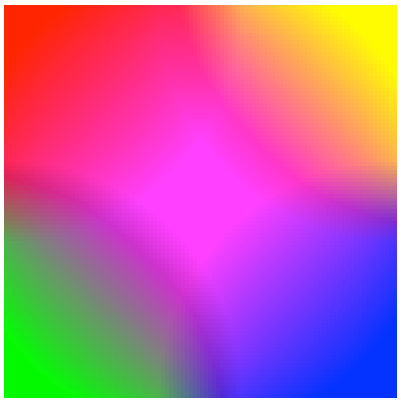

Conceptional image

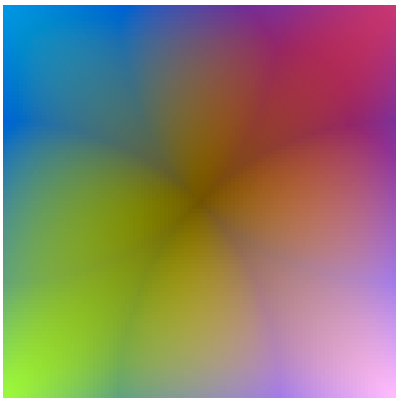

PCA-based false-color image

Four Endmembers

Spatial: 100×100
Spectral: 473 bands
Range: 200nm–3000nm

Source: USGS

Note: In each corner one constituent was placed.

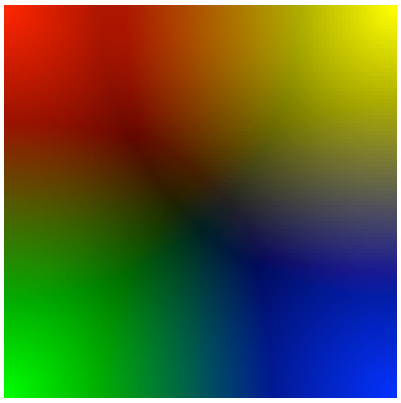

Conceptional image

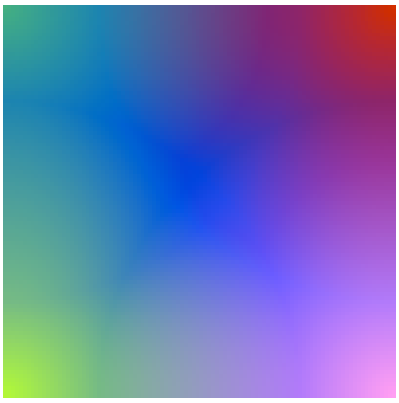

PCA-based false-color image

Sources:

CAVE	`http://www.cs.columbia.edu/CAVE/databases/multispectral`
CGMM	The CRM datasets are kindly provided by the Research Group for *Computer Graphics and Multimedia Systems* at the University of Siegen (`http://www.cg.informatik.uni-siegen.de/en`).
HiFreq	The CRM datasets are kindly provided by the Research Group for *High Frequency and Quantum Electronics* at the University of Siegen (`https://www.hqe.eti.uni-siegen.de/en`).
MultiSpec	`https://engineering.purdue.edu/~biehl/MultiSpec/hyperspectral.html`
NASA	`http://aviris.jpl.nasa.gov/html/aviris.freedata.html`
USGS	`http://speclab.cr.usgs.gov/spectral.lib06/ds231/datatable.html`

Appendix B

Formulas

B.1 Distance Measures

Distance metrics are applied to two n-dimensional spectra (vectors) $\vec{x}$ and $\vec{y}$; $\mu\vec{x}$ and $\mu\vec{y}$ denote the mean values of vectors $\vec{x}$ and $\vec{y}$, respectively; $\langle\cdot,\cdot\rangle$ is the inner product; $\langle\cdot\rangle^2$ is the sum of squares of vector components; $\{\cdot,\cdot\}$ is the cross product of two vectors; sign refers to the signs of vector components; $\circ$ is the component-wise Hadamard product; vector powers operate as powers on each vector component; $\vec{1}$ is the n-dimensional vector of ones;

Spectral Angle Distance

$$\mathrm{SAD}(\vec{x},\vec{y}) = \arccos\left(\frac{\langle\vec{x},\vec{y}\rangle}{\|\vec{x}\|_2\|\vec{y}\|_2}\right) \tag{B.1}$$

Spectral Correlation Angle

$$\mathrm{SCA}(\vec{x},\vec{y}) = \arccos\left(\frac{\mathrm{SC}(\vec{x},\vec{y})+1}{2}\right) \text{ with } \mathrm{SC}(\vec{x},\vec{y}) = \frac{\langle\vec{x}-\mu\vec{x},\vec{y}-\mu\vec{y}\rangle}{\|\vec{x}-\mu\vec{x}\|_2\|\vec{y}-\mu\vec{y}\|_2} \tag{B.2}$$

$\mathrm{SC}(\vec{x},\vec{y})$ yields values between -1 and 1. The final spectral correlation angle is calculated with $\mathrm{SCA}(\vec{x},\vec{y})$ to achieve an angle-like distance [RG05].

Spectral Information Divergence [Cha99]

$$\mathrm{SID}(\vec{x},\vec{y}) = \left\langle \frac{\vec{x}}{\mu\vec{x}} - \frac{\vec{y}}{\mu\vec{y}}, \log\left(\frac{\vec{x}}{\mu\vec{x}}\right) - \log\left(\frac{\vec{y}}{\mu\vec{y}}\right)\right\rangle \tag{B.3}$$

Spectral Gradient Angle

$$\begin{aligned}&\mathrm{SGA}(\vec{x},\vec{y}) = \mathrm{SAD}\left(\mathrm{SG_x},\mathrm{SG_y}\right) \\ &\text{with } \mathrm{SG_x} = \left(x_2-x_1, x_3-x_2, \ldots, x_n-x_{n-1}\right),\ \mathrm{SG_y} \text{ analog}\end{aligned} \tag{B.4}$$

Normalized Euclidean Distance

$$\mathrm{NED}(\vec{x},\vec{y}) = \left\| \frac{\vec{x}}{\|\vec{x}\|_2} - \frac{\vec{y}}{\|\vec{y}\|_2} \right\|_2 \tag{B.5}$$

Root Mean Square Error

$$\mathrm{RMSE}(\vec{x},\vec{y}) = \frac{1}{n}\sum_{i=1}^{n}\left[(\vec{x}_i - \vec{y}_i)^2\right]^{\frac{1}{2}} \tag{B.6}$$

Minkowski distance

$$\mathrm{MD}(\vec{x},\vec{y}) = (\sum_{i=1}^{n}|\vec{x}_i - \vec{y}_i|^p)^{1/p} \tag{B.7}$$

$$\partial\mathrm{MD}(\vec{x},\vec{y})/\partial\vec{y} = -\mathsf{sign}(\vec{x}-\vec{y}) \circ |\vec{x}-\vec{y}|^{p-1} \cdot (\sum_{i=1}^{n}|x_i - w_i|^p)^{\frac{1}{p}-1} \tag{B.8}$$

where real values $p \geq 1$ are allowed.

Pearson correlation [SSVS09]

$$\mathrm{PC}(\vec{x},\vec{y}) = \frac{\{\vec{\mathsf{x}} - \mu_{\vec{x}}, \vec{y} - \mu_{\vec{y}}\}}{\sqrt{\langle\vec{\mathsf{x}} - \mu_{\vec{x}}\rangle^2 \cdot \langle\vec{w} - \mu_{\vec{y}}\rangle^2}} \tag{B.9}$$

$$\partial\mathrm{PC}(\vec{x},\vec{y})/\partial\vec{y} = \left(\frac{\vec{x} - \mu_{\vec{x}}}{\{\vec{\mathsf{x}} - \mu_{\vec{x}}, \vec{y} - \mu_{\vec{y}}\}} - \frac{\vec{y} - \mu_{\vec{y}}}{\langle\vec{w} - \mu_{\vec{y}}\rangle^2}\right) \cdot \frac{\{\vec{\mathsf{x}} - \mu_{\vec{x}}, \vec{y} - \mu_{\vec{y}}\}}{\sqrt{\langle\vec{\mathsf{x}} - \mu_{\vec{x}}\rangle^2 \cdot \langle\vec{w} - \mu_{\vec{y}}\rangle^2}} \tag{B.10}$$

γ-divergence

$$\mathrm{GD}(\vec{x},\vec{y}) = \log\frac{\{\vec{\mathsf{x}}^{\gamma+1}, \vec{1}\}^{1/(\gamma\cdot(\gamma+1))} \cdot \{\vec{y}^{\gamma+1}, \vec{1}\}^{1/(\gamma+1)}}{\{\vec{\mathsf{x}}, \vec{y}^{\gamma}\}^{1/\gamma}} \tag{B.11}$$

$$\partial\mathrm{GD}(\vec{x},\vec{y})/\partial\vec{y} = \frac{\vec{y}^{\gamma}}{\{\vec{w}^{\gamma+1}, \vec{1}\}} - \frac{\vec{x} \circ \vec{y}^{\gamma-1}}{\{\vec{\mathsf{x}}, \vec{y}^{\gamma}\}} \tag{B.12}$$

a choice of $\gamma \in [0;1]$ is recommended [VHS*10].

B.2 Non-Negative Inverse Unmixing Operation

Image Space Reconstruction Algorithm (ISRA) [DWM86] iteratively estimates non-negative coefficients, for any input set of endmembers, per pixel (x,y) and achieves convergence in a finite number of iterations.

$$\alpha_j(x,y)_j^{m+1} = \alpha_j(x,y)_j^m \cdot \frac{\sum_{\lambda=1}^{n} v_j(\lambda)\,\vec{s}(x,y,\lambda)}{\sum_{\lambda=1}^{n} v_j(\lambda)\sum_{i=1}^{q}\vec{v}_i(\lambda)\,\alpha_j(x,y)_i^m} \tag{B.13}$$

Where m is the index of the iteration and again n and q are the numbers of the bands and endmembers, respectively.
Since the nominator of the formula contains the spectrum of the current pixel, which can be considered as an actual measurement, the nominator typically is called the measured projection. The denominator commonly is refereed to as the calculated projection, since it calculates the projection based on the currently estimated coefficients and the input set of endmembers. Based on both projections, the ratio between these quantities is used to multiplicative modify the coefficients.

B.3 Color Matching Functions

The tristimulus **color matching functions** $\bar{x}(\lambda)$, $\bar{y}(\lambda)$, and $\bar{z}(\lambda)$ of the International Commission on Illumination (CIE) are used to transform spectra into colors. Based on the CIE's standard observer, these functions numerically describe the chromatic response and therefore can be seen as spectral sensitivity curves, see Fig. B.1, which yield the tristimulus values X, Y, and Z when are applied to a spectrum

$$X = \int_{380}^{780} I(\lambda)\,\bar{x}(\lambda),\;\; Y = \int_{380}^{780} I(\lambda)\,\bar{y}(\lambda),\;\; Z = \int_{380}^{780} I(\lambda)\,\bar{z}(\lambda), \tag{B.14}$$

where $I(\lambda)$ describes the spectral power distribution. The perceived tristimulus values now can be transformed into an other color space, for instance to RGB

$$\begin{bmatrix} R \\ G \\ B \end{bmatrix} = \begin{bmatrix} 0.41847 & -0.15866 & -0.082835 \\ -0.091169 & 0.25243 & 0.015708 \\ 0.0009209 & -0-0025498 & 0.1786 \end{bmatrix} \cdot \begin{bmatrix} X \\ Y \\ Z \end{bmatrix}. \tag{B.15}$$

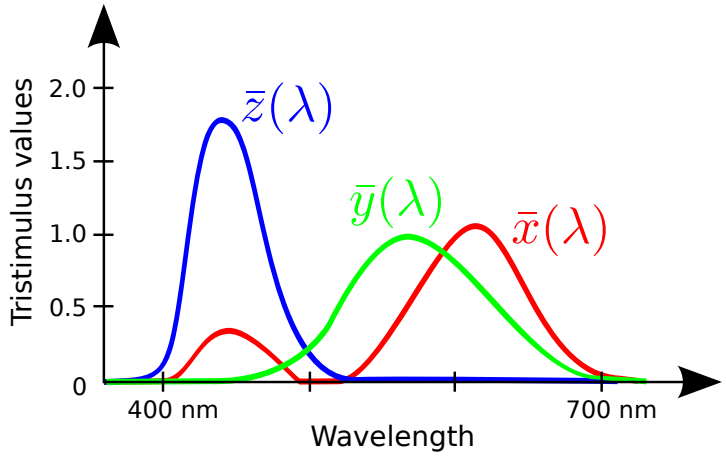

Figure B.1: The CIE color matching functions based on the standard observer.

B.4 Conversion from Radiance to Reflectance

According to the U.S. Geological Survey [U.S11], the conversion from radiance L_λ to reflectance R_λ can be achieved by applying the following equation:

$$R_\lambda = \frac{\pi L_\lambda d^2}{ESUN_\lambda \cos(\theta_s)}, \tag{B.16}$$

where d is the distance between the earth and the sun, $ESUN_\lambda$ is the solar spectral irradiance and θ_s is the sun zenith angle.

Bibliography

[AEL*10] ALBUQUERQUE G., EISEMANN M., LEHMANN D. J., THEISEL H., MAGNOR M.: Improving the visual analysis of high-dimensional datasets using quality measures. In *Proc. IEEE Symposium on Visual Analytics Science and Technology (VAST)* (2010), pp. 19–26.

[AGDJ09] ANDERSON J. C., GOSINK L. J., DUCHAINEAU M. A., JOY K. I.: Interactive visualization of function fields by range-space segmentation. *Computer Graphics Forum 28*, 3 (2009), 727–734.

[AI08] ART-INNOVATION: Underdrawings of paintings. `http://www.art-innovation.nl/index/Nicolas%20Frances.html`, 2008. [Online; accessed 9-July-2013].

[AL97] ACTON S., LANDIS J.: Multi-spectral anisotropic diffusion. *International Journal of Remote Sensing 18*, 13 (1997), 2877–2886.

[AUK*11] AKBARI H., UTO K., KOSUGI Y., KOJIMA K., TANAKA N.: Cancer detection using infrared hyperspectral imaging. *Cancer science 102*, 4 (2011), 852–857.

[BC93] BATESON C., CURTISS B.: A tool for manual endmember selection and spectral unmixing. In *Summaries 4th Annu. JPL Airborne Geoscience Workshop* (1993), vol. 1, pp. 3–6.

[BC96] BATESON A., CURTISS B.: A method for manual endmember selection and spectral unmixing. *Remote Sensing of Environment 55*, 3 (1996), 229 – 243.

[BCA95] BASEDOW R. W., CARMER D. C., ANDERSON M. E.: Hydice system: Implementation and performance. In *SPIE's 1995 Symposium on OE/Aerospace Sensing and Dual Use Photonics* (1995), International Society for Optics and Photonics, pp. 258–267.

[BDN08] BIOUCAS-DIAS J. M., NASCIMENTO J. M.: Hyperspectral subspace identification. *IEEE Trans. Geoscience and Remote Sensing 46*, 8 (2008), 2435–2445.

[BDP10] BIOUCAS-DIAS J., PLAZA A.: Hyperspectral unmixing: geometrical, statistical, and sparse regression-based approaches. In *Proc. SPIE* (2010), vol. 7830, p. 78300A.

[BDPD*12] BIOUCAS-DIAS J. M., PLAZA A., DOBIGEON N., PARENTE M., DU Q., GADER P., CHANUSSOT J.: Hyperspectral unmixing overview: Geometrical, statistical, and sparse regression-based approaches. *IEEE Journal of Selected Topics in Applied Earth Observations and Remote Sensing 5*, 2 (2012), 354–379.

[BG04] BAJCSY P., GROVES P.: Methodology for hyperspectral band selection. *Photogrammetric engineering and remote sensing 70* (2004), 793–802.

[BH65] BALL G. H., HALL D. J.: *ISODATA, a novel method of data analysis and pattern classification*. Tech. rep., DTIC Document, 1965.

[BJ01] BOYKOV Y. Y., JOLLY M.-P.: Interactive graph cuts for optimal boundary & region segmentation of objects in ND images. In *Proc. IEEE Int. Conf. Computer Vision (ICCV)* (2001), vol. 1, IEEE, pp. 105–112.

[BKG95] BOARDMAN J. W., KRUSE F. A., GREEN R. O.: Mapping target signatures via partial unmixing of AVIRIS datas. *Summaries of the Fifth Annual JPL Airborne Geoscience Workshop 1* (1995).

[BL02] BIEHL L., LANDGREBE D.: Multispec: a tool for multispectral–hyperspectral image data analysis. *Computers and Geosciences 28* (2002), 1153–1159.

[BLGK11] BADER J., LABITZKE B., GRZEGORZEK M., KOLB A.: *Biometrics - 2010 Monograph*. Faculty of Biomedical Engineering, Silesian University of Technology, 2011, ch. Multispectral Pattern Recognition Techniques for Biometrics, pp. 87–116.

[BSA10] BRAUERS J., SEILER C., AACH T.: Direct psf estimation using a random noise target. In *Proc. of SPIE-IS&T Electronic Imaging* (2010), International Society for Optics and Photonics, pp. 75370B–75370B.

[BvL05] BROERSEN A., VAN LIERE R.: Transfer functions for imaging spectroscopy data using principal component analysis. In *Eurographics / IEEE VGTC Symp. Visualization* (2005), Brodlie K., Duke D., Joy K., (Eds.), Eurographics Association, pp. 117–123.

[CD04] CHANG C.-I., DU Q.: Estimation of number of spectrally distinct signal sources in hyperspectral imagery. *IEEE Trans. Geoscience and Remote Sensing 42*, 3 (2004), 608–619.

[Cen05] CENSSIS SOLUTIONWARE: Hyperspectral image analysis toolbox. `http://www.censsis.neu.edu/software/hyperspectral/hyperspectral.html`, 2005. [Online; accessed 16-July-2013].

[CGNT09] COUPRIE C., GRADY L., NAJMAN L., TALBOT H.: Power watersheds: A new image segmentation framework extending graph cuts, random walker and optimal spanning forest. In *Proc. IEEE 12th Int. Conf. Computer Vision (ICCV)* (2009), pp. 731–738.

[CH00] CHANG C.-I., HEINZ D. C.: Constrained subpixel target detection for remotely sensed imagery. *IEEE Trans. Geoscience and Remote Sensing 38*, 3 (2000), 1144–1159.

[Cha99] CHANG C.-I.: Spectral information divergence for hyperspectral image analysis. In *Proc. IEEE Int. Geoscience and Remote Sensing Symposium (IGARSS)* (1999), vol. 1, pp. 509–511.

[Cha03] CHANG C.-I.: *Hyperspectral imaging: techniques for spectral detection and classification*. Springer, 2003.

[Cha05] CHANG C.-I.: Orthogonal subspace projection (OSP) revisited: a comprehensive study and analysis. *IEEE Trans. Geoscience and Remote Sensing 43*, 3 (2005), 502–518.

[Cha07] CHANG C.-I. (Ed.): *Hyperspectral Data Exploitation: Theory and Applications*. John Wiley & Sons, 2007.

[CJZ*10] CHO T. S., JOSHI N., ZITNICK C. L., KANG S. B., SZELISKI R., FREEMAN W. T.: A content-aware image prior. In *Proc. IEEE Conf. Computer Vision and Pattern Recognition (CVPR)* (2010), pp. 169–176.

[CKG*11] CHAN S. H., KHOSHABEH R., GIBSON K. B., GILL P. E., NGUYEN T. Q.: An augmented lagrangian method for total variation video restoration. *IEEE Trans. Image Processing 20*, 11 (2011), 3097–3111.

[CKS09] CHUNG S.-W., KIM B.-K., SONG W.-J.: Detecting and eliminating chromatic aberration in digital images. In *Proc. IEEE Int. Conf. Image Processing (ICIP)* (2009), IEEE, pp. 3905–3908.

[CM02] COMANICIU D., MEER P.: Mean shift: A robust approach toward feature space analysis. *IEEE Trans. Pattern Analysis and Machine Intelligence 24*, 5 (2002), 603–619.

[CPLP06] COLANTONI P., PILLAY R., LAHANIER C., PITZALIS D.: Analysis of multispectral images of paintings. In *Proc. European Signal Processing Conference* (2006), EURASIP.

[CRHW09] CUI M., RAZDAN A., HU J., WONKA P.: Interactive hyperspectral image visualization using convex optimization. *IEEE Trans. Geoscience and Remote Sensing 47*, 6 (2009), 1673–1684.

[CZJ*12] CHO T. S., ZITNICK C. L., JOSHI N., KANG S. B., SZELISKI R., FREEMAN W. T.: Image restoration by matching gradient distributions. *IEEE Trans. Pattern Analysis and Machine Intelligence 34*, 4 (2012), 683–694.

[DHT10] DIEING T., HOLLRICHER O., TOPORSKI J. (Eds.): *Confocal Raman Microscopy*, vol. 158 of *Springer Series in Optical Sciences*. Springer-Verlag Berlin Heidelberg, 2010.

[DP93] DE PIERRO A. R.: On the relation between the ISRA and the EM algorithm for positron emission tomography. *IEEE Trans. Medical Imaging 12*, 2 (1993), 328–333.

[DQW*03] DU H., QI H., WANG X., RAMANATH R., SNYDER W. E.: Band selection using independent component analysis for hyperspectral image processing. In *Proc. Applied Imagery Pattern Recognition Workshop* (2003), IEEE, pp. 93–98.

[DRC03] DU Q., REN H., CHANG C.-I.: A comparative study for orthogonal subspace projection and constrained energy minimization. *IEEE Trans. Geoscience and Remote Sensing 41*, 6 (2003), 1525–1529.

[DWM86] DAUBE-WITHERSPOON M. E., MUEHLLEHNER G.: An iterative image space reconstruction algorthm suitable for volume ECT. *IEEE Trans. Medical Imaging 5*, 2 (1986), 61–66.

[ED07] ELLIS G., DIX A.: A taxonomy of clutter reduction for information visualisation. *IEEE Trans. Visualization and Computer Graphics 13*, 6 (2007), 1216–1223.

[EDT10] ECHES O., DOBIGEON N., TOURNERET J.-Y.: Estimating the number of endmembers in hyperspectral images using the normal compositional model and a hierarchical bayesian algorithm. *IEEE Journal of Selected Topics in Signal Processing 4*, 3 (2010), 582–591.

[EM98] EGAN W. J., MORGAN S. L.: Outlier detection in multivariate analytical chemical data. *Analytical Chemistry 70*, 11 (1998), 2372–2379.

[Eur13] EUROPEAN CENTRAL BANK: Security features - additional features. `http://www.ecb.europa.eu/euro/banknotes/security/additional/html/index.en.html`, 2013. [Online; accessed 9-July-2013].

[EXE13] EXELIS VISUAL INFORMATION SOLOUTIONS: Envi. `http://www.exelisvis.com/ProductsServices/ENVI/ENVI.aspx`, 2013. [Online; accessed 16-July-2013].

[FG88] FATTINGER C., GRISCHKOWSKY D.: Point source terahertz optics. *Applied Physics Letters 53*, 16 (1988), 1480–1482.

[FH09] FUCHS R., HAUSER H.: Visualization of multi-variate scientific data. *Computer Graphics Forum 28*, 6 (2009), 1670–1690.

[GB00] GIBSON J. D., BOVIK A.: Al bovik, handbook of image and video processing, 2000.

[GBSC88] GREEN A. A., BERMAN M., SWITZER P., CRAIG M. D.: A transformation for ordering multispectral data in terms of image quality with implications for noise removal. *IEEE Trans. Geoscience and Remote Sensing 26*, 1 (1988), 65–74.

[GC11] GOLDLUECKE B., CREMERS D.: Introducing total curvature for image processing. In *Proc. IEEE Int. Conf. Computer Vision (ICCV)* (2011), IEEE, pp. 1267–1274.

[GGB07] GELADI P., GRAHN H., BURGER J.: Multivariate images, hyperspectral imaging: background and equipment. *Techniques and Applications of Hyperspectral Image Analysis* (2007), 1–15.

[Gra84] GRAY R.: Vector quantization. *ASSP Magazine, IEEE 1*, 2 (april 1984), 4 –29.

[HC94] HARSANYI J. C., CHANG C.-I.: Hyperspectral image classification and dimensionality reduction: an orthogonal subspace projection approach. *IEEE Trans. Geoscience and Remote Sensing 32*, 4 (1994), 779–785.

[HCIC01] HEINZ D. C., CHEIN-I-CHANG: Fully constrained least squares linear spectral mixture analysis method for material quantification in hyperspectral imagery. *IEEE Trans. Geoscience and Remote Sensing 39*, 3 (2001), 529–545.

[Hei11] HEIDE F.: *Deblurring of multispectral images*. Master thesis, Computer Graphics Group, University of Siegen, August 2011.

[HGM*97] HOFFMAN P., GRINSTEIN G., MARX K., GROSSE I., STANLEY E.: DNA visual and analytic data mining. In *Proc. IEEE Visualization* (1997), pp. 437–441.

[HKW12] HABEL R., KUDENOV M., WIMMER M.: Practical spectral photography. *Computer Graphics Forum 31*, 2pt2 (May 2012), 449–458.

[HPA*10] HADJIMITSIS D. G., PAPADAVID C., AGAPIOU A., THEMISTOCLEOUS K., HADJIMITSIS M., RETALIS A., MICHAELIDES S., CHRYSOULAKIS N., TOULIOS L., CLAYTON C.: Atmospheric correction for satellite remotely sensed data intended for agricultural applications: impact on vegetation indices. *Natural Hazards & Earth System Sciences 10*, 1 (2010).

[HR98] HEIJMANS H. J., ROERDINK J. B. (Eds.):. *Mathematical Morphology and its Applications to Image and Signal Processing* (1998), Proc. Int. Symp. Mathematical Morphology (ISMM).

[HRH*13] HEIDE F., ROUF M., HULLIN M., LABITZKE B., HEIDRICH W., KOLB A.: High-quality computational imaging through simple lenses. *ACM Trans. Graphics* (2013). in print (presented on SIGGRAPH 2013).

[HSB02] HARDEBERG J. Y., SCHMITT F., BRETTEL H.: Multispectral color image capture using a liquid crystal tunable filter. *Optical Engineering 41*, 10 (2002), 2532–2548.

[HV02] HAMMER B., VILLMANN T.: Generalized relevance learning vector quantization. *Neural Networks 15* (2002), 1059–1068.

[ID90] INSELBERG A., DIMSDALE B.: Parallel coordinates: a tool for visualizing multi-dimensional geometry. In *Proc. IEEE Conf. Visualization* (1990), pp. 361–378.

[JA10] JORDAN J., ANGELOPOULOU E.: Gerbil - A Novel Software Framework for Visualization and Analysis in the Multispectral Domain. In *Int. Workshop Vision, Modeling & Visualization (VMV)* (Goslar, 2010), Koch R., Kolb A., Rezk-Salama C., (Eds.), vol. 1, The Eurographics Association, pp. 259–266.

[JA11] JORDAN J., ANGELOPOULOU E.: Edge detection in multispectral images using the n-dimensional self-organizing map. In *Proc. IEEE Int. Conf. Image Processing (ICIP)* (2011), IEEE, pp. 3181–3184.

[JA12] JORDAN J., ANGELOPOULOU E.: Supervised multispectral image segmentation with power watersheds. In *Proc. IEEE Int. Conf. Image Processing (ICIP)* (2012), IEEE, pp. 1585–1588.

[JG05] JACOBSON N. P., GUPTA M. R.: Design goals and solutions for display of hyperspectral images. *IEEE Trans. Geoscience and Remote Sensing 43*, 11 (2005), 2684–2692.

[JM03] JOYE W. A., MANDEL E.: New features of saoimage ds9. In *Astronomical Data Analysis Software and Systems XII* (2003), Payne H. E., Jedrzejewski R. I., Hook N., (Eds.), vol. 295 of *ASP Conference Series*, Astronomical Society of the Pacific, pp. 489–492.

[JMF99] JAIN A. K., MURTY M. N., FLYNN P. J.: Data clustering: a review. *ACM computing surveys (CSUR) 31*, 3 (1999), 264–323.

[JMP12] JIMENEZ I., MARTIN G., PLAZA A.: A new tool for evaluating spectral unmixing applications for remotely sensed hyperspectral image analysis. *Int. Conf. Geographic Object-Based Image Analysis (GEOBIA)* (2012), 644–648.

[Joh67] JOHNSON S. C.: Hierarchical Clustering Schemes. *Psychometrika 2* (1967), 241–254.

[Jol02] JOLLIFFE I. T.: *Principal component analysis*. Springer verlag, 2002.

[JSK08] JOSHI N., SZELISKI R., KRIEGMAN D.: Psf estimation using sharp edge prediction. In *Proc. IEEE Conf. Computer Vision and Pattern Recognition (CVPR)* (2008), pp. 1–8.

[JZSK09] JOSHI N., ZITNICK C. L., SZELISKI R., KRIEGMAN D.: Image deblurring and denoising using color priors. In *Proc. IEEE Conf. Computer Vision and Pattern Recognition (CVPR)* (2009), pp. 1550–1557.

[KAF*08] KEIM D., ANDRIENKO G., FEKETE J. D., GÖRG C., KOHLHAMMER J., MELANÇON G.: Visual analytics: Definition, process, and challenges. In *Information Visualization*, Kerren A., Stasko J., Fekete J.-D., North C., (Eds.), vol. 4950 of *Lecture Notes in Computer Science*. Springer Berlin Heidelberg, 2008, pp. 154–175.

[Kan07] KANG S. B.: Automatic removal of chromatic aberration from a single image. In *Proc. IEEE Conf. Computer Vision and Pattern Recognition (CVPR)* (2007), pp. 1–8.

[KBF*07] KLERK L. A., BROERSEN A., FLETCHER I. W., LIERE R. V., HEEREN R. M. A.: Extended data analysis strategies for high resolution imaging ms: New methods to deal with extremely large image hyperspectral datasets. *Int. Journal of Mass Spectrometry 260* (2007), 222–236.

[KBH03] KRUSE F. A., BOARDMAN J. W., HUNTINGTON J. F.: Comparison of airborne hyperspectral data and EO-1 hyperion for mineral mapping. *IEEE Trans. Geoscience and Remote Sensing 41*, 6 (2003), 1388–1400.

[KEG*13] KARACA A. C., ERTÜRK A., GÜLLÜ M. K., ELMAS M., ERTÜRK S.: Automatic waste sorting using shortwave infrared hyperspectral imaging system. In *Int. IEEE Workshop Hyperspectral Imaging and Signal Processing: Evolution in Remote Sensing (Whispers)* (2013).

[Kei02] KEIM D. A.: Information visualization and visual data mining. *IEEE Trans. Visualization and Computer Graphics 8*, 1 (2002), 1–8.

[Kes03] KESHAVA N.: A survey of spectral unmixing algorithms. *Lincoln Laboratory Journal 14*, 1 (2003), 55–78.

[KF09] KRISHNAN D., FERGUS R.: Fast image deconvolution using hyper-laplacian priors. In *Proc. Conf. Neural Information Processing Systems (NIPS)* (2009), vol. 22, pp. 1–9.

[KHK*12] KIM M. H., HARVEY T. A., KITTLE D. S., RUSHMEIER H., DORSEY J., PRUM R. O., BRADY D. J.: 3D imaging spectroscopy for measuring hyperspectral patterns on solid objects. *ACM Transactions on Graphics (Proc. SIGGRAPH 2012) 31*, 4 (2012), 38:1–11.

[KLB*93] KRUSE F., LEFKOFF A., BOARDMAN J., HEIDEBRECHT K., SHAPIRO A., BARLOON P., GOETZ A.: The spectral image processing system (sips)–interactive visualization and analysis of imaging spectrometer data. *Remote Sensing of Environment 44*, 2-3 (1993), 145 – 163. Airbone Imaging Spectrometry.

[KM02] KESHAVA N., MUSTARD J. F.: Spectral unmixing. 44–57.

[KPCW11] KEE E., PARIS S., CHEN S., WANG J.: Modeling and removing spatially-varying optical blur. In *Proc. IEEE Int. Conf. Computer Vision (ICCV)* (2011), IEEE, pp. 1–8.

[Kru64] KRUSKAL J. B.: Multidimensional scaling by optimizing goodness of fit to a nonmetric hypothesis. *Psychometrika 29*, 1 (1964), 1–27.

[KV11] KÄSTNER M., VILLMANN T.: Functional relevance learning in learning vector quantization for hyperspectral data. In *Int. IEEE Workshop Hyperspectral Image and Signal Processing: Evolution in Remote Sensing (WHISPERS)* (june 2011), pp. 1–4.

[KWH06] KIVINEN J., WARMUTH M. K., HASSIBI B.: The p-norm Generalization of the LMS Algorithm for Adaptive Filtering. *IEEE Trans. Signal Processing 54* (2006), 1782–1793.

[KZD*10] KIM S. J., ZHUO S., DENG F., FU C.-W., BROWN M.: Interactive visualization of hyperspectral images of historical documents. *IEEE Trans. Visualization and Computer Graphics 16*, 6 (2010), 1441–1448.

[LAK*11] LAWRENCE J., ARIETTA S., KAZHDAN M., LEPAGE D., O'HAGAN C.: A user-assisted approach to visualizing multidimensional images. *IEEE Trans. Visualization and Computer Graphics 17*, 10 (2011), 1487 –1498.

[Lan02] LANDGREBE D.: Hyperspectral image data analysis. *IEEE Signal Processing Magazine 19*, 1 (2002), 17–28.

[LBK12] LABITZKE B., BAYRAKTAR S., KOLB A.: Generic visual analysis for multi- and hyperspectral data. *Data Mining and Knowledge Discovery, Special Issue: Intelligent Data Visualization* (2012), 117–145.

[LFDF07] LEVIN A., FERGUS R., DURAND F., FREEMAN W. T.: Image and depth from a conventional camera with a coded aperture. *ACM Transactions on Graphics (TOG) 26*, 3 (2007), 70.

[LFH08] LI H., FU C.-W., HANSON A.: Visualizing multiwavelength astrophysical data. *IEEE Trans. Visualization and Computer Graphics 14*, 6 (2008), 1555–1562.

[LK13] LABITZKE B., KOLB A.: Efficient and accurate linear spectral unmixing. In *Int. IEEE Workshop Hyperspectral Imaging and Signal Processing: Evolution in Remote Sensing (Whispers)* (2013).

[LMHM02] LENNON M., MERCIER G., HUBERT-MOY L.: Nonlinear filtering of hyperspectral images with anisotropic diffusion. In *Proc. IEEE Int. Geoscience and Remote Sensing Symposium (IGARSS)* (2002), vol. 4, IEEE, pp. 2477–2479.

[LMM95] LI H., MANJUNATH B., MITRA S. K.: Multisensor image fusion using the wavelet transform. *Graphical models and image processing 57*, 3 (1995), 235–245.

[LPK13] LABITZKE B., PALTIAN M., KOLB A.: Radviz-based visual analysis of multispectral images. In *Proc. Colour and Visual Computing Symposium (CVCS)* (2013), pp. 1–6.

[Luc74] LUCY L.: An iterative technique for the rectification of observed distributions. *The astronomical journal 79* (1974), 745.

[LUK13] LABITZKE B., URRIGSHARDT F., KOLB A.: Expressive spectral error visualization for enhanced spectral unmixing. In *Proc. Int. Workshop Vision, Modeling and Visualization* (2013).

[LWB90] LEE J. B., WOODYATT A. S., BERMAN M.: Enhancement of high spectral resolution remote-sensing data by a noise-adjusted principal components transform. *IEEE Trans. Geoscience and Remote Sensing 28*, 3 (1990), 295–304.

[Mac67] MACQUEEN J.: Some methods for classification and analysis of multivariate observations. In *Proc. Berkeley symposium on mathematical statistics and probability* (1967), vol. 1, p. 14.

[Mig10] MIGNOTTE M.: A multiresolution markovian fusion model for the color visualization of hyperspectral images. *IEEE Trans. Geoscience and Remote Sensing 48*, 12 (2010), 4236–4247.

[MKL90] MAUSEL P., KRAMBER W., LEE J.: Optimum band selection for supervised classification of multispectral data. *Photogrammetric Engineering and Remote Sensing 56* (1990), 55–60.

[MM91] MAHAJAN V. N., MAHAJAN V. N.: *Aberration theory made simple*. SPIE optical engineering press Bellingham, Washington, USA, 1991.

[ND04] NASCIMENTO J. M. P., DIAS J. M. B.: Vertex component analysis: A fast algorithm to unmix hyperspectral data. *IEEE Trans. Geoscience and Remote Sensing 43* (2004), 898–910.

[PCI13] PCI GEOMATICS: Geomatica. `http://www.pcigeomatics.com/products/geomatica2013`, 2013. [Online; accessed 16-July-2013].

[Per13] PERKIN ELMER: Nuance ex multispectral tissue imaging system. `http://www.perkinelmer.com/Catalog/Product/ID/130926`, 2013. [Online; accessed 23-August-2013].

[Pho09] PHOTONICS.COM: Spectral imaging of melanoma. `http://www.photonics.com/Article.aspx?AID=38309`, 2009. [Online; accessed 9-July-2013].

[PMP*10] PLAZA A., MARTÍN G., PLAZA J., ZORTEA M., SÁNCHEZ S.: Recent developments in spectral unmixing and endmember extraction. *Optical Remote Sensing* (2010), 235–267.

[PMPP02] PLAZA A., MARTÍNEZ P., PEREZ R., PLAZA J.: Spatial/spectral endmember extraction by multidimensional morphological operations. *IEEE Trans. Geoscience and Remote Sensing 40*, 9 (2002), 2025–2041.

[PMPP04] PLAZA A., MARTÍNEZ P., PEREZ R., PLAZA J.: A quantitative and comparative analysis of endmember extraction algorithms from hyperspectral data. *IEEE Trans. Geoscience and Remote Sensing 42*, 3 (2004), 650–663.

[PMZ09] PLAZA A., MARTÍN G., ZORTEA M.: On the incorporation of spatial information to endmember extraction: Survey and algorithm comparison. In *Int. IEEE Workshop Hyperspectral Imaging and Signal Processing: Evolution in Remote Sensing (Whispers)* (2009), pp. 1–4.

[PvdH01] POLDER G., VAN DER HEIJDEN G. W.: Visualization of spectral images. In *Visualization and Optimization Techniques* (2001), Censor Y., Ding M., (Eds.), vol. 4553, Proceedings of SPIE.

[PVdHY02] POLDER G., VAN DER HEIJDEN G., YOUNG I.: Spectral image analysis for measuring ripeness of tomatoes. *Trans. American Society of Agricultural Engineers 45*, 4 (2002), 1155–1162.

[QFMSP12] QUINTANO C., FERNÁNDEZ-MANSO A., SHIMABUKURO Y. E., PEREIRA G.: Spectral unmixing. *Int. Journal of Remote Sensing 33*, 17 (2012), 5307–5340.

[RG05] ROBILA S. A., GERSHMAN A.: Spectral matching accuracy in processing hyperspectral data. In *Proc. IEEE Int. Signals, Circuits and Systems Symposium (ISSCS)* (2005), vol. 1, pp. 163–166.

[RGC*98] ROBERTS D., GARDNER M., CHURCH R., USTIN S., SCHEER G., GREEN R.: Mapping chaparral in the santa monica mountains using multiple endmember spectral mixture models. *Remote Sensing of Environment 65*, 3 (1998), 267–279.

[Ric72] RICHARDSON W. H.: Bayesian-based iterative method of image restoration. *Journal of the Optical Society of America (JOSA) 62*, 1 (1972), 55–59.

[RIS*04] ROMAN C., ICHIM O., SARGER L., VIGNERAS V., MOUNAIX P.: Terahertz dielectric characterisation of polymethacrylimide rigid foam: the perfect sheer plate? *Electronics Letters 40*, 19 (2004), 1167–1169.

[RNB08] ROWE R. K., NIXON K. A., BUTLER P. W.: Multispectral fingerprint image acquisition. In *Advances in biometrics*. Springer, 2008, pp. 3–23.

[RS00] ROWEIS S. T., SAUL L. K.: Nonlinear dimensionality reduction by locally linear embedding. *Science 290*, 5500 (2000), 2323–2326.

[SATC11] SOMERS B., ASNER G. P., TITS L., COPPIN P.: Endmember variability in spectral mixture analysis: A review. *Remote Sensing of Environment 115*, 7 (2011), 1603–1616.

[SBH*02] STEIN D. W., BEAVEN S. G., HOFF L. E., WINTER E. M., SCHAUM A. P., STOCKER A. D.: Anomaly detection from hyperspectral imagery. *IEEE Signal Processing Magazine 19*, 1 (2002), 58–69.

[SBS*10] SCHNEIDER P., BUNTE K., STIEKEMA H., HAMMER B., VILLMANN T., BIEHL M.: Regularization in matrix relevance learning. *IEEE Trans. Neural Networks 21*, 5 (2010), 831–840.

[Sch04] SCHEUNDERS P.: Wavelet thresholding of multivalued images. *IEEE Trans. Image Processing 13*, 4 (2004), 475–483.

[SHHS11] SCHULER C. J., HIRSCH M., HARMELING S., SCHÖLKOPF B.: Non-stationary correction of optical aberrations. In *Proc. IEEE Int. Conf. Computer Vision (ICCV)* (2011), IEEE, pp. 659–666.

[SHHS12] SCHULER C. J., HIRSCH M., HARMELING S., SCHÖLKOPF B.: Blind correction of optical aberrations. In *Proc. European Conference on Computer Vision (ECCV)*. Springer, 2012, pp. 187–200.

[SKS*09] STRICKERT M., KEILWAGEN J., SCHLEIF F. M., VILLMANN T., BIEHL M.: Matrix metric adaptation for linear discriminant analysis of biomedical data. In *Bio-Inspired Systems: Computational and Ambient Intelligence* (2009), Cabestany J., Sandoval F., Prieto A., Corchado J., (Eds.), vol. 5517 of *Lecture Notes in Computer Science*, Springer, pp. 933–940.

[SL11] SHARIFAHMADIAN E., LATIFI S.: Advanced hyperspectral remote sensing for target detection. In *Proc. IEEE Int. Conf. Systems Engineering (ICSEng)* (2011), IEEE, pp. 200–205.

[SLB11] STRICKERT M., LABITZKE B., BLANZ V.: Partial generalized correlation for hyperspectral data. In *IEEE Symp. Computational Intelligence and Data Mining* (2011), IEEE, pp. 365–372.

[SLKV11] STRICKERT M., LABITZKE B., KOLB A., VILLMANN T.: Multispectral image characterization by partial generalized covariance. In *Proc. European Symposium on Artificial Neural Networks (ESANN), Computational Intelligence and Machine Learning* (April 2011), pp. 105–110.

[SMP10] SÁNCHEZ S., MARTÍN G., PLAZA A.: Parallel implementation of the N-FINDR endmember extraction algorithm on commodity graphics processing units. In *Proc. IEEE Int. Geoscience and Remote Sensing Symposium (IGARSS)* (2010), pp. 955–958.

[SMPC10] SÁNCHEZ S., MARTÍN G., PLAZA A., CHANG C.-I.: GPU implementation of fully constrained linear spectral unmixing for remotely sensed hyperspectral data exploitation. In *SPIE Optical Engineering and Applications* (2010), Huang B., Plaza A. J., Serra-Sagrista J., Lee C., Li Y., Qian S.-E., (Eds.), vol. 7810, International Society for Optics and Photonics, pp. 78100G–78100G–11.

[SOKH08] SIESLER H. W., OZAKI Y., KAWATA S., HEISE H. M.: *Near-infrared spectroscopy: principles, instruments, applications*. John Wiley & Sons, 2008.

[SP10] SÁNCHEZ S., PLAZA A.: GPU implementation of the pixel purity index algorithm for hyperspectral image analysis. In *Proc. IEEE Int. Conf. Cluster Computing Workshops and Posters* (2010), pp. 1–7.

[Spe12] SPECTIR: Vegetation. `http://www.spectir.com/applications/vegetation-airborne-hyperspectral/`, 2012. [Online; accessed 9-July-2013].

[SPK04] SOTOCA J. M., PLA F., KLAREN A. C.: Unsupervised band selection for multispectral images using information theory. In *Proc. IEEE Int. Conf. Pattern Recognition (ICPR)* (2004), vol. 3, IEEE, pp. 510–513.

[SPT*07] SETOAIN J., PRIETO M., TENLLADO C., PLAZA A., TIRADO F.: Parallel morphological endmember extraction using commodity graphics hardware. *IEEE Geoscience and Remote Sensing Letters 4*, 3 (2007), 441–445.

[SPTT08] SETOAIN J., PRIETO M., TENLLADO C., TIRADO F.: GPU for parallel on-board hyperspectral image processing. *Int. Journal of High Performance Computing Applications 22*, 4 (2008), 424–437.

[SSS*06] STRICKERT M., SEIFFERT U., SREENIVASULU N., WESCHKE W., VILLMANN T., HAMMER B.: Generalized relevance LVQ (GRLVQ) with correlation measures for gene expression data. *Neurocomputing 69* (2006), 651–659.

[SSVS09] STRICKERT M., SCHLEIF F.-M., VILLMANN T., SEIFFERT U.: *Similarity-Based Clustering - Recent Developments and Biomedical Applications*, vol. 5400 of *Lecture Notes in Computer Science*. Springer, 2009, ch. Unleashing Pearson Correlation for Faithful Analysis of Biomedical Data, pp. 70–91.

[Sun12] SUN D.-W.: Hyperspectral imaging technology: A non-destructive tool for food quality and safety evaluation and inspection. *Sun DW, editor* (2012), 1–8.

[SW02] SOCOLINSKY D. A., WOLFF L. B.: Multispectral image visualization through first-order fusion. *IEEE Trans. Image Processing 11*, 8 (2002), 923–931.

[SZPA12] SOMERS B., ZORTEA M., PLAZA A., ASNER G. P.: Automated extraction of image-based endmember bundles for improved spectral unmixing. *IEEE Journal of Selected Topics in Applied Earth Observations and Remote Sensing 5*, 2 (2012), 396–408.

[TD04] TAX D. M. J., DUIN R. P. W.: Support vector data description. *Machine Learning 54* (2004), 45–66.

[TDSL00] TENENBAUM J. B., DE SILVA V., LANGFORD J. C.: A global geometric framework for nonlinear dimensionality reduction. *Science 290*, 5500 (2000), 2319–2323.

[TNI*10] TSUCHIYAMA R., NAKAMURA T., IIZUKA T., ASAHARA A., MIKI S.: *The OpenCL Programming Book*. Fixstars Corporation, 2010.

[U.S11] U.S. GEOLOGICAL SURVEY: How do you convert radiance to reflectance? `http://eo1.usgs.gov/faq/question?id=21`, 2011. [Online; accessed 8-June-2014].

[U.S12] U.S. ARMY GEOSPATIAL CENTER: Hypercube. `http://www.agc.army.mil/Missions/Hypercube.aspx`, 2012. [Online; accessed 16-July-2013].

[VG88] VANE G., GOETZ A. F.: Terrestrial imaging spectroscopy. *Remote Sensing of Environment 24*, 1 (1988), 1–29.

[VG08] VEGANZONES M. A., GRAÑA M.: *Endmember Extraction Methods: A Short Review*. No. Part 3 in Lecture Notes in Computer Science. Springer Berlin / Heidelberg, 2008, ch. Knowledge-Based Intelligent Information and Engineering Systems, pp. 400–407.

[VGC*93] VANE G., GREEN R. O., CHRIEN T. G., ENMARK H. T., HANSEN E. G., PORTER W. M.: The airborne visible/infrared imaging spectrometer (AVIRIS). *Remote Sensing of Environment 44*, 2–3 (1993), 127–143. Airbone Imaging Spectrometry.

[VHS*10] VILLMANN T., HAASE S., SCHLEIF F.-M., HAMMER B., BIEHL M.: The mathematics of divergence based online learning in vector quantization. In *Artificial Neural Networks in Pattern Recognition*, Schwenker F., El Gayar N., (Eds.), vol. 5998 of *LNCS*. Springer Berlin / Heidelberg, 2010, pp. 108–119.

[VP06] VALENCIA D., PLAZA A.: Fpga-based hyperspectral data compression using spectral unmixing and the pixel purity index algorithm. In *Int. Conf. Computational Science*. Springer, 2006, pp. 888–891.

[Win99] WINTER M. E.: N-FINDR: an algorithm for fast autonomous spectral endmember determination in hyperspectral data. In *Storage and Retrieval for Image and Video Databases* (1999).

[WWM*64] WIENER N., WIENER N., MATHEMATICIAN C., WIENER N., WIENER N.: *Extrapolation, interpolation, and smoothing of stationary time series: with engineering applications*, vol. 8. MIT press, 1964.

[YSQS07] YUAN L., SUN J., QUAN L., SHUM H.-Y.: Image deblurring with blurred/noisy image pairs. In *ACM Transactions on Graphics (TOG)* (2007), vol. 26, ACM, p. 1.

[YSQS08] YUAN L., SUN J., QUAN L., SHUM H.-Y.: Progressive inter-scale and intra-scale non-blind image deconvolution. In *ACM Transactions on Graphics (TOG)* (2008), vol. 27, ACM, p. 74.

[ZFS*08] ZUZAK K., FRANCIS R., SMITH J., TRACY C., CADEDDU J., LIVINGSTON E.: Biomedical optics & medical imaging novel hyperspectral imager aids surgeons. *Proc. SPIE Newsroom 3* (2008).

[ZYQ*08] ZHOU H., YUAN X., QU H., CUI W., CHEN B.: Visual clustering in parallel coordinates. In *Computer Graphics Forum* (2008), vol. 27, Wiley Online Library, pp. 1047–1054.

List of Figures

List of Tables

Abbreviations

AMEE	Automated morphological endmember extraction 19, 34, 64–66, 68, 72, 130, 131
ANC	Abundance non-negativity constraint 17, 74, 79, 82, 86, 87, 95
ASC	Abundance sum-to-one constraint 17, 74, 110
AVIRIS	Airborne Visible/Infrared Imaging Spectrometer (AVIRIS) [VGC*93] 9, 140
CPU	Central processing unit 54, 79
CRM	Confocal Raman microscopy 71, 72, 100, 103, 113, 116, 134, 141, 142, 173
CUDA	NVIDIA's compute unified device architecture 64, 75, 79
DP	Distance pursuit 55, 58, 59
ENVI	ENvironment for Visualizing Images [EXE13] 34, 35
FCLSU	Fully constraint linear spectral unmixing 17, 18, 75, 82, 84, 86, 110, 111
FWHM	Full width at half maximum 173
GPU	Graphics processing unit 32, 54, 64
HIAT	Hyperspectral Image Analysis Toolbox [Cen05] 33–35
HYDICE	Hyperspectral Digital Imagery Collection Experiment (HYDICE) [BCA95] 9, 140
ISRA	Image Space Reconstruction Algorithm, see Eq. (B.13) 17, 75, 76, 78–80, 82, 84–87, 162

LSU Linear spectral unmixing 34, 103, 173

MDS Multidimensional scaling 13, 23
MNF Maximum Noise Fraction 10, 11

NAPC Noise Adjusted Principal Components 10
NCLSU Non-negative constraint linear spectral unmixing 17, 75, 84–86, 110, 111
NED Normalized Euclidean Distance, see Eq. B.5 11, 12, 44, 114, 131
NN Nearest neighborhood 63, 90, 93, 96, 102, 103, 122, 131

OSP Orthogonal subspace projection 19, 20, 34, 43–46, 64–68, 72, 74, 78, 82, 83, 87, 96, 99–101, 113–115, 118, 122, 130, 131
OSPCE Orthogonal subspace projection based coefficient estimator 78–80, 82, 84–87, 162

PCA Principal component analsysis 13, 14, 18, 22, 24, 25, 55, 60, 69, 71, 91, 92, 98–100, 117, 121, 123, 125, 128–131, 137–142, 161
PCP Parallel coordinate plot [ID90] 18, 23–25, 35, 37, 117
PPI Pixel purity index 19, 64–68, 72, 96, 97, 113–115, 130, 131, 162
PSF Point Spread Functions 3, 48–52

Radviz Radial visualization [HGM*97] 23–25, 37, 89, 117–124, 126, 128–130, 133
RMSE Root Mean Square Error, see Eq. B.6 34, 85, 86, 110

SAD Spectral Angle Distance, see Eq. B.1 11, 12, 19, 54, 122, 128
SAR Synthetic Aperture Radar 34
SCA Spectral Correlation Angle, see Eq. B.2 11
SGA Spectral Gradient Angle, see Eq. B.4 11, 113, 114
SID Spectral Information Divergence, see Eq. B.3 11, 12, 128
SMA Spectral Mixture Analysis 174

SNR Signal-to-noise-ratio 2, 10, 14, 21, 31, 60, 61

TIR Total Internal Reflectance 31

UCLSU Unconstrained linear spectral unmixing 17, 74

Symbols

$\alpha_j(x,y)$	Coefficient of an endmember for pixel (x,y) 17, 74, 79, 80
$\vec{v}_j$	Endmember (one constituent of dataset) 16, 74, 76, 78–80
V	Set of endmembers 16, 17, 75, 76, 78, 79, 90, 93, 94
λ	Spectral dimension that contains discrete spectral bands over a continuous spectral range. 5
(x,y)	Pixel position that represents the 2D-location of a spectrum 5, 17, 19, 70, 79, 80, 92, 106, 144
$\vec{n}(x,y)$	Noise vector of a pixel 17
n	The number of spectral bands 1, 5, 19, 20, 23, 117, 122, 145
q	The number of endmembers in a set 76, 145
$\vec{s}(x,y)$	Discrete spectrum of a pixel 5, 17, 23, 77, 79, 90, 92, 94, 120
$\vec{s}(x,y,\lambda)$	Intensity value of a band λ at a pixel (x,y) 5

Glossary

A

AOTF Acousto-optic tunable filter (AOTF) for electronically controlling of the spectral transmittance based on the interaction of electromagnetic and acoustic waves [SOKH08]. 9

C

Chromatic aberration In optics many types of distortions can arise. One of them is the chromatic aberration which is the wavelength depended miss-focusing of colors by a lens. 39–41, 47, 50, 61

CRM Confocal Raman microscopy (CRM) is a combination of confocal microscopy, delivering sharp 3D image of semi-transparent materials, and Raman spectroscopy, which provides multispectral data in high spatial resolution. 8, 71, 167

E

Endmember Endmembers are constituent spectra of a mixed spectrum. 14–18, 20, 21, 37, 44–46, 53, 54, 61–70, 72–87, 89–107, 110–116, 118, 122, 126, 130, 131, 133, 144, 145, 162, 174

F

FWHM Full width at half maximum (FWHM) expresses the difference between to function arguments which represent the half of the maximum function value. 9, 17, 40, 41, 167

L

LCTF Liquid crystal tunable filter (LCTF) for electronically controlling of the spectral transmittance [HSB02]. 9, 40, 41, 137–139

LSU Linear spectral unmixing (LSU) is the decomposition of a mixed pixel into its constituents by assuming a linear mixing model of the constituent spectra. 16, 17, 34, 36, 37, 43, 44, 46, 52–54, 74, 76, 87, 89–95, 100, 102–105, 110–113, 130, 131, 133, 134, 168

M

Metamers Different spectra that produce the same tristimulus response. 51, 52

R

Raman Raman spectroscopy is a popular method used to examine the chemical composition of measured samples since each distinct molecule structure has a different fingerprint in its Raman spectrum. Thus, the Raman spectra of a mineral show unique characteristics related to mineral's chemical composition. 8, 69–71, 95, 167, 173

S

SMA Spectral mixture analysis (SMA), also referred to as spectral unmixing, is the procedure which decomposes mixed spectra into a set of constituent spectra, so-called endmembers, and the corresponding fractions that indicate the proportion of each endmember in each pixel. 14, 61, 103, 116–118, 124, 126, 128, 168

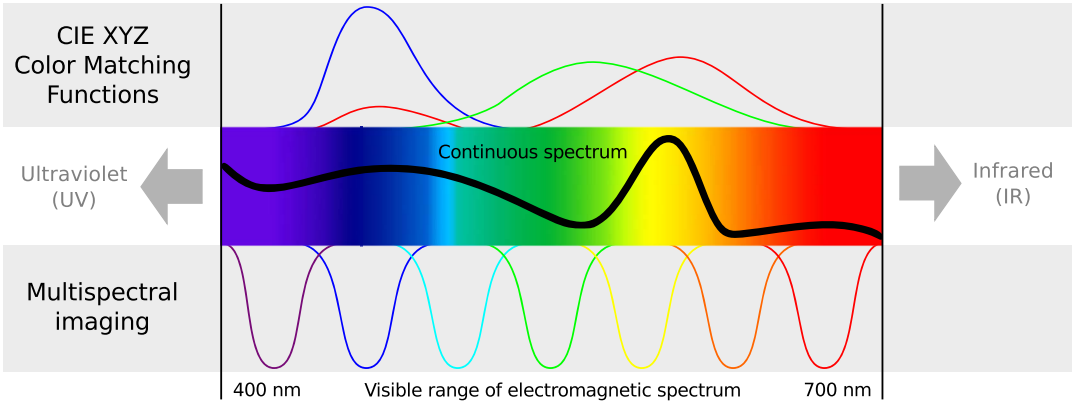

Figure 1.2: Illustrative comparison of RGB camera and multispectral imaging, where the common tristimulus CIE XYZ color matching functions, confer Appendix B.3, are used to visualize the concept of RGB cameras. As can be seen, multispectral imaging achieves a more accurate representation of the continuous spectrum. Thus, allows to for instance distinguish a mixed and a pure yellow tone.

sensus of the literature poses that, the distinction mainly is related to the number of spectral bands and the spectral density:

- Hyperspectral imaging usually consists of hundreds of narrow bands that typically cover a large range of the electromagnetic spectrum.
- Multispectral imaging usually consists of a smaller number of bands, typically lower than 100, and the spectral density is broader and covers a smaller range of the electromagnetic spectrum, e.g. 400 - 1000 nm.

Since there is no strict definition of the term hyperspectral and for the sake of simplicity, both techniques multi- and hyperspectral imaging and the corresponding data are collectively referred to as multispectral imaging and multispectral data in this thesis.

1.2 Multispectral Image Processing – A General Overview

Multispectral imaging is the process of acquiring images series of a specific range of frequencies across the electromagnetic spectrum. As seen in the previous section, this image series also can be considered as an multispectral image cube, where each pixel in fact has associated a discrete spectrum, which approximates the continuous electromagnetic spectrum. Compared to traditional RGB cameras, where the continuum of an electromagnetic spectrum is converted into three discrete values, the denser sampling and more narrow filters used in multispectral imaging lead to a more accurate, but still discrete representation of the continuum of a spectrum, see Fig. 1.2. Based on the more detailed representation of a continuous spectrum, one can more precisely differentiate materials, not only according to color but also according to spectral properties beyond the visible range. However, due to the associated complexity of the

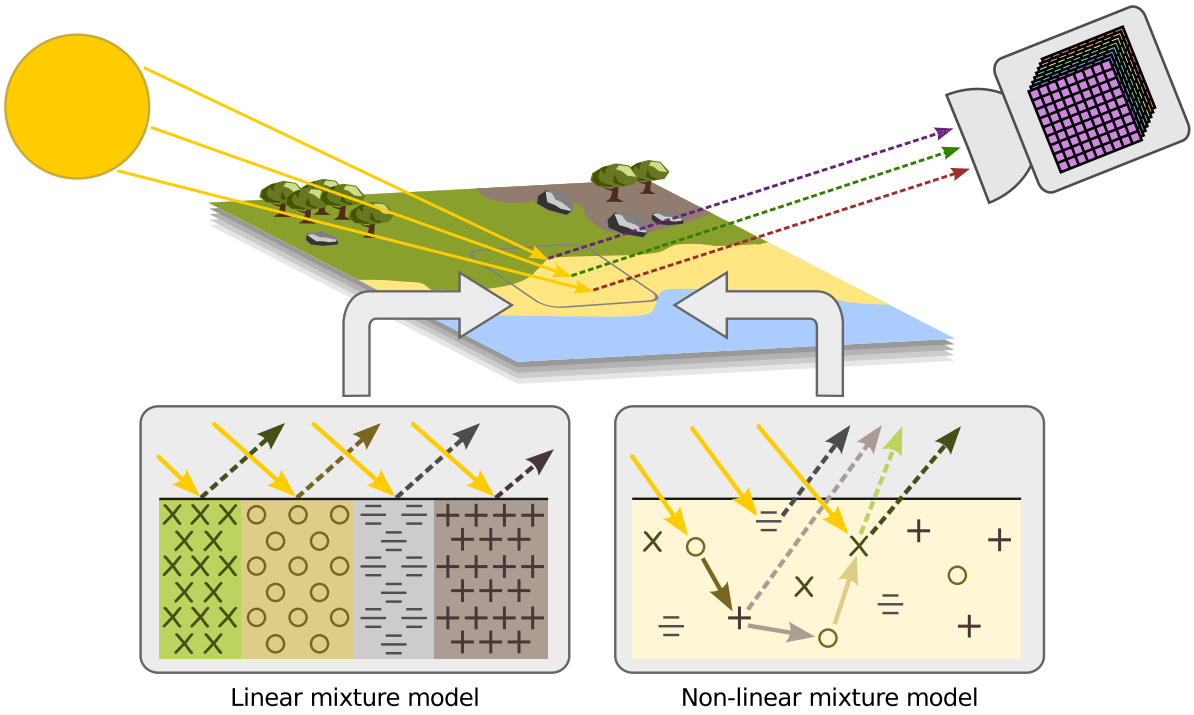

Figure 1.5: Illustration of linear and non-linear mixture models. While the linear mixture model assumes regular ordered materials like in a checkerboard, the non-linear mixture model allows that incident light multiple can scatter with different materials.

- Regardless of the imaging system, mixed spectra can also occur when distinct materials are combined to **homogeneous mixtures** (e.g. soil and grass or the overlay of semi-transparent materials). This kind of mixtures are also referred to as intimate mixtures.

The unmixing requires a model how constituent spectra in a pixel are combined to yield a mixed spectrum. The literature distinguishes two, linear and non-linear, models that represent the underlying physics that are the foundation for the inverse unmixing task [Kes03]. Both mixing models are conceptionally illustrated in Fig. 1.5. As can be seen, the non-linear mixing model describes the more realistic, but also more complicated, scenario. Compared to the linear model, the materials are not regularly ordered and incident radiation can scatter several times with different materials. Thus, resulting mixed spectra may not uphold linear proportions of the constituent spectra, as in the simpler linear model [Kes03]. Although many research on the non-linear model is already in progress, the current research level is immature compared to the linear mixing, which has been paid a tremendous research attention in the past decade, as stated by Bioucas-Dias et al. [BDPD*12]. The authors further mentioned, that the general requirement of a priori knowledge about the endmember in the data is one of the major limitations of the non-linear-based unmixing. A more detailed discussion of the non-linear mixture model would be beyond the scope of this thesis. Therefore readers that

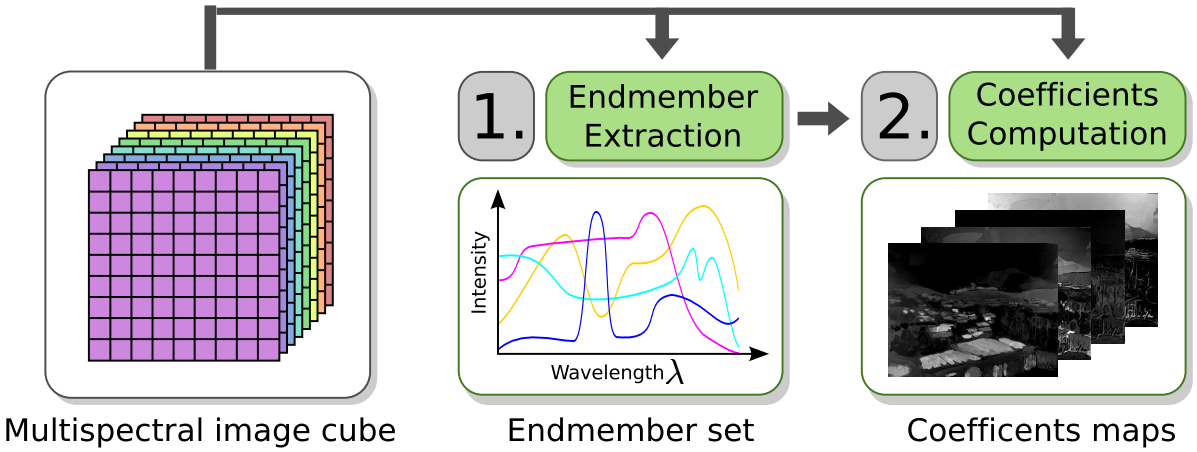

Figure 1.6: The process of linear spectral unmixing: In the first step the endmembers are selected, e.g. by automatic algorithms and then the corresponding coefficients are computed by inverse operations. Based on both, the endmember set and the coefficients maps, the original cube can be reconstructed and mixtures can be explored.

are interested in more details about this topic are referred to the common literature, where [Kes03, BDPD*12] are good starting points.

Although the linear mixture model assumes minimal secondary reflections and/or multiple scattering effects in the data collection procedure [PMP*10], the spectral unmixing based on the linear mixing model, also called linear spectral unmixing (LSU), has become a standard method that is applied in various applications, e.g. remote sensing [PMP*10] or confocal Raman microscopy [DHT10], and the number of applications is still increasing [QFMSP12]. Figure 1.6 illustrates the process of LSU, which usually consists of two steps [Kes03], an initial **endmember extraction** step and a consequential step for the **computation of the corresponding coefficients**. The details of both steps are discussed in the following paragraphs.

Endmember Extraction: This step identifies the set $V = \{\vec{v}_1, \ldots, \vec{v}_q\}$ of constituent spectra (endmembers), where q is the number of endmembers $\vec{v}_j$. According to Keshava [Kes03], there are two viewpoints for the identifications of endmembers:

- Mathematical: The search for V is comparable to the estimation of a non-orthogonal subset of basis vectors.
- Physical: Non-negativity of the spectra is required to be physically realizable. Moreover, the physical characteristics of the constituent substances should be retained by the endmembers.

The autonomous determination of endmembers with the constrained to satisfy both viewpoints is a challenging task and is the hardest part of the unmixing problem [Kes03]. At once,

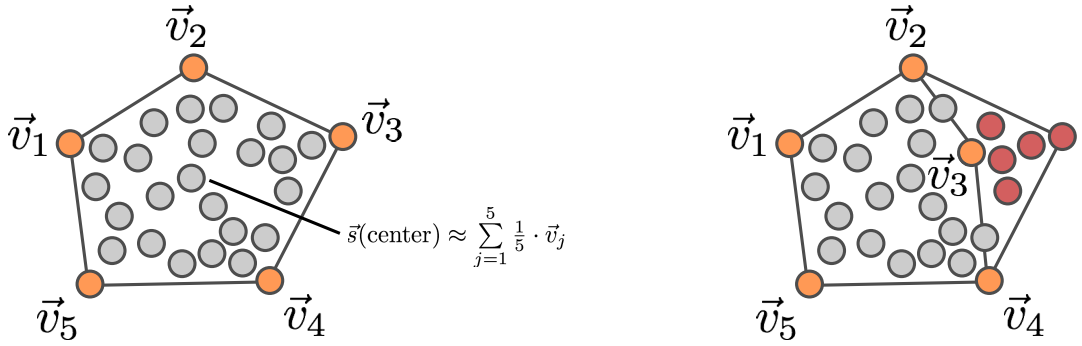

Figure 1.7: Two-dimensional example illustration of the linear mixture model, which is based on the endmembers $\vec{v}_j$. The quality of the reconstruction mainly depends on the correctly estimated set of endmembers, which define the convex hull of the dataset (left). In case of FCLSU, i.e. convex combination, it is obvious that a not optimal estimated set of endmembers (right) lead to insufficient reconstructions (red points).

of applied filters. These challenges are avoided when the search of constituents is directly done in the observed data. In the following an overview of manual and automatic endmember selection methods are shown.

Manual Endmember Selection Early endmember determination approaches were based on the expert knowledge of humans, for instance the prior knowledge about the contents of the imaged terrain was used to select some candidate endmember spectra from a reference database [VG08]. But this task can be quite challenging, as already seen above. Furthermore, reference databases also can be incomplete [BC93]. Therefore, especially in cases of new application domains, the determination of endmembers within the observed dataset is a very important analysis task. Bateson and Curtiss [BC93, BC96] have presented a method for manual selection of endmembers, that is based on PCA and parallel coordinate plots (PCPs) [ID90]. Initially, the dataset is projected into the space of the first two principal components. The extremes, i.e. points on the convex hull, of the resulting scatter plot can be interactively added to the set of endmembers. Consequently, the visualization is 2D for the first three selections and 3D of the fourth selection, which gets cluttered in high-dimensional space. Here, a PCP is applied to overcome this visualization shortcoming. According to the authors [BC93, BC96], the main weaknesses of this method are:

- The requirement of human intervention time in order to judge the endmember set.
- The possibility that different analysts can achieve somewhat different endmembers.

More information about the mentioned visualization techniques are provided in the upcoming section 1.2.3 .

Endmember Extraction Algorithms Many algorithms can be found in the literature that perform an automatic search for the constituent spectra of a dataset. Complementary to the

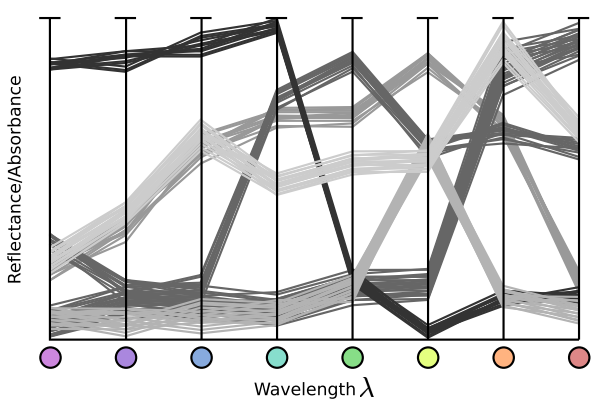

Parallel coordinate plot

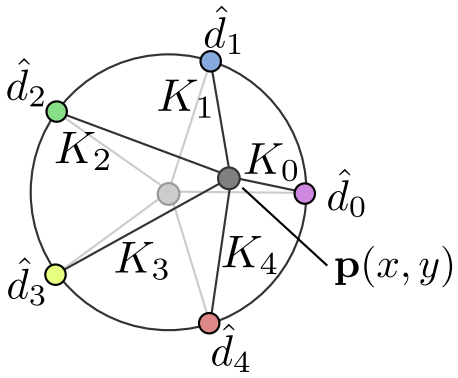

Radviz plot

Figure 1.9: Conceptional illustrations of two multivariate plotting techniques: PCP in the left and the Radviz mapping in the right.

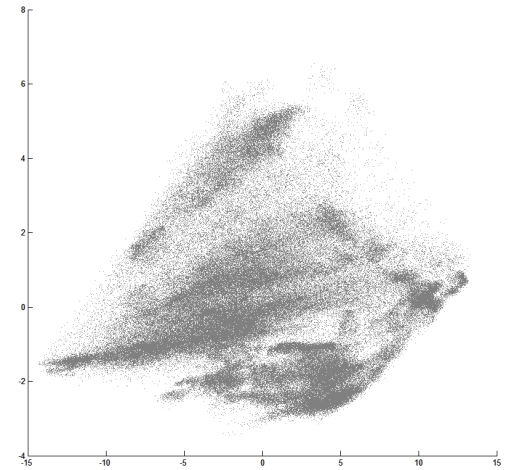

Scatter plot of the first two principal components

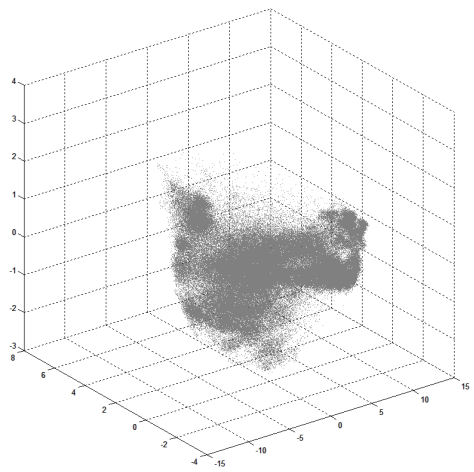

Scatter plot of the first three principal components

Figure 1.10: Example of PCA-based scatter plots, again based on the dataset *Watercolors* (see Appendix A). The left 2D scatter plot is based on the first two principal components and the 3D scatter plot additionally uses the third principal component.

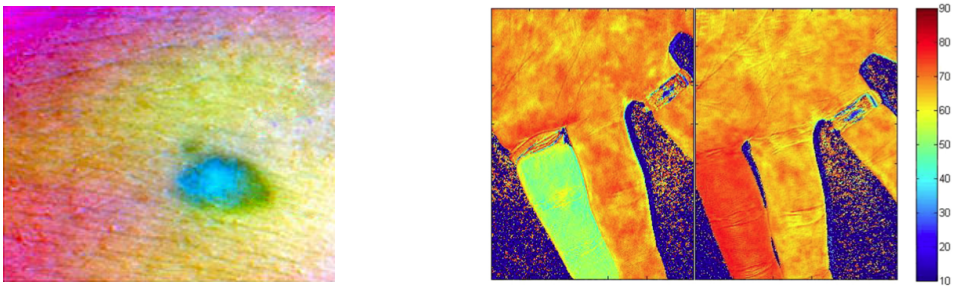

Detection of melanoma (cyan) Oxyhemoglobin in blood (in %)

Figure 2.3: Examples for medical applications. The left image image shows a false-color image of skin where a melanom was identified, retrieved from [Pho09]. The right image shows the oxyhemoglobin in blood for both, with temporarily restrict blood flow in a finger and released restriction that caused a hyperfusion, retrieved from [ZFS*08].

Medical Multispectral imaging has become affordable, reliable and usually noninvasive method for many medical tasks. Beside others, during the recent years many studies have applied multispectral imaging for the early detection and diagnostics of cancer [AUK*11]. Also the distinction of melanoma from other skin diseases is in the focus of research, as exemplarily shown in Fig. 2.3 [Pho09]. Moreover, the concentration of oxyhemoglobin in blood can be analyzed by the utilization of multispectral imaging, e.g. to assist surgeons [ZFS*08]. A simple example of the detection of oxyhemoglobin concentration is shown in Fig. 2.3.

Food Quality The potential for material analysis of multispectral image data also has been studied for the analysis of food quality. The potential of multispectral imaging has been analyzed for a huge variety of foods, e.g. the ripeness of tomatoes [PVdHY02] or the quality of meat and fish [Sun12] and so on. For instance the sugar distribution of melons is visualized in Fig. 2.4 by utilizing the strong inverse correlation of the sugar concentration and the absorbance of band 676 nm [Sun12].

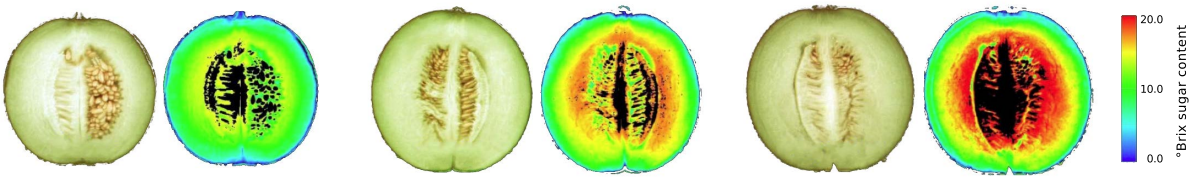

Unripe Mature Fully mature

Figure 2.4: Examples for food quality inspection. The °Brix sugar concentration of melons of different ripeness are shown together with their color images [Sun12]. Adapted from [Sun12].

Conventional TIR image

Multispectral imaging based image

Figure 2.7: Example for application field of biometrics. A conventional TIR image is compared to a composed multispectral fingerprint image of one finger. As can be seen, fine structures are visible throughout the multispectral image. Adapted from [RNB08].

Beside features that can be simply felt or seen, there are also additional features that are getting visible under specific illumination, e.g. see Fig. 2.6 to see a five euro banknote under infrared light [Eur13].

Biometrics Nowadays, multispectral imaging can be used to compensate uncontrolled conditions, like insufficient illumination or low scanning resolutions, to improve the detection of features in biometrics [BLGK11]. In the field of fingerprint acquisition, typically total internal reflectance (TIR) sensors are used that acquire the points of optical contact between sensor platen and material. Comparing this conventional sensors to a multispectral based sensor reveals that fine structures of fingerprints are visible throughout the multispectral image (cf. Fig. 2.7) [RNB08].

2.2 Requirements and Challenges

Having some application domains in mind, this section presents subtle requirements and challenges of the distinct steps of the introduced multispectral processing pipeline with respect to the main aims of this dissertation. Here, the main aims are the proposal of visual analysis methods to facilitate the generic analysis of multispectral image data and the discussion of more fundamental challenges when processing multispectral image data in general.

Acquisition Many applications require a reliable determination of spectral characteristics, e.g. to identify cancers in medical applications. However, analysis results do not solely depend on the capabilities of the analysis methods, they partly also depend on the quality of the acquired image data, e.g. from SNR. For this reason, although the main scope of this thesis is the analysis of the data, the acquisition of multispectral images will be roughly addressed. As seen in the fundamentals, many multispectral data suffer from noise, but also other reasons for image degradation, like outlier and blur, can frequently be found in such data. Therefore,

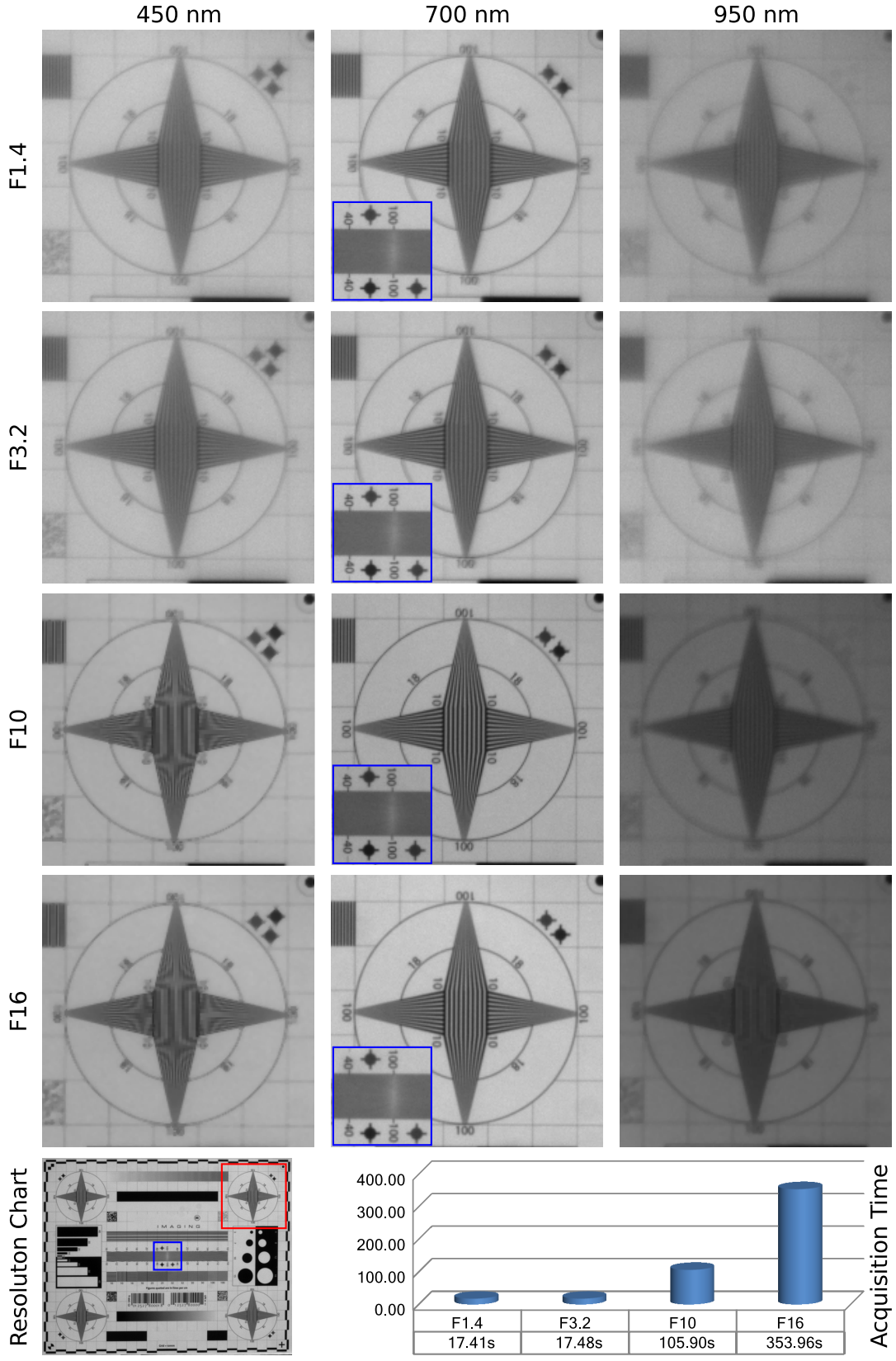

Figure 3.2: Resolution charts and acquisition times for different wavelength and apertures.

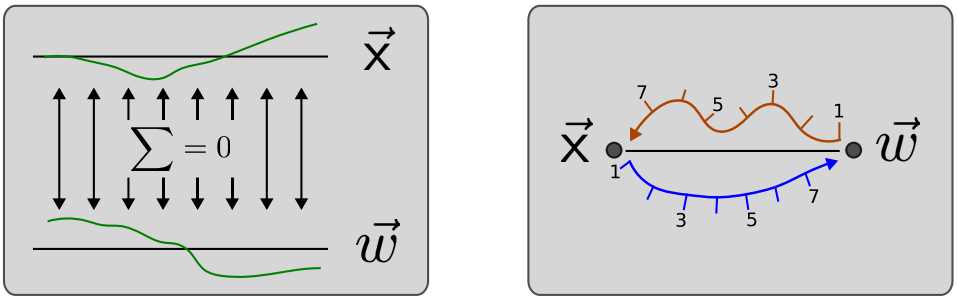

Figure 4.1: Illustration of two challenges of an optimum transformation in high-dimensional space.

Algorithm 1 distance pursuit $\mathrm{DP}_{\{\vec{b},g\}}(\vec{x},\vec{w},t)$

// input $\vec{x}$ target vector; $\vec{w}$ source vector; t number of steps
$g \leftarrow 0$; $\vec{b} \leftarrow \vec{0}_n$ // Initialize target variables
// Visit distance sequence elements, excluding m_0
for $m \leftarrow m_1$ to m_t **do**
  $\vec{v} \leftarrow \arg\min_{\vec{w}^*} |m - \mathrm{d}(\vec{x},\vec{w}^*)|$ // optimum vector at m, starting at $\vec{w}^* = \vec{w}$
  $\vec{\Delta} \leftarrow \vec{v} - \vec{w}$ // differential displacement
  $\vec{w} \leftarrow \vec{w} + \vec{\Delta}$ // move on to identified location $\vec{w} = \vec{v}$
  $\vec{b} \leftarrow \vec{b} + \vec{\Delta}$ // integrate changes per attribute
  $g \leftarrow g + \sqrt{\langle\vec{\Delta}\rangle^2}$ // line integral
end for
return $g, \vec{b}$

Distance pursuit A pragmatic solution to traverse the optimum path between a source vector $\vec{w}$ and a target vector $\vec{x}$ can be formulated in an iterative manner. This iterative procedure is outlined in Algorithm 1 and in principle is illustrated in Fig. 4.2.

First, a monotonic distance sequence $\vec{m} = \{m_0 = \mathrm{d}(\vec{x},\vec{w}),\ldots,m_t = \mathrm{d}_{target}\}$ from the initial vector distance m_0 to the maximum possible degree of similarity d_{target} is created with $\mathrm{d}_{target} = 0$ for metrics and divergence measures and $\mathrm{d}_{target} = 1$ for Pearson correlation. An equidistant sampling of $t = 10$ sub-intervals, such as done in this work, is pragmatic but not mandatory. The vector $\vec{w}$ moves along the minimum path following increasing steps of similarity towards the target vector $\vec{x}$. During the transformation of $\vec{w}$, the two quantities are collected:

1. g, the overall line integral summing up path fragment lengths and
2. $\vec{b}$, the integrated differential attribute vector.

Thus, a piecewise linear approximation in n-dimensional Euclidean space is conducted to effectively assess attribute properties of the data under the distance measure of interest.

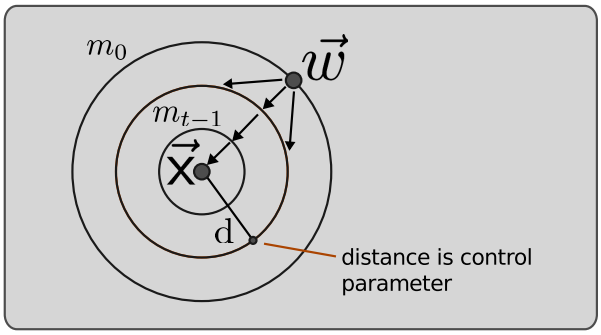

Figure 4.2: Euclidean illustration of the distance pursuit principle.

Line 5 of the Algorithm 1 provides the important identification of the next position of vector $\vec{w}$ for getting a bit more similar to vector $\vec{x}$. Gradient-based optimization methods can be used for minimizing the distance discrepancies between the current position and the next step of the target distance imposed by line 4. For distances $\mathrm{d}(\vec{x}, \vec{w}^*)$, the Minkowski distance (B.7), the Pearson correlation (B.9), and the γ-divergence (B.11), see Appendix , are utilized in this method. The gradient of the arg min operation, required for optimization, is

$$\delta = -\mathsf{sign}(s - \mathrm{d}(\vec{x}, \vec{w}^*)) \cdot \partial \mathrm{d}(\vec{x}, \vec{w}^*) / \partial \vec{w}^* \,. \tag{4.1}$$

Alternatively, a least squares expression can be employed in line 5, but it tends to generate numerical underflows during convergence.

Common gradient-based methods find zero discrepancy solutions desired in line 5. Yet, since optima for reaching a given similarity s are not unique, only minimum norm results for Δ are valid to get minimum path lengths. Else, for example with Minkowski metrics usually two points along the search line would yield valid optima at distance s to the target vector $\vec{x}$. Possible oscillations would be integrated out in line 8 for attribute variability, but the line integral in line 9, based on repeated calculations of $\langle\vec{\Delta}\rangle^2 := \langle\vec{\Delta}, \vec{\Delta}\rangle$, would be over-estimated.

Different gradient-based optimizers were tried using a reference implementation of Minkowski metrics with line integrals being standard Euclidean distance and attribute variability being standard variance, irrespective of the choice of the metric order p. Memory-limited Broyden-Fletcher-Goldfarb-Shanno (BFGS) turned out to provide the best mix of speed, memory requirement, and accuracy, in comparison to full BFGS, conjugate gradients, and steepest gradient descent.

4.1.3 Generalized Partial Covariance

The result of the distance pursuit algorithm is used as building block in a general formula for measuring the attribute variability of a dataset $\mathsf{X} = (x_{lk})_{l=1\ldots m,\, k=1\ldots n}$ with m data vectors (in rows) containing n attributes. Considering the reformulated text book term of standard

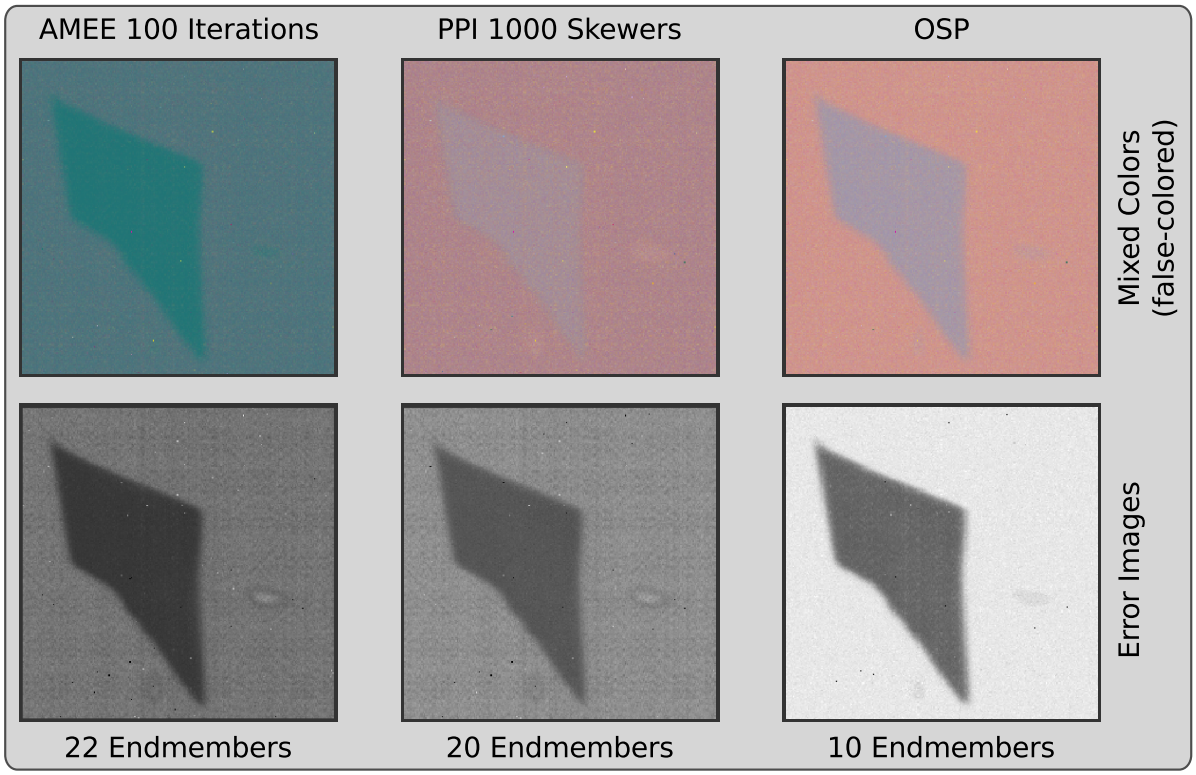

Figure 4.8: Three results that have been achieved with the semi-automatic endmember determination are compared. As can be seen, the reconstruction quality of AMEE (left), PPI (middle), and OSP (right) is quite comparable. But, in all cases the reconstruction quality is not fully satisfying, since all error images still reveal high error values.

4.2.4 Summary

This section has presented the first part, the semi-automatic endmember extraction, of the proposed visual analysis approach for the generic identification of constituent spectra. The here discussed first part mainly has addressed the challenge to achieve a proper parameterisation for endmember extraction algorithms, if necessary. Without discussing details of the visualization of the second part, the discussed usage examples have already shown the general potential of visual feedback to find the best initial endmember set by parameter fine-tuning. The details of the second part, the manual refinement of the endmember set, are subject in section 5.1.2, thus, to mainly tackle cases where these algorithms are not able to determine a reliable set of constituents. Beside these quality aspects of a set, also the runtimes of the endmember extraction algorithms for datasets with different spatial as well as spectral resolution were discussed. This discussion has turned out that these algorithms can be rather slow, therefore should preferably used as preprocessing in a visual analysis approach.

Moreover, this section already has revealed one major circumstance, i.e. outliers, in the

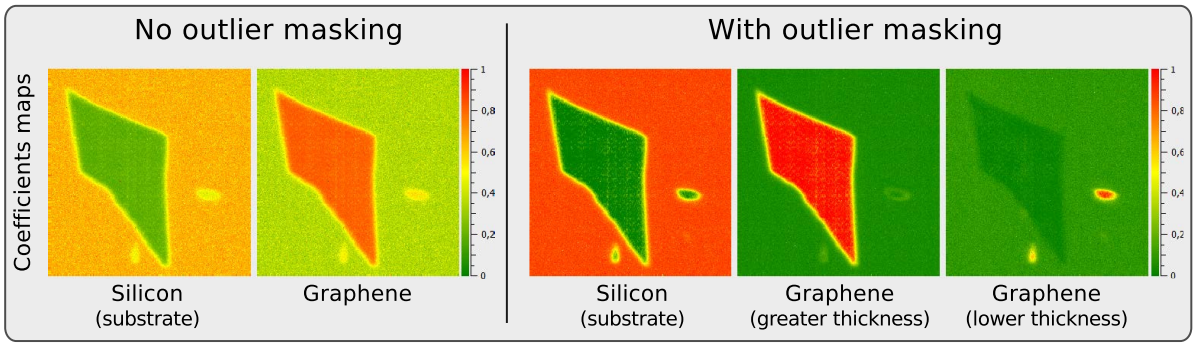

Figure 4.12: The coefficient maps for both, without *(left)* and with outlier masking *(right)*. All images are normalized. The lower values, that are poor representations of the selected material, are represented by green, while high values, indicating proper material assignments, are colored red.

4.4 Unmixing Coefficients for Interactive Applications

Beside the important determination of a proper set of endmembers, the LSU reconstruction requires an inversion process in order to achieve the necessary coefficients $\alpha_j(x,y)$ for the endmembers $\vec{v}_j$ in each pixel. As seen in Sec. 1.2.2, typically both physical constraints, ANC and ASC, are enforced to achieve physical plausibility. In this case, the calculation of the coefficients typically can be very expensive, especially for complex high-dimensional multispectral data with a large set of endmembers [SL11]. Therefore, interactive applications should utilize the LSU as preprocessing and focusing on the exploration of the static results. But, when the exploration leads to the result that a modification of the endmember set is necessary, then an analyst is interested in getting a fast response when modifying the set. Typically, modifications on a set of endmembers are done in a progressive way, which implies a frequent usage of inverse operations. Thus, this section presents three approaches that allow a more efficient utilization of LSU in interactive applications, i.e. visual analysis-based approaches.

Starting with an overview of the related work in section 4.4.1, the next section discusses a progressive utilization of the inversion step. The section 4.4.3 shows a method for the prediction of new coefficients in case of modification of the endmember set and section 4.4.4 discusses an efficient OSP-based solver for the computation of ANC coefficients. Results of the last two approaches are presented in section 4.4.5.

4.4.1 Background

Applying UCLSU, e.g. using least-squares methods like Moore-Penrose pseudoinverse, achieves fast results, but do not incorporate the physical plausibility as when impose ANC and ASC. UCLSU can result into negative coefficients which consequently lead to unnatural negative endmembers. But, as discussed above, if the non-negativity constraint is

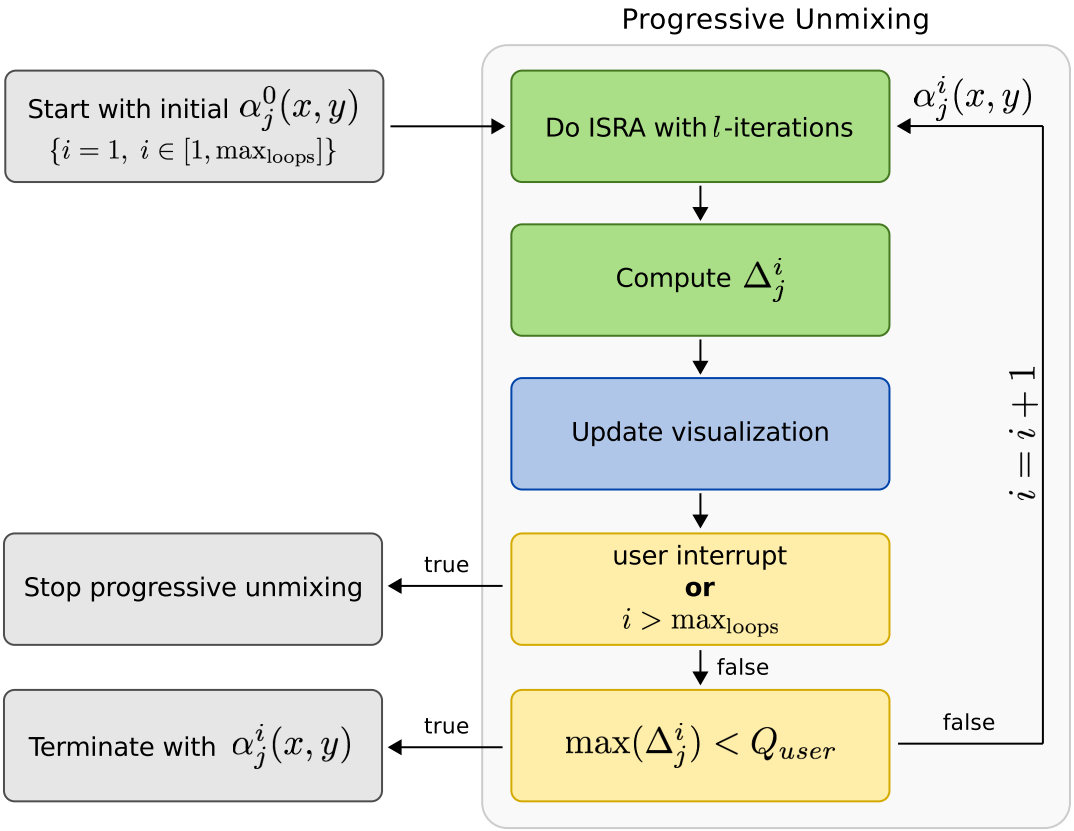

Figure 4.13: The workflow of the progressive unmixing, where Q_{user} is a quality threshold for the averaged relative l_2-error Δ_j^i.

claimed, non-negative methods, e.g. [CH00, HCIC01], are involved which can be computationally very expensive by itself [VG08]. Furthermore, ISRA Eq. (B.13) [DWM86, DP93], which guarantees convergence in a finite number of iterations, can be applied. Recently, Sánchez et al. [SMPC10] presented a CUDA-based implementation of ISRA that has turned out to be a great improvement in terms of runtime. In a test scenario, the authors gained a significant speedup of the GPU version (∼126 sec) compared to a sequential CPU implementation (∼3351 sec). But in terms of an interactive exploration, it is far too slow.

4.4.2 Progressive Unmixing Scheme

In interactive applications, a key-factor is the visual feedback which has to enable a user to sufficiently steer the application and to extract the significant information. However, when a set of endmembers V is found or an existing set is modified the unmixing has to be applied in order to update the visual feedback, e.g. the complimentary visualization described in Sec. 5.1. But, as discussed before, the inversion step for NCLSU as well as FCLSU typically is too time consuming for interactive approaches. Therefore, a progressive unmixing scheme

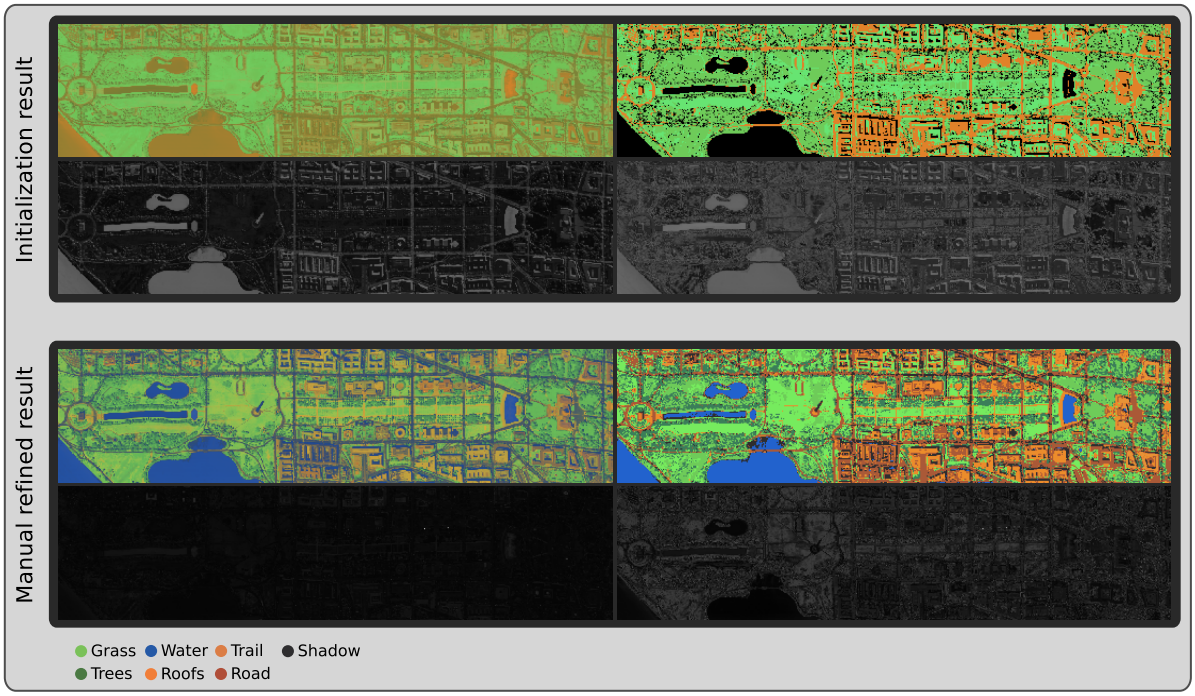

Figure 5.9: The result of the presented approach for the *Washington DC Mall* data (see Appendix A). The columns show the result of the linear spectral unmixing and nearest neighbor visualization for the initial result, based on OSP limited to 10 endmembers, *(top)* and the manual refined result *(bottom)*. Both results are shown with corresponding grayscaled error images respectively beneath.

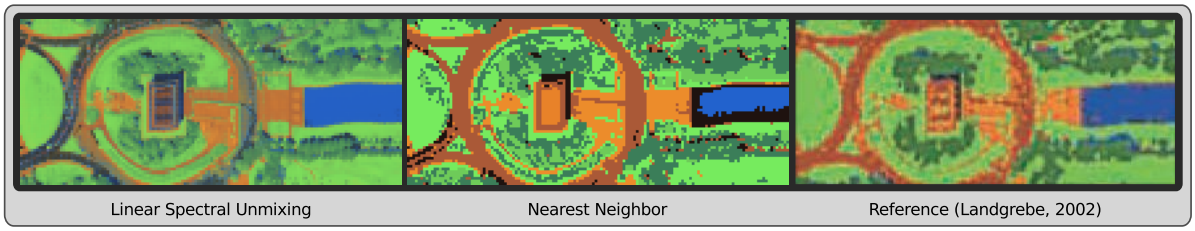

Figure 5.10: This figure shows a close-up of the final result around the area of the "Lincoln Memorial". Compared to the nearest neighbor visualization *(middle)*, smooth and detailed structures are visible in the linear spectral unmixing *(left)*. Furthermore, it is obvious that the corresponding endmember of *shadow* has too high influence in the convex combinations for the road and the roof of the Memorial. For comparison, also a close-up of the corresponding area of the result from [Lan02] is shown in the *right*.

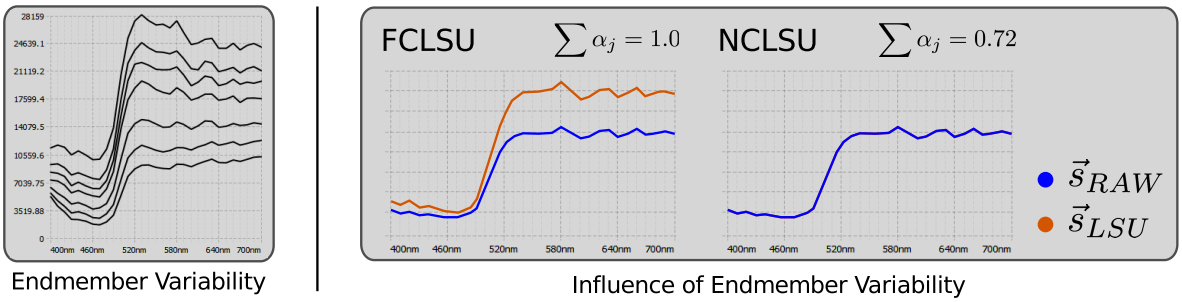

Figure 5.16: The left figure shows an example for the variability in an endmember class. The variability based abundance estimation error in FCLSU is illustrated on the right, in comparison to NCLSU.

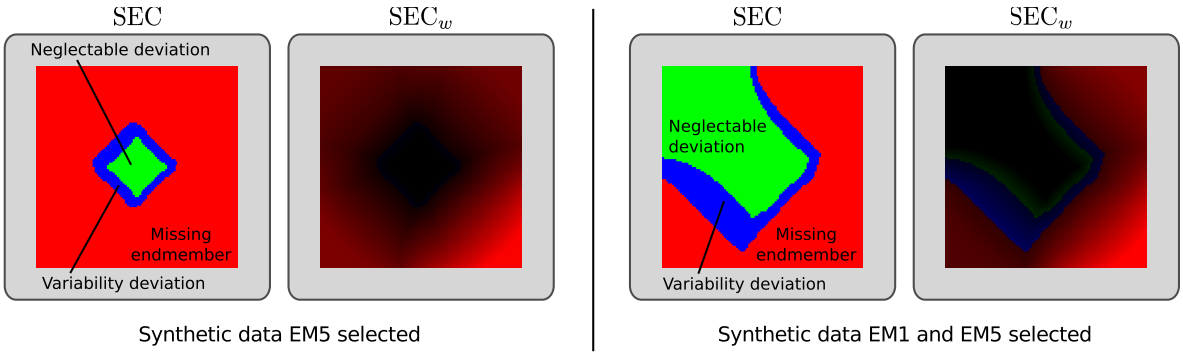

Figure 5.17: Two examples of the proposed spectral error classification. Here, the first example is based on the LSU-result already presented in Fig. 5.13 (left). Moreover, a second scenario is depicted in order to better illustrate the weighting in SEC_w

in order to easier discover pixels that have major deviations. Here, q is again the number of endmembers and for a pixel that is classified as *missing endmember*, the normalized $d^{NC}(x,y)$ is used as weighting factor for $sec(x,y)$. In all other cases, the endmember variability is expressed in $sec_w(x,y)$ by the difference between the sum of the coefficients of the endmembers of the NCLSU $\alpha_j^{NC}(x,y)$ and the FCLSU, which is one. Consider again Fig. 5.17 for an example of this weighting scheme.

5.2.5 Interactive Exploration

The graphical user interface of this supplemented visual analysis approach is shown in Fig. 5.18 and consists of several linked views. Beside several 2D data visualizations, e.g. sRGB color representation by the usage of CIE standard observer color matching functions (see Appendix B.3), the global visualizations mainly consists of the two proposed **expressive spectral error visualizations** for global guidance to identify pixels for further local investigations. The local visualizations allow the analysts to explore the currently selected pixel to validate the reconstruction, e.g. by exploring the composition of a mixed spectrum. In the reconstruction and composition views, the white line shows the raw spectrum $\vec{s}_{RAW}(x,y)$ and the

Appendix A

Datasets

Multispectral Scene Data

Balloons

Spatial: 512×512
Spectral: 31 bands
Range: 400nm–700nm
Device: LCTF

Source: CAVE

sRGB-image

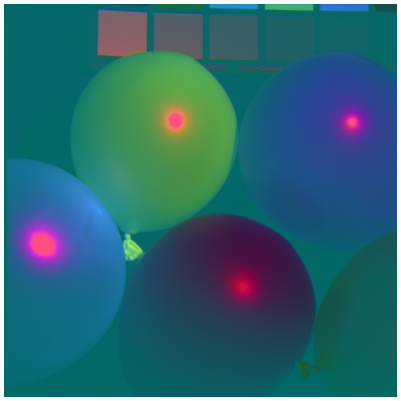

PCA-based false-color image

Cucumber

Spatial: 416×408
Spectral: 51 bands
Range: 450nm–950nm
Device: LCTF

Source: CGMM

sRGB-image

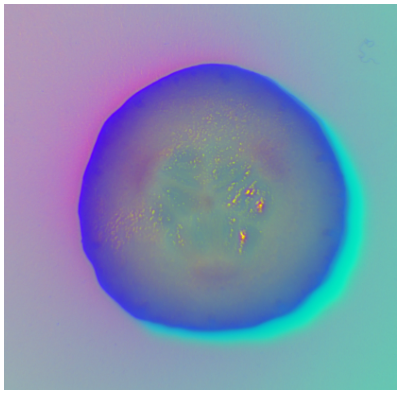

PCA-based false-color image

Egyptian statue

Spatial: 240×450
Spectral: 31 bands
Range: 400nm–700nm
Device: LCTF

Source: CAVE

Note: The dataset was cropped to the area of the statue.

sRGB-image

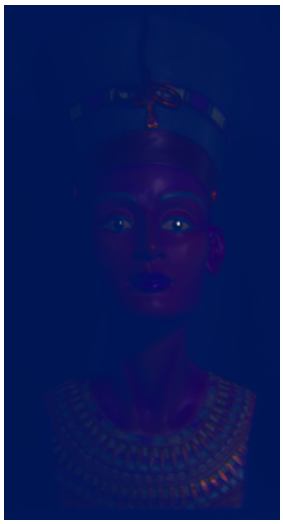

PCA-based false-color image

Flowers

Spatial: 512×512
Spectral: 31 bands
Range: 400nm–700nm
Device: LCTF

Source: CAVE

sRGB-image

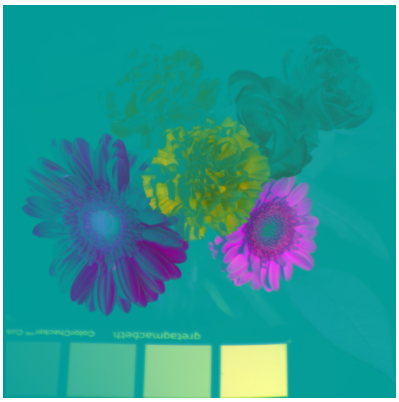

PCA-based false-color image

Glass tiles

Spatial: 512×512
Spectral: 31 bands
Range: 400nm–700nm
Device: LCTF

Source: CAVE

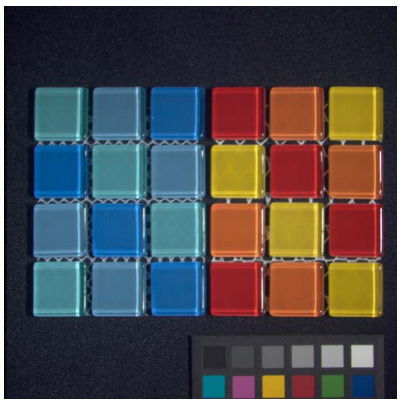

sRGB-image

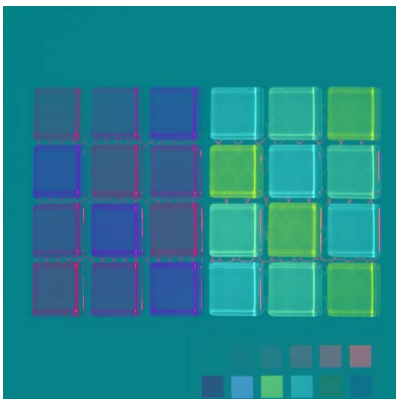

PCA-based false-color image

Lemons

Artificial *(left)* and real *(right)* lemons

Spatial: 512×512
Spectral: 31 bands
Range: 400nm–700nm
Device: LCTF

Source: CAVE

sRGB-image

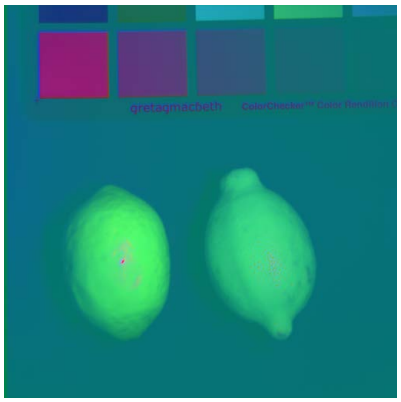

PCA-based false-color image

Peppers

Artificial and real peppers

Spatial: 512×512
Spectral: 31 bands
Range: 400nm–700nm
Device: LCTF

Source: CAVE

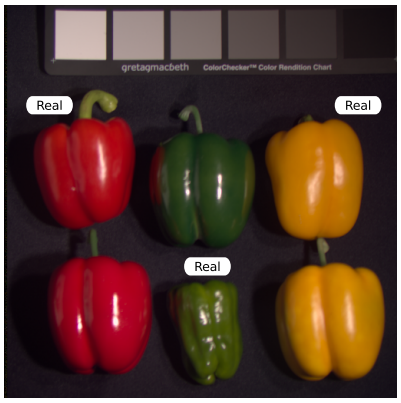

sRGB-image

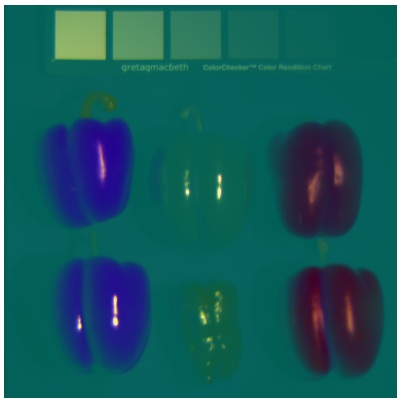

PCA-based false-color image

Watercolors

Watercolors painting

Spatial: 480×376
Spectral: 31 bands
Range: 400nm–700nm
Device: LCTF

Source: CAVE

Note: The dataset was cropped to the area of painting.

sRGB-image

PCA-based false-color image

Five Endmembers

Spatial: 100×100
Spectral: 473 bands
Range: 200nm–3000nm

Source: USGS

Note: Four constituents were placed at the four corners and one constituent was placed at the center position.

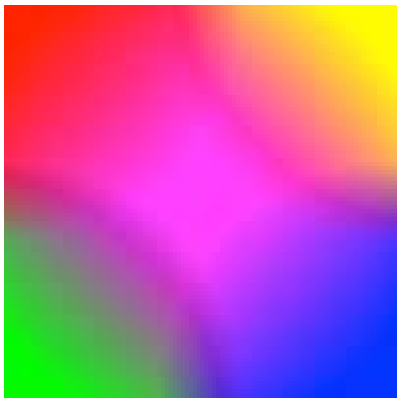

Conceptional image

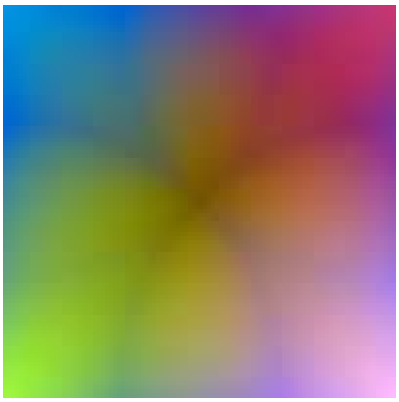

PCA-based false-color image

Four Endmembers

Spatial: 100×100
Spectral: 473 bands
Range: 200nm–3000nm

Source: USGS

Note: In each corner one constituent was placed.

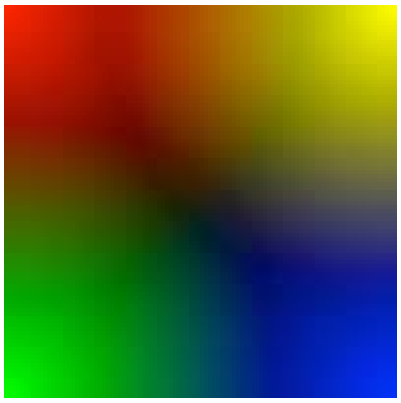

Conceptional image

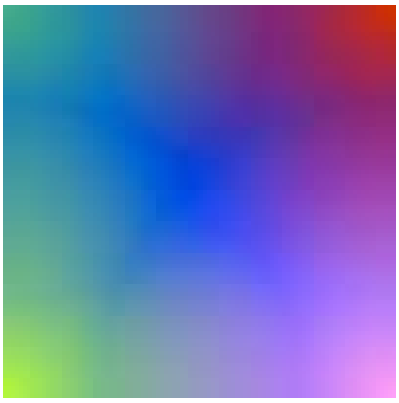

PCA-based false-color image

Sources:

CAVE	`http://www.cs.columbia.edu/CAVE/databases/multispectral`
CGMM	The CRM datasets are kindly provided by the Research Group for *Computer Graphics and Multimedia Systems* at the University of Siegen (`http://www.cg.informatik.uni-siegen.de/en`).
HiFreq	The CRM datasets are kindly provided by the Research Group for *High Frequency and Quantum Electronics* at the University of Siegen (`https://www.hqe.eti.uni-siegen.de/en`).
MultiSpec	`https://engineering.purdue.edu/~biehl/MultiSpec/hyperspectral.html`
NASA	`http://aviris.jpl.nasa.gov/html/aviris.freedata.html`
USGS	`http://speclab.cr.usgs.gov/spectral.lib06/ds231/datatable.html`